TRANSITION METAL OVERLAYERS ON TUNGSTEN AND MOLYBDENUM (110) SURFACES

by

Vinod Ramji Dhanak

A Thesis submitted for the Degree of Doctor of Philosophy of the University of London and the Diploma of Membership of Imperial College of Science and Technology.

Department of Physics
Imperial College of Science and Technology
London, February 1982

In memory of my Father

ABSTRACT

The structure and properties of sub-monolayer and monolayer films of rhodium on the (110) surfaces of tungsten and molybdenum have been studied in atomic detail by field ion microscopy and low energy electron diffraction. Theoretical calculations of electronic structure have also been made for the rhodium tungsten system and are used to account for some important aspects of the behaviour of rhodium.

The mobility and thermal stability of individual adatoms and adatom clusters were studied in the field ion microscope. Rhodium adatoms on both tungsten and molybdenum (110) surfaces formed linear chain clusters aligned along the substrate <111> directions prior to the formation of two-dimensional islands, but chain clusters on molybdenum (110) were significantly less stable than on tungsten (110). Mobility on tungsten (110) surfaces decreased with increasing cluster size and the activation energy for migration showed the trend $Rh < Rh_3 < Rh_4$. The activation energy for migration of single adatoms on molybdenum (110) surfaces was less than on tungsten (110) surfaces. Rhodium dimers were rather unstable on both the surfaces.

Monolayer films developed by the growth of islands after chain to island transformation on molybdenum (110) surfaces and by island nucleation at chain-chain intersection on tungsten (110) surfaces. Temperatures for rearrangement and dissociation of clusters and islands were determined. Low energy electron diffraction patterns showed that ordered structures formed at lower temperatures on molybdenum (110) than on tungsten (110) surfaces. Sub-monolayer coverages on tungsten (110) resulted in streaks in the LEED pattern, indicative of chain arrays in the adlayer. Similar LEED patterns were observed on both the surfaces with increasing coverage, including patterns from a pseudomorphic

type of structure for the monolayer, satellite spot patterns arising by multiple diffraction from a strained rhodium (111) layer and the substrate, and ordered patterns from well oriented rhodium (111) crystals. The results are indicative of a Stranski-Krastanov type of growth mode.

To account for the linear-chain structures for clusters, which dictates the nature of island nucleation, the electronic structure and energy of small clusters of tungsten and rhodium on tungsten (110) surface have been calculated within a d-electron tight-binding approximation using the recursion method. The calculations demonstrate the important role of non-bonding electrons in orbitals localised in the ad-layer plane in determining the stable overlayer structure when, as for rhodium, the adsorbate d-shell is more than half-filled.

ACKNOWLEDGEMENTS

I would like to express my gratitude to Dr. D.W. Bassett and Dr. P.J. Dobson for their continual guidance and invaluable assistance throughout the course of this work. I am also indebted to Dr. David Pettifor for his help with the tight-binding calculations.

I would also like to thank Dr. D.O. Hayward for kindly allowing the use of laboratory facilities and Mr. G. Millhouse for printing the photographs in the text.

Financial support of the Science Research Council is gratefully acknowledged.

CONTENTS

		Page
	ABSTRACT	3
	ACKNOWLEDGEMENTS	5
1.	THE GROWTH OF VAPOUR-DEPOSITED METAL FILMS ON TRANSITION METAL SURFACES	11
	1.1 Introduction	11
	1.2 Studies on microcrystals	14
	1.2.1 Effect of surface structure on diffusion	17
	1.2.2 Effect of adatom binding on diffusion	21
	1.2.3 The nature and properties of adatom clusters	22
	1.2.4 Formation of monolayer islands	28
	1.3 Studies on large single crystals	30
	1.3.1 The initial layers	31
	1.3.2 The dense overlayers	35
	1.4 The present study	38
2.	FIELD ION MICROSCOPY	40
	2.1 Basic principles	41
	2.2 Field ionization	43
	2.3 Imaging	47
	2.4 Field evaporation	49
	2.5 Practical aspects of FIM	54
3.	LOW ENERGY ELECTRON DIFFRACTION AND AUGER ELECTRON SPECTROSCOPY	57
	3.1 Low energy electron diffraction	57
	3.1.1 Kinematic theory	59
	3.1.2 Coherence width	66

		Page
3.1.3	LEED patterns from disordered structures	67
3.1.4	Satellite spot patterns	72
3.2	Auger electron spectroscopy	74
3.2.1	The Auger process	74
3.2.2	Principles of detection of Auger electrons	77
3.2.3	Practical aspects of AES	80
4.	EXPERIMENTAL	87
4.1	Field ion microscopy	87
4.1.1	The apparatus	87
4.1.2	Evacuation procedure	90
4.1.3	Specimen preparation	93
4.1.4	Image observation	94
4.1.5	Detection of contaminants	100
4.1.6	Tip temperature measurement and precision	101
4.2	Experimental studies by FIM	103
4.2.1	Measurement of single adatom diffusion	103
4.2.2	Analysis of diffusion data	105
4.2.3	Cluster diffusion	108
4.2.4	Cluster stability	109
4.2.5	Film growth	111
4.3	Low energy electron diffraction and Auger electron spectroscopy	112
4.3.1	The apparatus	112
4.3.2	Specimen holder	115
4.3.3	Rhodium evaporators	118
4.3.4	The LEED optics	120
4.3.5	The Auger analysers	121

Page

4.3.6 Evacuation procedure 123

4.3.7 Gas handling lines 124

4.3.8 Specimen preparation 126

4.3.9 Crystal temperature measurement 135

4.3.10 Rhodium coverage determination 137

4.4 Experimental studies by LEED/AES 138

4.4.1 Deposition of rhodium on clean surfaces 138

4.4.2 Effect of gas adsorption on the rhodium overlayers 139

4.4.3 Surface diffusion of rhodium overlayers 140

5. EXPERIMENTAL STUDIES BY FIELD ION MICROSCOPY: RESULTS 142

5.1 Rhodium on tungsten 142

5.1.1 Cluster structure 142

5.1.2 Cluster mobility 146

5.1.3 Cluster stability 154

5.1.4 Film growth 160

5.2 Rhodium on molybdenum 169

5.2.1 Adatom mobility 169

5.2.2 Adatom cluster behaviour 169

5.2.3 Film growth 177

6. EXPERIMENTAL STUDIES BY LOW ENERGY ELECTRON DIFFRACTION AND AUGER ELECTRON SPECTROSCOPY: RESULTS AND INTERPRETATION 181

6.1 Rhodium on tungsten 181

6.1.1 AES characterization of Rh film growth 181

6.1.2 LEED observations of Rh overlayer structures 188

6.1.3 Effect of oxygen on the growth of Rh films 204

		Page
6.2	Rhodium on molybdenum	210
6.2.1	AES characterization of Rh film growth	210
6.2.2	LEED observations of Rh overlayer structures	213
6.2.3	Effect of oxygen on the growth of Rh films	223
6.2.4	Carbon-monoxide adsorption on Rh(111) overlayer	226
6.3	Summary of LEED/AES results	228
7.	A TIGHT BINDING MODEL CALCULATION	231
7.1	Introduction	231
7.2	Details of the calculations	234
7.2.1	The tight binding Hamiltonian	234
7.2.2	Adsorption geometry	236
7.2.3	Evaluation of the recursion coefficients	236
7.2.4	Evaluation of integrals and self-consistency	239
7.2.5	Accuracy in the calculation	245
7.3	Results and discussion	245
7.3.1	The pure surface	245
7.3.2	Local densities of states for tungsten adatoms	247
7.3.3	Orbital and bond energies for tungsten adatoms	252
7.3.4	Densities of states and bond energies for rhodium on W(110)	254
7.3.5	The relative stability of linear and triangular clusters of tungsten and rhodium	258
7.3.6	Calculation of a core repulsion term	269
7.3.7	The d-electron contribution to diffusion energies	271

		Page
8.	DISCUSSION	273
	8.1 Single adatom diffusion	273
	8.2 Properties of adatom dimers	276
	8.3 Adsorbate clustering	280
	8.4 High coverage film structure	285
	8.5 Concluding remarks	288
APPENDICES		289
REFERENCES		301

1. THE GROWTH OF VAPOUR-DEPOSITED METAL FILMS ON TRANSITION METAL SURFACES

1.1. Introduction

The surface characteristics of overlayers of one metal condensed on another are of considerable importance in many technological situations. Crystal growth, the preparation of chemically selective catalysts or electron emitting surface layers and thin film coating are just a few examples. To understand such systems and to establish rules by which their properties may be chosen by design, it is necessary to start from a knowledge of the atomic interactions at the interface and the mechanisms by which the films grow. This information is best obtained from studies of film growth on well-defined surfaces, for which single crystal surfaces are ideally suited. Many such studies have been reported and some important aspects of them are described below.

From an atomistic point of view, figure 1.1, film growth begins with an atom arriving at a surface from the vapour phase. On becoming trapped in the surface potential well, the atom is thermally accommodated. Subsequently, if thermally activated, such an adatom may gain enough energy to surmount the barriers in the surface potential between sites so that it can diffuse by hopping from one site to another. Provided the adatom neither evaporates nor is lost from the surface by other means (for example by local place-exchange with surface atoms to form a reconstructed surface or by diffusing away from the surface into the bulk) its migration over the surface may result in encounters with other adatoms. If the adatom-adatom interaction is favourable,

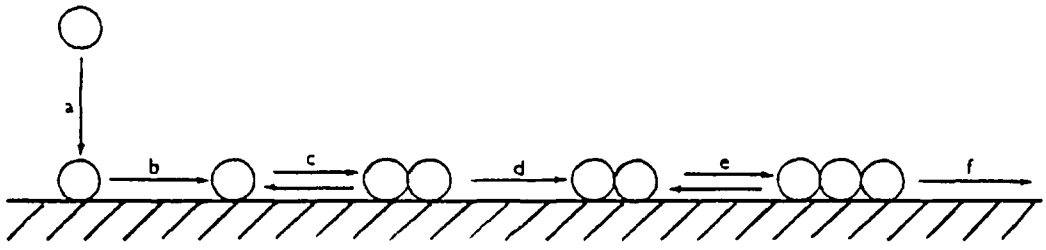


Figure 1.1 Atomic Process of Cluster Formation and Growth on a Substrate. (a) Arrival, (b) adsorption and migration of adatom, (c) formation and dissociation of cluster, (d) migration and rearrangement of cluster, (e),(f) formation and dissociation of larger clusters and further growth.

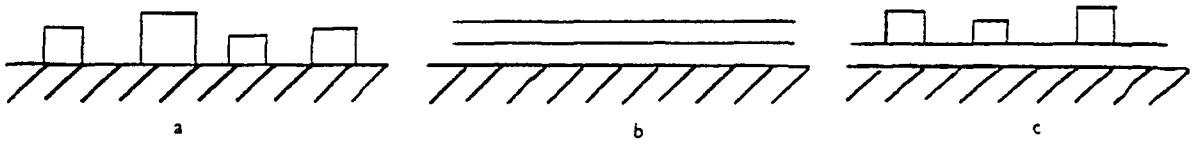


Figure 1.2 Basic Growth Modes. (a) Island or Volmer-Weber growth, (b) layer-by-layer or Frank-Van der Merwe growth and (c) layer(s) followed by islands or Stranski-Krastanov growth.

such collisions can produce clusters, that may grow further to form the nuclei for subsequent growth of monolayer islands. On a macroscopic surface, many such islands form and the overlayer then develops by the islands either growing into contact or coalescing during migration.

Adatom-adatom and adatom-substrate interactions, E_{aa} and E_{as}, in principle determine the structure and growth characteristics of the overlayer. On single crystal surfaces the growth may result in ordered overlayer structures, termed epitaxial layers, which bear a specific structural relationship to the substrate lattice. Epitaxial growth processes may be described in terms of a simple scheme which distinguishes between three basic growth modes[1,2], figure 1.2. The particular growth mode by which an overlayer is formed depends on the competition between E_{aa} and E_{as}. Qualitatively, if $E_{aa} >> E_{as}$ the critical cluster size for nucleation may be just one or two atoms and three-dimensional islands form readily, (figure 1.2a). This is known as the Volmer-Weber growth mode, which occurs most frequently for metals on alkali-halide crystals. For the case $E_{aa} < E_{as}$, growth proceeds layer-by-layer by the Frank-Van der Merwe mechanism (figure 1.2b). Intermediate between these cases is the Stranski-Krastanov growth mode in which at least one stable layer is formed, followed by growth of three-dimensional crystallites (figure 1.2c). In this case the stable layer(s) effectively screen the substrate from adatoms condensed on top and the interaction, E'_{aa}, of these adatoms with the adatoms of the adsorbed layer is such that $E_{aa} > E'_{aa}$. The Stranski-Krastanov growth mode is frequently observed in metal-metal systems and is found to be critically temperature dependent. Thus, at low temperatures layer-by-layer growth

is often observed, while at elevated temperatures growth proceeds in the Stranski-Krastanov mode.

In metal-metal systems the substrate has a strong influence on the structure of the initial "transition" layer(s). The initial layer may conform to the substrate surface structure, in which case it is pseudomorphic, or it may adopt structures in between that of the substrate surface and the bulk adsorbate that are to some degree strained. The evidence for these ideas about film growth in vapour deposition on metallic single crystal substrates come from a variety of experimental techniques. The experiments can be split conveniently into two groups: (i) those using microcrystals as the substrate and (ii) those using large single crystals. Field ion microscopy (FIM) and field emission microscopy (FEM) form the first group, while low energy electron diffraction (LEED), reflection high energy electron diffraction (RHEED), scanning electron microscopy (SEM), Auger electron spectroscopy (AES) and thermal desorption spectroscopy (TDS) are included in the second group. A brief description of all these techniques has been given by Prutton[3].

1.2 Studies on microcrystals

In the FEM[4] and FIM[5,6] electrons or ions are used to obtain a high resolution image of the surface of a microscopic hemispherical single crystal tip. The growth of metal films vapour deposited on the tip surface can be studied directly through the change in image contrast produced by the adsorbate. In FEM the overlayer is imaged at a resolution of 20-30 Å, mainly through the change in the work function due to the adsorbate. At this resolution layer-by-layer growth and the formation of discrete crystallites can be readily observed. For

example, Jones[7] has shown for Cu on W that multilayer formation precedes the appearance of discrete crystallites, which were observed to nucleate preferentially on the stepped vicinal regions around the (100) face. A disadvantage of the method is that the resolution is not sufficient for the determination of the overlayer structure, except when discrete crystallites become sufficiently large to show their orientation in the FEM patterns. Thus, reports of pseudomorphic type structures for the overlayers should be treated with caution, except possibly for Ni on W(110) for which Jones and Martin[8] were able to determine the angles of monolayer island edges. Another disadvantage of the method is that the behaviour of adsorbate metal on one crystal plane cannot be isolated from that on other faces. The microcrystals are extremely small so that during annealing, the adsorbate may be transported readily from one plane to another. This creates problems in determining the coverage on a given plane[9]. Nevertheless, FEM studies have provided interesting information on both the changes in surface structure that occur after annealing, such as the interfacial reconstruction in the Ni-W system[10], and on the processes of transport and desorption of the adsorbate[7]. The growth mode and orientation relationship of crystallites have also been determined for a number of systems. For example, Stranski-Krastanov type of growth has been observed for Ni on W(110)[8,10], although the thickness of the initial layers is not known for certain. The crystallites show the orientation Ni(111)||W(110) with Ni<211>||W<1$\bar{1}$0>. Similar results have been obtained for Cu on W(110)[11], which also shows the orientation Cu<211>||W<1$\bar{1}$0>. In contrast, Fe on W appears to form crystallites in the Volmer-Weber growth mode[12].

Experiments directly analogous to those carried out in the FEM have also been carried out using FIM in which the resolution of 3-4 Å obtained by ion imaging at cryogenic temperatures is sufficient to show overlayers in atomic detail. Such studies, for instance, have shown that thick layers of Ir, Pd, Pt and Rh deposited on Ir and Rh tip surfaces[13] at temperatures above some well defined epitaxial temperature have a high degree of structural perfection. FIM imaging has also been used for Ni on W[8,10] to confirm the observations of FEM studies. However, the disadvantage that the behaviour of the overlayer on one face is not independent of that on another remains in these FIM studies. Also, the resolution is not sufficient to deduce the overlayer structure unambiguously, especially for the close-packed planes such as the W(110) which is of interest here. For instance, reports by Jones and Martin[8] that the first monolayer of Ni conforms to the substrate structure are not clear evidence of pseudomorphic structure. FIM images of thick Ni crystallites on W(110) have been observed[8] but the epitaxial orientation could not be deduced. Sugata and co-workers[14] have imaged Pt films on W but did not observe any crystallites on the W(110) plane. Deposition of Ir on Mo has been studied by Whitmell[15] who observed the epitaxial relation Ir(111)||Mo(110) with Ir<110>||Mo<111>, although this does not prove that this will also be the orientation of individual crystallites on Mo(110). Under the conditions of the experiments, it is likely that nucleation occurred on (110) steps.

The atomic resolution of the FIM is not used to the best advantage, however, in studies of the overall process of film growth on a hemispherical crystal. The unique value of the FIM is that it makes possible

the direct study of the individual atomic processes of film growth depicted in figure 1.1 of the preceding section. Individual adatoms may be vapour-deposited on atomically perfect single-crystal planes. It is then possible to study directly their diffusion, the interactions that lead to cluster formation and the growth of clusters of monolayers[16]. The results of studies of metal adsorbate diffusion and cluster properties have been reviewed recently by Bassett[17] and Ehrlich[18].

1.2.1 The effect of surface structure on diffusion

Field ion microscopy has been used to study single adatom self-diffusion and adsorbate diffusion on a variety of low-index planes of tungsten[19-30] (a body-centred-cubic metal), and rhodium[31], platinum[32] and nickel[33] (face-centred-cubic metals). The activation energy for adatom diffusion determined in these studies are presented in figures 1.3a and b.

These studies show that the dependence of adatom jump paths on surface structure is roughly consistent with a simple broken-bond model. The adatom moves in directions which involve least bond breaking and the smallest displacement perpendicular to the surface. For instance, the model successfully predicts the one-dimensional motion observed on the channelled b.c.c. (211) and (321) planes, and f.c.c. (113), (133) and (110) planes. Similarly, observations of two-dimensional diffusion on a flat plane, such as (110) tungsten, is also consistent with this model and Casanova and Tsong[34] have recently shown that the distribution of the diffusing tungsten adatoms is in accordance with their motion along the surface channels. However, such a simple

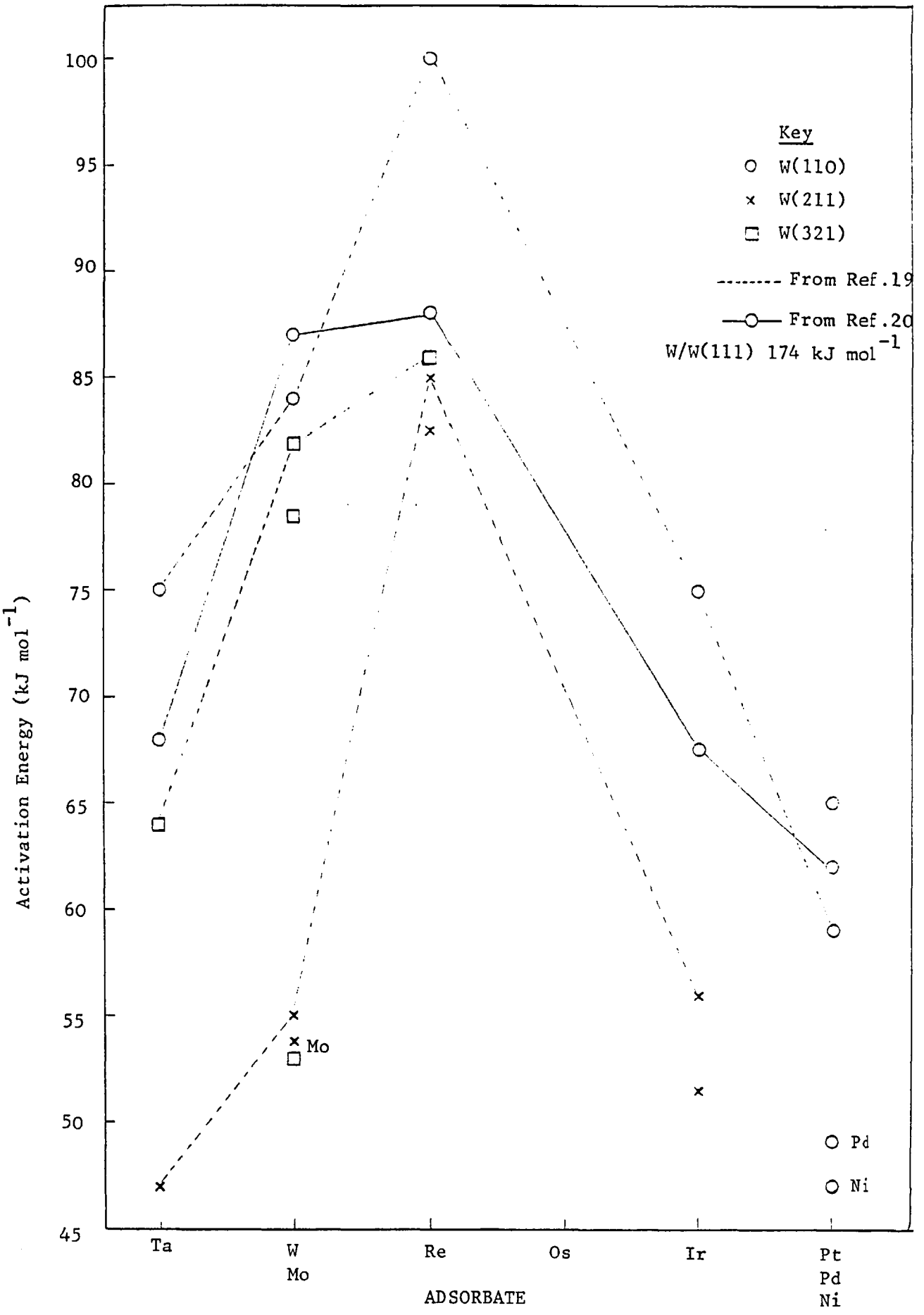


Figure 1.3a Activation Energy for Adatom Diffusion on Tungsten Surfaces. (From references 19-30).

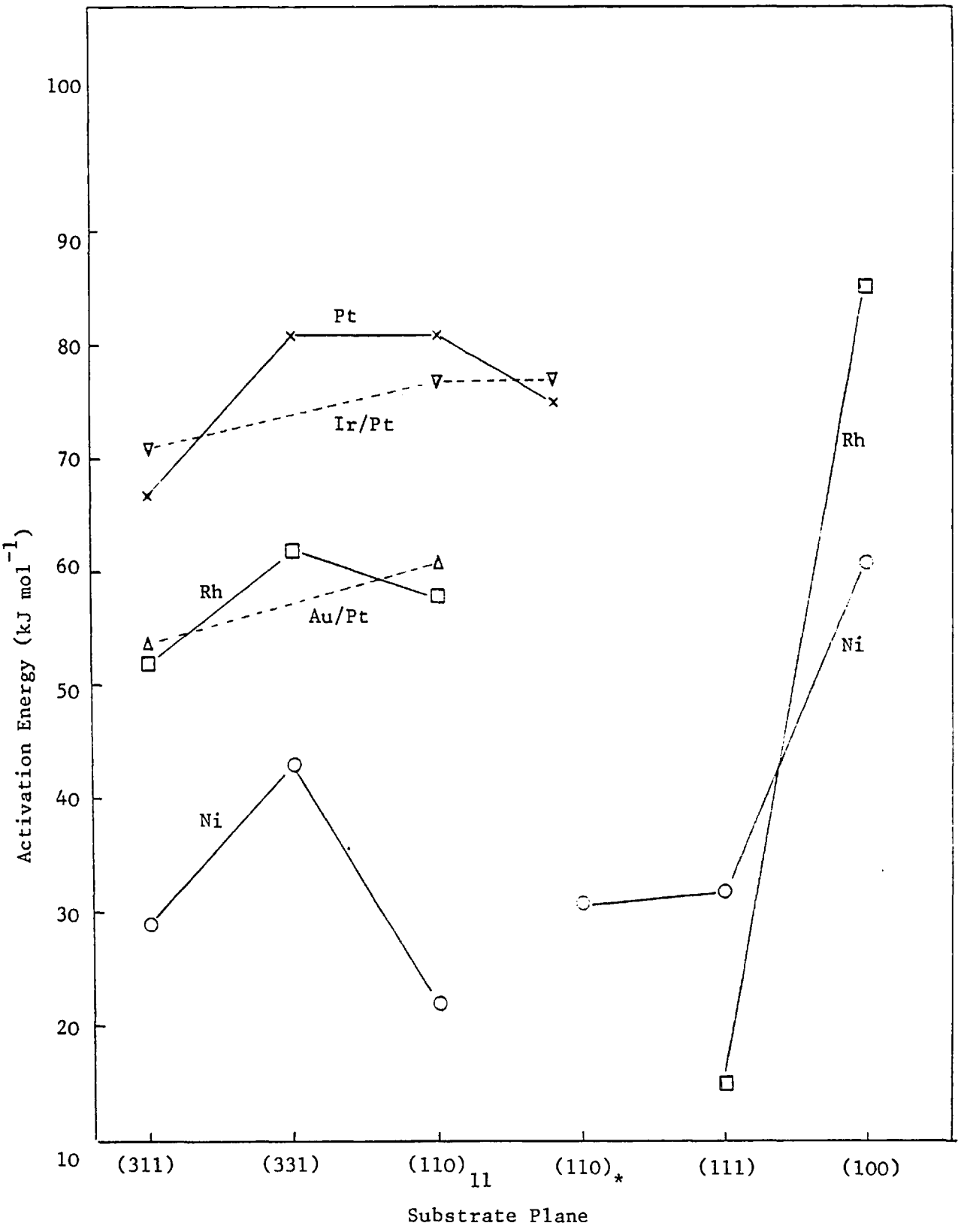


Figure 1.3b Activation Energy for Self-diffusion on f.c.c. Surfaces. The broken lines represent data for Ir and Au adatom diffusion on Pt surfaces. (From references 31-33).

model fails when considering the diffusion measurements in detail. For example, the order of decreasing diffusion energies is expected to show the trend (321) > (211) > (110) while the observed trend is (110) > (321) > (211). Similarly, for fcc metals such as rhodium, diffusion along (110) channels is expected to be easier than on (100) while the reverse is the case. The correct ordering of activation energies in pair-wise model calculations is obtained when lattice relaxations are included[35]. However, serious discrepancy still exists between calculated and experimental values of activation energies, especially on tungsten. The problem is that there is no satisfactory way of deciding how much relaxation should be included and recently Flahire and Graham[35] have concluded from their calculations that any agreement between such calculations and experiment is fortuitous.

The importance of lattice relaxations is further demonstrated by the unexpected observation of two-dimensional diffusion on the channelled (110) planes of platinum[32], iridium[36] and nickel[33]. For each of these metals it was observed that diffusion across the channel (termed cross-channel diffusion) occurred at a rate comparable to that for diffusion along the channel, although pair potential calculations show that adatom jumps over a channel wall require an extremely large activation energy compared to migration involving jumps along the channel. Subsequently, it has been shown in atom-probe studies[36] that cross-channel diffusion involves a place exchange mechanism in which a channel wall atom and the adatom are exchanged. Molecular dynamics calculations[47] show that the place exchange mechanism takes place by an unsymmetrical displacement of a channel wall atom and its replacement by the adatom.

1.2.2 Effect of adatom binding on diffusion

While surface structure plays a dominant role in determining the directional character of surface diffusion, the adatom-substrate interaction determines the magnitudes of the diffusion activation energies. These are effectively a measure of the change in binding energy along the jump paths between adjacent sites. The results for the diffusion of the 5d transition metal adatoms on tungsten show this as the electronic configuration of the adatom varies across the series (figure 1.3a). The diffusion activation energy increases to a maximum for Re and thereafter decreases. A similar trend has been observed by Plummer and Rhodin[37] for the binding energy of the 5d transition metal adatoms on various planes of tungsten, although the values were obtained from field desorption data and are therefore subject to considerable uncertainty[19]. The cohesive energy of the bulk transition metals also shows a similar trend, rising to a maximum near the middle of the series and falling thereafter. Qualitatively, the trend in the diffusion and binding energies has been explained as due to filling of bonding valence states up to Re and thereafter, anti-bonding states get filled, causing a gradual fall in the binding energies. A number of attempts have been made to calculate adatom binding energies theoretically. For example, Cyrot-Lackmann and Ducastelle[38] have used a tight-binding approach to calculate binding energies for a variety of transition metal adatoms on several low index planes of a range of transition metals. Although their model included only d-electrons, their results are qualitatively in agreement with the trend in diffusion and binding energies of the 5d metals on tungsten.

Diffusion activation energies obtained from mass-transfer experiments show a good correlation with bulk properties related to bond strength, for example melting temperature. In an analogous way single adatom diffusion energies have also been compared with bulk melting temperatures[17], although in this case a good correlation is not obtained. For example, activation energies for self-diffusion on Ni, Rh, Pt and Ir surfaces and adsorbate diffusion on W(110) surface show only an approximate scaling with bulk adsorbate melting temperatures, (figure 1.4). Nevertheless, in the absence of any reliable information on binding energies, such comparisons serve as a useful guide for correlating the diffusion data.

1.2.3 The nature and properties of adatom clusters

Migration of clusters has been studied in the FIM in a way directly analogous to the single adatom studies. Cluster migration is observed to involve frequent changes in cluster configuration. For example, Pt_2 dimers on W(110), which are observed in FIM micrographs to be aligned along the close packed W<111> directions, figure 1.5, often appear re-oriented after a diffusion interval[28]. On the channelled W(211) plane, the motion of adatoms in neighbouring channels is strongly coupled. Detailed diffusion studies have been performed for W_2,[39] Ir_2 [27] and Re_2 [24] on the W(211) plane and Pt_2 [28] on W(110). These studies show that the adatoms of the dimer are coupled by a weak mutual interaction and the diffusion mechanism involves sequential hopping of one adatom at a time. In contrast, Tsong and Casanova[40] conclude from the distribution of displacements for W_2 on W(110) that the hopping of the adatoms may be partly correlated in this case.

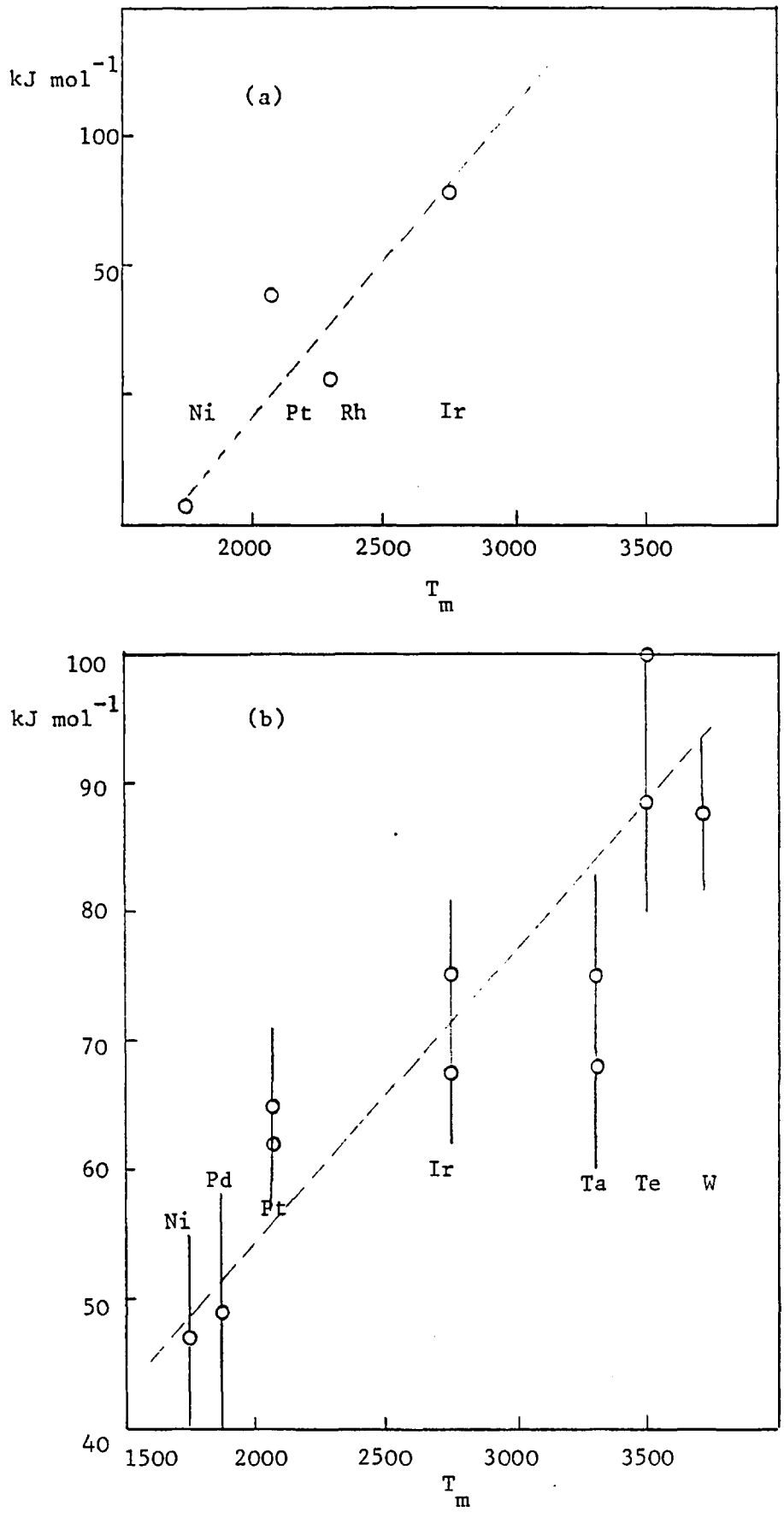


Figure 1.4 The Dependence of Diffusion Activating Energy on Bulk Melting Temperature, T_m, for (a) self-diffusion on (311) surfaces of f.c.c. metals, (b) adatom diffusion on W(110) surface. (From ref. 17).

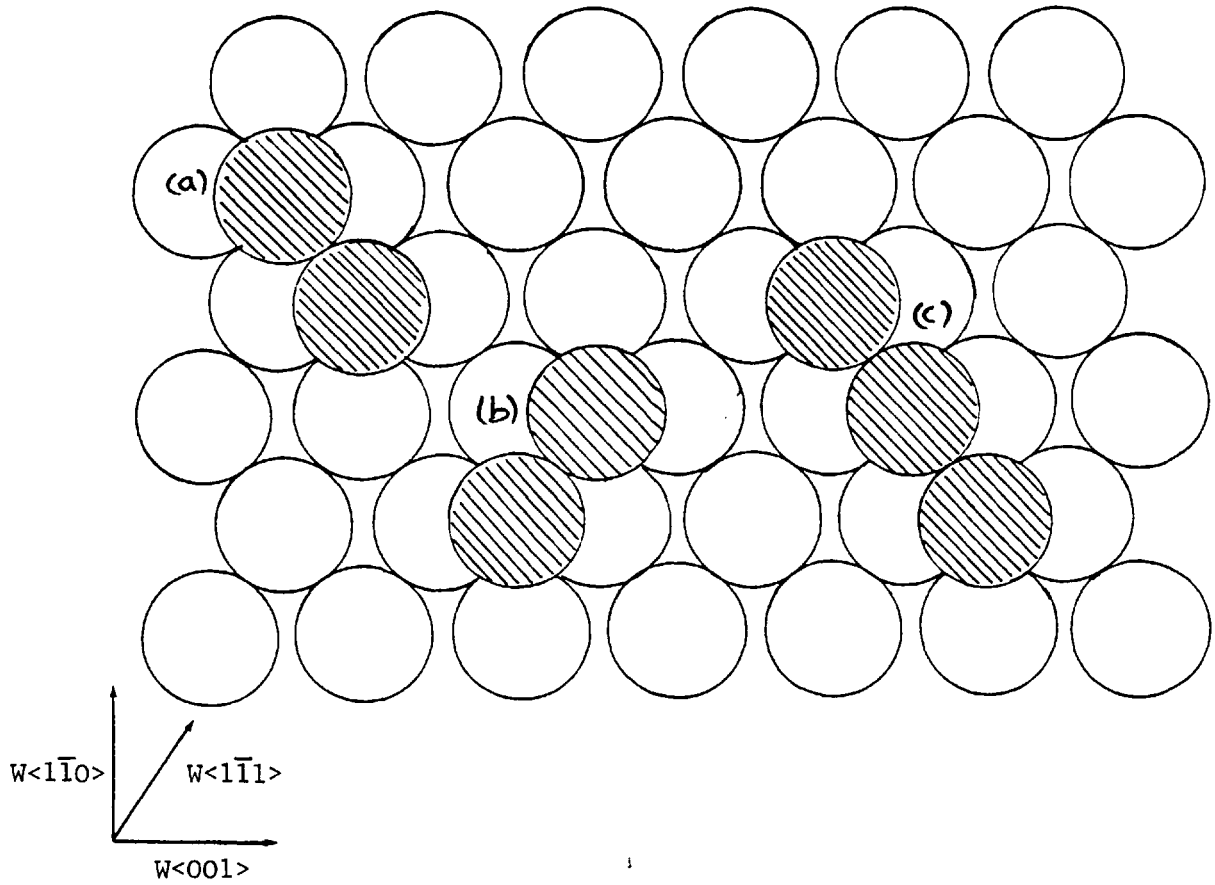


Figure 1.5 Schematic diagram showing adatom clusters on W(110) surface. (a),(b), Dimers oriented along the two equivalent W<111> directions, (c) linear chain cluster. The adatoms are assumed to occupy lattice sites and the inter-atomic spacing in the clusters is equal to 2.74 Å, the nearest neighbour distance in bulk tungsten.

Adatom dimers on W(110) are observed to show strong chemical specificity in their properties. For example, the binding energies of the 5d transition metal adatom pairs, determined from studies of the kinetics of formation and dissociation of dimers[41,42], show an interesting trend with the d-electron configuration of the adatoms, figure 1.6. The binding energy decreases to a minimum for Re_2 and thereafter remains small. This variation contrasts strongly with the binding energy of the bulk 5d transition metals, which is a maximum at the middle of the series. Re adatoms on W(110), which were reported in the preceding section to exhibit strong binding to the substrate, appear not to form dimers at all. These results are unexpected on the basis of the simple broken-bond model or pairwise interaction calculations, indicating the inadequacy of these approaches to estimating cluster stability.

Strong chemical specificity is also observed in the properties of larger adatom clusters on W(110). For instance, Ta and W have been observed to form two-dimensional clusters[43], while the later transition metals Ni, Pd, Pt[29] and Ir[44,45] form one-dimensional clusters aligned along the close-packed W⟨111⟩ directions, (figure 1.5). The behaviour of Re appears to be intermediate since Re_3 trimers have been observed in both linear and triangular forms[44,46]. Bonding in these clusters appears to be both restricted and directional, and strongly associated with the d-band filling of the adatoms. Migration of the clusters involves occasional re-orientation. Detailed diffusion studies have been performed only for Pt_3 and Pt_4 linear chain-clusters[28]. Some of the quantiative results of this study are presented in table 1.1 together with the diffusion data for single Pt adatoms and Pt_2 dimers

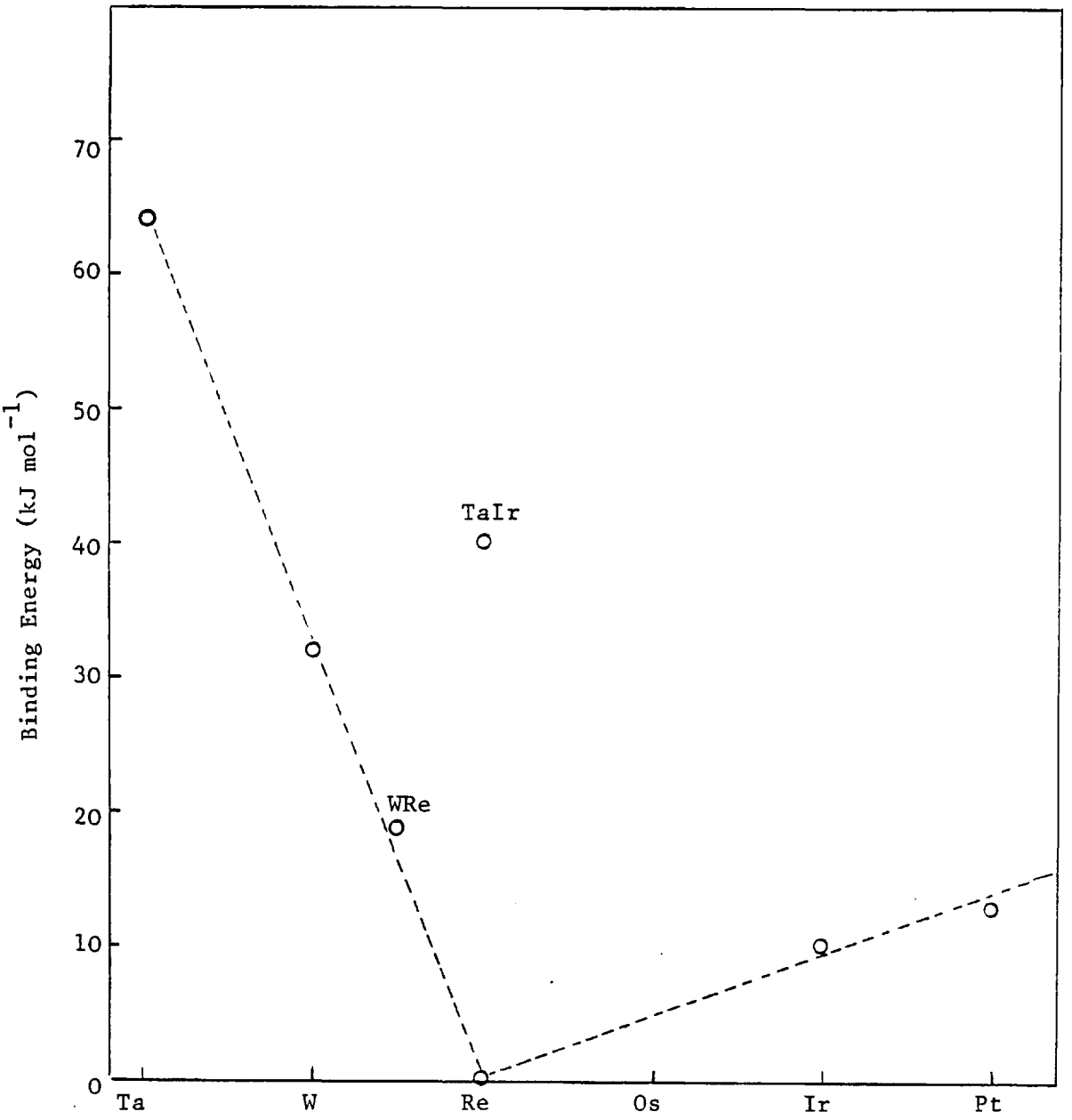


Figure 1.6 Binding energies for transition metal dimers on W(110). (From refs. 41, 44).

Table 1.1 Activation Energy ΔE (kJ mol^{-1}) and pre-exponential factor D_0 (cm^2 s^{-1}) for Pt cluster diffusion on W(110) (ref. 28).

	ΔE	D_0
Pt	65 ± 6	3×10^{-3}
Pt_2	65 ± 6	9×10^{-4}
Pt_3	77 ± 15	2×10^{-3}
Pt_4	84 ± 15	5×10^{-3}

on W(110). These results show that the cluster mobility decreases with increasing cluster size, with little change in the diffusion activation energies. Just as for Pt_2 dimers, the mechanism for diffusion of Pt_3 and Pt_4 clusters appears to involve sequential hopping of one adatom at a time.

The thermal stability of linear chain-clusters of Ir and Pt adatoms increases with increasing chain length, indicating that there is a non-additive contribution to the bonding in these clusters. It has frequently been observed that these chains grow parallel to each other, with an inter-chain separation much greater than near-neighbour sites on W(110). For example, parallel Ir adatom chains with a separation of about 15Å have been observed[46]. These observations suggest that there may be long range interactions between adatoms on W(110). Theoretical calculations[48] suggest that interaction via the substrate conduction electrons should result in long range and oscillatory interaction between pairs of adatoms. Evidence for this has recently been found in FIM studies on W(110) of the equilibrium pair distribution of WPd and RePd pairs by Fink, Faulian and Bauer[49] and of WIr and Ir_2 by Casanova and Tsong[34].

1.2.4 Formation of monolayer islands

Two-dimensional islands of Ta and W on W(110) have been readily observed in the FIM[44]. For the later transition metal adatoms on W(110), however, there appears to be a nucleation barrier to the formation of two-dimensional islands on W(110). For example, Ir and Pt form two-dimensional islands only after nucleation at chain-chain or chain-step intersection[44,45]. In contrast, for Ni and Pd there appears

to be a critical size of chain-cluster beyond which the chains become thermally unstable and transform to a two-dimensional cluster[29]. For instance, chains containing more than four Ni atoms or ten Pd atoms transformed to two-dimensional islands upon heating. The atomic structure of the islands could not be resolved in these studies but island edge angles were measured for Ni, Pd and Pt[29]. Multiple positioning of islands was observed and interfaces were seen between islands that came in contact. The results of this study indicate that the islands have a strained pseudomorphic type of structure.

Recently, Fink and Ehrlich[50] have examined two-dimensional islands of Pt, Pd, Ir and Re on W(110). By using extremely sharp tips and imaging at temperatures below 20 K, they have managed to resolve individual atoms in the two dimensional islands of the Pt group metals. They ascribe open structures of the form p(n×n) (n > 1) for the resolved islands, although a value for n is not specified since absolute distances are not readily obtainable in FIM. The islands were also observed to undergo structural transformations upon heating. For instance, the overall shape of an Ir island containing sixteen resolved atoms changed upon successive heating cycles at 450 K. It is interesting to observe that removal of one atom from the island also caused its overall shape to change, while a cluster of twelve Ir atoms was unstable and transformed to a linear-chain cluster. These results indicate that there is a critical size for two-dimensional iridium islands to be stable. The atomic structure of the islands was not resolved when thoroughly equilibrated, suggesting that the structure in this case corresponded closely to that of W(110). For Re, only two-dimensional islands, with a structure similar to that of W(110), were observed.

1.3 Studies on large single crystals

While FIM investigations are restricted to transition metal systems with only film growth on tungsten having been studied in detail, experiments on large single crystals have been performed for a variety of metal-metal systems over a wide coverage range. An exhaustive list has recently been compiled by Biberian and Somorjai[51] and recent reviews have been given by Rhead[52] and Bauer[53]. Most such studies have used low energy electron diffraction (LEED) for monitoring the structure of overlayers. The LEED pattern consists of an array of spots, the positions and intensities of which are determined by the surface structure, but only the unit cell dimension and symmetry can be readily deduced from the pattern. In studies of transition metal overlayers detailed determination of overlayer structure from LEED has not usually been attempted, but Hahn and coworkers[54] have recently shown that diffraction spot intensity profiles can reveal island sizes in some situations. The use of LEED instruments for studies of film growth has the advantage that other techniques for characterising the surface can usually be incorporated. For example, Auger electron spectroscopy (AES), thermal desorption spectroscopy (TDS), measurements of work function change ($\Delta\phi$) can be readily used and deposition rates can be monitored with quartz-crystal microbalances.

Studies using large single crystal substrates can be divided into two groups, one dealing with the initial stages of film growth studied primarily by LEED/AES, and the other with dense overlayers for which electron microscopy has also been particularly useful. It is convenient to discuss these separately.

1.3.1 The initial layers

One of the first transition metal systems to be examined by LEED was the growth of copper overlayers on W(110) studied by Taylor[55]. At room temperature, submonolayer coverages of Cu (estimated from the temperature and pressure of a Knudsen source) produced a 7×1 LEED pattern with the long periodicity in the W<1$\bar{1}$0> direction. Taylor attributed this to the formation of a Cu-W alloy. However, this system was re-examined by Moss and Blott[56] who observed the same pattern but gave a different interpretation. They attributed the pattern to a close-packed structure in which the Cu periodicity was identical to that of tungsten along the W<001> direction and smaller than that of tungsten along the W<1$\bar{1}$0> direction. The extra spots were then explained as arising from multiple diffraction between the strained Cu(111) and W(110) lattices. In contrast, Bauer and coworkers[57] found that although substrate LEED spots became diffuse no new spots were observed up to one monolayer coverage, which they determined accurately using a quartz-crystal microbalance. The extra spots of the strained Cu(111) pattern were actually observed only with the commencement of the second layer. In addition a metastable strained Cu(111) structure that had been observed by Taylor[55] and Moss and Blott[56], was found to correspond to the third layer. Bauer and co-workers[57] interpretation was that the first Cu layer had a highly strained pseudomorphic structure, on top of which the strained Cu(111) structure formed. The first two layers were strongly bound to the W(110) surface while the metastable third layer transformed to three dimensional crystallites upon annealing. Strong support for this model was provided by a good correlation between their TDS results and changes in Auger peak heights. Bauer and

co-workers have used similar techniques to examine Cu on W(100)[57], Ag, Au and Pd on W(110) and (100)[58-60], and Cu and Ag on Mo(100)[61]. The results for W(110) show that at least one stable strained pseudomorphic type layer is formed by these adsorbates before the onset of three-dimensional crystallization. For example, Ag formed a strained (111) monolayer at all temperatures and an additional metastable layer at room temperature. Au formed only a pseudomorphic layer at room temperature while at 700 K two layers which have a strained (111) structure are formed. Similar results have been obtained by Augustus and Jones[62]. Pd at submonolayer coverages formed a strained (111) structure provided the specimen was heated at 450 K. In contrast, Butz and Wagner[63], in their studies of the diffusion of Pd overlayers on W(110), observed a half-monolayer state. At a coverage of one monolayer, Schlenk and Bauer[59] observed a (1×1) LEED pattern, indicating a pseudomorphic structure. The room temperature Pd deposits showed a diffuse (1×1) spot pattern with considerable background intensity. These features in the LEED pattern were attributed to island formation or random filling of the (1×1) sites available on the surface. Similar LEED patterns have recently been observed for Pd on Nb and Ta (110) surfaces[64].

The work function change measured on W(110) supports island formation at submonolayer coverages. Edge adatoms of islands contribute an additional dipole moment compared to adatoms within islands. The work function decreases due to Smoluchowski smoothing[65]. Besocke and Wagner[66] have shown that the Helmoltz equation for work function change, $\Delta\phi$, can be related to the number of edge atoms by

$$\Delta\phi \propto \sqrt{n_i}\ \sqrt{\theta} \qquad (1.1)$$

where n_i is the island density and θ is the coverage. A parabolic decrease in $\Delta\phi$ with coverage is qualitatively observed in the data available for the transition metals on W(110), in agreement with equation 1.1.

More direct evidence for island formation has been obtained recently by Hahn and co-workers[54]. By measuring LEED spot intensity profiles, which vary periodically with increasing beam energy between a narrow profile and a broadened profile, they deduced the size or separation of islands of W on W(110) over a wide temperature and coverage range. Their results show that with increasing temperature the island distance becomes larger and the number of islands correspondingly smaller, in agreement with nucleation theory[2]. They deduced the number of atoms per island from the total coverage and by extrapolating to zero coverage show that the critical nucleus size contains less than ten atoms, although LEED cannot determine the orientation of such small nuclei. However, this work appears to be the first to demonstrate the potential of LEED for studying the early stages of film growth.

From the data available on W(110) for transition as well as alkali metal adsorbates, Bauer[53] has devised empirical rules which qualitatively predict adsorbate behaviour on W(110). The rules were based on Pauling's expression for the heat of adsorption given as

$$E_a = \frac{1}{12}(E_{sa} + E_{ss}) + (\chi_a - \chi_s)^2 \qquad (1.2)$$

where E_s and χ are the sublimation energy and electronegativity, respectively, for the adsorbate and substrate. Large electronegativity difference ($\Delta\chi$) results in dipoles with mutual repulsion which leads

to the formation of hexagonal structures with large lattice constants at sub-monolayer coverages. With increasing coverage the adsorbate lattice contracts continuously due to mutual depolarization and metallization of the layer. This type of behaviour has been observed for alkali metals on W(110)[67]. For transition metals, however, $\Delta\chi$ is negligible in which case attractive interactions between adatoms predominate over the dipole repulsion term and lead to formation of islands with a structure that minimizes the strain energy due to lattice mismatch. The competition between adatom-adatom and adatom-substrate interactions results in structures which are strained (111) or pseudomorphic. However, models based on thermodynamic quantities like sublimation energies cannot account for a number of experimental observations. For instance, Fe on W(110), which is expected to form two-dimensional layers on the basis of its lower sublimation energy compared to tungsten, has been observed in FEM and LEED to form three-dimensional crystallites[12]. Other examples are the (nxn) superstructures observed in the FIM by Fink and Ehrlich[50] for Pd, Pt and Ir islands on W(110), which imply repulsive near-neighbour interactions in these islands.

Some workers have used calculations assuming pairwise interaction to predict the structure of the adlayer. Lennard-Jones potentials have been used to calculate adsorption energies of Cu[56], Au[62], and Pb[68] on W(110) surfaces. However, bcc (110) surfaces modelled by Lennard-Jones potentials are inherently unstable. More realistic Morse potentials have been used with limited success by Stoop[69], who also included surface relaxation, to calculate the stability of various structures of Pb and Cu on W(110) and (100) surfaces. The inadequacy

of this approach has already been pointed out in the preceding sections. In addition, it should be noted that pairwise interaction models predict an outward relaxation of the surface layer, contrary to LEED observations[70].

Direct correlation of LEED observations with FIM studies has not yet been done successfully. The strained pseudomorphic type of structure observed by Schlenk and Bauer[59] for sub-monolayers of Pd on W(110) is qualitatively in agreement with the FIM observations of Bassett[29]. However, the structure of the islands in the two cases could be quite different because of the different annealing temperatures used. Also, the size of the ordered region observed in LEED is considerably larger than the island sizes observed in FIM. Brief LEED studies of Pt film growth on W(110) by Naumovets and Fedorus[71] do not show any evidence of patterns that could be attributed to the linear-chain structures observed in the FIM.

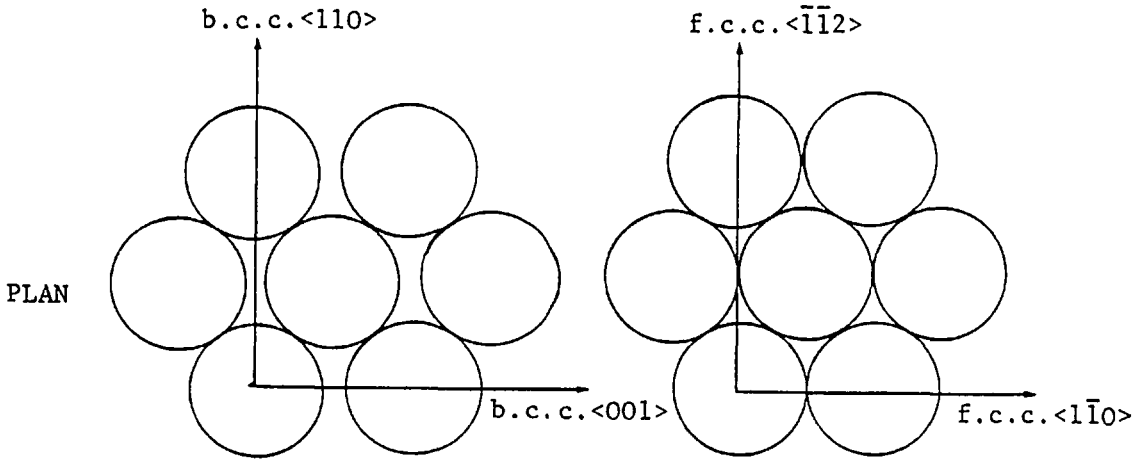
1.3.2 Dense overlayers

An adsorbed monolayer is the first stage in both the Frank-van der Merwe and the Stranski-Krastanov modes of film growth. However, these modes then diverge and in principle can be distinguished by plotting the Auger signal for both the adsorbate and the substrate as a function of time (AST plots)[52]. In the Frank-van der Merwe growth mode the AST plots are expected to show a series of straight lines with "breaks" in both signals at the completion of each successive layer. In contrast, the Stranski-Krastanov growth mode is expected to show one "break" in the signal at the completion of the monolayer, followed by a slowly varying change in the signals. Bauer and co-workers[57-61] have observed sharp breaks and straight line segments

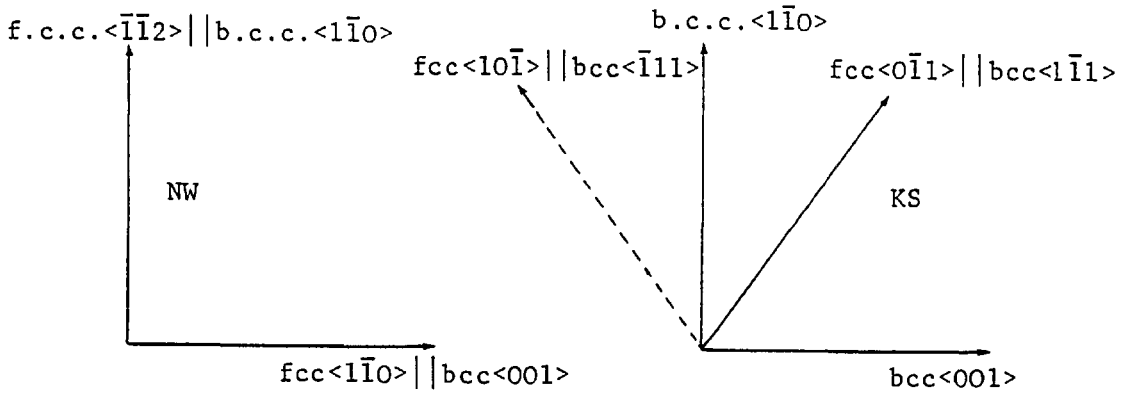
in their AST plots, although others[72,73] have seen a "knee" rather than sharp breaks, and oscillations in the signals near the completion of a layer rather than straight line segments. The latter behaviour has been attributed to the growth of a succeeding layer before the completion of the preceding one, or to changes in sticking probability.

In general, transition metals on tungsten have been observed to follow the Frank-van der Merwe growth mode at low temperatures, while the Stranski-Krastanov mode is usually observed at elevated temperatures. The temperature dependence of the growth mode has also been demonstrated in the UHV scanning electron microscope studies of nucleation of Ag on W(110) and Mo(100) surfaces by Venables and co-workers[74,75]. Their results show that after the completion of the intermediate layers, three-dimensional islands grow with a density which is strongly temperature dependent, indicating the importance of surface diffusion of adatoms on the adsorbed layers. The Frank-van der Merwe growth mode is then interpreted as an extreme case of the Stranski-Krastanov growth with a high island density.

For deposition of f.c.c. metals on b.c.c. (110) surfaces the final crystallites epitax (111) f.c.c.||(110) bcc in one of two orientations, figure 1.7: $\langle 1\bar{1}0\rangle$fcc||$\langle 001\rangle$bcc (Nishiyama-Wassermann relation) or, $\langle 0\bar{1}1\rangle$fcc||$\langle \bar{1}11\rangle$bcc or $\langle 10\bar{1}\rangle$fcc||$\langle 1\bar{1}1\rangle$bcc (Kurdjumov-Sachs relation). LEED studies indicate that Cu(111)[55] epitaxed deposits are aligned NW while Ag[58] and Au[58,62] (111) epitaxed in the KS alignment, although for Au a transition alignment between the NW and KS alignment was also observed. The NW relation appears to be a metastable alignment for Au and Pd[59] crystallites, which re-orient to the KS alignment at elevated temperatures. Bruce and Jaeger[76-79] have recently studied a



(a) b.c.c. (110) and f.c.c. (111) surface structures



(b) Transition Metals Epitax f.c.c.(111)||b.c.c.(110) in one of two alignments, f.c.c.<1$\bar{1}$0>||b.c.c.<001> (Nishiyama-Wassermann) or f.c.c.<0$\bar{1}$1>||b.c.c.<$\bar{1}$11> and f.c.c.<10$\bar{1}$>||b.c.c.<1$\bar{1}$1> (Kurdjumov-Sachs).

Figure 1.7

wide range of fcc-bcc metal pairs using TEM. From their studies they have developed a model, based on geometrically superimposing substrate and deposit planes, to predict the final orientation of deposits. The success of their model shows that adatom size effects are a dominant factor in the structural relationships at the interface between the substrate and a dense overlayer.

1.4 The present study

It can be seen from the above review that a complete description of film growth, covering both the atomistics of monolayer development and the detailed structure of multi-layer deposits, is not available for any individual metal-metal system. In principle, a combination of FIM and LEED studies should provide a reasonably complete picture of the processes involved but so far different systems have been examined under differing experimental conditions by the two techniques. In the present study we therefore seek to obtain as complete a picture of film growth as possible by combining FIM and LEED studies of rhodium on the (110) surfaces of tungsten and molybdenum, for which the initial stages of film growth are of special interest.

FIM studies have shown that the later transition series metals form linear chain clusters on tungsten (110) surfaces. For such adsorbates there is thus an unexpected barrier to the formation of two-dimensional islands, although so far no evidence for the pre-nucleation stage has been found in LEED studies. The formation of linear-chain clusters appears to be linked to the electronic configuration of the adsorbate metal, occurring when the adsorbate d-shell is more than half-filled. However, no quantitative description of the

bonding in such clusters has been given and it is also not known if the behaviour is general for fcc metals on bcc (110) surfaces. With this in mind we have chosen to study the behaviour of rhodium on the (110) surfaces of both tungsten and molybdenum. Extension of the studies to a substrate metal with a different electronic configuration, such as tantalum or niobium would have been desirable, but this was not practicable.

FIM studies have been carried out to characterize individual atomic processes in sub-monolayer rhodium films, such as adatom diffusivity and the formation and nature of clusters. The growth and structure of monolayer and thicker layers have also been examined by LEED and AES. These studies confirm that rhodium behaves like other later transition metals in forming chain clusters before island nucleation occurs. In order to understand the nature of the bonding that controls this stage of film growth, calculations have been made of the electronic structure and energy of small clusters of tungsten and rhodium on a tungsten (110) surface. These calculations were made within a d-electron tight binding approximation using the recursion method of Haydock, Heine and Kelly[80]. It is well known that the bonding in transition metals is mainly due to the d-electrons[81], and the same appears to be true for the binding energies of transition metal adatoms adsorbed on transition metal surfaces[38], thus justifying to a first approximation our neglect of the sp conduction states in the calculation. The results indicate the importance of the non-bonding d electrons in determining the stable cluster structure and provide a basis for discussion of the present work and other experimental observations of transition metal film growth.

2. FIELD ION MICROSCOPY

Field ion microscopy[5,6] (FIM) is a unique technique enabling the direct study of single atom processes at solid surfaces. The FIM was developed during attempts to improve the resolution of the field emission microscope (FEM). The FEM[4] operates by field emission of electrons into vacuum from a field emitter specimen in the form of a fine needle tip, which is held at a negative potential with respect to a fluorescent screen facing it. With sufficient voltage applied, the field at the emitter reaches 3-5 V nm^{-1} and electrons tunnel through the field deformed energy barrier at the surface. The emitted electrons follow radial trajectories to the fluorescent screen where they form an image. The intensity distribution in this image reflects the local barrier tunnelling probability at the surface, which is determined by the local field and work-function. The magnification of the FEM is usually about a million while the resolution is in the range 2-3 nm. The resolution is determined by the lateral velocity component of electrons which tunnel at the Fermi level, and by a diffraction limit due to the de Broglie wavelength or the Heisenberg uncertainty principle. Both these factors are experimentally uncontrollable and the realisation of this limitation led to the discovery of the field ion microscope.

In the FIM, imaging is done with ions originating at the surface of the specimen by field ionization in which electrons tunnel from an external gas atom into the solid leaving an ion that accelerates away to the screen. The de Broglie wavelength of the ions is negligible and the lateral velocity of the ions can be controlled by cooling the specimen surface. In this way the potential resolution is

improved to 0.3-0.4 nm and with a magnification of several million and a local ionization rate that is sensitive to the surface atomic structure, the FIM provides an image showing the surface in atomic detail.

2.1 Basic Principles

The basic design of the FIM is shown schematically in figure 2.1. The specimen is in the form of a sharply pointed needle 10-100 nm in radius at its tip. It is mounted vertically on leads which serve the dual purpose of thermal contact with the coolant through which they pass, and electrical connection to either a variable high tension power supply or a temperature controller for heating the tip. Following evacuation, the microscope is filled with an inert gas, usually helium or neon, to a pressure of about 5×10^{-3} torr. The tip is cooled to cryogenic temperatures, usually 78 K using liquid nitrogen in the "cold finger", and a high positive potential is applied to the specimen, producing a field of the order of 50 V nm^{-1} at the surface. This field is sufficient to cause field ionization of the imaging gas in the vicinity of the surface. The imaging voltage is adjusted so that ionization occurs preferentially at high field regions above protruding atoms. A narrow pencil beam of ions is accelerated from each of the protruding atoms to impinge upon a phosphor screen where it forms an image of the atom, (figure 2.2). Thus, isolated atoms and plane edges appear brighter in FIM images.

When a tip is heated to a high temperature, typically above one-half of its melting point, surface migration of atoms causes rearrangement of the surface to a shape with minimum free surface energy. The

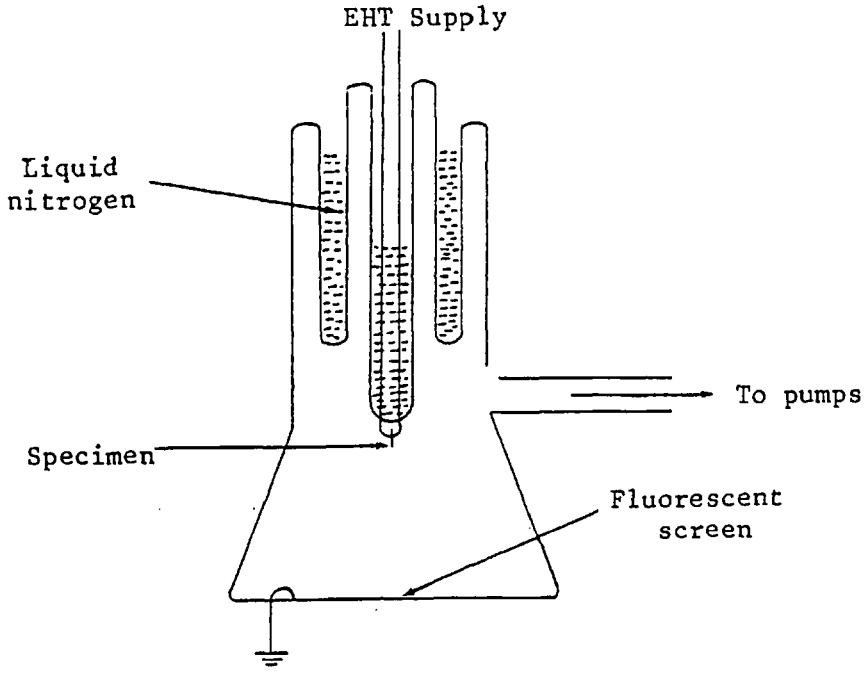


Figure 2.1 The Basic Design of a Field Ion Microscope.

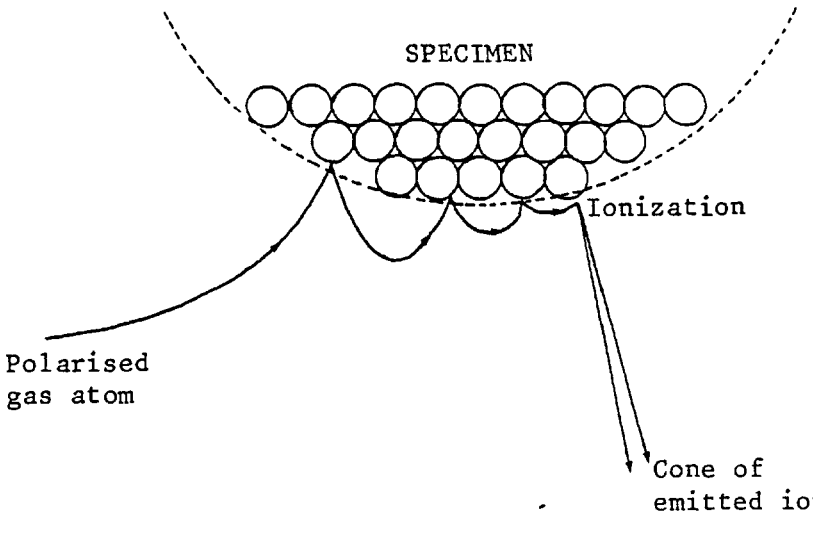
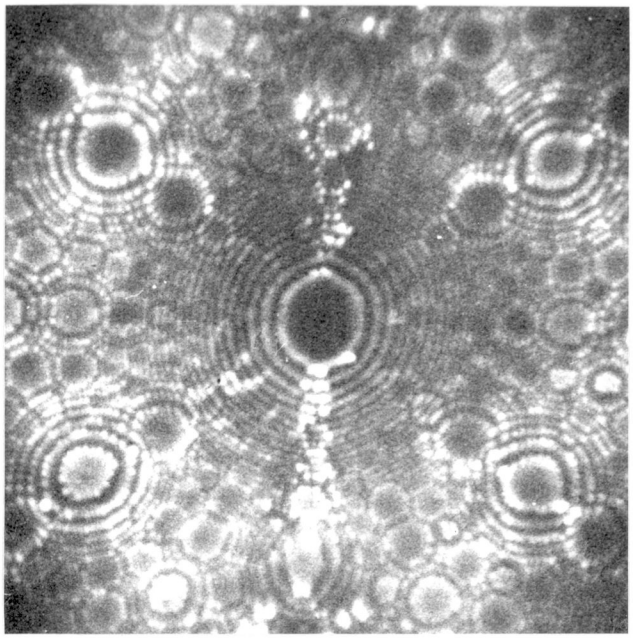


Figure 2.2 Schematic Diagram of the Process of Image formation; Ionization of the Image Gas over the high field region of a specimen tip.

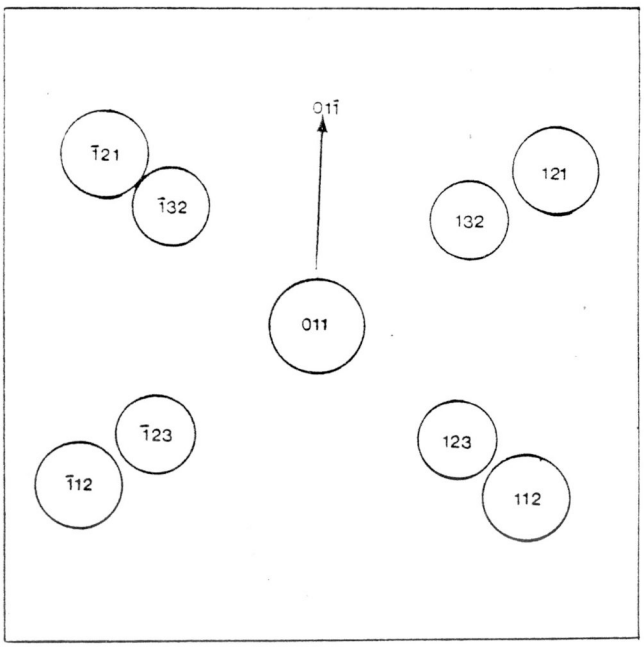
resulting annealed end-form of the specimen is quite smooth but in FIM a higher degree of surface perfection is required. This is achieved by the process of field evaporation, which corresponds to field ionization and desorption of atoms of the surface itself. Metal atoms like tungsten can be evaporated from the surface at a controlled rate by gradually increasing the voltage above the imaging voltage. This process produces a surface which is atomically smooth and crystallographically perfect, and exhibiting a variety of low Miller-index planes. As an example, figure 2.3 shows a characteristic FIM image of a field evaporated end-form of a (110) oriented tungsten tip. Each spot in the image corresponds to an individual atom in the tip surface over which ionization of the imaging gas atoms has occurred, and the rings of spots correspond to the edges of prominent crystal planes exposed at the curved surface of the specimen.

2.2 Field ionization

Any imaging gas atom that enters the high field region over the tip surface is strongly attracted to the surface due to induced dipole interactions with the strong field at the surface. The dipole attraction causes the atom to impinge upon the tip surface from where it is reflected with some loss of energy. If sufficient energy has been lost by the atom in the first encounter with the surface, it remains trapped in the field. The atom, attracted by the dipole forces, then returns to the surface in a series of hops which decrease in height as it loses energy in its collisions with the surface. Eventually it is fully thermally accommodated to the tip temperature and is ionized when it enters a region of high local field above a protruding atom.



(a)



(b)

Figure 2.3 (a) Field ion image of a (011) oriented field-evaporated tungsten tip; (b) key to the micrograph showing some low Miller index planes.

Field ionization[82] occurs when an electron in the ground state of the image gas atom tunnels into the metal surface through the field-deformed barrier between the atomic potential well and the surface, (figure 2.4). In the metal all states below the Fermi level are occupied, so field ionization is possible only when the electronic ground level of the gas atom is above the Fermi level. Thus field ionization of atoms near a metal surface can only occur beyond a critical distance, x_c, away from the surface, given approximately by[5]

$$x_c = \frac{I - \phi}{Fe} \qquad (2.1)$$

where I is the ionization potential of the gas atom, ϕ is the work function of the metal, F is the applied field and e is the electronic charge. x_c is calculated to be about 0.5 nm for the noble gases most commonly used in FIM.

An important consequence of the high imaging field is the existence of an adsorbed state of the imaging gas above protruding surface atoms[83,84], the bond being due to field-induced dipole-dipole attraction between the polarized gas atom and the metal atom. In contrast to ordinary physisorption or chemisorption, which usually require the adatom to be located on the surface with bonds to several surface atoms, the dipole bonding requires the image gas atoms to be located at the apex of the protruding metal atom, (figure 2.5). The significance of the apex location is that electron tunnelling from a hopping imaging gas atom occurs through the adsorbate gas atoms which are too close to the surface to be field ionized themselves. An incoming image gas atom does not see the potential profile of the metal surface but rather a modified potential due to the adsorbed atom. Rendulic[85] has shown

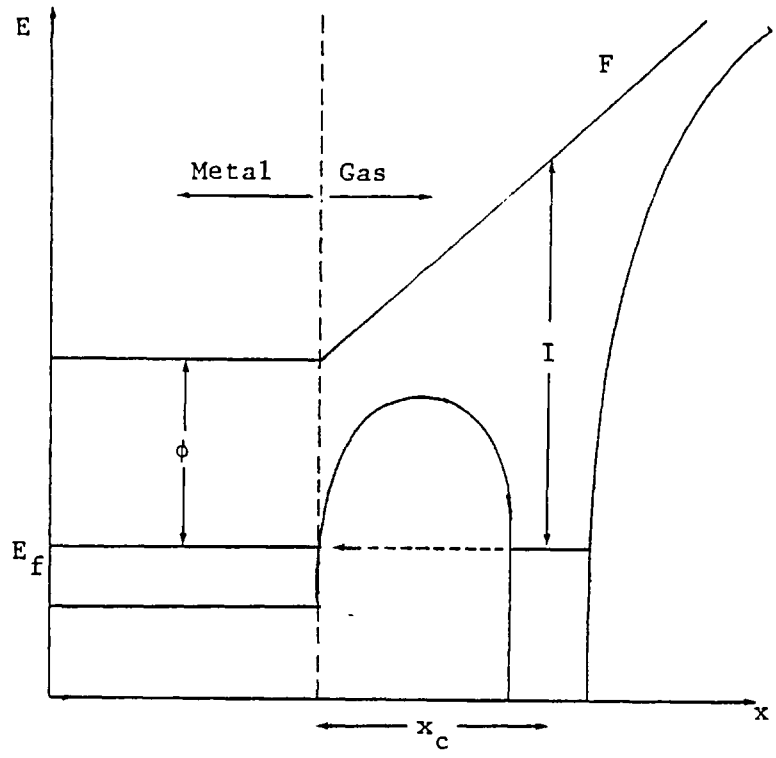


Figure 2.4 Electronic Potential Energy Diagram for Field Ionization.

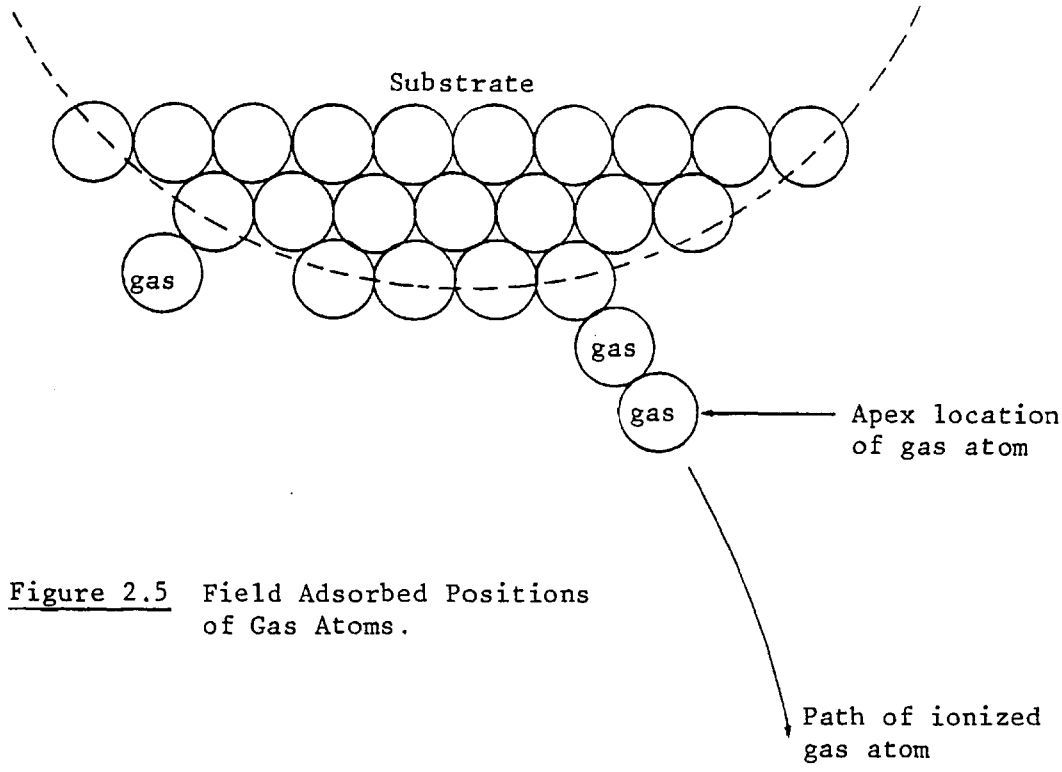


Figure 2.5 Field Adsorbed Positions of Gas Atoms.

that the imaging gas atom is bound in a potential well above the adsorbed atom. The result is that the ionization probability of the image gas atom is increased due to a higher "dwelling time" at the site, with a corresponding increase in image brightness. It has been found that an even more enhanced image is obtained if Helium imaging is used in a Helium-Neon mixture[86], in which case Ne is field adsorbed and He ions are formed above the Ne atoms. The ionization rate is determined by the ionization probability and the gas supply function[87]. With increasing field the latter becomes the limiting factor, with the result that the image contrast decreases. However, under normal imaging conditions it is not clear whether ionization probability or the gas supply function is the dominating factor determining the image brightness.

2.3 Imaging

Once ionization has occurred, the gas ions so formed are accelerated away from the tip along radial trajectories, following the force lines of the field and forming an image on the fluorescent screen. To a good approximation, this image is a stereographic projection of the tip, with the magnification M given by[6]

$$M = \frac{D}{br_t} \tag{2.2}$$

where D is the tip to screen distance, r_t is the tip radius and the field compression factor b is a constant of order 1.5-2.0 dependent upon the geometry of the microscope. The geometrical factor b is actually a function of local tip radius so that the magnification M applicable to the (ijk) plane is given by

$$M_{ijk} = \frac{D}{b_{ijk} r_t} \qquad (2.3)$$

where b_{ijk} varies from plane to plane, and in different directions across a plane. In practice, the magnification at any plane is determined indirectly, as will be seen later (section 4.2.1, chapter 4).

The resolution of the FIM is limited by

(i) the beam broadening due to the radial divergence of the beam and scattering of the ions due to collisions with gas atoms on their way to the screen;

(ii) the Heisenberg uncertainty or the de Broglie diffraction limit in the spot size at the screen; and

(iii) the initial tangential velocity of the ions leaving the surface.

The scattering of the ions is minimised by using only a low pressure of imaging gas ($\sim 5 \times 10^{-3}$ torr). This would appear to severely limit the image brightness but for the presence of the high field around the tip, which enhances the gas supply some 10 to 100 times with respect to the ordinary gas kinetic arrival rate due to the dipole attraction of the polarised gas atoms[5]. Since the radial divergence of the ion beam is inversely proportional to the tip radius, an optimum value of the order of 100 Å is normally chosen to give good sharp images on the screen. The tangential velocity of the ions is kept small by thermally accommodating the gas atoms at the tip surface to cryogenic temperatures. This also initiates adsorption of the imaging gas atoms to produce the enhanced imaging described above.

The resolution, d, has been calculated by adding up the diameter, d_0, of the imaging gas atom and the contributions due to the de Broglie wavelength and the tangential thermal component of the velocity of the ions. It is given by[5]

$$d = d_0 + \left\{ 4\left(\frac{b^2 r_t h^2}{2KemF_0}\right)^{\frac{1}{2}} + 16\left(\frac{b^2 r_t kT}{KeF_0}\right)^{\frac{1}{2}} \right\} \tag{2.4}$$

where K is a factor, of the order of 4 to 8, relating the field F_0 at the surface of the tip with radius r_t to the applied voltage V_0 by $F_0 = V_0/Kr_t$, m is the mass of the ion, k is the Boltzmann's constant and h is Planck's constant. Since the last term in 2.4, due to the tangential thermal velocity of the ions, is the major limiting factor in determining the resolution, the expression for d can be approximated by[6]

$$d \approx \left(\frac{6 \times 10^{-4} T r_t}{F_0} \right)^{\frac{1}{2}} \tag{2.5}$$

where T is the tip temperature. Under normal operating conditions with liquid nitrogen cooling of the tip, d is of the order of 0.3-0.4 nm.

2.4 Field Evaporation

In the process of field evaporation used for surface cleaning in the FIM the adsorbed atoms or surface atoms are removed from the surface as ions. The detailed mechanism of field evaporation remains poorly understood but the process has been discussed in terms of two models[88]. These are the Schottky hump model and the intersection model. Both models have been described in terms of one-dimensional potential energy diagrams. Figure 2.6 shows the potential energy diagrams for a surface atom and a surface ion with charge ne in the presence of a field F. If the field is absent, the energy difference Q_{On} between the zero level of the ionic potential and the bottom of

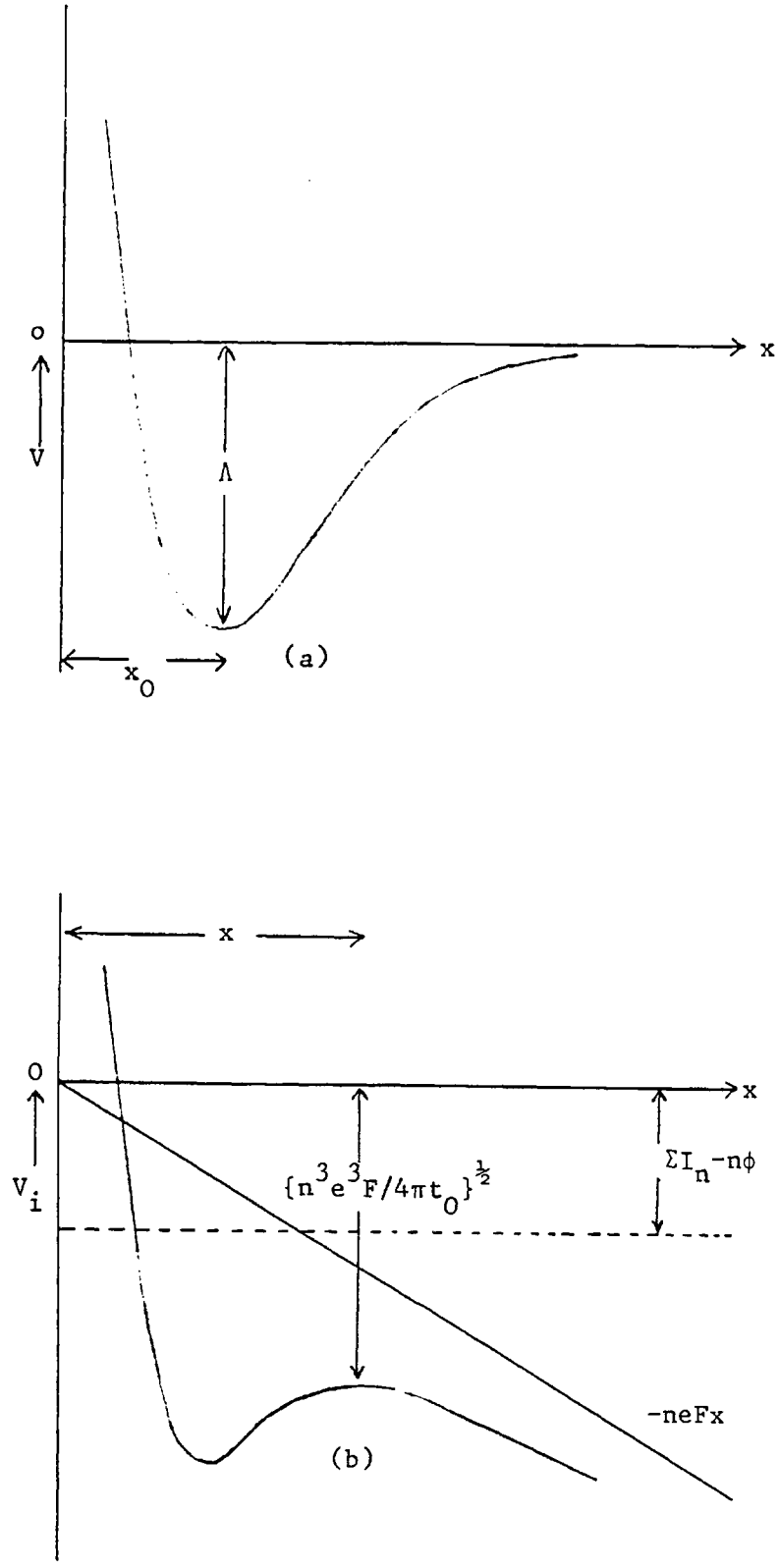


Figure 2.6 Potential Energy Diagrams for
(a) a surface atom,
(b) a surface ion in the presence of a field.

the atomic potential can be written as

$$Q_{On} = \Lambda - n\phi + \Sigma I_n \tag{2.6}$$

The ionic potential $V_i(x,F)$ in figure 2.6b is approximately given by

$$V_i(x,F) = -neFx - \frac{n^2e^2}{16\pi\varepsilon_0 x} \tag{2.7}$$

where x is the distance from the metal surface and ε_0 is the electric constant. The first term in 2.7 is associated with the applied field while the second term is due to an attractive image force term. The location and magnitude of the potential energy maximum is given by

$$x_m = \left\{ \frac{ne}{4F} \right\}^{\frac{1}{2}} \tag{2.8a}$$

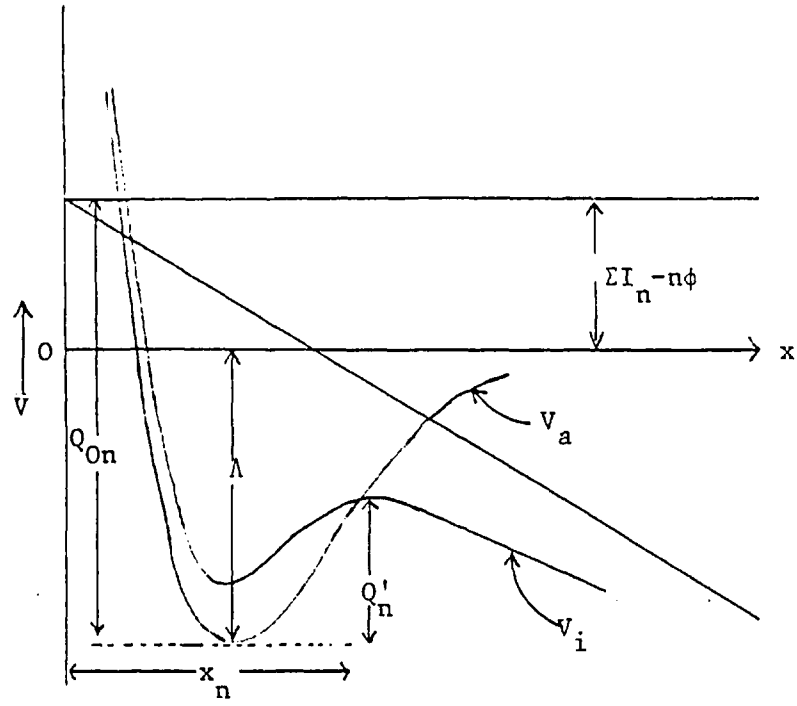
and

$$V(x_m) = -\left\{ \frac{n^3e^3F}{4\pi\varepsilon_0} \right\}^{\frac{1}{2}} , \tag{2.8b}$$

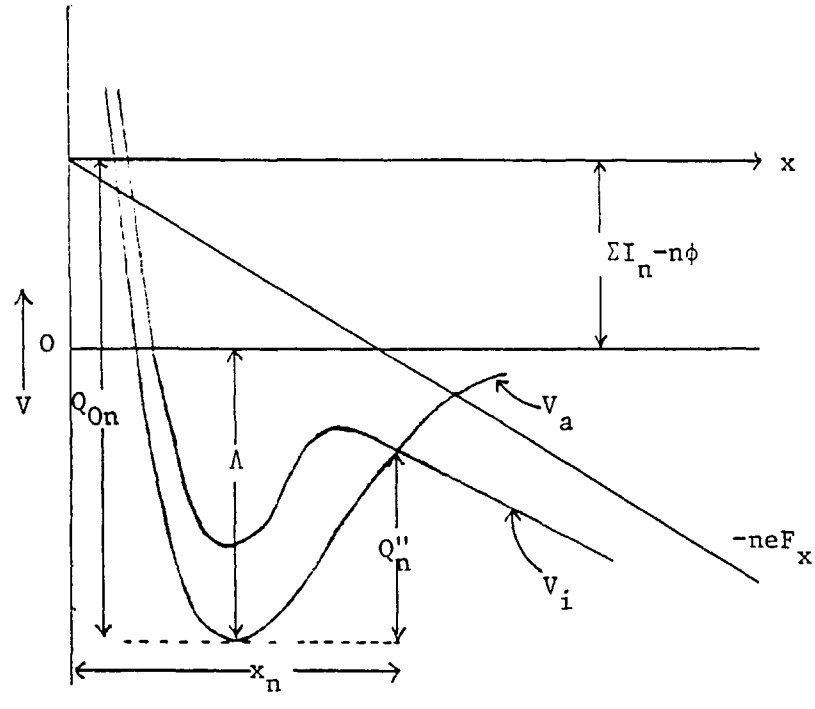
respectively.

The two models differ in the way the atomic and ionic potentials are superimposed, the point of intersection of the two potential curves being the point at which the ion is formed. In the Schottky hump model, ionization is followed by desorption over the Schottky barrier, figure 2.7a. This implies an activation energy for field desorption after the ion is formed, and is given by the difference between the ionic potential at the Schottky hump maximum and the minimum of the atomic potential. From equations 2.6 and 2.8b, this is given by

$$Q'_n = Q_{On} - \left\{ \frac{n^3e^3F}{4\pi\varepsilon_0} \right\}^{\frac{1}{2}} \tag{2.9}$$



(a) Schottky Hump Model.



(b) Intersection Model.

Figure 2.7 Potential Energy Diagrams for the Field Evaporation Models. (a) Evaporation over the image hump after transition from the atomic to ionic state at x_n, (b) ionization at x_n followed by immediate evaporation.

In contrast, in the intersection model ionization is followed immediately by desorption, figure 2.7b. In this case, the energy required for the atom to reach the point of ionization defines the activation energy which from equations 2.6 and 2.7 is given by

$$Q''_n = Q_{On} - neFx_n - \frac{n^2e^2}{16\pi\varepsilon_0 x_n} \qquad (2.10)$$

where x_n is the distance of the point of intersection from the metal surface.

For both the models, the evaporation rate is given by the Arrhenius equation

$$k_n = \nu_n \exp\left(-\frac{Q_n}{kT}\right) \qquad (2.11)$$

where ν_n is the Arrhenius constant and is equal to the evaporation rate at the field F_{On}.

A number of refinements have been added to equations 2.9 and 2.10 to improve the two models. For example, energy shifts due to differences in the polarisability of the atom and ion in the high electric field have been included[89], field penetration into the metal surface and the resulting change in the image potential has been considered[90], energy level shifts and broadening effects[91], and recently[98] a field dependence term for x_n in equation 2.10 have been included.

However, the process of field evaporation is so complex that a satisfactory theory has not yet been obtained. The simple Schottky hump model is doubtful since at the high fields necessary to field evaporate the refractory metals, the Schottky hump (from equation 2.8a) appears at a distance of about 0.1 nm from the metal surface, which does not even allow for the radius of most ions and, hence, has no

real meaning in the classical sense. Also, Tsong[93] has shown that no Schottky hump occurs for field evaporation of the lower charged atomic states M^+, M^{2+} and possibly M^{3+}. Vesely and Ehrlich[94] showed that field evaporation rate measurements for tungsten atoms at kink sites as well as for tungsten adatoms on the (110) plane of tungsten could be satisfactorily represented by the Schottky hump model. However, they assumed a doubly charged tungsten ion as the product of field evaporation while experimental evidence from atom-probe studies has revealed three-fold and four-fold charged ions[83]. None of the theories can successfully account for the evaporation of these multiply charged ions or the metal gas complexes that have been observed in the atom-probe studies. Furthermore, the one-dimensional models do not account for the lateral migration of the evaporating atom prior to desorption, which has been observed in imaging atom probe studies[95]. In this case, field evaporation is seen as a multi-step process in which the atom evaporates by first moving from a kink site onto the terrace (figure 2.8). It may then migrate on the terrace before field evaporating, frequently in a high charge state.

2.5 Practical aspects of FIM

Two conditions have to be fulfilled in order to image a material in the FIM:

(i) the onset of ionization of the imaging gas must occur at a field below that required for field evaporation of the metal under study, and

(ii) the specimen must be able to withstand the mechanical stress of the field.

The choice of imaging gas is further restricted by the requirement that it be chemically inert, thus only rare gases such as helium, neon or argon may be used. The highly refractory metals are readily imaged in He which provides the best resolution and the brightest images. Imaging with Ne or Ar requires image intensification since the phosphor (screen) efficiency for the ions of these gases is low. This is best done in microscopes equipped with a channel plate which is a device containing microchannel electron multiplier arrays which convert the ion image into a much brighter electron image.

The present study involves the imaging of tungsten and molybdenum in a microscope with only direct ion imaging facility. Thus, He was the only imaging gas used. The experimentally observed field evaporation field for tungsten and molybdenum is 57 V nm^{-1} and 46 V nm^{-1}, respectively[82], while the best image field for He is about 45 V nm^{-1}. Thus, tungsten is readily imaged with He while much care is required in imaging molybdenum.

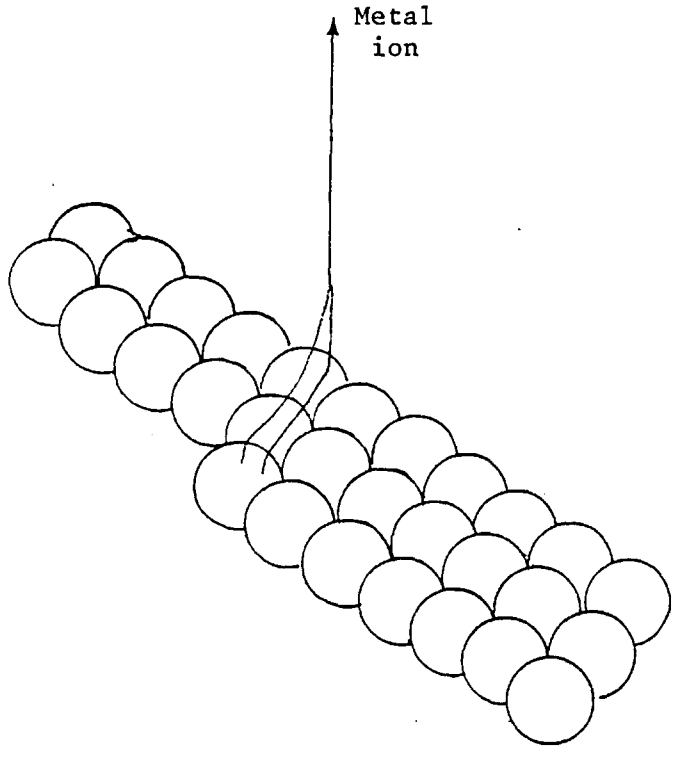


Figure 2.8 Schematic diagram illustrating a migration step preceding field evaporation of a kink site atom. The atom "rolls" up over the ledge in which it originates and moves on the surface before evaporating away (ref. 95).

3. LOW ENERGY ELECTRON DIFFRACTION AND AUGER ELECTRON SPECTROSCOPY

3.1 Low Energy Electron Diffraction (LEED)

Diffraction of electrons from a crystalline solid is a consequence of their wavelike property. In LEED[96-99], a beam of electrons of energy around 100 eV is directed towards the specimen and back-scattered electrons are observed. A typical experimental arrangement for observing LEED patterns is shown schematically in figure 3.1. The atomic cross-sections for scattering of low energy electrons are large, hence, LEED is a highly surface sensitive technique.

Several characteristic features of LEED can be explained using the kinematic theory of diffraction[100]. A basic assumption of this theory is that the interaction of the incident electron wave with a scatterer is relatively weak so that the scattered wave does not interact with neighbouring scatterers. This allows each scattering event to be treated independently, with the total scattered amplitude at some large distance being expressed as a single sum over the scattering array of the whole crystal. However, the strong electron-solid interaction which is responsible for the surface-sensitivity of LEED also has the effect that multiple scattering is quite important. The result is that the energy dependence of the scattered intensity shows complicated structure which cannot be explain by the kinematic theory. The present study primarily involved the determination of the unit cell dimensions of adsorbate structures, which can be adequately obtained using the kinematic theory as outlined below. No account is therefore given here of the dynamical theory of LEED, which is used to

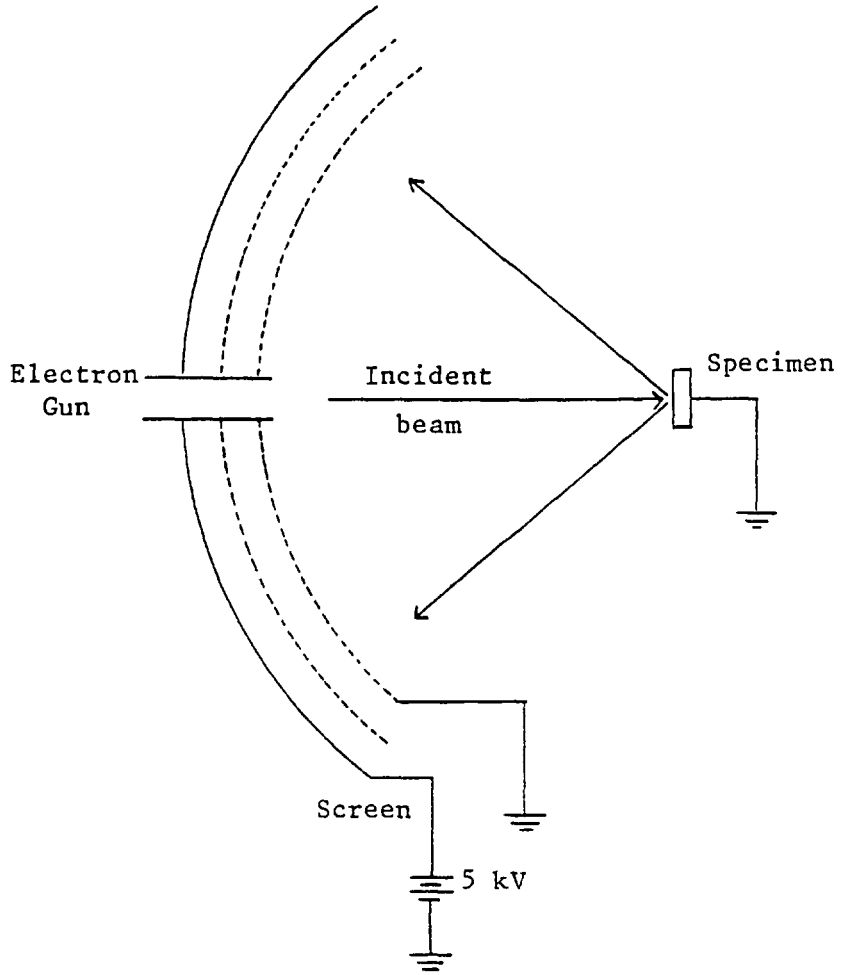


Figure 3.1 Diagram Illustrating the Experimental Arrangement for Observing a LEED Pattern.

account for multiple scattering effects. Details of the dynamical theory may be found in reference 101.

3.1.1 Kinematic theory

Consider scattering of a plane wave from two points, A and B, separated by a distance $\underline{r}$, (figure 3.2). The phase difference between the two scattered waves is given by

$$\delta = |\underline{r}| \frac{2\pi}{\lambda} (\sin \phi - \sin \theta) \qquad (3.1a)$$

where $2\pi/\lambda$ is the magnitude of the wave-vector. In terms of $\underline{k}$ and $\underline{k}'$, the vectors defining the incident and scattered waves, respectively, 3.1a can be written as

$$\delta = \underline{r} \cdot (\underline{k} - \underline{k}') \qquad (3.1b)$$

Elastic scattering requires the conservation of energy and momentum:

$$|\underline{k}| = |\underline{k}'| = \frac{2\pi}{\lambda} \; ; \quad \underline{k}' = \underline{k} + \underline{\Delta\kappa} \qquad (3.2)$$

where $\underline{\Delta\kappa}$ is known as the scattering vector. The scattered wave can be represented by $\psi = A \exp\{-i\underline{r} \cdot \underline{\Delta\kappa}\}$, where A is the initial wave amplitude.

Consider now a crystal consisting of a three-dimensional array of point scatterers. We need to find the direction of a diffracted wave $\underline{k}'$ in terms of the incident wave $\underline{k}$ and the unit vectors $\underline{a}$, $\underline{b}$, $\underline{c}$ defining the positions of the scatterers. Any point in the crystal may be located by a vector, $\underline{\delta}_{mnp}$, from the origin as

$$\underline{\delta}_{mnp} = m\underline{a} + n\underline{b} + p\underline{c} \qquad (m,n,p \text{ integers}) \; ,$$

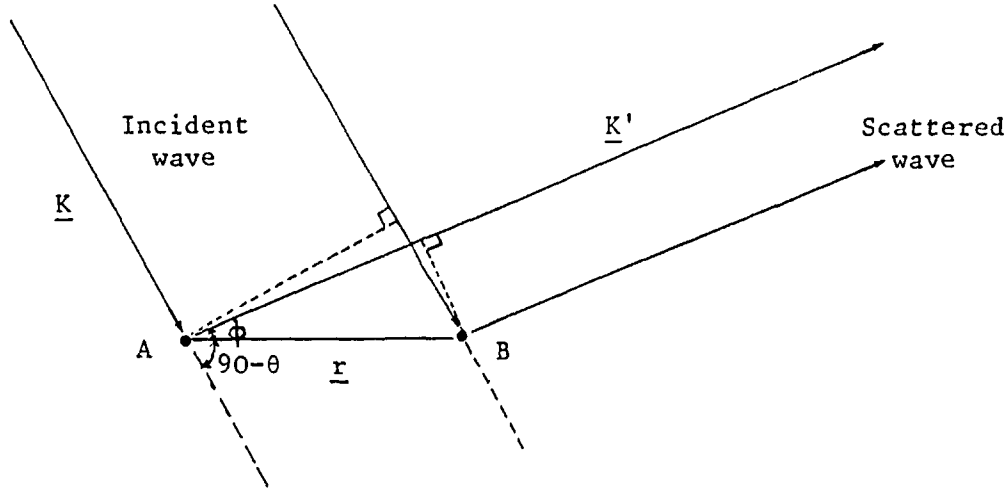


Figure 3.2 Scattering of a plane wave by two points. Phase factor due to the relative positions of the scatterers is $\exp(i\underline{k}.\underline{r}-i\underline{k}'.\underline{r})$.

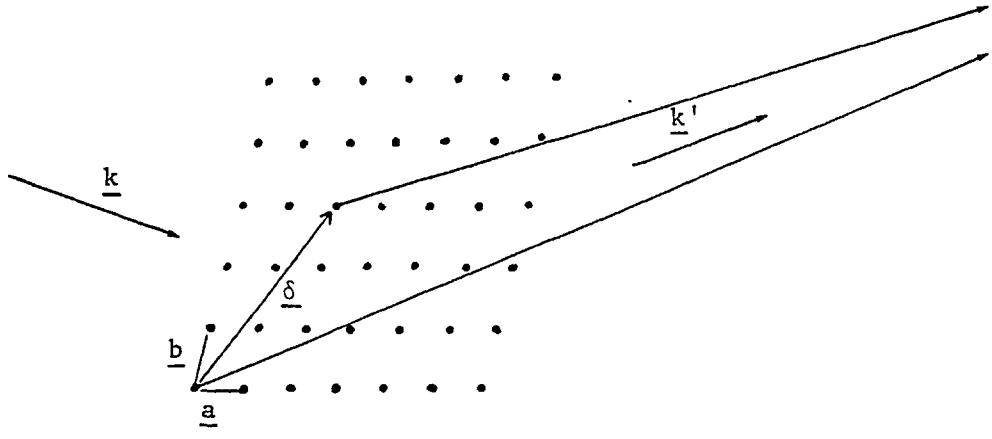


Figure 3.3. Scattering from a crystal. The phase factor at a large distance R is $\exp(i\underline{\delta}.(\underline{k}-\underline{k}'))$.

(figure 3.3). From 3.1, the phase difference between the origin and a point located by δ_{mnp} is given by $\underline{\delta}_{mnp} \cdot \underline{\Delta\kappa}$. Since each scatterer emits a spherical wavelet of the form $\psi = \{A/r\}\exp(-i\underline{k}r)$, at a large distance R, the scattered wave, ψ_{sc}, can be written in the form

$$\psi_{sc} = \frac{A \exp(i\underline{k}.\underline{R})}{R} \; f \exp(-i\underline{\delta}_{mnp} \cdot \underline{\Delta\kappa}) \qquad (3.3)$$

where the atomic form factor, f, takes account of the nature of the scatterer. For the moment, we consider that all the scatterers are identical. The interesting quantity is then the sum of the individual phase factors over the whole crystal, which is given by

$$a = \sum_{mnp} \exp(-i\{m\underline{a} + n\underline{b} + p\underline{c}\} \cdot \underline{\Delta\kappa}) \qquad (3.4)$$

a is called the scattering amplitude and has maxima when

$$(m\underline{a} + n\underline{b} + p\underline{c}) \cdot \underline{\Delta\kappa} = 2\pi(\text{integer}) \qquad (3.5)$$

Equation 3.5 is the Laue condition, which determines the directions of the diffracted beams.

A co-ordinate system can be constructed for the wave-vectors, with unit vectors $\underline{a}^*$, $\underline{b}^*$, $\underline{c}^*$ such that

$$\underline{\Delta\kappa} = G^*_{hk\ell} = h\underline{a}^* + k\underline{b}^* + \ell\underline{c}^* \qquad (h,k,\ell \text{ integers}) \qquad (3.6)$$

In these co-ordinates the Laue condition is satisfied if the vectors a*, b*, c* are defined by the conditions

$$\underline{a}^*.\underline{a} = \underline{b}^*.\underline{b} = \underline{c}^*.\underline{c} = 2\pi$$

and $$\underline{a}^*.\underline{b} = \underline{b}^*.\underline{a} = \underline{c}^*.\underline{b} = \ldots = 0 \qquad (3.7)$$

Expressions for a*, b*, c* that satisfy 3.7 are

$$\underline{a}^* = 2\pi \frac{\underline{b}\times\underline{c}}{\underline{a}.\underline{b}\times\underline{c}}, \quad \underline{b}^* = 2\pi \frac{\underline{c}\times\underline{a}}{\underline{b}.\underline{c}\times\underline{a}}, \quad \underline{c}^* = 2\pi \frac{\underline{a}\times\underline{b}}{\underline{c}.\underline{a}\times\underline{b}} \tag{3.8}$$

The lattice defined by these vectors is called the reciprocal lattice of the crystal structure and the Laue condition corresponds to requiring that $\underline{\Delta\kappa}$ shall be a vector of the reciprocal lattice. In the reciprocal lattice the Laue condition can be geometrically represented by drawing a sphere of radius $|\underline{\kappa}| = |\underline{\kappa}'| = 2\pi/\lambda$, known as the Ewald sphere. The Laue conditions are satisfied whenever the sphere intersects a reciprocal lattice point, (figure 3.4).

In order to use these ideas in LEED, the surface can be considered as a two-dimensional array of point scatterers. In this case, one of the Laue conditions for the direction normal to the surface is relaxed. This effectively means that $\underline{c} \to \infty$, so $\underline{c}^* \to 0$ giving a continuum in this direction. The reciprocal lattice now consists of a set of rods perpendicular to the surface (figure 3.5). The points where the Ewald sphere intersects the rods determine the directions of the diffracted beams which now satisfy the condition

$$G^*_{hk} = \underline{\Delta\kappa}_{11} \tag{3.9}$$

where $\underline{\Delta\kappa}_{11}$ is the component of $\underline{\Delta\kappa}$ parallel to the surface. The observed LEED patterns are simply sections of the reciprocal lattice perpendicular to the rods. Measurement of the positions of the diffraction beams then allows the determination of the unit cell parameters (a,b). Figure 3.6 shows a LEED pattern from a single crystal tungsten (110) surface. The reciprocal lattice and the corresponding real lattice are also shown to demonstrate the above ideas. The diffracted beams are labelled

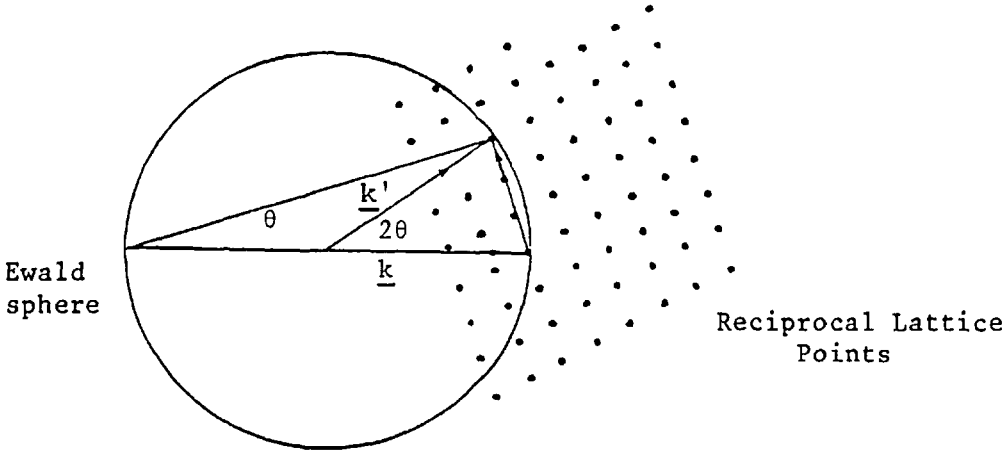


Figure 3.4 Ewald Sphere construction. The vector $\underline{k}$ is drawn in the direction of the incident beam and it terminates at any reciprocal lattice point. A sphere of radius $k = 2\pi/\lambda$ is drawn about the origin of $\underline{k}$. Diffraction beams are formed if the sphere intersects any other reciprocal lattice points.

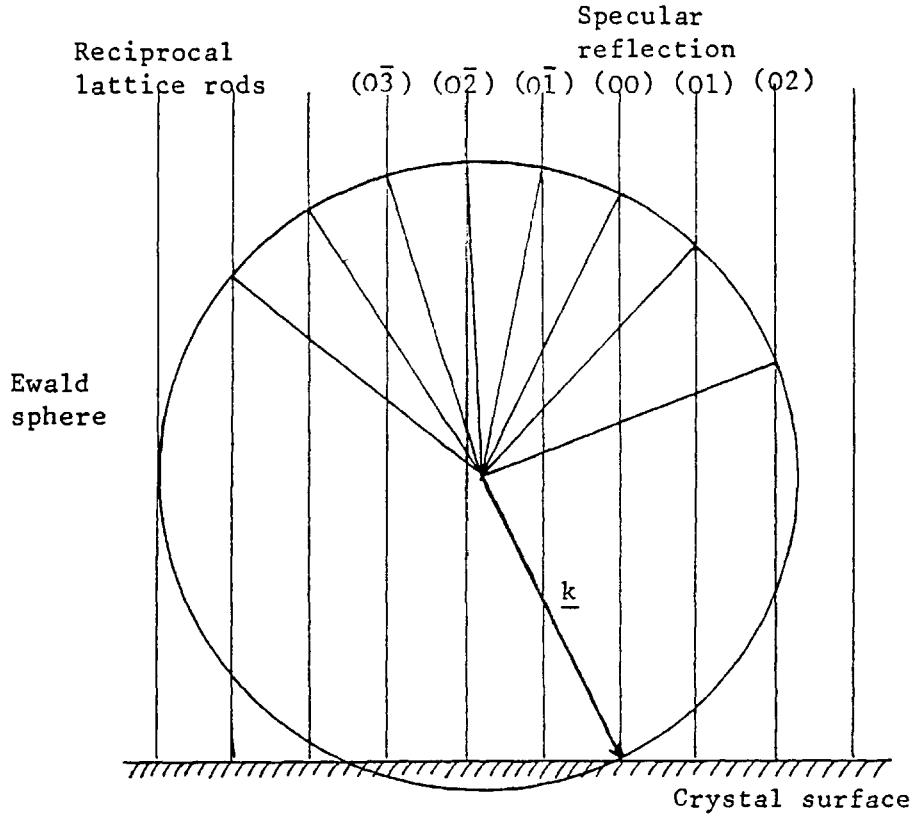
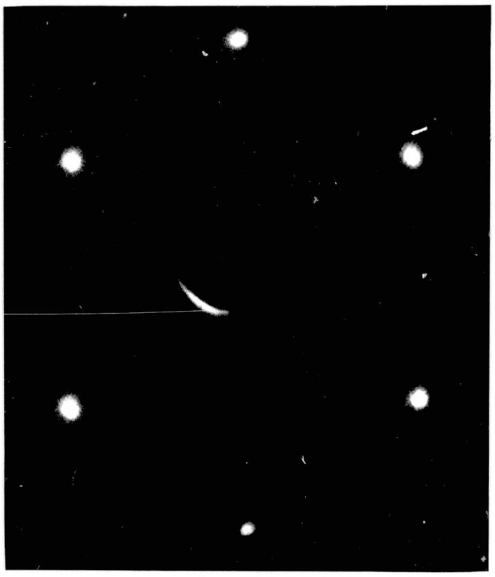


Figure 3.5 Ewald Sphere construction applied to LEED. The reciprocal lattice in this case is a series of rods. Diffracted beams occur in directions given by the intersections of the Ewald sphere with these rods.



a 64

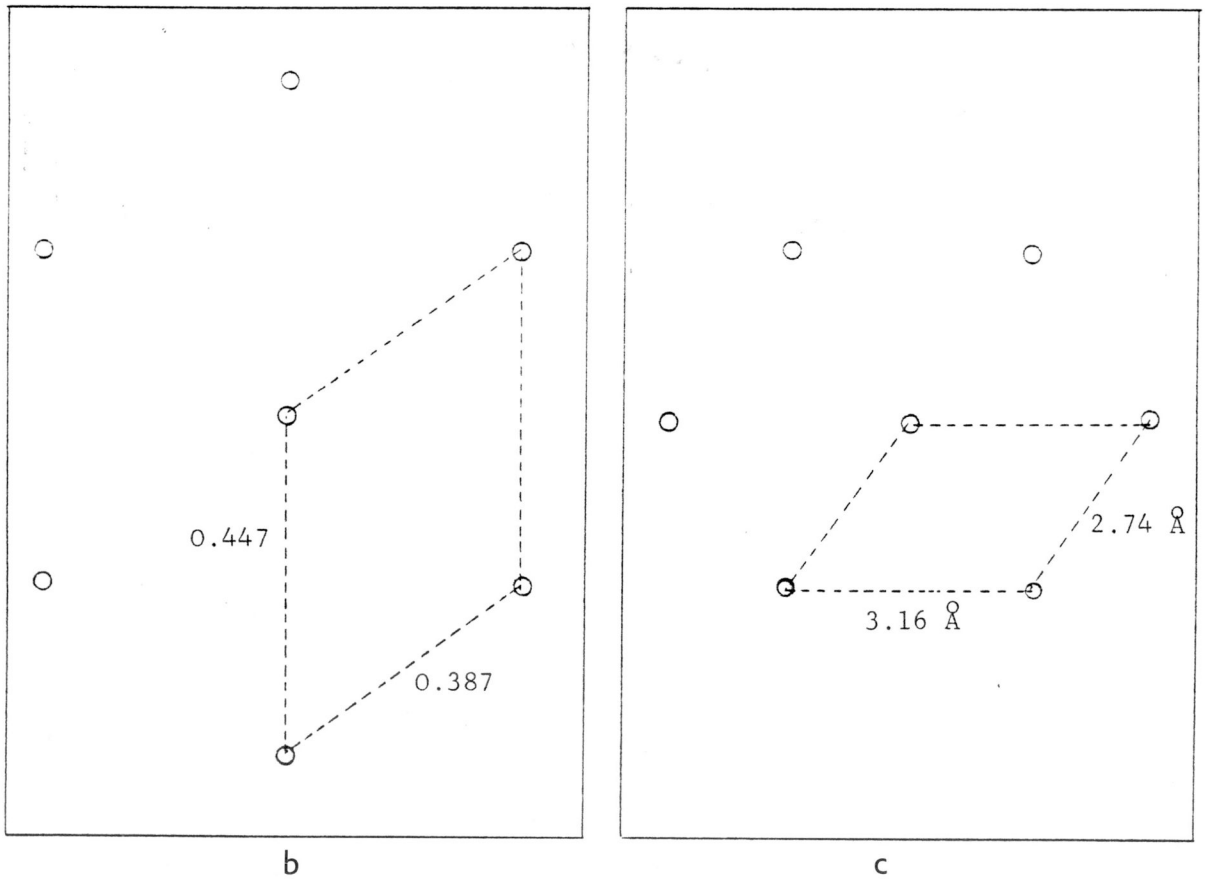


Figure 3.6 (a) LEED Pattern from W(110) surface, (b),(c) Reciprocal and real lattice unit cells of W(110) surface structure, respectively.

with the indices (hk) of their respective reciprocal lattice rods, where the (00) is taken to be the termination of the incident wave-vector. Extra spots, for instance due to adsorbed overlayers, are given fractional indices.

In the ideal case of a single layer with one atom per unit cell, to a first approximation (neglecting any $\underline{\Delta\kappa}$ dependence of the atomic form factor in equation 3.3) all the diffracted beams in the pattern will have equal intensity. The reciprocal lattice rods in this case are of identical and uniform diameter. In practice, the electrons penetrate to a depth of a few atomic layers. The spot positions are still determined by a two dimensional array involving only $\underline{a}$ and $\underline{b}$ since the periodicity in the $\underline{c}$ direction will not be sufficiently extensive to enable a third Laue condition to be established. However the effect of the finite electron penetration into the sub-layer is to modulate the lattice rods along their length. This has the effect that as the energy of the electron beam, and hence the radius of the Ewald sphere, is varied, the diffracted beam intensities will vary according to the modulation along the rods. This phenomenon is displayed in an intensity vs. voltage plot for a particular diffraction beam, the detailed analysis of which requires the dynamical theory.

So far it has been assumed that the unit cell of the lattice contains only one atom. However, it is possible that the unit cell can contain more than one atom. In this case, if there are q atoms in the unit cell at positions defined by the vectors

$$\underline{r}_q = x_q\underline{a} + y_q\underline{b} + z_q\underline{c}$$

relative to the cell origin δ_{mnp}, the total scattered amplitude from the crystal can be written as

$$a_c = \sum_{mnp} \exp(-i\underline{\delta}_{mnp}\underline{\Delta\kappa}) \sum_{q} f_q \exp(-i\underline{r}_q \cdot \underline{\Delta\kappa}) \qquad (3.10a)$$

where f_q is the atomic form-factor of the q^{th} atom in the unit cell. The second summation in 3.10a is called the structure factor. The intensity of the diffraction beam is given by $I = |a_c|^2$ which for a lattice consisting of M×N×P unit cells gives[98]

$$I \propto \frac{\sin^2\{\tfrac{1}{2}M\underline{a}.\underline{\Delta\kappa}\}.\ \sin^2\{\tfrac{1}{2}N\underline{b}.\underline{\Delta\kappa}\}.\ \sin^2\{\tfrac{1}{2}P\underline{c}.\underline{\Delta\kappa}\}}{\sin^2\{\tfrac{1}{2}\underline{a}.\underline{\Delta\kappa}\}.\ \sin^2\{\tfrac{1}{2}\underline{b}.\underline{\Delta\kappa}\}\ .\ \ \sin^2\{\tfrac{1}{2}\underline{c}.\underline{\Delta\kappa}\}} \qquad (3.10b)$$

(3.10b) has a half-width inversely proportional to the size of the scattering array.

3.1.2 Coherence width

In the preceding section, it was assumed that the incident electron beam is a single monochromatic plane wave emanating from a point source of an ideal instrument. In practice, however, the beam is emitted from a hot cathode of finite size so that it has a finite spread of energies and direction of propagation. In addition, there is a lack of ideal focussing by the electron optics. The electron wave therefore behaves as a coherent wave only over a short distance, called the coherence width, at the surface[102,103]. Recent experiments by Wang and Lagally[104] suggest that the coherence width is of the order of 100 Å or less. Since the incident beam has a finite width of the order of 1 mm^2 in a typical LEED apparatus, it may be considered as consisting of a large number of "pencils" of coherent radiation, each producing a diffraction pattern from a small area of the surface. The observed LEED pattern is then due to the superimposition of all these patterns. For a flat

perfect crystal surface the diffraction pattern will consist of spots which have a finite width set by the instrumental limitations. In the absence of any external perturbation such as stray magnetic fields within the instrument, changes in the pattern can occur if the state of the surface alters, for instance by the adsorption of atoms. Several changes in the LEED pattern due to the adsorbate can be accounted for by the kinematic theory[105-7].

3.1.3 LEED patterns from disordered structures

LEED patterns due to adsorbate covered surfaces are strongly dependent on coverage and temperature. At low coverage and temperature the adatoms may occupy sites on the surface at random. The effect of this is to reduce the intensity of the diffraction spots and increase the background intensity. This is analogous to the changes in intensity observed due to thermal disordering of an otherwise ordered scattering array[106,108]. If the adatoms are thermally activated, their migration over the surface can lead to the formation of islands (or domains) which have a particular order and symmetry relative to the substrate surface. At sub-monolayer coverage, the islands will be separated by "clean" substrate surface region so that the LEED pattern will consist of spots due to the "clean" surface and additional features due to the adsorbate domains. The effect of domains which are smaller than the coherence width is to cause a broadening of the diffraction spots. For example, if a single domain with M unit cells in an island edge is formed within the coherence width, the diffraction spots will be broadened by 1/M (equation 3.10b). In practice, several islands may nucleate within the coherence width. Since the islands may have

formed independently of each other, they may have anti-phase boundaries separating them. In this case the scattering amplitude from all the domains add and the effect of interference between domains must be included in the structure factor (Equation 3.10). As an example, consider two domains of an overlayer shifted relative to each other by vector $\underline{d}$, which can be expressed in terms of the substrate unit vectors $\underline{a}$, $\underline{b}$, $\underline{c}$:

$$\underline{d} = d_x\underline{a} + d_y\underline{b} + d_z\underline{c} \tag{3.11}$$

(figure 3.7). From equation 3.10a the structure factor can be written as[99,107]

$$s = \sum_{q=0}^{1} \exp(-i\underline{d}_q.\underline{\Delta\kappa}) \tag{3.12}$$

where all the atomic form factors have been set to one for convenience. Substituting from equations 3.6 and 3.11, s can be expressed as

$$\begin{aligned} s &= 1 + \exp\{-2\pi i(d_x h + d_y k + d_z \ell)\} \\ &= 0 \quad \text{for} \quad d_x h + d_y k + d_3 \ell = \frac{1}{2}(2n+1) \qquad (n = \text{integer}) \end{aligned} \tag{3.13}$$

For the particular example of the c(2×2) layer shown in figure 3.7, the diffraction spots can be labelled as[98]

$$h,k = \frac{1}{2}h', \quad \frac{1}{2}k'$$

If h', k' are both odd, the half-order spots of the overlayer are obtained. If both are even, the substrate (1×1) spots are obtained. Ignoring the d_z dependence for the moment, equation 3.13 is satisfied if both h', k' are odd, hence the half-order spots will be split. The

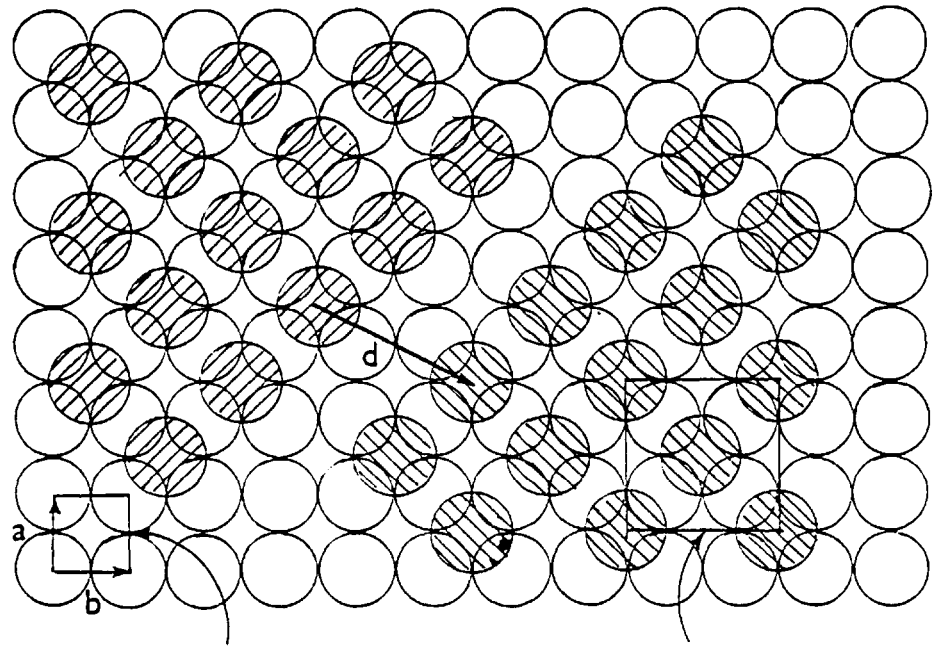
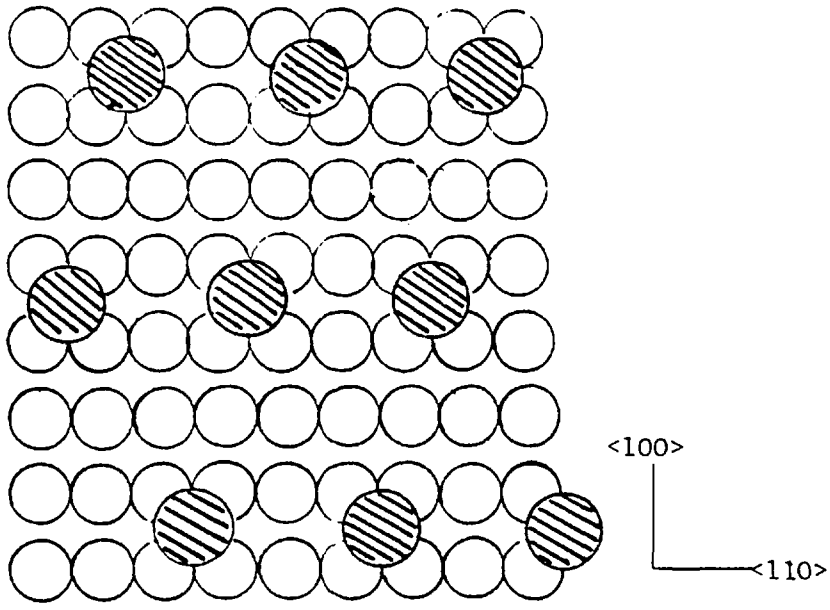


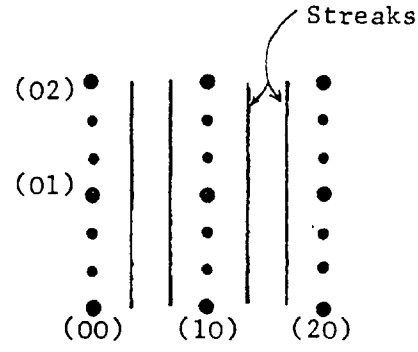
Figure 3.7 Antiphase domains of a c(2×2) structure on a square lattice. The two domains are connected by the displacement vector $\underline{d}$.

term in d_3 in 3.13 gives the energy dependence in the interference, since the ℓ values are sampled as the Ewald sphere is varied. The appearance of a diffraction spot, thus, varies from a normal spot, when domains scatter in phase, to split spots when domains scatter out of phase. Such a feature in the LEED pattern is analogous to that of a surface containing a regular array of steps in a preferred direction. In general, there will be many domains with irregular anti-phase boundaries, in which case spot broadening is observed. The size and shape of domains can be determined in principle by measuring the spot intensity profile, as has recently been demonstrated by Hahn and co-workers[54] for tungsten islands on tungsten (110).

In the case of islands that grow in a preferred direction, streaking may be observed in the LEED pattern. For example, Gerlach and Rhodin[109] have observed streaks in the diffraction pattern from sodium overlayers on Ni(110). The diffraction pattern they observe at a coverage of about 0.25, and the proposed structure are shown schematically in figure 3.8. The sodium atoms are one-dimensionally incoherent with respect to the Ni substrate and adjacent rows are out of phase with each other. The structure can therefore be thought of as consisting of one-dimensional "disorder" running in the $\langle 1\bar{1}0\rangle$ direction between rows of sodium atoms. Gerlach and Rhodin assign an uncorrelated phase distance in the $\langle 1\bar{1}0\rangle$ direction and obtain an analytic expression for the scattering factor. Their results show that cones of diffraction are produced by the rows of evenly spaced sodium atoms when the "one-dimensional" Laue condition $\underline{\Delta\kappa}.\underline{a} = 2\pi n$ is satisfied. Streaks are observed when the cones intersect the spherical LEED screen. A similar one-dimensional disorder is considered in the present study to account for streaked features in the LEED patterns from rhodium overlayers on W(110) at low coverage, (section 6).



(a) Alternate troughs are occupied by adatoms (shaded) which are triple spaced within any trough; rows are randomly shifted relative to each other in the <110> direction.



(b) LEED pattern from the structure of (a).

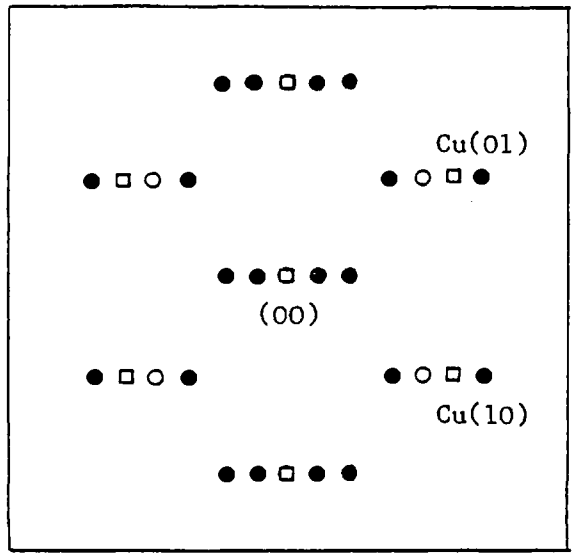
Figure 3.8 Na on Ni(110) for θ = 0.1 (ref. 109).

3.1.4 Satellite spot patterns

Because of the finite penetration of low energy electrons, it is possible to observe interference between scattered waves from the overlayer and substrate surface. The result is that in addition to diffraction spots from the overlayer and substrate surface structure, there are "extra" or satellite spots in the pattern. An example of a satellite spot pattern, due to Cu(111) overlayer on W(110)[55], is shown schematically in figure 3.9. A similar pattern has been observed in the present study of rhodium on both tungsten and molybdenum (110) surfaces (see chapter 6). The satellite spots are the result of multiple scattering between the overlayer and substrate. In the simple kinematic theory, the diffracted waves from the overlayer are treated as a set of new plane waves incident on the substrate surface[55,110]. The positions of the satellite spots are determined by the reciprocal lattice vector $\underline{\Delta G}$ obtained by adding or subtracting integral multiples of the reciprocal lattice vectors g_a^* and g_s^* of the adsorbate and substrate lattices, respectively:

$$\underline{\Delta G} = mg_a^* + ng_s^* \qquad (m,n = \text{integers})$$

This effectively means drawing the LEED pattern of the adsorbate structure centred on each spot of the substrate pattern. Although the simple kinematic theory qualitatively explains the occurrence of the satellite spots, it also predicts, contrary to observation, that below a cut-off energy only spots from one of the structures will be observed. Palmberg and Rhodin[111] have shown that a satisfactory explanation is obtained by a rigorous treatment of the kinematic theory, using evanescent rather than plane waves. These authors have also shown that in some situations where certain parameters are modulated,



Key

○ Primary W diffraction spot

□ Primary Cu diffraction spot

● "Multiple diffraction" spots

Figure 3.9 Schematic diagram corresponding to a "multiple diffraction" LEED pattern from Cu(111) on W(110). (ref. 55).

for example atom positions normal to the surface so that the overlayer is not flat but "puckered", it is sufficient to consider only single scattering in order to account for the satellite spots. An example where this may be the case is the tungsten carbide pattern discussed in section 4.3.8, chapter 4.

3.2 Auger electron spectroscopy (AES)

Electrons back-scattered from a surface generally have an energy spectrum which can be divided into three distinct regions[112], figure 3.10. Region I consists mainly of a sharp well-defined peak of elastically scattered electrons which are used in diffraction experiments. Regions II and III constitute the inelastically scattered electrons. Region II consists of electrons which have lost discrete amounts of energy, for example due to plasmon excitation in the specimen, while region III consists of a broad peak of true secondary electrons. Superimposed on the secondary peak are subsidiary maxima due to Auger electrons.

3.2.1 The Auger process

In Auger electron spectroscopy[113,114], an atom is initially ionized by an incident radiation and the relaxation of the ionized atom causes the emission of an Auger electron. The Auger process is schematically represented in figure 3.11. The initial ionization leaves a hole in one of the inner shells of the atom, and this is filled by an electron from an outer shell. The energy released from this excitation is absorbed by a third electron which is ejected from the atom as an Auger electron. The atom is left in a doubly ionized state

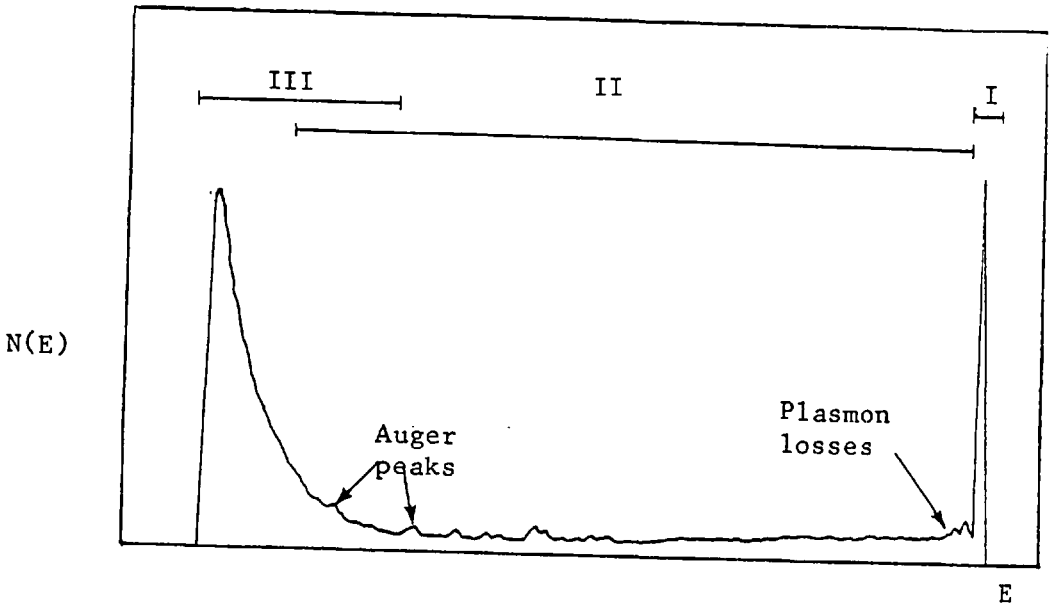


Figure 3.10 Energy Distribution of Scattered Electrons.

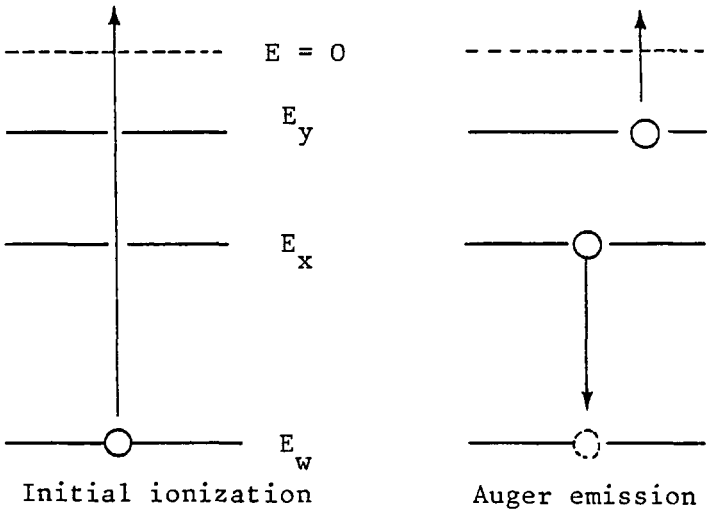


Figure 3.11 Schematic representation of the Auger process.

before being neutralized by the capture of free electrons.

To a first approximation the energy of an Auger electron is given by

$$E(z)_{\text{Auger}} = E_w(z) - E_x(z) - E_y(z) \qquad (3.14)$$

where z is the atomic number of the atom, and $E_w(z)$, $E_x(z)$ and $E_y(z)$ are the energy levels of the atom in the neutral state. However, the initial ionization effectively reduces the screening of the nuclear charge, with the result that electron energy levels are shifted. An expression for the Auger electron energy, which accounts for this effect has been given by Chung and Jenkins[115]:

$$E(z)_{\text{Auger}} = E_w(z) - \frac{1}{2}\{E_x(z) + E_x(z+1) + E_y(z) + E_y(z+1)\}, \qquad (3.15)$$

which means that in the presence of the initial hole, the energy levels of the atom have an average value between corresponding levels of atoms with atomic number z and z+1. The measured Auger energy includes the work function of the detector.

The Auger electrons are labelled according to the energy levels taking part in the process. For example, if an electron hole in a K shell is filled by an electron from the L_1 shell and the excess energy is given to an electron in the M_3 shell, the Auger transition is labelled KL_1M_3. Transitions which involve valence electrons are specified with a V, for example MVV. The intensity of an Auger line depends mainly on the ionization cross-section for creating the initial hole and on the probability of emission of the Auger electron by filling the hole. The most intense line observed for tungsten is at

about 182 eV due to an $N_4N_6N_6$ transition. Such transitions which involve the same electron shell are termed Coster-Kronig transitions.

3.2.2 Principles of detection of Auger electrons

The current associated with an Auger transition is usually of the order of 10^{-12} A, hence, sensitive techniques are required to separate the Auger electrons from the background current of secondary electrons[116]. A number of energy analysers are available for this purpose. The basic principles of the retarding field analyser (RFA) and the cylindrical mirror analyser (CMA), which were used in the present study, are outlined below.

(a) The retarding field analyser.

The RFA usually forms an integral part of the LEED optics, figure 3.12a. The first grid and the specimen are held at earth potential to provide a field free region for the back-scattered electrons. The second grid is biased with a negative potential, V_r, so that only electrons with energy greater than V_r pass through to the collector, which receives the current I given by

$$I(E) = \int_{V_r}^{E_p} N(E)dE \qquad (3.16)$$

where E_p is the energy of the exciting electrons and N(E)dE is the number of electrons with energy between E and E + dE. The Auger electrons are detected by electronic differentiation of the collector current. A small high frequency modulating signal, $V_m \sin \omega t$, is superimposed on the bias voltage. The collector current $I(V_r + V_m \sin \omega t)$ can be expressed as

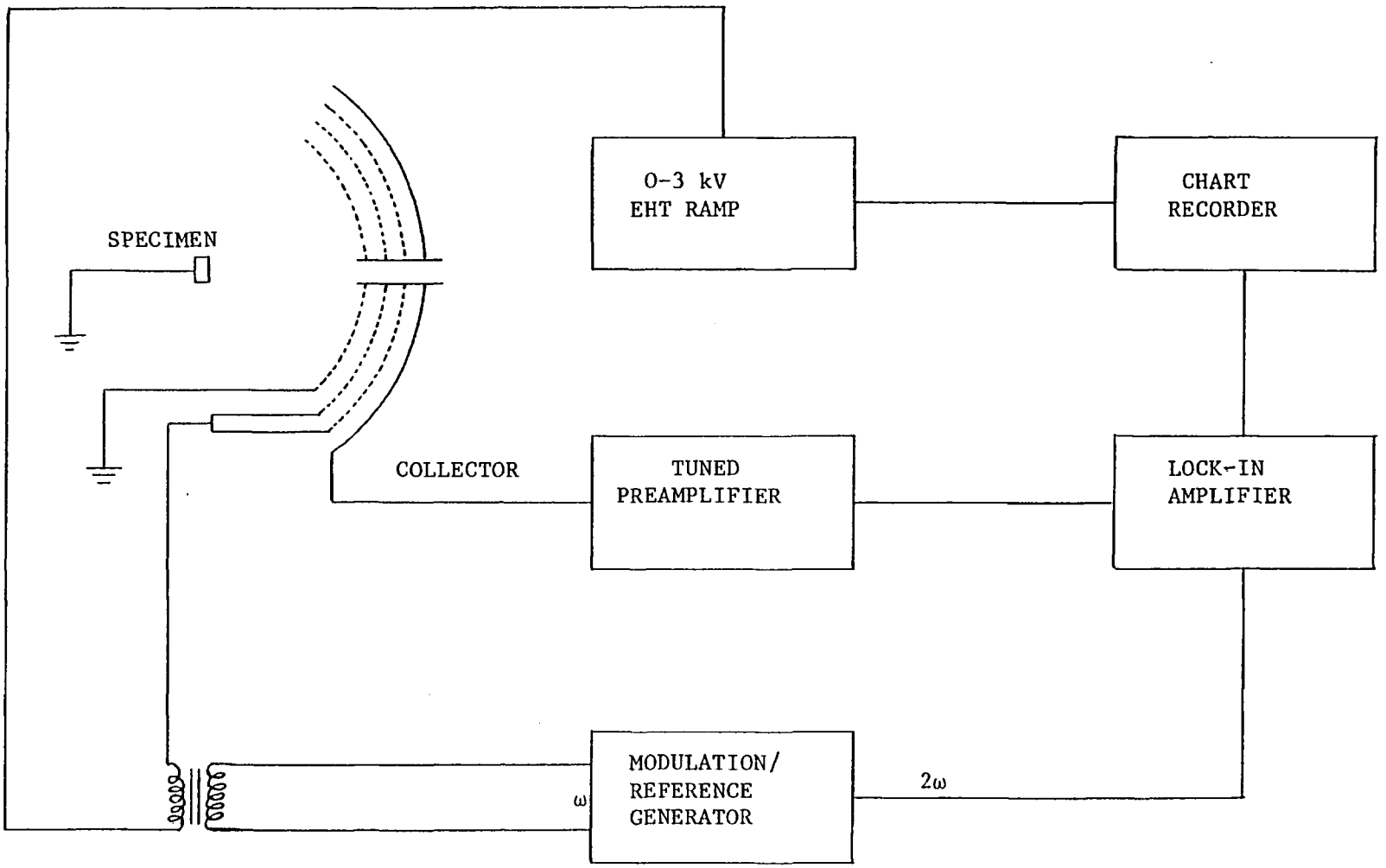


Figure 3.12a Schematic diagram of the RFA detection system.

$$I(V_r + V_m \sin \omega t) = I(V_r) + I'(V_r)V_m \sin \omega t + \frac{I''(V_r)V_m^2 \sin^2 \omega t}{2!} + \ldots\ldots\ldots \quad (3.17)$$

where I' denotes differentiation with respect to V_r. The a.c. signal sampled at frequency ω is proportional to dI/dE and hence to N(E). Similarly, the signal at 2ω is proportional to dN/dE. Usually the 2ω term is selected by amplifying the a.c. signal from the collector with a tuned pre-amplifier which produces a voltage output proportional to the current input at 2ω. This signal is fed to a synchronous phase sensitive detector driven by a signal from the modulation oscillator, and a smoothed d.c. signal is obtained. This output is fed to the Y-axis of a chart recorder. The X-axis of the recorder is driven by a potential obtained from a ramped power supply providing the bias voltage. The advantage of using dN/dE is that the Auger peaks in the energy spectrum are well-defined. Furthermore, the capacitatively coupled current between the collector and grid has no 2ω component and is therefore not detected. However, a disadvantage of the RFA is that the collector current is composed of all secondary electrons with energy exceeding V_r. This introduces considerable shot-noise and consequently, the amplifier band-width has to be decreased. The result is that long times are required to record a spectrum. Nevertheless, the RFA has been widely used because of the convenience of using the LEED optics as an energy analyser.

(b) The cylindrical mirror analyser

In the CMA, figure 3.12b, a potential V_a is applied between the co-axial cylindrical electrodes which focusses electrons, with energy in the range between E and E + dE, onto the collector. The CMA thus behaves as a band pass device and the collector current is given as

$$I(E) \propto N(E)dE.$$

Just as in the RFA, a phase-sensitive technique is used to obtain the Auger peaks, but in this case the first harmonic (ω term) is detected since the first derivative is proportional to dN(E)/dE. A major advantage of the CMA compared to the RFA is the reduction in shot noise, since only electrons within a small energy range dE are collected. Consequently the scan times to record a spectrum are considerably smaller compared to the RFA.

3.2.3 Practical aspects of AES

Since the energy of an Auger electron depends on the atomic number of the emitting atom (equation 3.15), an Auger spectrum can reveal the identity of atoms in the surface region. For example, Figure 3.13 shows characteristic Auger peaks of rhodium deposited on a clean tungsten (110) surface. The width of an Auger line is partly influenced by the lifetime of the initial hole, related to the Uncertainty principle, and by the widths of the energy levels participating in the transition. The energy levels of the atom may be affected by the interaction of the atom with its environment and this may affect the shape of the Auger line. For example, Haas, Grant and Dooley[117] have observed distinct differences in the Auger peak of

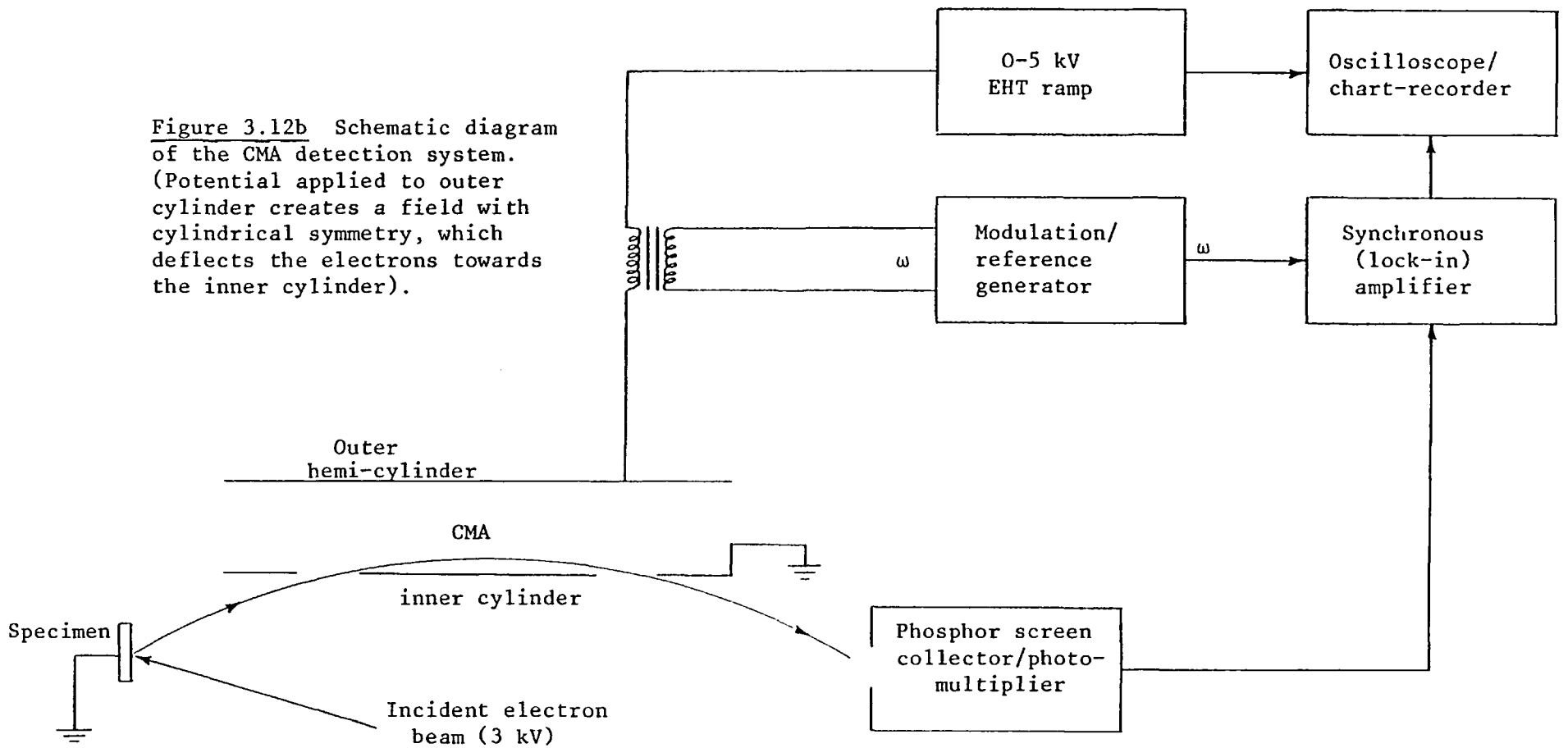


Figure 3.12b Schematic diagram of the CMA detection system. (Potential applied to outer cylinder creates a field with cylindrical symmetry, which deflects the electrons towards the inner cylinder).

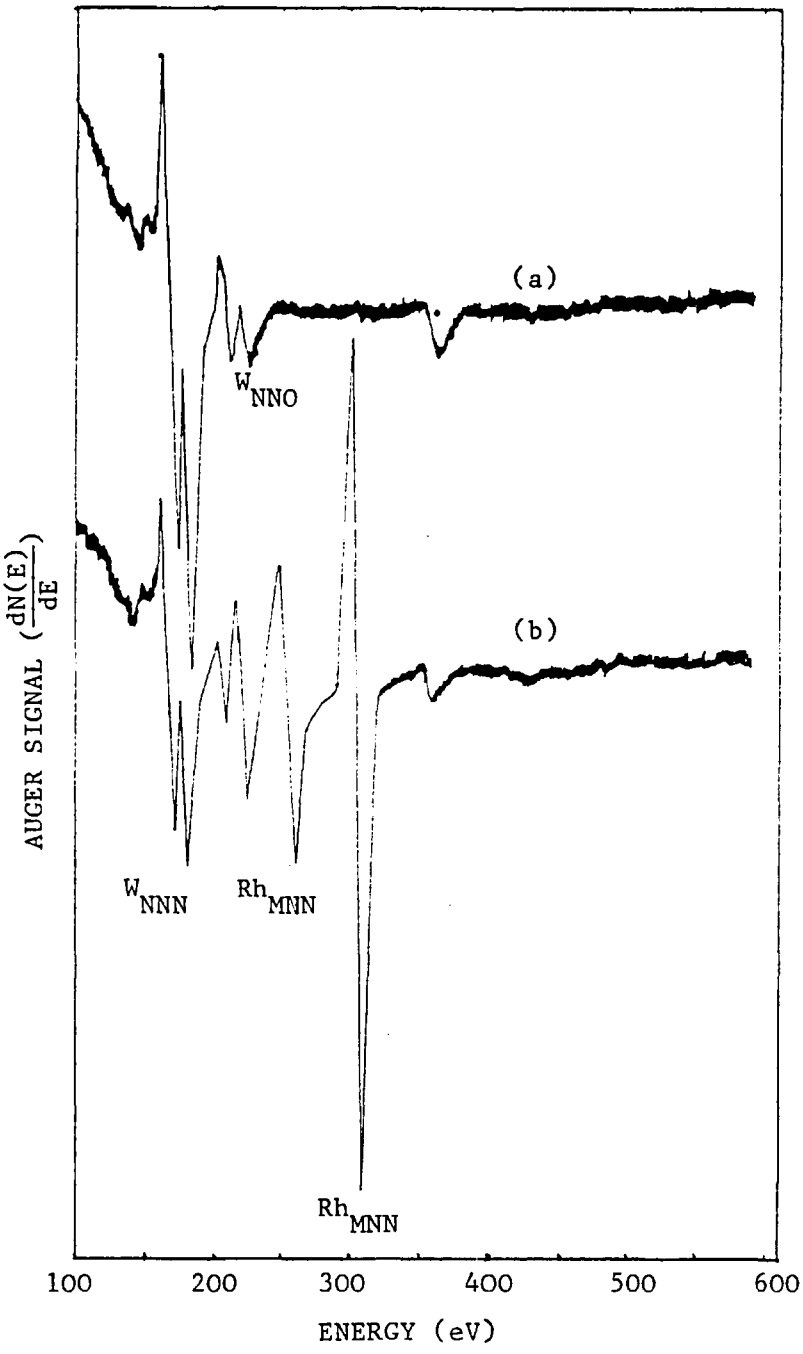


Figure 3.13 Auger spectra from (a) clean W(110) surface and (b) Rh on the W(110) surface, obtained with a CMA (scan rate: 1.7 v s^{-1}, time constant: 300 mS, modulation: 8 V p.t.p., primary electron energy: 2.5 kV). The tungsten peaks in (b) have decreased because the Auger signal from the substrate is partially attenuated by the overlayer (see text).

carbon depending on the form of carbon examined. In principle, an analysis of the width, shape and energy of an Auger line may provide information regarding the chemical environment of the atom but in practice this is difficult because three different energy levels are involved in the transition.

In a typical AES experiment the primary electron beam has an energy of the order of 1 keV. Although the incident electrons penetrate deeply into the surface region, the Auger electrons, which have relatively lower energies, are strongly attenuated. The observed Auger electrons are therefore from the first few layers of the surface. The attenuation coefficients of electrons through a given material are expressed in terms of the inelastic mean free paths (IMFP), λ_m, which have recently been compiled by Seah and Dench[118] for a range of materials. From the data available, they have obtained an empirical expression for λ_m, written as[118]

$$\lambda_m = 0.41(aE)^{\frac{1}{2}} \qquad (3.18)$$

where λ_m is in monolayers, E is the electron energy and a is the monolayer thickness given by

$$a^3 = \frac{W}{\rho N} \times 10^{24} \quad \text{(nm)} \qquad (3.19)$$

W is the atomic weight, ρ is the bulk density in kg m^{-3} and N is Avogadro's number. If an adsorbate A forms a uniform layer of monolayer thickness, covering a fraction x of the substrate surface B, the Auger intensities from the adsorbate and substrate can be expressed as[118]

$$I^A = XI^A_\infty R\left\{1 - \exp\left(\frac{-\sec\theta}{\lambda^A_m(E_A)}\right)\right\}$$

and

$$I^B = I^B_\infty \left\{ 1 - X + X \exp\left(\frac{-\sec\theta}{\lambda^A_m(E_B)} \right) \right\} \qquad (3.20)$$

In equations 3.20 I^A and I^B are the signals from pure bulk standards for the adsorbate and substrate, respectively, R accounts for back-scattered Auger electrons and in most cases is close to unity, $\lambda^A_m(E_B)$ is the IMFP of the substrate Auger electrons, of energy E_B, through the adsorbate layer and sec θ depends on the geometry of the Auger analyser, (effectively, sec θ = 1/0.74 for both the RFA and the CMA)[118]. The exponential term represents the attenuation coefficient. Equations 3.20 show that with increasing coverage the adsorbate signal increases and the substrate signal decreases linearly until a complete layer of monolayer thickness is formed. If further adsorption results in the growth of m uniform layers, each of monolayer thickness, then 3.20 can be modified to

$$\frac{I^A}{I^A_\infty} = 1 - \exp\left(- \frac{m \sec\theta}{\lambda^A_m(E_A)} \right)$$

and

$$\frac{I^B}{I^B_\infty} = \exp\left(- \frac{m \sec\theta}{\lambda^A_m(E_B)} \right) \qquad (3.21)$$

The expected variation in the Auger signal with increasing coverage, on the basis of equation 3.21, is shown schematically in figure 3.14. for the three basic growth modes[52]. Although in principle the Auger intensity should be plotted in order to determine the growth mode for a particular system of adsorbate and substrate, in practice it has often been found sufficient to plot the Auger peak-to-peak heights

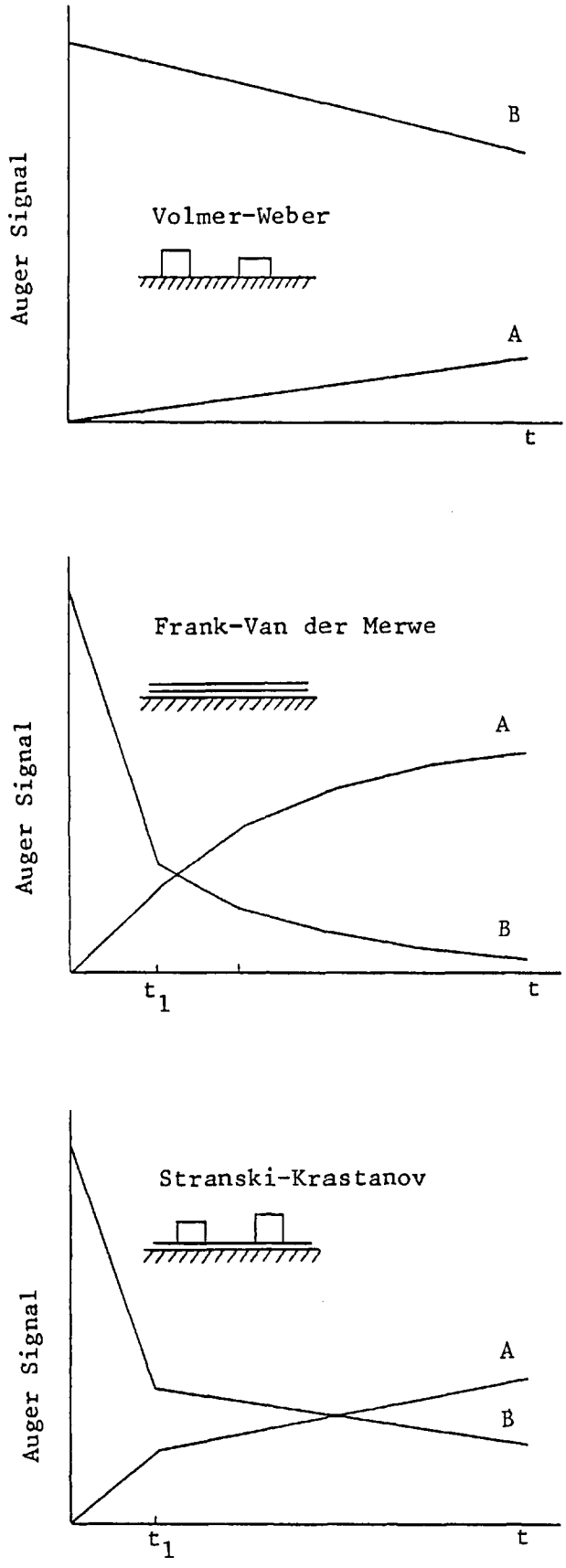


Figure 3.14 Variations of Auger signals for the substrate B and the adsorbate A during film growth by different mechanisms. t_1 : time to complete the first monolayer.

from the derivative spectra. Examples of this may be found in references 57-61.

4. EXPERIMENTAL

For any study of surfaces to be meaningful it is essential that clean surfaces are obtained and maintained. In the present studies by low energy electron diffraction and field ion microscopy this requirement was met by the use of ultra high vacuum techniques. The principles of such techniques have been discussed in detail in several books[119] and only the essential features of the LEED and FIM systems used and their operations will be outlined here.

4.1 Field Ion Microscopy

4.1.1 The Apparatus

The FIM system used is shown in figure 4.1. The microscope tube and the mercury diffusion pumps were made mainly of pyrex glass. The system was constructed originally by Parsley[120] but now included improved facilities for gas admission and a differently designed microscope tube, figure 4.2. In this tube the specimen is mounted vertically on a "cold finger" within a liquid nitrogen cooled jacket, and the image is produced on a horizontal screen of zinc silicate (Willemite) phosphor. To avoid particles of copper oxide (from the copper gaskets normally used for metal-flanged joints) falling on the screen during specimen changing, the specimen assembly was mounted on a flange using a gold wire seal. However, for the metal vapour source (evaporator) assemblies, normal copper gasket flange seals were used, although great care was required to avoid damaging the glass-ware during flange tightening.

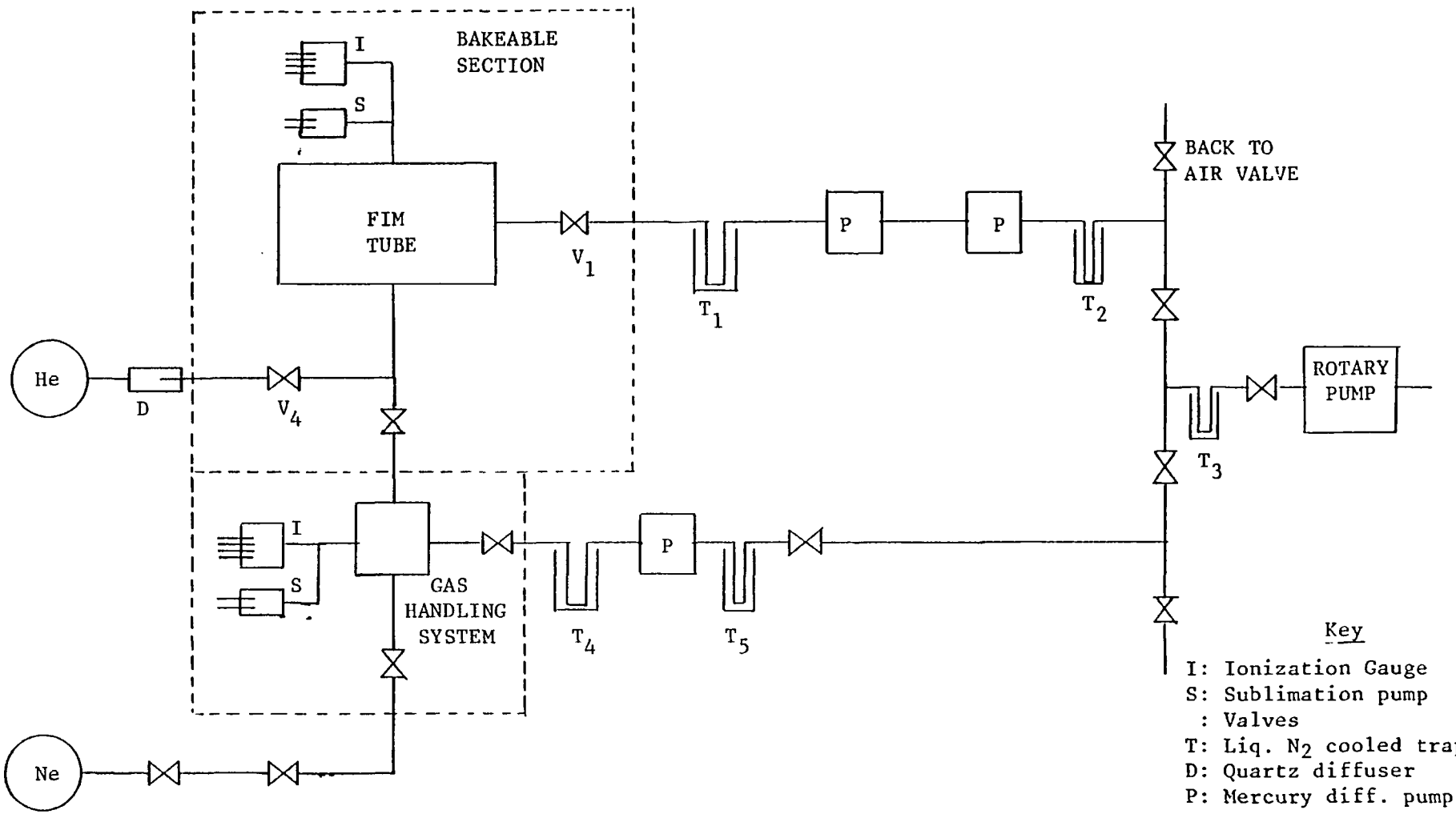


Figure 4.1 Schematic layout of the FIM System.

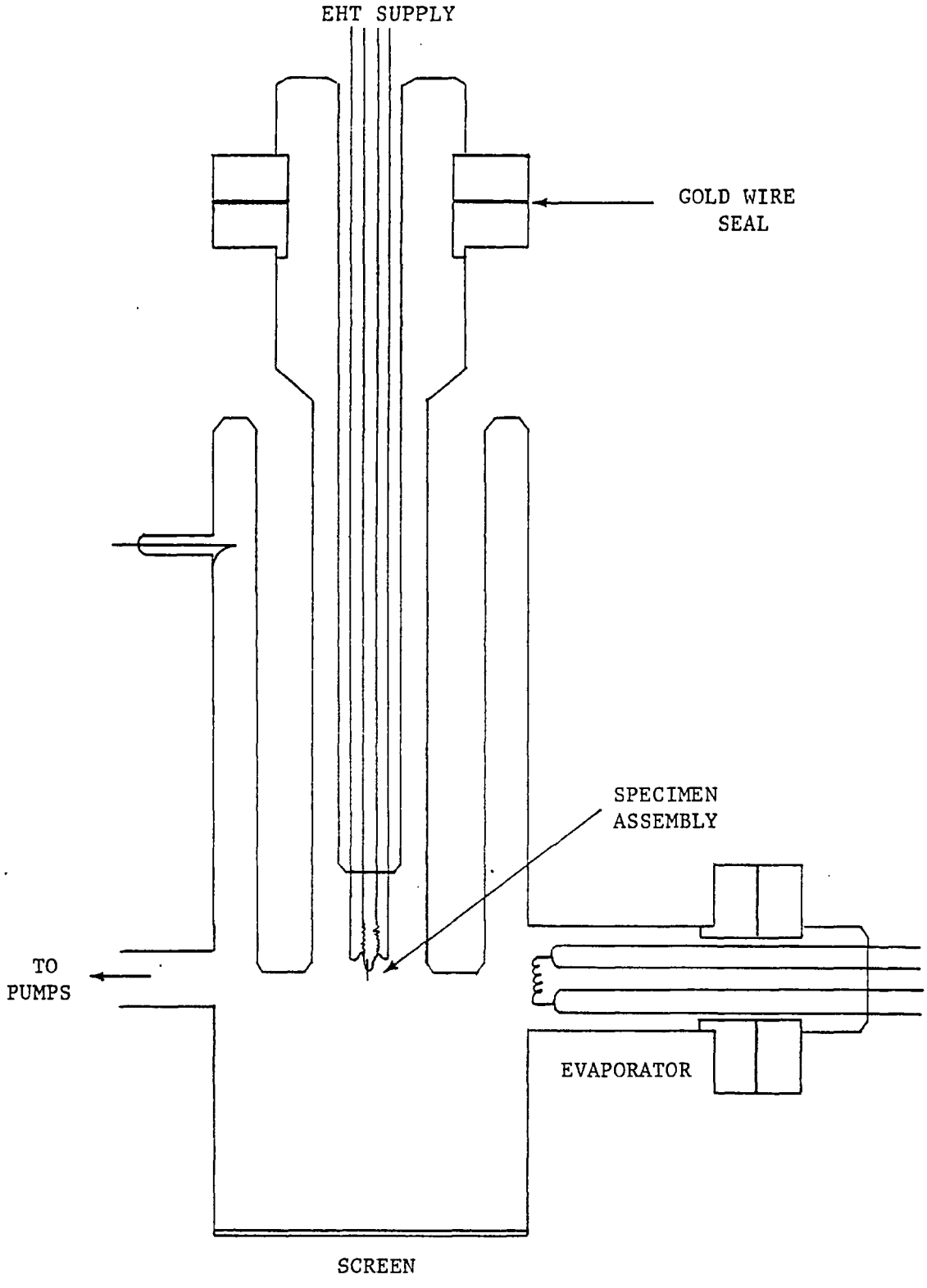


Figure 4.2 Field Ion Microscope Tube.

The specimen was spot-welded onto a 0.25 mm tantalum wire heating loop, figure 4.3a, to which were spot-welded two 0.05 mm tungsten wire potential leads for the purpose of determining the temperature of the tip by resistance measurement. The tantalum loop and the potential loads were spot-welded to 1 mm tungsten rods mounted on a tungsten/glass vacuum feedthrough on the cold finger.

The evaporators consisted of a resistively heated spec-pure metal wire coil from which metal atoms could be evaporated onto the tip. The construction of the evaporators is shown schematically in figure 4.3b. This design facilitated adequate degassing of the coil prior to deposition.

In addition to the FIM tubex, the bakeable section of the apparatus contained an Alpert-type ionization gauge for pressure measurement and a molybdenum getter tube for use as a sublimation pump. The EHT supplies for the microscope and the specimen temperature controller were as described by Parsley[120] and Webber[121]. The resistance of the tip support loops could be monitored continuously by means of an analogue divider providing an output of 10 x V_{fil}/I_{fil} to a digital voltmeter (D.V.M.).

4.1.2 Evacuation procedure

Following specimen or evaporator changes, the FIM was pumped from atmosphere to UHV using standard procedures. If no leaks were found during pump down, the microscope was baked overnight at about 200 ^{o}C and metal components in the microscope were thoroughly de-gassed. Afterwards pressures below 1 x 10^{-9} torr were normally obtained, sufficing for preliminary testing of new specimens (section 4.1.3). The microscope was then baked again and the ultimate vacuum obtained

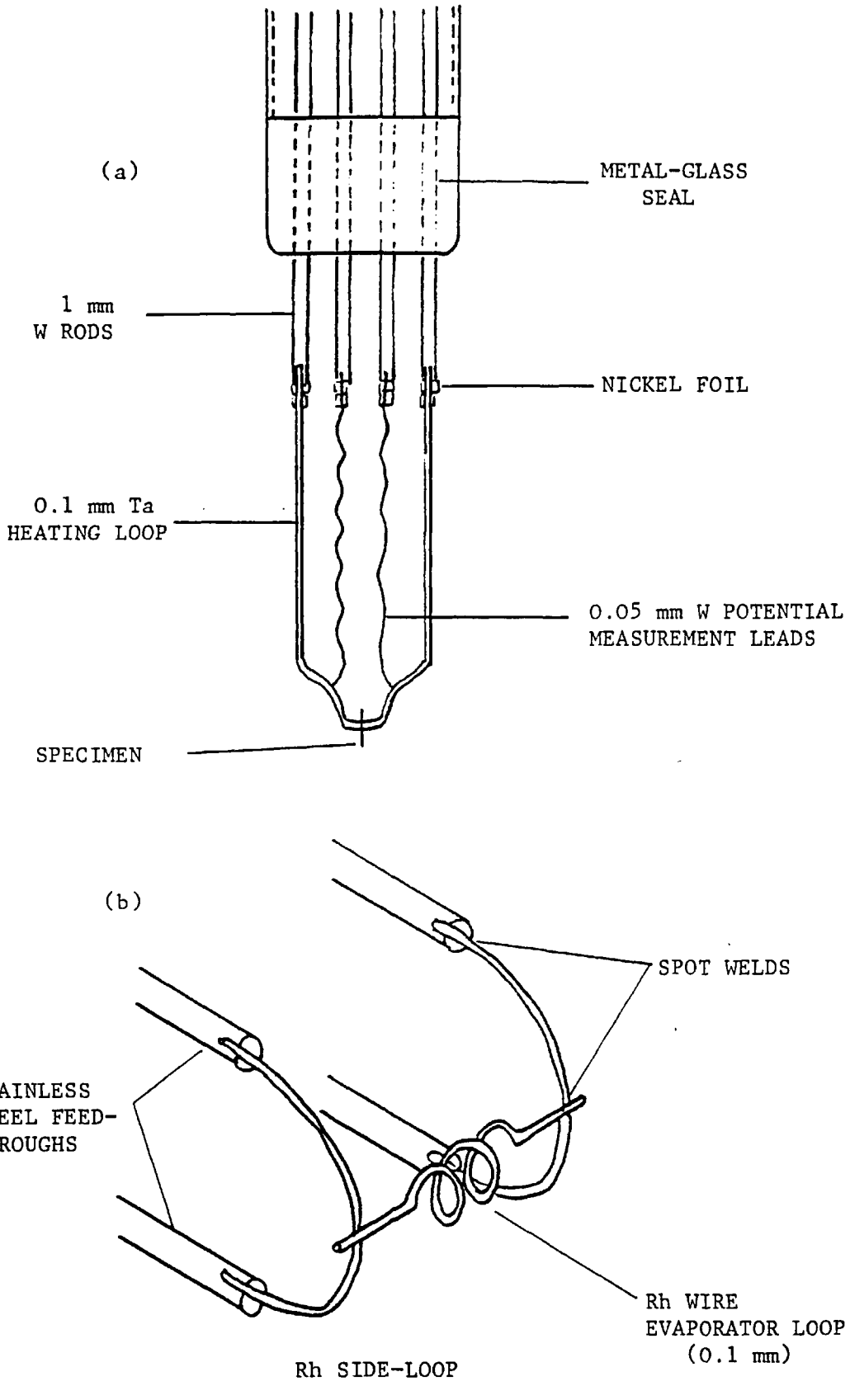


Figure 4.3 (a) Specimen assembly, (b) Evaporator assembly. (Ref. 121)

after degassing metal components was below 2 x 10^{-10} torr. During operation the FIM is shut off from the diffusion pumps and back-filled to about 1 x 10^{-3} torr with the helium image gas, but pumping of chemically active gases was maintained by depositing a molybdenum film in the getter bulb.

Helium of ultra-high purity for imaging was admitted to the microscope via a heated quartz membrane diffuser and a metal valve V_4 (figure 4.1b). Neon, used for in-situ cleaning and sharpening of tips by ion bombardment[122], was admitted from the gas-handling system after standing in contact with a freshly-deposited molybdenum film.

The commonest difficulty encountered in establishing UHV conditions was associated with saturation of the liquid nitrogen trap T_1 (figure 4.1b) with CO_2 which resulted in an ultimate vacuum of $\sim$1 x 10^{-8} torr. This was overcome by shutting-off the microscope from the diffusion pumps, warming the trap to evaporate the condensed CO_2 and then re-establishing UHV in the pump-line by briefly baking the line with a tape-heater. After operational shut-downs, for instance at week-ends, UHV conditions could be restored after a brief bake.

To avoid excessive contamination during specimen or evaporator changing, the system was normally returned to atmospheric pressure using Argon from a cylinder.

4.1.3 Specimen preparation

Specimen tips were sharpened after spot-welding the wire on to the support loop. Both tungsten and molybdenum specimens were prepared by electropolishing whilst under observation through a x100 optical microscope. A pulsed D.C. voltage was applied to the specimen wire immersed about 2 mm in the polishing solution. The final sharpness of the specimens was judged after removing the tips from the solution and observing through a x500 microscope. The attainment of a smoothly tapered shank in the immediate vicinity of the unresolved tip was taken to be a criterion of a usable specimen.

Tungsten tips were prepared from a 0.12 mm diameter wire in a solution of 2N sodium hydroxide, using a pulsed D.C. voltage of 13 volts. The molybdenum tips were prepared from a 0.2 mm diameter wire in a solution of 1:7 sulphuric acid: methanol, using a pulsed D.C. voltage of 6 volts.

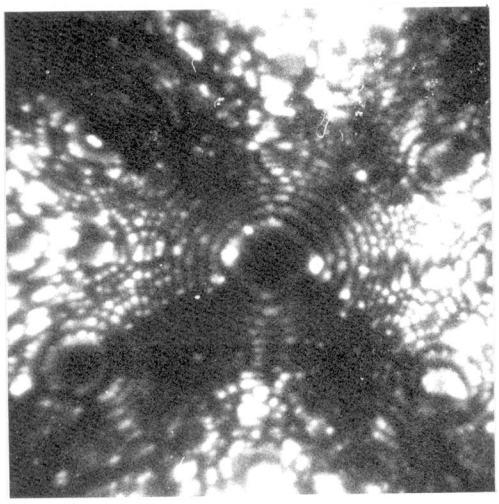
After preparation and installation in the microscope, and one bake-out, specimens were annealed and degassed before being imaged. Annealing at approximately 1000 ^{o}C for 15 sec. intervals was carried out until the field-emission pattern became symmetrical, i.e. showed clear 4-fold symmetry for b.c.c. W and Mo. Alternatively, to avoid excessive blunting of the tip during annealing, field desorption was used to clean the surface, although to avoid destruction of the tip by catastrophic field evaporation, it was necessary to increase the desorption voltage in steps and to monitor the surface condition after each step. Once a symmetrical field emission pattern was obtained, helium was admitted into the chamber and liquid nitrogen poured into the cold finger. The specimen surface was then field evaporated under direct observation until a perfectly ordered surface was obtained. If

the tip survived this initial field evaporation and was sufficiently sharp to be usable, the chamber was given a second bake.

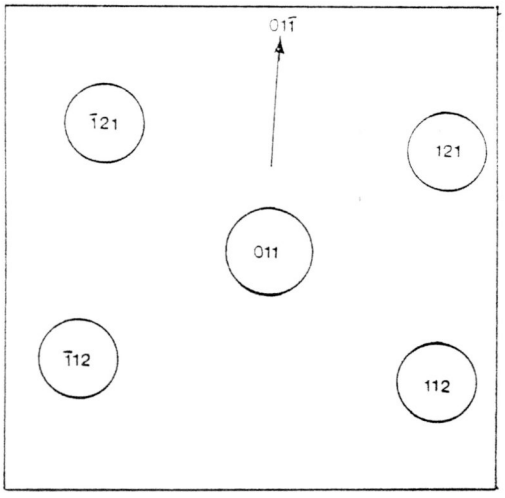
Following the final clean-up of the chamber and before any experimental run, several cycles of annealing and controlled field evaporation were performed. These removed any weakly bound adsorbates, for example hydrogen, from the tip shank that might otherwise diffuse from the shank into the imaged region during experiments in which the specimen is heated. The tips were usually sufficiently blunted by this procedure to image at about 10 kV.

4.1.4 Image Observation

The FIM images formed by direct impingement of the ions at the phosphor screen are of very low intensity since the ion current at the screen is typically of the order of 1×10^{-10} amps[6]. Consequently images were observed, after dark adaptation of the eyes, in a completely darkened room. The images could be observed through binoculars directed at a mirror located under the microscope tube. The mirror could be rotated away to reveal a Shackman 35 mm camera with Wray f1 optics for recording the image on Kodak 103 aG spectroscopic film. The film exposure times varied with the imaging voltage. As noted in section 2.5, stable He ion images of tungsten were readily obtained at the best image voltage (BIV) while lower voltages had to be used for imaging molybdenum. Thus, typically, film exposure time for tungsten varied from 2-3 min. at 12 kV to about 5-6 min. at 8 kV, while for molybdenum the exposure times were higher by up to 2-3 min. at similar voltages. A characteristic field evaporated end-form of a (110) oriented molybdenum tip surface is shown in figure 4.4 (cf. figure 2.3 for tungsten).



(a)



(b)

Figure 4.4 (a) Field ion image of a (011) oriented field-evaporated molybdenum tip; (b) key to the micrograph showing some low Miller index planes.

While computer simulations of the FIM image for perfectly spherical surfaces of f.c.c. and b.c.c. metals can represent many features of the images[123], in practice images from field-evaporated surfaces of real metals show contrast variations that vary from one metal to another and depend on temperature[124]. Thus although both W and Mo are b.c.c. metals, their FIM images look quite different. The reasons for such differences are not well understood, but one factor is variations in local surface curvature characterising the shape of the field evaporated end-form. Thus, highly curved regions image more brightly. However, why the anisotropy of field evaporation behaviour should be so different for metals as similar as W or Mo is not clear. Differences in the electronic structure of the metals, and possibly in the energetics of any surface migration step in the field evaporation process (c.f., section 2.4, figure 2.8) may be important.

Another striking difference in the micrographs is the degree of zone decoration of atoms. Muller[124] has suggested that these atoms are field-stabilized in protruding low co-ordination sites by polarization binding. In the case of tungsten, this leads to a bright decoration of atoms on the [001] zone between the (130) plane and (310) plane through the central (110) plane, while a similar decoration in the case of molybdenum is much more diffuse. It is also possible that zone-line decoration atoms could be due to a diffusion-step in field evaporation process[95].

In a typical FIM micrograph, the bright spots represent only about 10% of the surface atoms[6]. It is therefore important to consider imaging of adsorbates. In general any metal adatom protrudes sufficiently above the mean surface envelope as defined in computer simulations to

image wherever it is placed. In practice, the protrusion may be (i) so large that the local field experienced by the atom is so high that it desorbs before a useful imaging voltage is reached, or (ii) too small for a bright enough image at optimum imaging conditions. In the present work we are primarily concerned with the behaviour of rhodium atoms deposited on the field evaporated (110) surfaces of tungsten and molybdenum. The visibility of such adatoms and adatom clusters is thus vital to success of the experiments and depends on (i) the size of the plane, (ii) the position of the adsorbate on the plane, and (iii) the nature of the substrate.

The (110) plane of the b.c.c. lattice is the most closely packed plane, hence protrusion of adatoms is higher on this plane compared to other planes. However, curvature is lowest at (110) and the image is dimmest there. Furthermore, the local field variation across the plane has the effect that adatoms near the edge of the plane image brightly compared to adatoms near the centre (figure 4.5). On very large planes, adatoms at the centre can be invisible. An optimum size for the (110) plane was therefore used, corresponding to an average radius of the order of 5 nm.

The field desorption of adatoms sets an upper limit to the imaging fields that can be used. The Rh adatoms could be imaged readily on W(110) but much care was required to image the adatoms on Mo(110) due to the lower fields required to image Mo.

The adatoms could be removed by field desorption. Removal of Rh from the tungsten surface was achieved normally, though adatoms were sometimes observed to "pop-up" just prior to desorption. In the popped-up situation, the brightness and apparent size of the adatom is greatly enhanced. A similar effect has been observed by others[19,37,121].

Bassett and Parsley[19] observed "pop-up" of iridium atoms on tungsten (211) planes and on (111) steps while Plummer and Rhodin[37] have noted similar effects with platinum and gold adatoms on tungsten. Webber[121] observed that gold adatoms on Pt(113) and (110) planes could be made to "pop-down" from a popped up situation by lowering the field before the adatom desorbed, thus indicating that this effect was not an artefact but involved a real movement of the adatom. On Mo(110), Rh adatoms were sometimes retained although a complete layer had been field evaporated; the adatoms appeared to have "dropped" onto the next layer while the Mo layer they were originally on evaporated away. In this case, Rh could usually be removed by fast field evaporation of several layers.

Imaging of adatom clusters on both W and Mo(110) planes required great care to avoid field-induced dissociation of the cluster as the imaging voltage was raised, and normally, voltages much below BIV were used for observing and recording images. Figure 4.6 shows a Rh adatom which has field-dissociated from the end of a linear-chain cluster on W(110). Field-induced dissociation of adatom clusters has been reported before[29,125]. Bassett[29] has observed field-dissociation of Ni, Pd and Pt clusters on W(110). Benecke, Faulian and Bauer[125] have also observed field-dissociation of Pd clusters on W(110). Such effects can be qualitatively attributed to the field gradient that exists across a plane, leading to greater polarization of adatoms towards the plane edge[20]. Also, the effective polarizability of an isolated adatom is probably larger than for a step or kink atom. The gain in polarization energy may be greater than the loss associated with bond-breaking, thus stabilizing the isolated adatom[124].

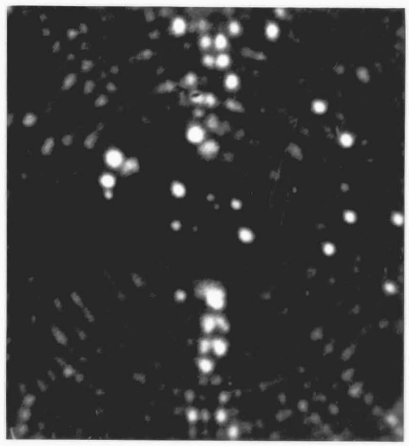


Figure 4.5 Micrograph illustrating the image brightness variations of adatoms (Rh) across the W(110) plane. Adatoms near the centre of the plane appear less brighter than those nearer the edge of the plane.

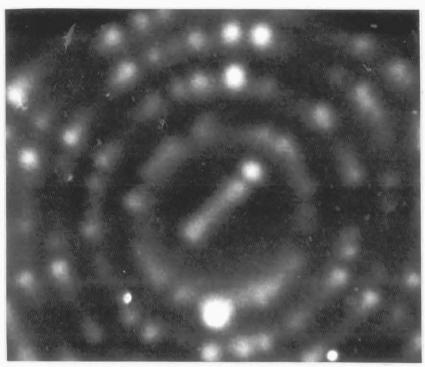


Figure 4.6 Micrograph showing an adatom which was dissociated from the end of a chain-cluster by the imaging field.

4.1.5 Detection of contaminants

In order to maintain clean surfaces it is essential to have procedures for detecting contaminants which can arrive in three ways:

(i) adsorption from the gas phase,

(ii) diffusion from the shank, or

(iii) from the evaporator during deposition.

The detection of contaminants was done by following standard techniques[120].

Contaminants from the gas phase could usually be detected by turning off the imaging field and slowly raising it again after a few minutes. Any gaseous impurity was then recognised by the appearance of bright scintillating spots which disappeared well below BIV. More thorough investigation of the vacuum conditions was often made in between experimental runs by observing the field emission pattern and checking the current through the Fowler-Nordheim relation[4], which is highly sensitive to contamination.

Contamination from the evaporator was kept to a minimum by using spec-pure materials and thorough degassing of all the evaporator parts. Short deposition times, usually about 15 sec., were used to avoid heating the glass walls surrounding the evaporator. Any gaseous contaminants from the evaporator could be recognised as described above.

Diffusion of contaminants over the tip surface from the tip shank or bulk was investigated by performing a "dummy" heating cycle before depositing any metal. After imaging and recording a clean pattern, the imaging field was turned off and the tip heated to the highest temperatures used in the experiments ($\gtrsim$500 K). After allowing the tip to cool down it was re-imaged and signs of contamination looked for as described above, and more precisely by recording the pattern and

comparing with the micrograph prior to heating. As an example, a tungsten surface contaminated by diffusion from the shank is shown in figure 4.7. The impurity is shown up as bright "extra" spots on the (110) steps.

It was generally found that by following standard UHV procedures described in the preceding sections, contamination problems were rarely encountered and the experiments described below were performed under clean UHV conditions. For each experimental run, prior to back-filling of the microscope with He, the evaporator and getter filament were flashed at full current; experiments were conducted only if no measurable pressure rise could be detected. He was then admitted and the tip cooled to 78 K, and contamination checks were performed as described above.

4.1.6 Tip temperature measurement and precision

The experiments performed with the FIM required that the specimen be heated at accurately controlled temperatures. The electronic temperature controller used for this purpose was calibrated by measuring the resistance of the tip loop at 78 K and room temperature. The measurement at 78 K was made after several hours of thermal equilibration of the tip with liquid nitrogen in the "cold finger" and the surrounding jacket (figure 4.2). The room temperature measurement was made after the liquid nitrogen had evaporated overnight. Both the measurements were made by passing a very small current ($\sim$50 mA) to avoid heating the loop, and voltage versus current plots made on an X-Y recorder, from which the resistance was evaluated. This procedure was repeated several times during an experimental run. The resistance

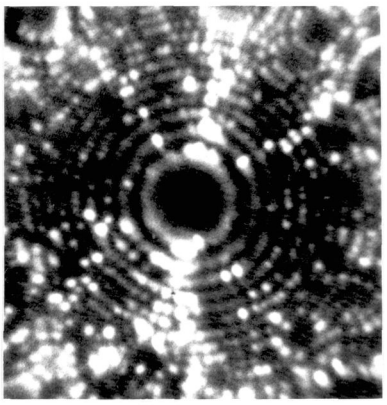


Figure 4.7 Micrograph of a contaminated tungsten tip. The 'extra' bright spots on the (110) steps are impurity atoms that appeared after heating the field-evaporated tip at 500 K.

measurements in the experiments were converted to temperature by assuming a linear resistivity relationship in the range 78-500 K.

The accuracy of the temperature depends on the measured resistance. In determining the tip temperature, the central portion of the tantalum loop (figure 4.3a) used for measuring the resistance is assumed to be at uniform temperature and in thermal equilibrium with the tip. Possible sources of error in this assumption have been discussed in detail by Webber[121]. The main sources are the finite heating up time and the non-uniform heating of the resistance section. When the temperature controller is switched on, observations of the swiftly changing current and voltage showed that the set resistance is achieved within 5 sec. By keeping the tip loop long compared to the central resistance portion, measurements in the non-uniform temperature areas are avoided. From these considerations, the overall temperature has been estimated to be about ±2 K.

4.2 Experimental Studies by FIM

In all the experiments described below, the imaging field was turned to zero during annealing of the tip and deposition of rhodium.

4.2.1 Measurement of single adatom diffusion

Single adatom diffusion was studied using procedures developed in this laboratory[120,121]. The surface for study, (110)W or Mo, was prepared by field evaporation of the tip, evaporation being stopped as the last remnant of a layer evaporated so that the plane was of the largest possible size. Rhodium was then deposited with the tip at 78 K. Usually, more than one adatom condensed on the plane but by selective

field evaporation[16], a single adatom could be retained on the plane. The position of the isolated adatom on the plane was recorded by photographing the image, and the tip heated for 60 s at a pre-set temperature. After allowing a 60 s cooling period, the tip was imaged again and the new position of the adatom recorded. After 5-10 heating cycles the adatom and substrate plane were field evaporated and the process repeated with a fresh deposit on a new plane, thus minimizing any possibility of effects due to contamination build up during a series of heating cycles. All the results for Rh on W(110) were obtained using a single adatom per plane but for Rh on Mo(110), some results were obtained with two or three adatoms per plane. In the latter case, however, the results were used only if the adatoms were far apart, thus eliminating adatom-adatom interaction effects. Between 50 and 80 heating cycles were performed at each temperature.

The displacements of the adatoms were measured by comparing successive micrographs using a two-colour comparator[120]. Distances between the initial and final positions of the centre of the adatom images were measured in arbitrary units with the eye-piece micrometer of the comparator telescope. Absolute calibration of the distance was obtained by two alternative methods.

(i) Following the procedure used by Ehrlich and Hudda[126] it was assumed that the magnification on the (110) plane was the same as the average value along the [111] zones between (110) and (321) or (110) and (211) planes. The magnification was then obtained by counting the number n of atomic ledges of height h, between the (110) and (321) or (110) and (211) planes on micrographs and calculating the tip radius, r_t, from the relation

$$r_t = \frac{nh}{1 - \cos \theta} \qquad (4.1)$$

where θ is the angle between the two planes considered.

(ii) By measurement of the smallest observed displacement, a fundamental jump length could be identified and related to the lattice spacing.

Both the methods have been used previously and give results which are generally in good agreement with each other[121].

4.2.2 Analysis of diffusion data

The aim of the above experiment is to relate the measured atomic displacements to the activation energy for surface diffusion and the diffusivity. In order to see how this can be achieved, consider first one-dimensional diffusion with the diffusion coefficient D given by Fick's law as

$$J = - D \frac{\partial c}{\partial x} \qquad (4.2)$$

where J is the particle current density and c is the particle concentration. In diffusion theory, the coefficient D is related to the mean square displacement $\langle x^2 \rangle$ of a particle undergoing an unrestricted random walk in a time interval τ by

$$D = \frac{\langle x^2 \rangle}{2\tau} \qquad (4.3)$$

From one-dimensional random walk theory[127] the mean square displacement is related to the number of jumps N by

$$\langle x^2 \rangle = N\ell^2 \qquad (4.4)$$

where ℓ is the single jump length. Expression 4.4 is valid only if successive adatom jumps are uncorrelated. This is satisfied if measurements are made at relatively low temperatures so that the diffusing adatom has enough time to reach equilibrium before making

another jump. A detailed study of the one-dimensional migration of W adatoms on the channelled W(211) plane has shown that the probability of double jumps is small[18].

It should be noted that on the small planes available on a field-evaporated surface an adatom cannot perform an unrestricted random walk since it can encounter the plane edge where it is either reflected or adsorbed. Consequently, the measured value of the mean square displacement $\langle x^2 \rangle$ is not equal to $N\ell^2$ but somewhat smaller, depending on the value of N and the plane size. It has been shown that for either a reflecting or adsorbing boundary the mean square atomic displacement of an adatom performing a walk along a line of length a, for $N < 1/10\ (a/\ell)^2$, is given by

$$\langle x^2 \rangle = N\ell^2\{1 - (\frac{4}{3a})(\frac{2N\ell^2}{\pi})^{\frac{1}{2}}\} \qquad (4.5)$$

The validity of equation 4.5 has been tested by Ayrault[128] using a computer simulation model of diffusion. The results showed that even for $N\ell^2 < a^2/6$, the error introduced by 4.5 is less than 1% of the true value of $\langle x^2 \rangle$.

For two-dimensional diffusion equation 4.3 is modified to

$$D = \frac{\langle r^2 \rangle}{4\tau} \qquad (4.6)$$

where $\langle r^2 \rangle = \langle x^2 \rangle + \langle y^2 \rangle$. If the migration is along surface channels of the crystal plane, then 4.6 is valid only when the channel network is highly symmetric[39]. On the (110) planes of W and Mo, the channels are in non-orthogonal directions, hence adatom diffusion is expected to show directional anisotropy. This has been demonstrated by Tsong for Re adatoms on W(110), in which case the mean square displacement in the

W<0$\bar{1}$1> direction was found to be twice that in the W<100> direction. However, following normal practice[39], the directional anisotropy in the diffusion on the (110) planes of W and Mo has been ignored in the present work and only a mean value of D determined through equation 4.6 after correcting for the finite size of the planes. For two-dimensional diffusion, the correction term is similar to equation 4.5 (with x replaced by r) but contains additional higher-order correction terms[129] which can be neglected to a first approximation. Thus, a mean square displacement $\langle r^2 \rangle$ was determined for a series of temperatures and $N\ell^2$ calculated from equation 4.5. The condition $N < \frac{1}{10}(a/\ell)^2$ originally set by Ehrlich was always fulfilled in the present work.

The number of jumps N can be related to the activation energy for diffusion, $\Delta E_{diff.}$, by

$$\frac{N\ell^2}{4\tau} = \nu_0 \ell^2 \exp(\frac{\Delta s}{k}) \exp(-\frac{\Delta E_{diff}}{kT})$$

$$= D_0 \exp(-\frac{\Delta E_{diff}}{kT}) \qquad (4.7)$$

where ν_0 is the atomic vibrational frequency, Δs is the entropy, k is Boltzmann's constant and T is the temperature. The pre-exponential factor, D_0, is referred to as the diffusivity. To obtain E_d and D_0, an Arrhenius plot of $\ln(\frac{N\ell^2}{4\tau})$ versus 1/T is made which yields a straight line of slope $-\frac{\Delta E_{diff}}{k}$ and intercept D_0.

The error in the measurement is set as follows. The measured mean square displacement $\langle r^2 \rangle$ is obtained from a finite sampling set of size n upon an essentially infinite population of true mean square displacement $\langle r_*^2 \rangle$ where

$$\langle r_*^2 \rangle \simeq \langle r^2 \rangle = \frac{1}{n} \sum_{i=1}^{N} r_i^2 \qquad (4.8)$$

The best estimate of the true standard deviation is the root mean square deviation, S_n, of the data measured from the mean given as[130]

$$S_n^2 = \frac{1}{n-1} \sum_i (r_i^2 - \langle r^2 \rangle)^2 \qquad (4.9)$$

The accuracy of $\langle r^2 \rangle$ as an estimate of $\langle r_*^2 \rangle$ is given by the standard error s, where

$$s = \frac{S_n}{\sqrt{N}} \qquad (4.10)$$

Equation 4.10 was used throughout the present work to give the error limits on measured quantities.

4.2.3 Cluster diffusion

The procedures for single adatom diffusion experiments were carried over for studying cluster mobility. However, due to the time-consuming nature of these studies, quantiative measurements were made only for Rh chain-clusters on W(110). Rh dimers were thermally too unstable for easy preparation and clusters of known size were difficult to prepare on Mo(110) surfaces due to the poor imaging conditions.

Clusters containing a known number of adatoms were prepared by the process of controlled clustering[16]. After getting the required number of adatoms on the (110) plane, the tip was heated to a temperature at which the adatom mobility was sufficient for there to be a high chance of adatom-adatom collisions resulting in the formation of the cluster. Heating cycles were performed as described for single adatom

mobility experiments. Between 15-50 heating cycles were performed at each of several temperatures. The number of cycles was least for Rh_4 clusters, reflecting the greater difficulty of cluster preparation. Only displacements involving translation of the whole chain-cluster were measured using the two-colour comparator. Individual atoms of the cluster were not generally resolved and so the apparent displacement of these atoms could not be measured. Thus, it was only meaningful to measure the centre-of-mass displacement of the clusters[28].

4.2.4 Cluster stability

Some attempts were made to determine the thermal stability of Rh adatom clusters using procedures similar to those developed by Tice[44]. Temperatures for dissociation and rearrangement of small adatom clusters were established but quantitative studies of cluster formation and dissociation kinetics were made only for Rh dimers on W(110). Such studies yield the activation energy for dimer dissociation, from which the strength of adatom-adatom interaction in dimers can be estimated. In these experiments deposits of two atoms were prepared as described above and the tip heated for 60 s at a preset temperature. After a 60 s cooling period the tip was imaged again and the deposit examined. If the state of the deposit was unchanged, the heating cycle was repeated. The deposit was changed every ten heating cycles to minimize contamination. Up to 100 heating cycles were performed at each of several temperatures and the fraction of heating cycles that resulted in formation of the dimer obtained. The same procedure was used in studying dimer dissociation, the initial state before heating being a dimer in this case. Dissociation resulted in two single adatoms. Dimer

formation and dissociation were usually studied together by using the terminal state of one cycle as the initial state for the next. The analysis of the data was done separately, however.

The dimer formation experiments yield f_s, the probability of the adatom remaining uncombined after a period t at temperature T, which is related to the lifetime τ_f of an adatom with respect to dimerization by

$$\ln f_s = \exp\left(-\frac{t}{\tau_f}\right) \tag{4.11}$$

τ_f is related to the activation energy for dimer formation, ΔE_f, by

$$\tau_f = \tau_0 \exp\left(-\frac{\Delta E_f}{RT}\right) \tag{4.12}$$

Combining equations 4.11 and 4.12 gives

$$\ln(-\ln f_s) = \ln\left(\frac{t}{\tau_0}\right) - \frac{\Delta E_f}{RT} \tag{4.13}$$

Similarly, the dissociation experiments yield f_d, the probability of a dimer surviving for a time t,

$$f_d = \exp\left(-\frac{t}{\tau_d}\right) \tag{4.14a}$$

or

$$\ln f_d = -k_1 t \tag{4.14b}$$

where τ_d is the dimer lifetime at temperature T and k_1 is the dissociation rate constant. However, equation 4.14b does not account for the probability of a recombination following dissociation before a deposit is next imaged. The rate constant is therefore evaluated from an integrated rate equation for a reversible dimer dissociation reaction[17,42]. In terms of f_d and its value at reaction equilibrium f_d^e,

$$\left[\frac{1 - f_d^e}{1 + f_d^e}\right] \ln \left[\frac{f_d - f_d^e}{1 - f_d f_d^e}\right] = -k_1' t \qquad (4.15)$$

Thus, from the temperature dependence of k_1',

$$\ln\left\{-\ln \left[\frac{f_d - f_d^e}{1 - f_d f_d^e}\right]\right\} = \frac{t}{\tau_d} \frac{1 + f_d^e}{1 - f_d^e} - \frac{\Delta E_d}{RT} \qquad (4.16)$$

where ΔE_d is the activation energy for dimer dissociation.

4.2.5 Film growth

A number of experiments were performed to examine aspects of the development of Rh adsorption layers to continuous monolayers on (110) planes of W and Mo. The experiments were done in two ways. One procedure that was most commonly used was to deposit incremental doses of Rh on the substrate at 78 K so that the effect of subsequent annealing to higher temperatures could be examined. Alternatively, the adsorbate was deposited in incremental doses with the substrate at temperatures sufficiently high for appreciable adatom mobility. Long deposition times (up to 30 min.) were required to achieve monolayer coverage with the microscope tip and evaporator geometry used. Consequently contamination problems occurred in some experiments, although field desorption of the contaminants during imaging at intermediate stages probably minimized their effect on the growing film.

4.3 Low Energy Electron Diffraction and Auger Electron Spectroscopy

4.3.1 The apparatus

The LEED/Auger experiments were performed in two different stainless steel UHV systems supplied by Vacuum Generators Ltd. The overall layout of the two systems, referred to here as I and II, is shown schematically in figure 4.8. Both the systems used oil diffusion pumps with Santovac 5, a polyphenylether, as the pumping fluid. In addition to the LEED and Auger facilities, system II also possessed facilities for molecular beam scattering experiments[131] but these are not considered here, since no gas scattering experiments were done.

The work chamber of system I was a 30 cm diameter stainless steel cylinder fitted with several side ports, figure 4.9a. The single crystal specimen was mounted on a bellows manipulator which allowed for rotational motion of the specimen about its vertical axis, and x-y-z motion of up to 10 mm in each direction. The crystal was positioned at the centre of curvature of a 3-grid display type LEED optics which was also used as a retarding field analyser for Auger electron spectroscopy. The chamber also contained an observation window, a V.G. Anavac-2 mass spectrometer head for residual gas analysis, an Alpert-type ionization gauge, a low energy Argon ion gun for ion bombardment of the crystal, and a rhodium evaporator. During deposition of Rh or high temperature heating of the crystal, the LEED optics could be covered with a stainless steel shield mounted on a shutter drive.

The work chamber of system II, figure 4.9b, was also a 30 cm stainless steel cylinder and has all the facilities of system I, but the design was completely different. In this case, the specimen holder

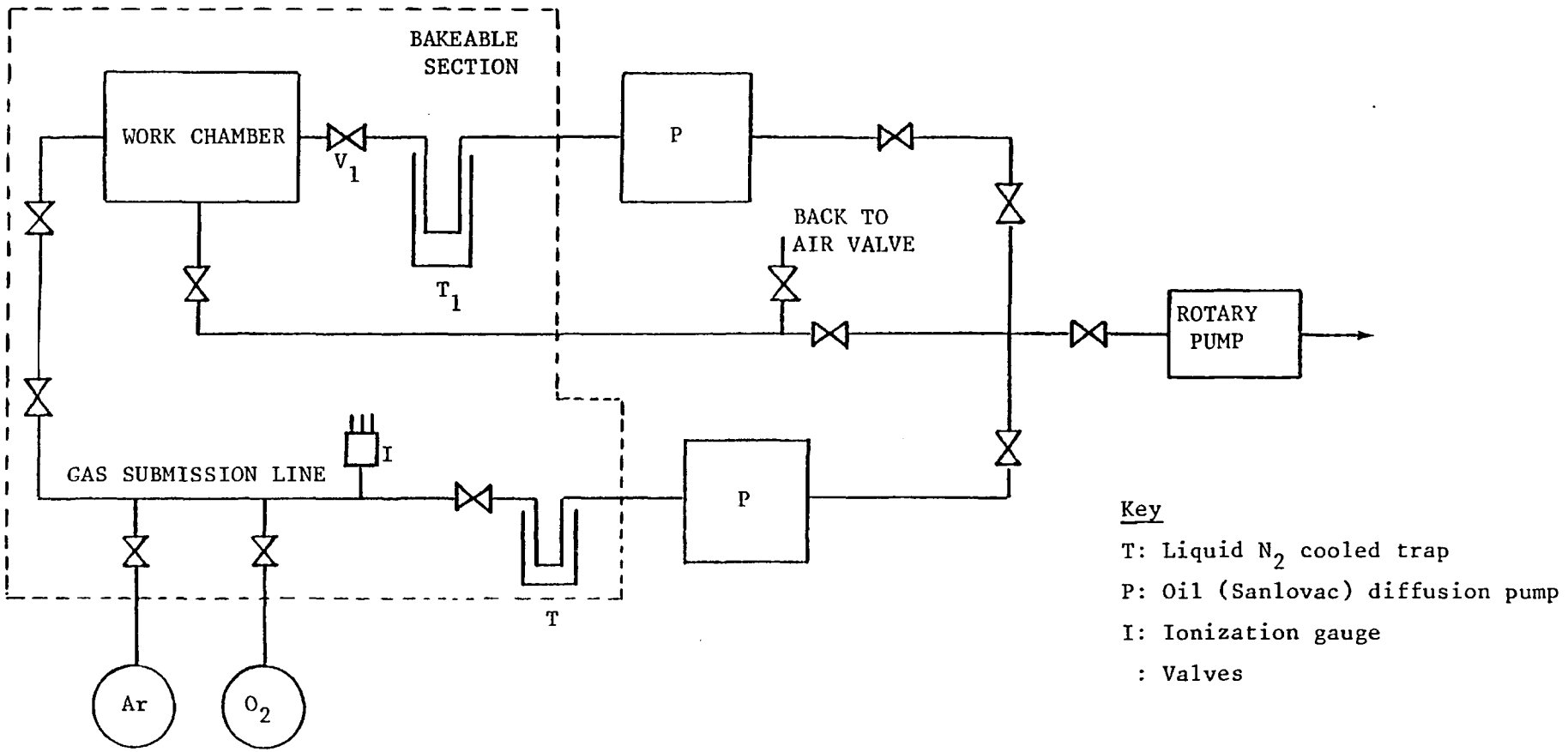


Figure 4.8 Schematic layout of the LEED/Auger system I. The vacuum system II was similar except for a differently designed gas submission line (see text for details).

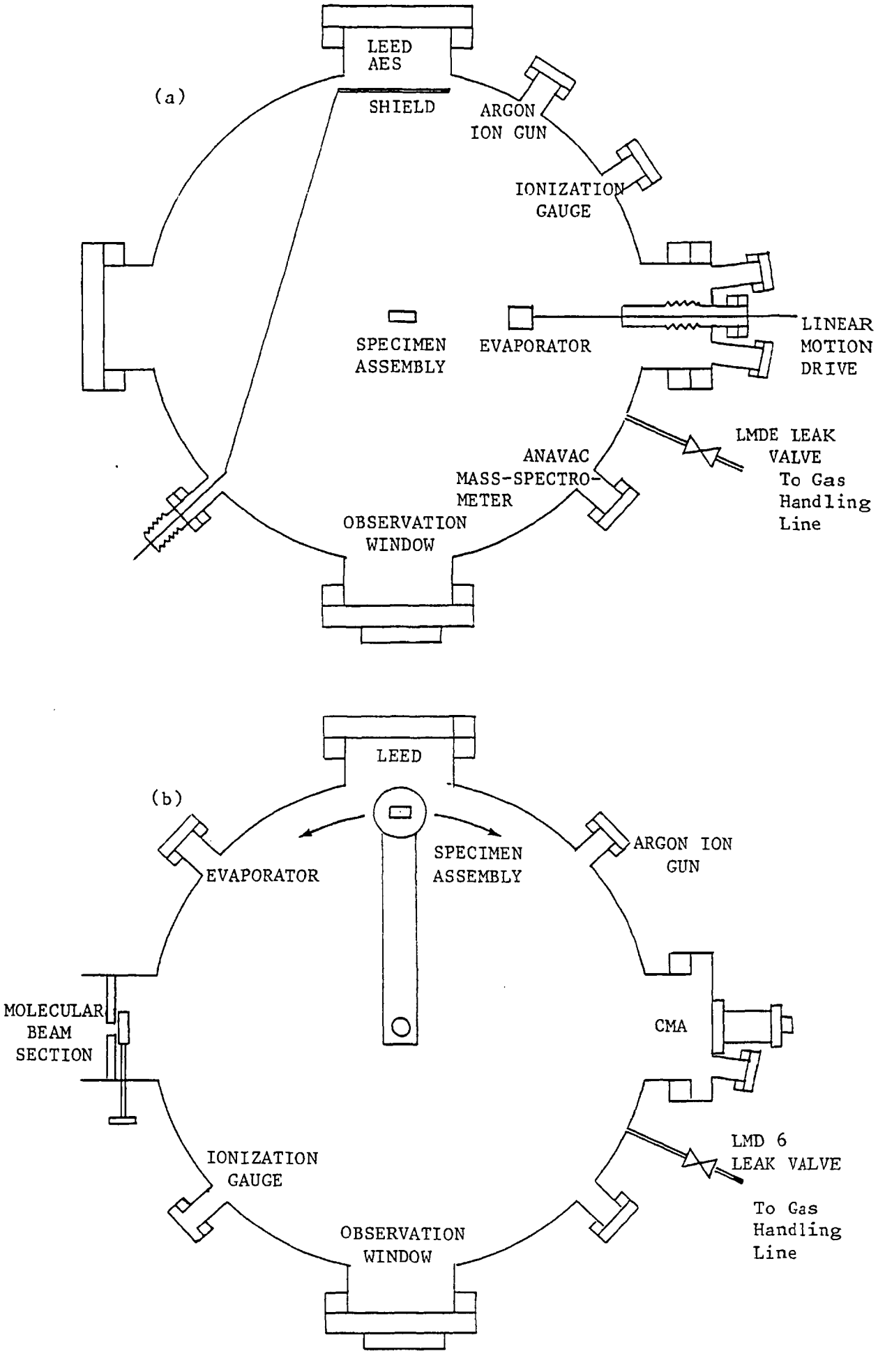


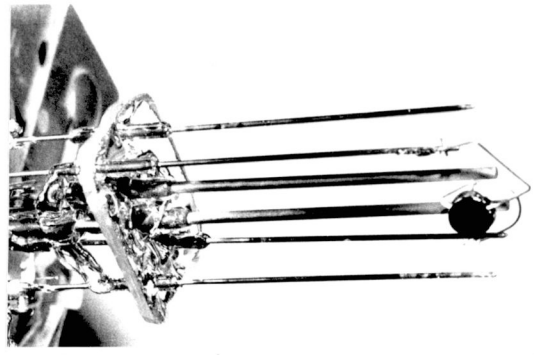
Figure 4.9 Schematic diagrams of the LEED/AES "Work" chambers of (a) System I and (b) System II.

is mounted on an arm of radius approximately 12 cm, which rotates about the central axis of the work chamber by means of a bellows manipulator. This allowed the specimen to be rotated 360^{o} around the chamber so that it could be placed in front of any port where deposition, LEED or Auger, could be carried out. The specimen could also be rotated about its vertical axis and had the usual x-y-z degrees of freedom. In contrast to the 3-grid LEED/Auger arrangement of system I, the work chamber in this case was fitted with a 2-grid display type LEED optics, and a hemi-cylindrical mirror analyzer was used for Auger electron spectroscopy.

4.3.2 Specimen holder

The principle of the specimen holding assembly was essentially the same for both systems but differed in detail due to the different manipulator designs.

The specimen holder for system I consists of six tungsten rods embedded in a glass disc via glass to metal seals, figure 4.10a. The crystal was supported by means of a wire loop spot welded to one of the rods. The loop was made from three 0.5 mm tungsten wires, the ends of which were etched to fit tightly into holes spark-machined on the side of the crystal. The crystal was heated by electron bombardment from a tungsten ribbon filament placed approximately 1 mm behind the crystal. A tungsten guard ring was sometimes kept over the filament to collimate the electrons. A W-W26%Re thermocouple junction, fitted tightly into one of the holes on the side of the crystal, was used to monitor the temperature. The assembly was mounted on the manipulator by means of a stainless steel barrel connector fitted to a short tungsten rod embedded at the centre of the disc. Copper braid was used to make the electrical connections to the feedthroughs on the manipulator.



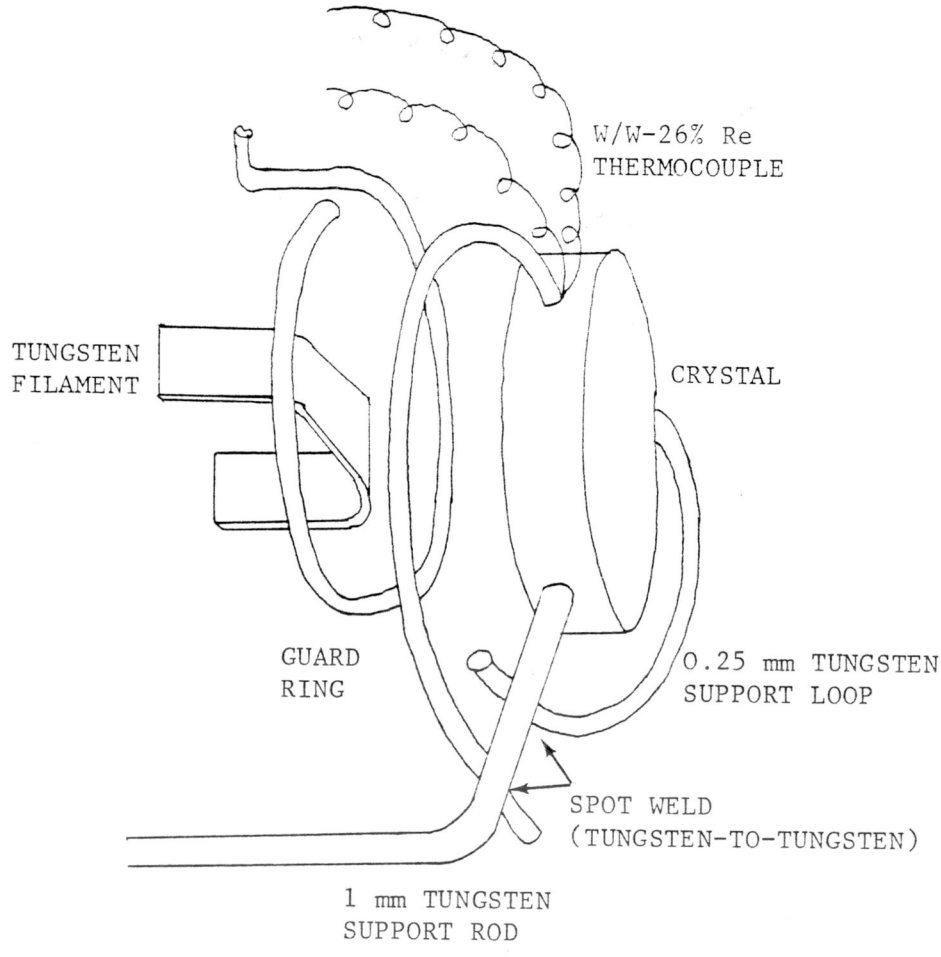


Figure 4.10a The photograph shows the specimen assembly for System II. The schematic diagram on the right shows the details of the specimen assembly with facility for electron bombardment heating. Holes were made in the crystal with a spark erosion machine.

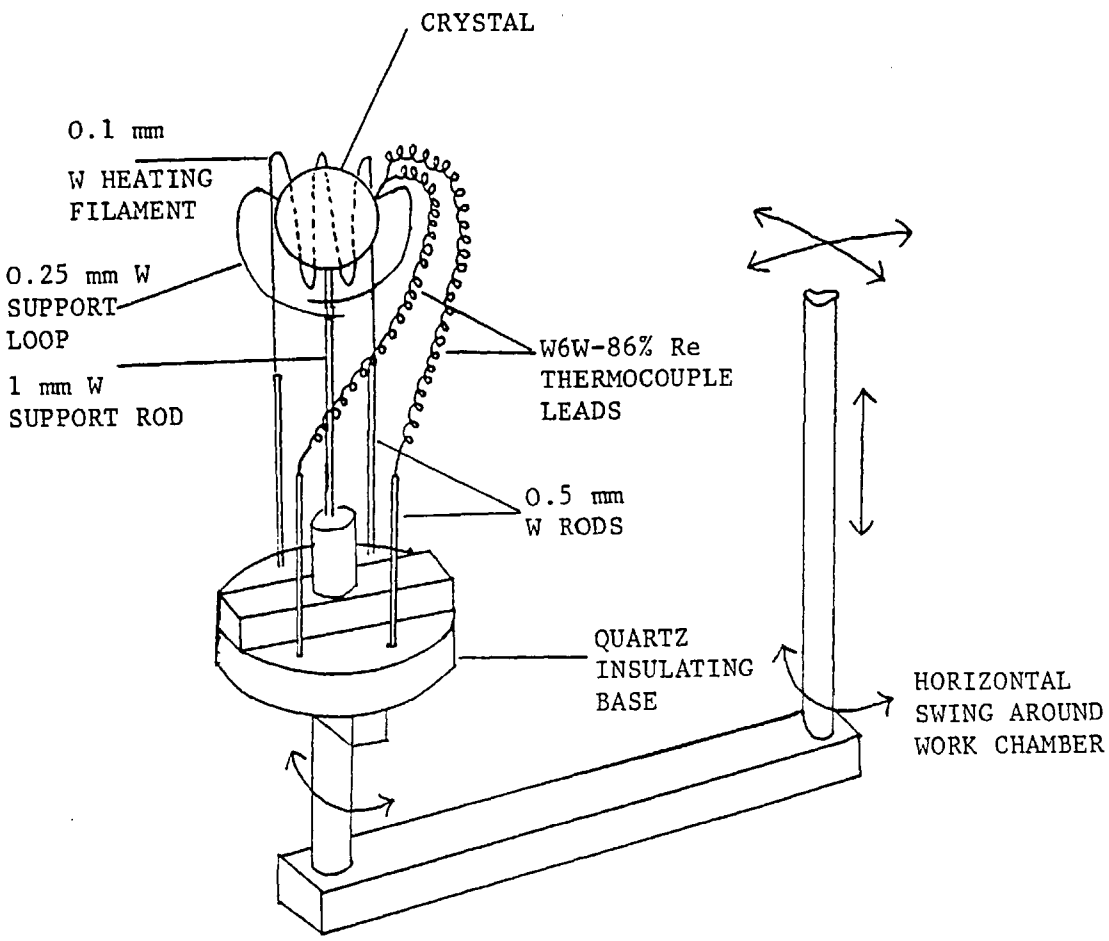
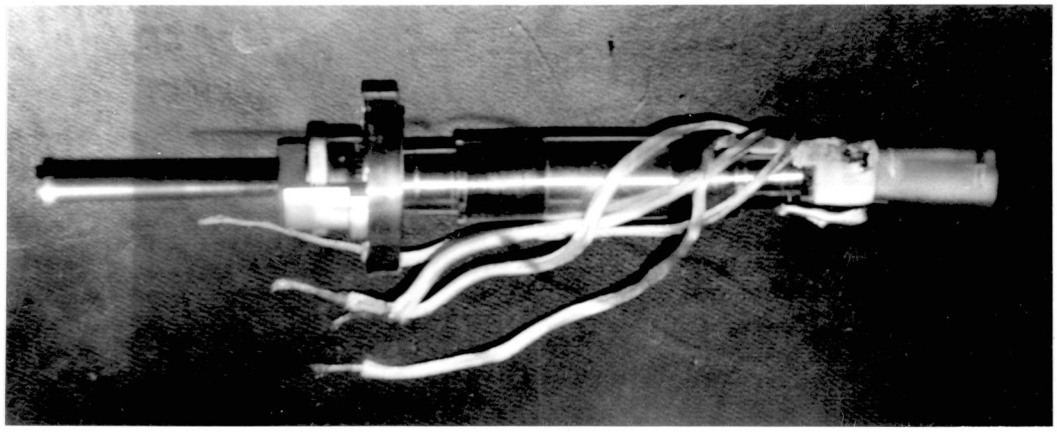


Figure 4.10b Specimen assembly for system II.

The specimen mounting assembly for system II is shown schematically in figure 4.10b. The crystal was supported on a 1 mm tungsten rod that had been etched to about 0.2 mm at one end which fitted into a hole on the crystal side. The crystal support was made rigid by a tungsten wire loop spot-welded to the rod. The other end of the tungsten rod fitted tightly into a hole bored in a stainless steel rod, which formed part of a cross-piece bolted onto a quartz disc insulator. A second cross-piece was bolted on the underside of the quartz disc to connect the assembly to the rotating arm of the manipulator. The quartz disc also supported tungsten rods on which the heating filament and thermocouple were mounted. The heating filament, for electron bombardment, was a 0.3 mm tungsten wire loop supported about 5 mm from the back of the crystal.

4.3.3 Rhodium evaporators

To avoid long deposition times, it was essential for the evaporator to be as close to the crystal as possible. To achieve this in system I the evaporator assembly was mounted on a Vacuum Generators Linear motion drive with a reach of up to 100 mm, which enabled the evaporator to be transported close to the crystal. The detailed construction of the evaporator assembly is shown schematically in figure 4.11. The basic principle of the evaporator design was the same as that used in the FIM. The evaporator side loops were spot-welded to 1 mm tungsten rods fitted onto a specially machined macor glass ceramic. A molybdenum shield was attached over the evaporator to confine the Rh vapour flux to the specimen. The shield could be degassed by electron bombardment from the evaporator coil.



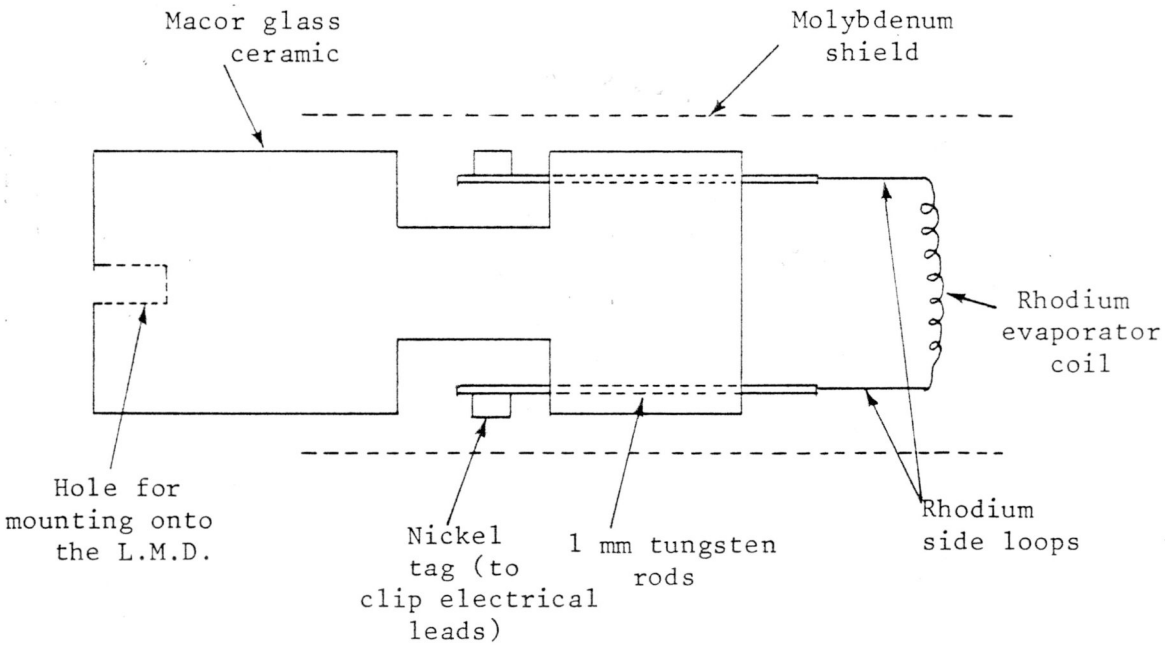


Figure 4.11 Evaporator assembly for system I. (a) Photograph showing the evaporator mounted on the linear motion drive (LMD); (b) Schematic diagram of the evaporator assembly (cross-section).

The Rh evaporator in system II was fixed on a four feedthrough conflat flange, as used in the FIM. The evaporator was confined within a pyrex glass shield with a narrow aperture. The crystal was transported in front of the aperture for deposition of the Rh. The evaporator feedthrough also supported a tungsten coil for the purpose of degassing the glass walls of the evaporator shield.

4.3.4 The LEED optics

The 3-grid optics of system I was fitted with a demountable combined LEED/Auger LEG3 electron gun. The gun had an energy range of 0-5 keV with a maximum beam current capacity greater than 100 μA. The experimental set up for LEED is shown schematically in figure 3.1 of chapter 3. The energy of the primary beam was normally set below 150 eV and a beam current, measured with the specimen biased at +90 V, was kept at about 1 μA. The inner two grids were strapped together and biased with a negative potential below that of the primary beam so that only elastically or nearly elastically scattered electrons passed through. After passing through the grids, the electrons were accelerated to the screen which was biased at +5 kV. This system also had mu-metal shielding to avoid stray magnetic fields which could deflect the electrons.

The experimental operating conditions of the 2-grid LEED optics of system II was essentially the same as above with the exception that the retarding bias was now provided by only one grid. This is a serious disadvantage if energy analysis or diffraction intensity measurements are made. The present work only involved the observation and measurement of diffraction spot pattern dimensions for which the 2-grid optics is sufficient.

The LEED patterns were recorded on either a Kodak film 2475 or 103aG using a 35 mm Zenit-E camera mounted rigidly onto the apparatus or on a tripod stand. The exposure times varied, typically about 30 sec. at f4 aperture setting for the 2475 film to about 5 sec. for the 103aG at the same aperture setting. The 103aG film was preferred since it produced less contrast in the photographs.

A disadvantage of system II was the presence of stray magnetic fields in the work chamber, which caused pattern distortions of up to 5%. However, this is not expected to cause a significant error in the present work since overlayer pattern measurements were made against the standard provided by the substrate patterns.

4.3.5 The Auger analysers

(a) The retarding field analyser.

The LEED optics of system I was used as an RFA in a manner outlined in section 3.2.1 (chapter 3). The capacitance between the screen and grid was neutralized by using a capacitance bridge network housed in a metal can that fitted over the LEED optics flange. This can also contained the pre-amplifier and a signal mixing unit that superimposed the modulation signal onto the retarding potential.

Because the RFA behaves as a high-pass energy filter, the signal from it contains considerable "shot noise". Much of this noise is reduced by a low-pass frequency filter in the phase-sensitive detection system. However, the time constant of this filter limits the ability of the system to follow rapid changes in the energy spectrum, hence the scan rate and the time constant have to be matched to avoid loss of detail in the spectra. The signal can be increased by choosing a

large modulation amplitude but this has the effect of smoothing out detail in the spectra. The primary beam current has to be kept low to avoid beam-induced effects such as heating of the substrate. These considerations require using optimum instrumental settings.

In the present work, a 2 keV normal-incidence primary electron beam, with a current of about 5 μA, was used. Typically, the modulation was set at 8 V p.t.p. and a time constant of 1 sec. was selected for a single scan over 200 V range in 1000 sec.

(b) The cylindrical mirror analyser

The Vacuum Generators CMA in system II contained an LEG3 electron gun that formed an integral part of the analyser. The gun could be operated at up to 5 keV and made an angle of approximately 20° to the specimen normal. The signal from the CMA was monitored by an externally mounted photomultiplier which measures the light emitted from a phosphor screen and induced by the impinging electrons. The Auger detection principles are similar to those of the RFA and have been outlined in section 3.2.1.

Since the CMA behaves as a band-pass energy filter, "shot noise" is not a serious hindrance to the operating conditions. Consequently, the Auger spectra could be displayed on an oscilloscope at a fast scan rate or recorded on an X-Y recorder at slower scan rates. The primary electron beam energy was typically set at 3 keV with a current of about 15 μA. The modulating voltage was normally set at 8 V p.t.p. amplitude. The Auger spectra were usually obtained on an X-Y recorder using an amplifier time constant of 300 msec. and a scan time of 300 sec. over an energy range of 500 eV.

4.3.6 Evacuation procedure

Following specimen or evaporator change, the apparatus was initially rough pumped, the gas flow by-passing the diffusion pump line. The chamber was then opened to the diffusion pump via the gate valve, V1 (figure 4.8), and evacuated to a pressure of the order of 1×10^{-7} torr. In the absence of any leaks the systems were baked at about 200 ^{o}C for several hours. The bakeable section of the apparatus also included the main trap, which separated the chamber from the pumps. Following the bake-out and while the system was still warm, the main trap was partially filled with liquid nitrogen and the ionization gauge, evaporator and crystal were briefly degassed. The system was then left to cool down and the trap topped up with liquid nitrogen. At this stage, the pressure in the chamber was usually about 3×10^{-10} torr and fell to below 1×10^{-10} torr after more thorough degassing of the various components. Additional pumping at low pressure could also be achieved by depositing a getter film from a molybdenum-titanium alloy filament situated at the bottom of the chamber. However, this form of pumping was not normally used since it was suspected that hydrocarbon impurities were released when the getter filament was heated.

As discussed in a following section, both tungsten and molybdenum crystals degassed considerably when first put into the systems and prolonged heating in oxygen was required to remove the carbon from the bulk of the specimens. The walls of the systems were then saturated with oxygen and had to be baked again. However, for the purpose of routine cleaning of the specimen surfaces, or gas adsorption studies, only small amounts of oxygen were needed and subsequent bake-out was

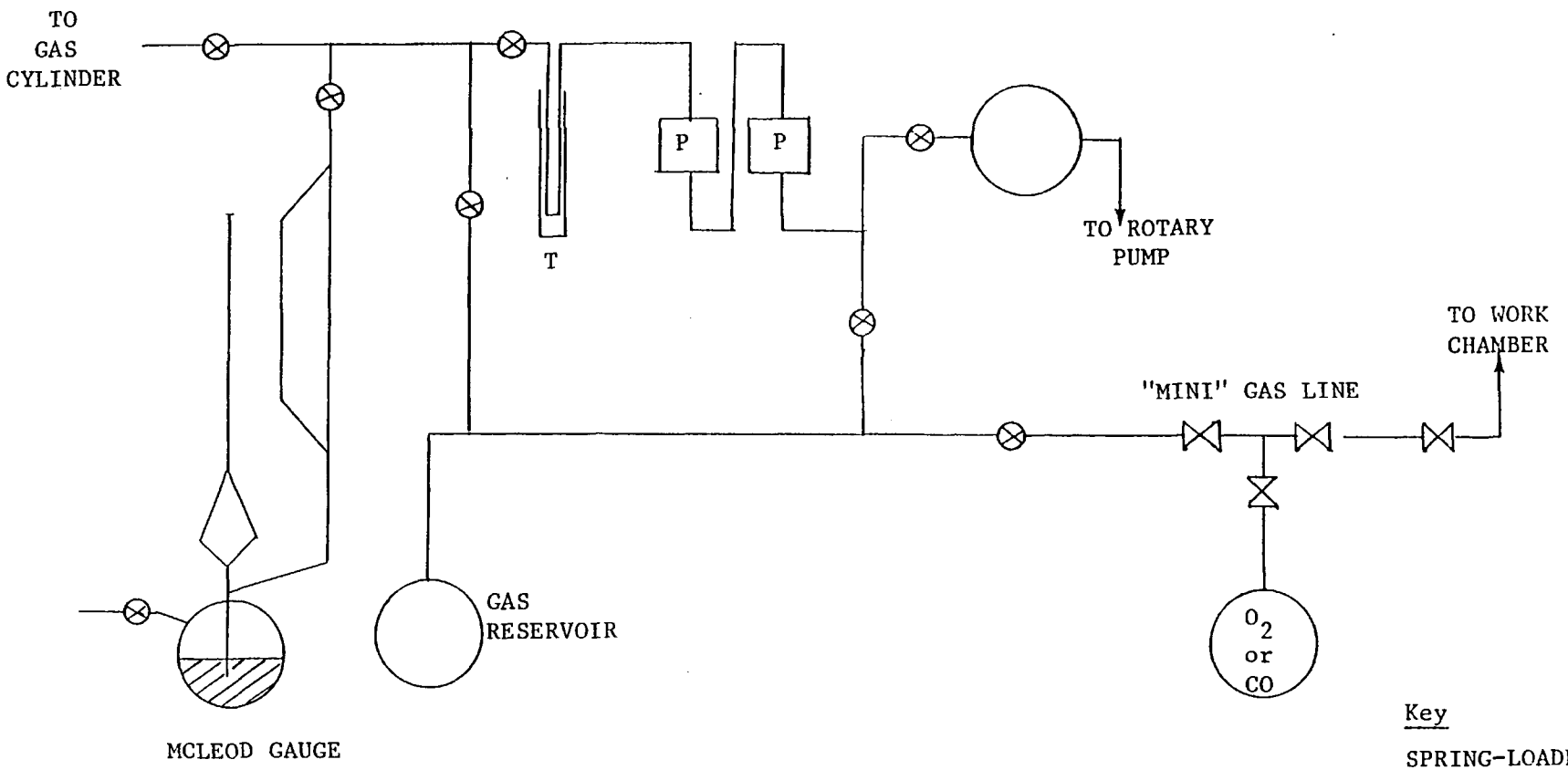
not usually required. In this case, UHV was recovered by leaving the chamber pumping for a few hours.

To avoid excessive contamination during specimen or evaporator changes, the systems were normally returned to atmospheric pressure with either argon from a cylinder or nitrogen from a liquid nitrogen reservoir.

4.3.7 Gas handling lines

System I was equipped with a bakeable stainless steel gas handling line evacuated by an oil diffusion pump (figure 4.8a). Under normal operating conditions the line could be pumped below 1×10^{-8} torr. Oxygen or argon, for the purposes of cleaning the specimens, was admitted into the line from spec-pure gas bottles. The gas could then be admitted into the work-chamber at the required pressure by manipulating an LMD6 leak valve.

The gas handling line in system II was an elaborate all-glass system originally designed to process and store helium and deuterium for the purpose of molecular beam scattering experiments. A part of the system, shown in figure 4.12, was adapted in the present work to admit oxygen or argon. The line was pumped by two mercury diffusion pumps isolated by liquid nitrogen cooled traps. Pressure was measured with a Macleod gauge. Springloaded greased stop-cocks and ball-socket joints were used throughout the line, resulting in poor vacuum conditions ($\lesssim 1 \times 10^{-5}$ torr). However, the system was adequate for storing and letting in oxygen for the purpose of cleaning the crystal, and argon for letting the work-chamber to atmospheric pressure. The gases were admitted into the chamber via a narrow bore stainless steel tube which formed part of a "mini" gas handling line. This line could be pumped



Key

SPRING-LOADED GREASED STOP-COCKS

METAL VALVES

P MERCURY DIFFUSION PUMP

T LIQ. N_2 COOLED TRAP

Figure 4.12 Gas Handling Line for System II.

directly by the main diffusion pump via a leak valve to a pressure below 1×10^{-8} torr. Facilities were provided for fitting a gas bottle to this line by means of a mini conflat flange. In the course of this work, oxygen and carbon monoxide bottles were fitted for gas adsorption studies. The oxygen was also used for routine cleaning up of the specimen surfaces.

4.3.8 Specimen preparation

The tungsten and molybdenum crystals used in this study were fabricated from high purity single crystal rods supplied by Metals Research Ltd. The tungsten rod was about 0.8 mm in diameter, with its central axis roughly oriented to within $\pm 5^{\circ}$ of the crystal <110> direction. The molybdenum rod was about 12 mm in diameter and was randomly oriented. Standard procedures were used for the orientation and preparation of the (110) surfaces of tungsten[132,133] and molybdenum[134].

(a) Orientation and initial preparation

Discs of tungsten and molybdenum were cut using a servomet spark machine. The rough cut discs were finely planed in the spark machine and lightly etched to remove the spark damaged layers. They were then fixed on a two circle goniometer and oriented to within $\pm 1^{\circ}$ of the (110) plane using the Laue X-ray back reflection technique[135]. The goniometer was then transferred to the spark machine and the crystal surfaces spark planed. The discs were machined to a thickness of about 1.5 mm. In addition, three 0.5 mm thick holes were spark machined within about 1 mm of the edge of each crystal. The crystals were then ground and polished on both sides with successively finer

grades of alumina or diamond paste using standard optical polishing techniques. The crystals were cleaned ultrasonically in distilled water between each polishing grade to ensure complete removal of particles embedded in the surfaces. The surfaces to be used in the experiments had a mirror finish following this procedure, with the final polishing done with 1/4 μm diamond paste.

Before mounting the crystals into the UHV systems, they were given a brief chemical etch to remove the topmost layers of the oriented surfaces, which would have been highly fragmented after the polishing treatment. The etchant used for both the crystals was a mixture of 65% lactic, 35% nitric and 5% hydrochloric acids. The crystal faces of interest were swabbed with this solution for about 5 sec. and then immersed in distilled water. This was repeated several times and the crystals were then subjected to prolonged ultrasonic cleaning in distilled water.

It was found that the chemical etching solution produced a vigorous reaction with the molybdenum surface, leaving it with a very slight "orange peel" effect. This effect has also been observed by others[136] and indicates that the surface is macroscopically not flat. In contrast, no visible signs of a reaction were observed with tungsten, which maintained a mirror-finish surface. Examination of the crystals under an optical microscope showed that the molybdenum surface had a high density of etch pits, especially near the edges. However, scanning electron micrographs of both the crystals showed that the surfaces of interest were smooth and flat. It should be noted that some workers have electropolished their crystals instead of chemically etching them. Tungsten has been electropolished in sodium hydroxide[137] or sodium phosphate[138] solution while molybdenum crystals have been electropolished

in a mixture of sulphuric acid and methanol. However, it was found in the course of this work that electropolishing tungsten crystals produces severe etch pits on the surface and often makes the crystal faces concave in shape. Chemical etching was therefore preferred in the present work.

After a crystal was mounted onto its holder, the whole specimen assembly was cleaned ultrasonically, first in trichloroethylene, followed by acetone, methanol and finally in distilled water.

(b) In-situ cleaning

Prior to any treatment in the vacuum chamber, the Auger spectra of the specimen surfaces showed peaks due to oxygen and carbon but no clear indication of the substrate Auger peaks. All the Auger transitions of interest in the present work are tabulated in Appendix A. This includes the main transitions of tungsten, molybdenum, rhodium, carbon, sulphur and oxygen. A LEED pattern could not be obtained at this stage, indicating the disordered and contaminated state of the surfaces. The crystals were then heated by electron bombardment (see section 4.3.9) for several minutes at about 1000 K and flahsed for 15 sec. periods at about 1800-2000 K. Considerable degassing occurred initially, with increases in pressures of up to 1×10^{-6} torr. Auger spectra of both tungsten and molybdenum surfaces after this initial heating showed peaks arising from substrate transitions as well as peaks due to carbon and sulphur, figure 4.13. The LEED patterns obtained at this stage are shown in figure 4.14.

The complex LEED patterns exhibited in figure 4.14a have been reported before and have been attributed to surface carbides[110,139-143]. The patterns are thought to arise from domains with two equivalent

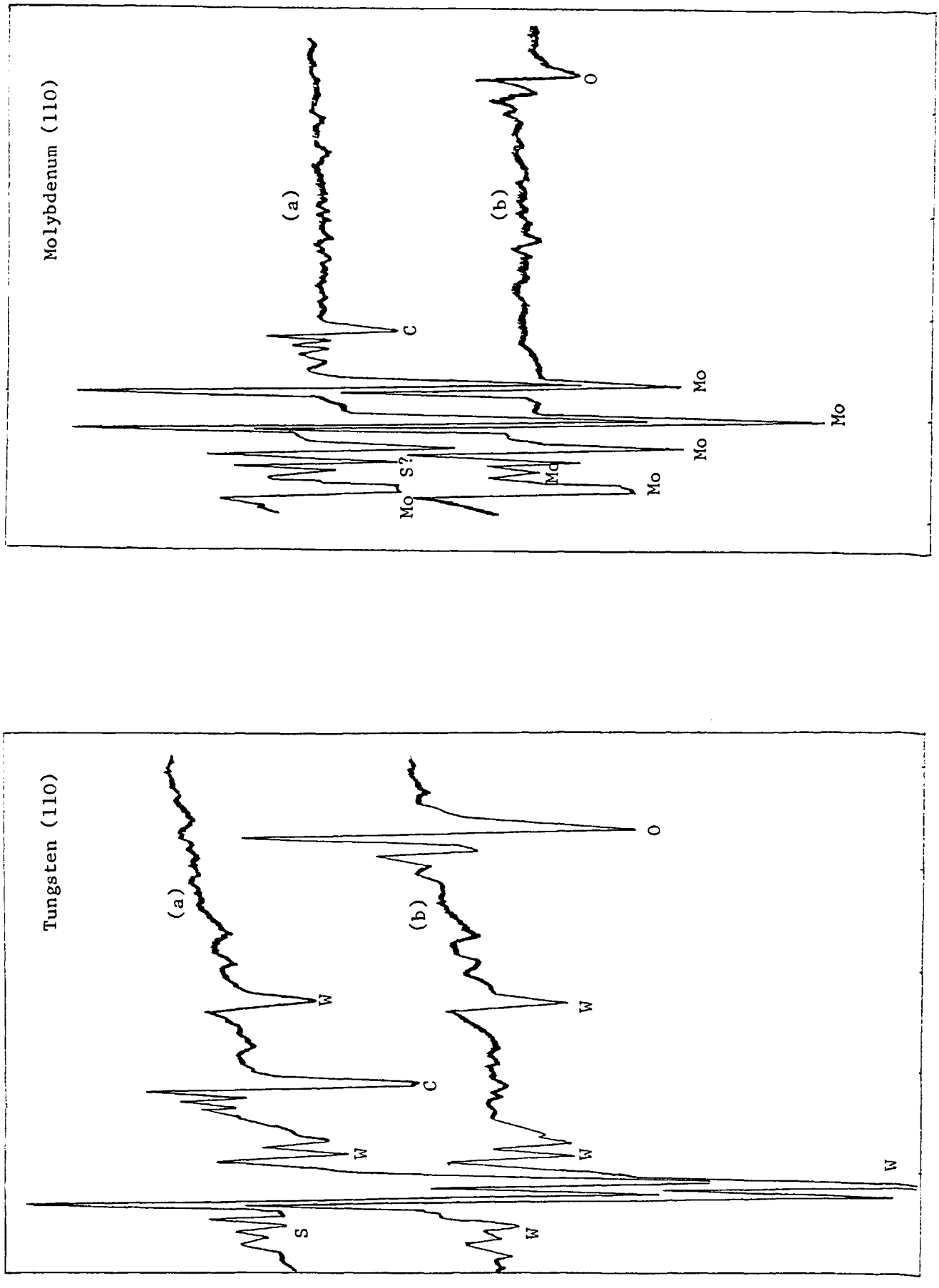


Figure 4.13 Auger spectra from tungsten and molybdenum (110) surfaces at the cleaning stage. (a) After initial heating in vacuum at 1200 K, showing the presence of carbon and sulphur; (b) After heating the surfaces of (a) in 5×10^{-8} torr O_2 at 1100 K for about 1 hr.

orientations. LEED patterns from predominantly a single domain orientation were also observed, figure 4.14b. Originally, Stern[139] had attributed the pattern to a dilute carbide of general formula $W_{15n}C$, where $n > 1$, but it is probably due to a dense carbide overlayer[110,142]. Bauer[110] interpreted the pattern as due to a ditungsten carbide, W_2C. The 'extra' spots were then thought of as arising by multiple diffraction between a surface hexagonal coincidence lattice of W_2C and the underlying tungsten substrate. However, such a model is not compatible with He scattering experiments which also show the same pattern[131,142]. Since He scatters from the top layer only, the observed LEED pattern is likely to be due to a surface carbide which is not flat. It has been suggested that the carbide layer is not a simple planar hexagonal layer but is "puckered" by the underlying substrate atoms[131]. As outlined in section 3.1.4, Palmberg and Rhodin[111] have shown that "extra" spots in LEED patterns can be attributed to single scattering from a non-planar surface layer.

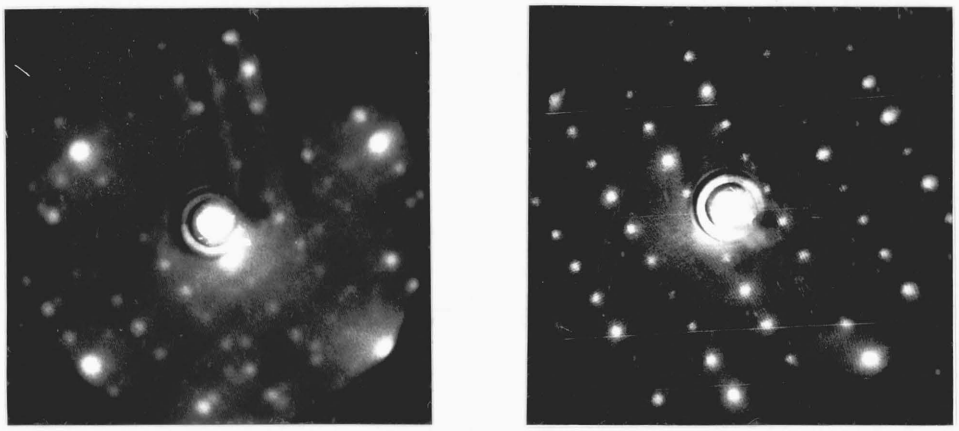
Carbon is the most common impurity present in most transition metals, including tungsten and molybdenum[144]. It appears on the surface either by diffusion from the bulk when the specimen is heated, or is formed by the decomposition of gas phase hydrocarbons. In addition to the inherent carbon content in the bulk, it could be added to the specimens in the present work during the spark machining and polishing stages[145]. Carbon could be chemically removed from the surface by heating in the presence of oxygen and in much of the published work, this is done routinely[146,147]. It was found that heating at 2000 K for a few minutes in oxygen at a pressure of 5×10^{-7} torr removed the surface carbon. The subsequent removal of oxygen from the specimen

surfaces requires heating in vacuo at temperatures of up to 2200 K[146,147]. However, when the crystals were flashed in vacuo at these high temperatures, it was found that carbon reappeared on the surfaces of both the specimens in the time required for the crystals to cool to room temperature ($\lesssim$10 m). Carbon had apparently segregated from the bulk of the crystals. To remove the bulk carbon, the crystals were heated in oxygen at 1 x 10^{-7} torr pressure for a long time at about 1200 K, when surface segregation in these materials is highest[139,148]. The tungsten crystal was heated for a total of about 70 hours while the molybdenum crystal was heated for about 25 hours. Subsequent flashing of the tungsten crystal did not result in carbon segregation as seen in the Auger spectra. On the molybdenum crystal, however, a trace of carbon was observed in the Auger spectra from the edges of the crystal. It is possible that the high density of pores near the edges of the crystal contained large quantities of carbon which could not be removed by the above procedure. However, the Auger spectra from the central region of the crystal ($\sim$3.5 mm extent) did not show a carbon peak. The crystal surface of interest was therefore considered free of carbon. Any subsequent carbon contamination of the surfaces, for example following exposure of the crystal to the atmosphere or bake-out of the system, could be removed readily by flashing in oxygen.

The extent of sulphur contamination in tungsten does not appear to have been investigated in the literature although its presence is clearly seen in Auger spectra. Senkew[131] observed a sulphur peak in the spectrum of an uncleaned W(110) crystal, and a sulphur peak is clearly seen in the spectra obtained by Bas and Baninger[149] following

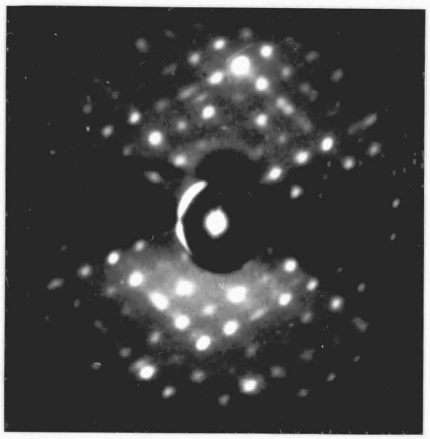
heat treatment in oxygen. In contrast, sulphur contamination on molybdenum has been investigated previously to some extent[150-152]. Bernasek and Staudt[151] found that exposure of the surface to hydrogen apparently brought about increased sulphur concentration at the surface. They observed this on a Mo(100) surface while attempting to reduce a surface oxide by heating the sample in hydrogen. Kuminori and co-workers[152] have observed surface segregation of sulphur along grain boundaries in polycrystalline molybdenum. In the present work, sulphur was detected initially on both the surfaces but no sign of it was found on tungsten after the prolonged heating in oxygen. In the case of molybdenum, however, the main sulphur Auger LMM transition coincides with a molybdenum MNN transition at about 150 eV. Thus, small traces of sulphur on molybdenum cannot be readily detected in conventional Auger spectroscopy. However, in a detailed discussion of this problem, Haas and co-workers[144] have concluded that if after repeated flashing of a molybdenum crystal in oxygen and in vacuo the peak at 150 eV does not change, then the Mo surface is likely to be free of sulphur. This was in fact found to be the case in the present work and hence, the Mo(110) surface was considered free of sulphur.

Oxygen was removed from the surfaces of tungsten and molybdenum by flashing the crystals to 2200 K as mentioned above. Some workers, however, have removed oxygen from tungsten[153] and molybdenum[151] surfaces by reducing in hydrogen, but in view of the results of sulphur segregation studies mentioned above, this method was thought to be inappropriate here. The LEED patterns from oxygen covered W and Mo(110) surfaces, observed during the cleaning procedure, are shown in figure 4.15. The oxide patterns have been reported before, both for tungsten[146] and molybdenum[147] (110) surfaces.



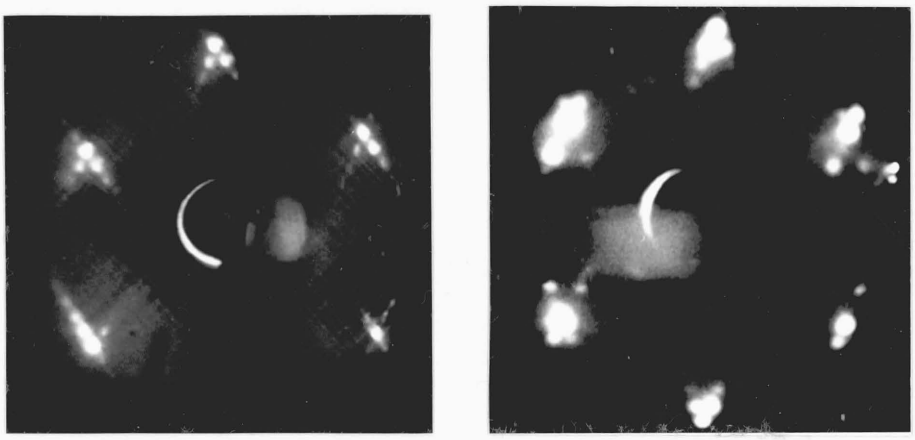
(a)

(b)



(c)

Figure 4.14 LEED patterns from (a),(b) W(110) and (c) Mo(110) after the initial heating periods at 1800 K in vacuum.



(a) (b)

Figure 4.15 LEED patterns from (a) W(110) and (b) Mo(110) after heating at 1200 K in 1 x 10^{-7} torr oxygen.

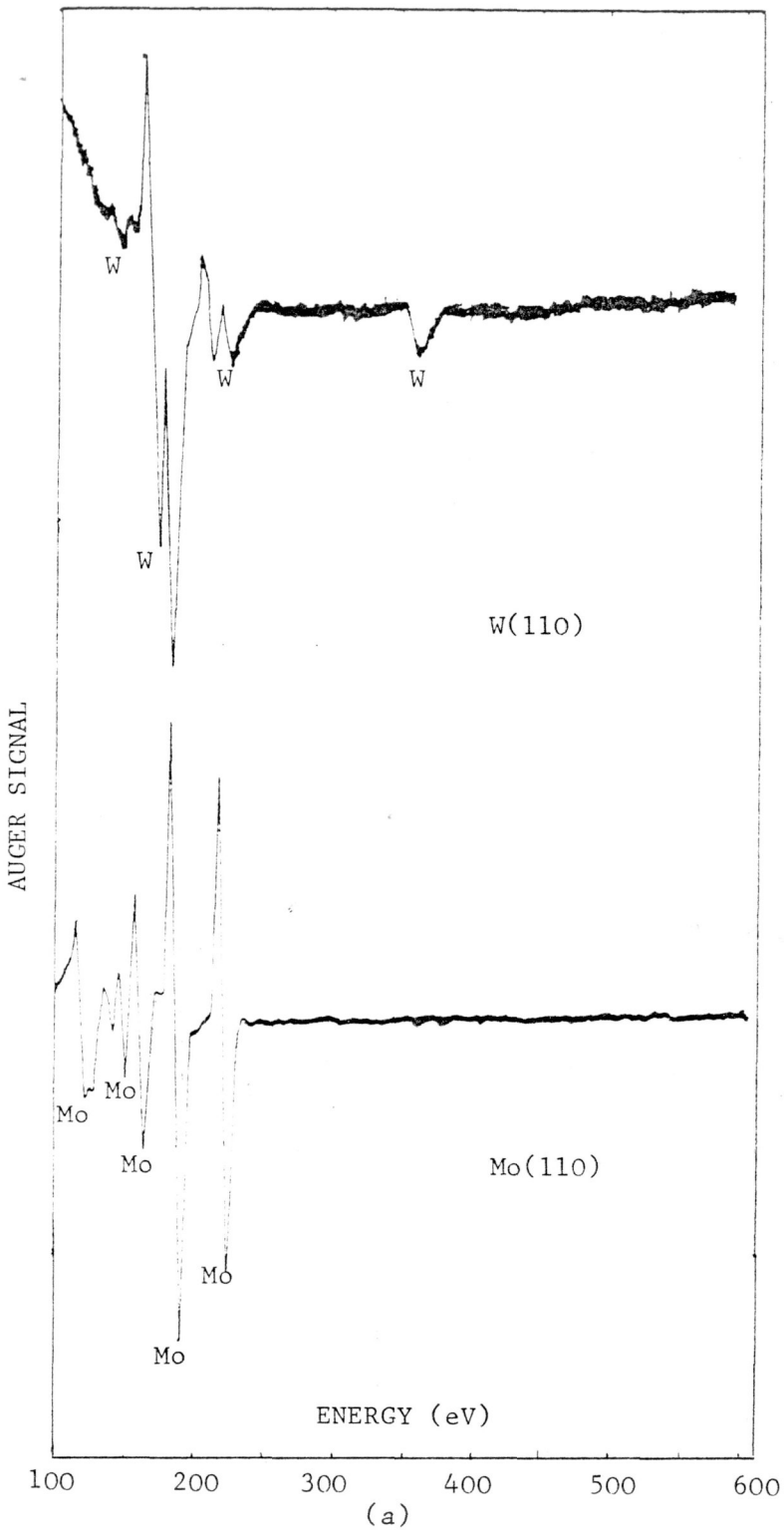
The state of the specimen surfaces throughout the cleaning operation was monitored by AES since it was found that LEED alone was not sensitive to small amounts of carbon. This has been noted previously[154,155] and Tharp and Schiebner[155] suggest that an ordered layer of carbon is necessary on the (110) surfaces of tungsten to be observable in LEED.

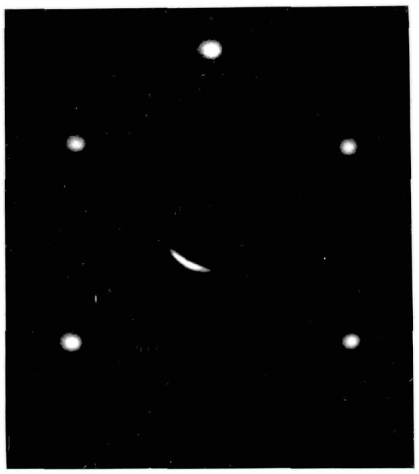
The Auger spectra of the clean tungsten and molybdenum (110) surfaces are shown in figure 4.16a and the corresponding LEED patterns in figure 4.16b.

4.3.9 Crystal temperature measurement

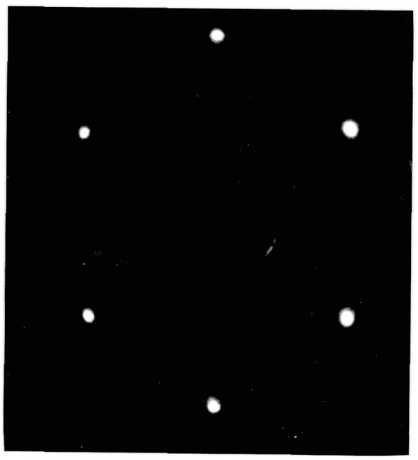
The crystals could be heated radiatively up to about 500 K by the hot tungsten filaments situated at the back (figure 4.10). For higher temperatures the crystals were heated by electron bombardment from the filament by applying a high positive potential (+ 1-3 kV) to the crystals.

The temperature was initially measured using the W-W26%Re thermocouple junction. The thermal e.m.f. could be measured on a D.V.M. either directly or via an opto-isolator circuit. The thermocouple was calibrated against an optical pyrometer for temperatures above 1000 K. Lower temperatures were then extrapolated from this calibration. However, during the course of the high temperature cleaning described in the preceding section, the thermocouple junction contact frequently became loose or detached from the crystal. Hence, reliable temperature measurements could not be made with the thermocouple. The temperatures were therefore estimated by a method used by Augustus and Jones[62]. The specimen temperatures above 1000 K were measured using an optical pyrometer and the observed relationship between the electron emission





Clean W(110)



Clean Mo(110).

(b)

Figure 4.16 Auger spectra from W and Mo (110) surfaces after complete oxygen treatment and high temperature flashing (a). The surfaces gave diffraction patterns such as those in (b). 74V

current and measured temperature was used to obtain estimates of lower temperatures. These measurements were made before and at the end of each experimental run. The error in the temperature measurement is estimated to be ±30-50 K.

4.3.10 Rhodium coverage determination

A quartz crystal deposition monitor could not be fitted due to limitation of ports available on the systems. Also, coverage calibration based on sharp changes of slope of Auger electron peak-to-peak height versus deposition plots, as described by figure 3.14 of chapter 3, was not possible due to noise in the curves (see chapter 6). The coverage was therefore estimated by using the relation between the substrate Auger electron escape depth in rhodium and the attenuation of the Auger peak-to-peak height, as outlined in chapter 3. The estimated mean free path, λ_m, and the attenuation coefficient, $\exp(-1/0.74\ \lambda_m)$, for the major tungsten and molybdenum Auger transitions at 182 and 188 eV, respectively, are listed in table 4.1.

In the experiments the deposition time required for the substrate Auger electron peak-to-peak height to decrease by a factor equal to the calculated attenuation coefficient was taken as the time required for depositing one monolayer of rhodium. The coverage values estimated in this way have an accuracy of not better than ±20% [156].

TABLE 4.1 Mean free path λ_m (monolayers) and the attenuation coefficient for substrate Auger electrons in rhodium

a_{Rh}	0.182
λ_m^{Mo} (188)	2.36
λ_m^{W} (182)	2.4
$\exp(-\frac{1}{0.74}\ \lambda_m)$	~0.6

4.4 Experimental Studies by LEED/AES

Just as in the case of FIM studies, the LEED/AES experiments were conducted under clean UHV conditions. The evaporator metal side loops and coil, and the evaporator shield were thoroughly degassed before each experiment. The crystals were flashed to 2200 K for 60 sec. prior to any deposition and the state of the surfaces was monitored by LEED and AES after the samples had cooled to room temperature ($\sim$10 min). Experiments were not performed if any carbon or oxygen impurity peak was detected in the Auger spectra, or if the pressure rose by over 2×10^{-11} torr during deposition.

4.4.1 Deposition of rhodium on clean surfaces

Before depositing rhodium, the evaporator coil was flashed at full current. Auger spectra and LEED photographs of the clean surfaces were taken. The evaporator coil was then heated to just below evaporating temperature and the crystal swung around in front of it, (in system I the evaporator was advanced towards the crystal until it was about 10 mm from the (110) face). The evaporator current was then raised and rhodium deposited for a fixed time, usually 15 or 30 sec. Larger deposition times were avoided to reduce contamination from the evaporator shield as it got hot. After each dose of rhodium, the crystals were swung back into the LEED/AES positions and the Auger spectra and LEED patterns recorded. Auger spectra were checked for the presence of contaminants, especially C or O. The position of the crystal for LEED/AES and deposition, the duration of deposition and the LEED/AES instrument settings were all standardised throughout the experiments for comparability between runs.

Deposition of rhodium at elevated temperatures was done by first depositing at room temperature followed by annealing at the required temperature. LEED patterns and Auger electron spectra were recorded before and after heating following each dose. For each experiment, the peak-to-peak height of the substrate and adsorbate Auger signals were measured and plotted as a function of time, in the manner described in section 3.2.3, Chapter 3.

After completion of an experiment, rhodium overlayers were removed from the surfaces of both the crystals by thermal desorption. Originally attempts were made to remove the Rh by argon ion bombardment but due to the low ion energies used, this procedure required a long time. It was found that to remove about a monolayer coverage on the tungsten surface required continuous ion bombardment of up to 15 hrs. Also, ion bombardment for such long periods led to carbon contamination of the surfaces from the gun filament. Electron-beam-induced deposition of carbon has been observed before. Thermal desorption was thus preferred. It was found that the Rh could be removed from the tungsten and molybdenum surfaces by flashing the crystals at above 1600 K and 1300 K, respectively. Once the crystal surfaces were cleaned, the experiment was repeated.

4.4.2 Effect of gas adsorption on the Rh overlayers

The behaviour of Rh deposited on oxidised W and Mo (110) surfaces was investigated. Spec-pure oxygen was leaked into the chamber at a pressure of about 5×10^{-8} torr for a few minutes while the crystals were maintained at about 700 K. This procedure was usually found to be sufficient to give chemisorbed oxygen patterns showing half-order spots in the diffraction patterns from the W(110) and Mo(110) surfaces. The

Rh evaporator was then thoroughly degassed and the procedure outlined above followed to deposit the Rh.

The effect of oxygen and carbon monoxide on the Rh overlayers was also studied. In this case Rh was first deposited on the surfaces. Oxygen or carbon monoxide was then leaked in and LEED/AES observations made.

4.4.3 Surface diffusion of Rh overlayers

A limited number of experiments were done to investigate the surface diffusion of Rh overlayers on W(110) surface using the CMA. Rh was first deposited at room temperature with the crystal in the position shown in figure 4.17. In this position, a Rh layer could be deposited with a boundary at about the middle of the crystal face. The crystal was then positioned in front of the Auger analyser and fast Auger scans were done across the boundary of the overlayer by moving the crystal vertically with respect to the Auger electron beam. The crystal was not moved in any other way, even while heating it, to ensure accurate positioning in front of the analyser throughout the experiment. LEED patterns were observed at the end of the experimental runs. The results of these experiments are presented in appendix C.

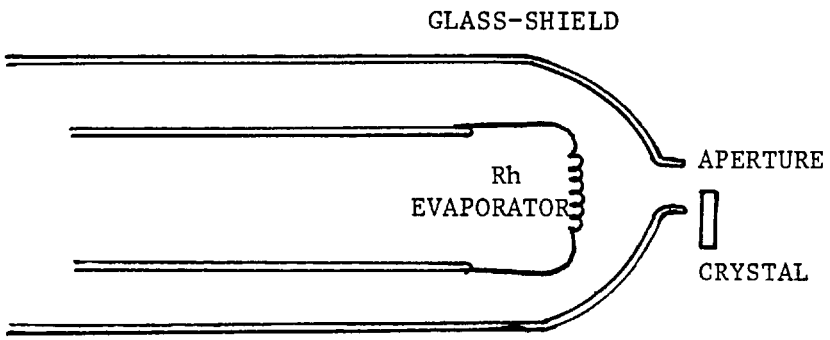


Figure 4.17 Schematic diagram showing the position of the crystal for deposition of Rhodium with a Step Profile for the Diffusion Experiment.

5. EXPERIMENTAL STUDIES BY FIELD ION MICROSCOPY: RESULTS

Following the procedures outlined in chapter 4 some aspects of the behaviour of rhodium on the (110) surfaces of tungsten and molybdenum were examined using the FIM. Single adatom diffusion was measured on both the substrates but quantitative diffusion measurements for three and four adatom clusters were made only on (110) surfaces of tungsten. The nature and stability of small clusters and islands was examined and the growth to monolayer films investigated. Qualitative observations of deposition and growth on a faulted tungsten specimen surface were also made and are reported in Appendix B.

5.1 Rhodium on Tungsten

5.1.1 Cluster structure

As already indicated in the preceding chapter, Rh adatoms on the (110)W surface combined to form linear chains, as shown in figure 5.1. This behaviour is similar to that observed for other fcc adsorbates, Ir[44,157], Ni, Pd and Pt[29] on (110)W surfaces and is indicative of an inter-adatom interaction that is both restricted and directional. Like the other adsorbate chains, Rh chains were observed to be accurately aligned with the substrate close-packed <111>W directions which lie at 35° to the decorated [1$\bar{1}$0] zone direction in micrographs. Although the atomic structure of Rh dimers was frequently resolved (figure 5.2) the adatom spacing in the clusters cannot be determined directly because of the unknown extra magnification in the micrographs of objects protruding above the specimen surface. For Ir

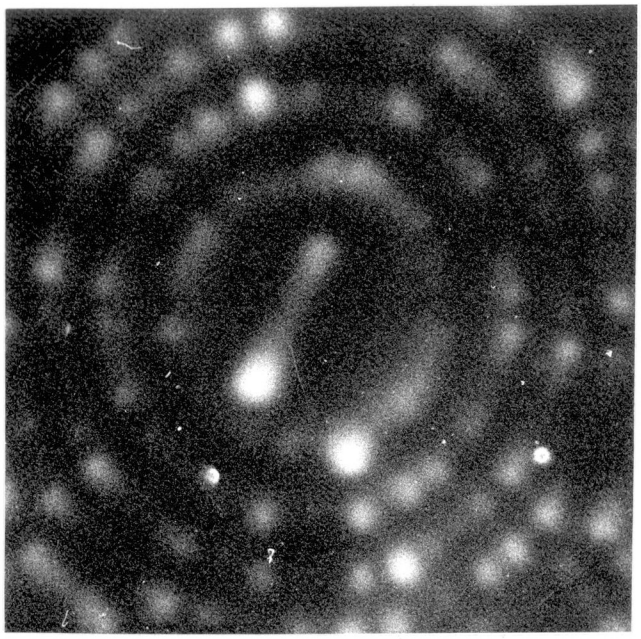
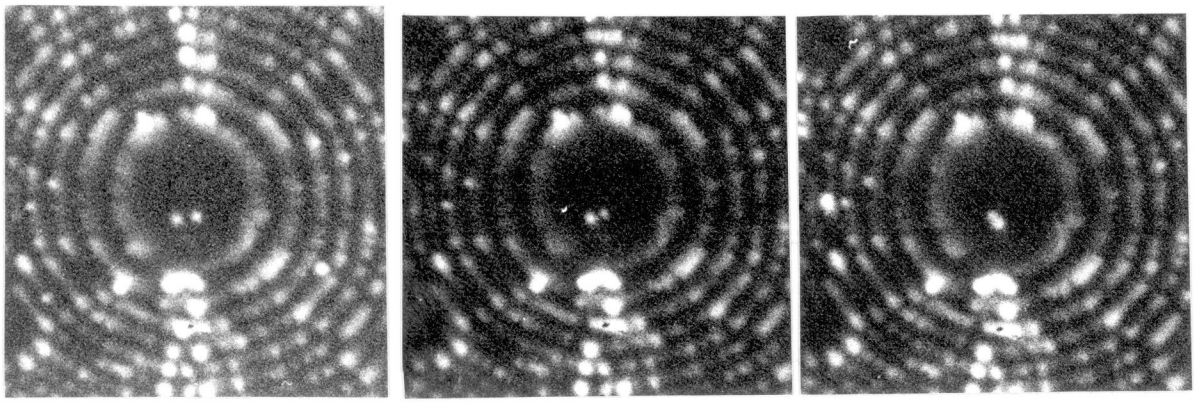


Figure 5.1 Micrograph showing a rhodium chain-cluster grown by deposition of Rh on W(110) at 78 K followed by annealing at 300 K.



a b c

Figure 5.2 Sequence of micrographs showing the formation of a Rh dimer after successive heating periods at 260 K. (a),(b) Single adatoms; (c) resolved dimer.

chains near the centre of the (110)W surface, Bassett[156] has found that the change in image length per Ir adatom for a cluster changing in size by gain or loss of adatoms was comparable to the mean displacement of adatoms moving between adjacent adsorption sites on the surface. The Ir-Ir spacing thus seemed to be comparable with the spacing of close-packed W atoms, which is 0.274 nm. The inter-adatom spacing in Pt[28] and Pd[29] chains was also considered to be 0.274 nm and it seems likely that this may be the case for the Rh chain clusters. However, it should be noted that Casanova and Tsong[34], in a recent study of Ir-Ir pair interaction on W(110), assume a bond length of 2 x 0.274 nm between the resolved adatoms of Ir_2 dimer. An inter-atomic spacing greater than 0.274 nm has also been assumed by Fink and Ehrlich[50] for their resolved two-dimensional islands of Pt, Ir and Pd on W(110). However, the linear chain clusters of these adsorbates in their studies were unresolved, which indicates that the adatoms in the chain clusters are close packed and probably with an inter-atomic spacing of 0.274 nm.

There are three possible positions that can be adopted by Rh adatom within the unit mesh of a bcc (110) surface, figure 5.3. These are the lattice site at the mesh centre where each adatom has two nearest and two next-nearest neighbours, and two equivalent surface sites in which the adatom has three-fold co-ordination. For a pair of adatoms occupying identical positions in the neighbouring unit meshes there are three possible positions for the centre-of-mass (centroid) of the cluster. Bassett[28] has mapped out Pt_2 dimer centroid locations on W(110) from FIM micrographs and has shown that the adatoms of the dimer occupy lattice sites although he notes that the possibility that

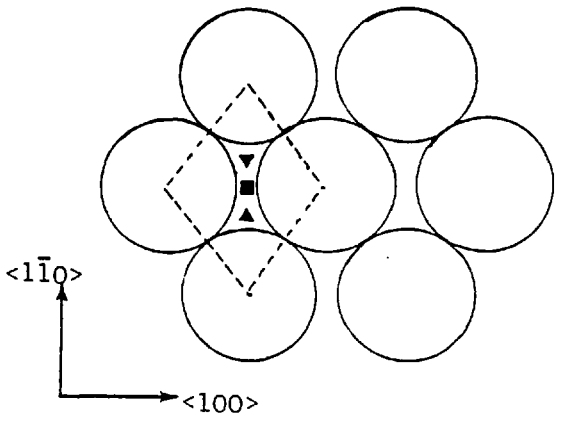


Figure 5.3 Schematic diagram showing the lattice site (■) and the two equivalent surface sites (▲▼) within the b.c.c. (110) unit mesh.

the adatoms occupy surface sites, as suggested by Tsong and coworkers[129], and move to the centre of the unit cell under stress of the imaging field cannot be ruled out. The true location of an adatom on the (110)W surface is thus an uncertainty at present although it is frequently assumed that adatoms occupy surface sites. For example, Fink, Faulian and Bauer[49], in their studies of long-range interactions between adatoms of W-Pd and Re-Pd pairs on W(110), assume that Pd and Re adatoms occupy surface sites. Also, Fink and Ehrlich[50] assume that adatoms of Pd, Pt and Ir islands on W(110) occupy surface sites.

5.1.2 Cluster mobility

The motion of single Rh adatoms on W(110) was two-dimensional (figure 5.4), as has been observed previously for other transition metal adatoms on W(110). The migration of clusters however is more complex than that of single adatoms, as noted by Bassett[28] for Pt cluster migration on the W(110) surface. At temperatures below that at which cluster dissociation occurs, migration of the linear cluster can lead to configurational change via intermediate states (figure 5.5). By sequential hopping of one adatom at a time, the cluster can be translated sideways along the substrate <111> direction, or it can be rotated so that its final (observed) configuration is one in which the linear-chain axis is aligned along the other equivalent close-packed direction. Figure 5.6 shows a Rh_3 trimer which has undergone significant migration, involving both translational as well as rotational motion. In the analysis of data, migrations involving only a simple translation of the clusters were considered since the proportion of observed displacements involving cluster re-orientation was not significant at the temperatures used. Qualitatively it was observed

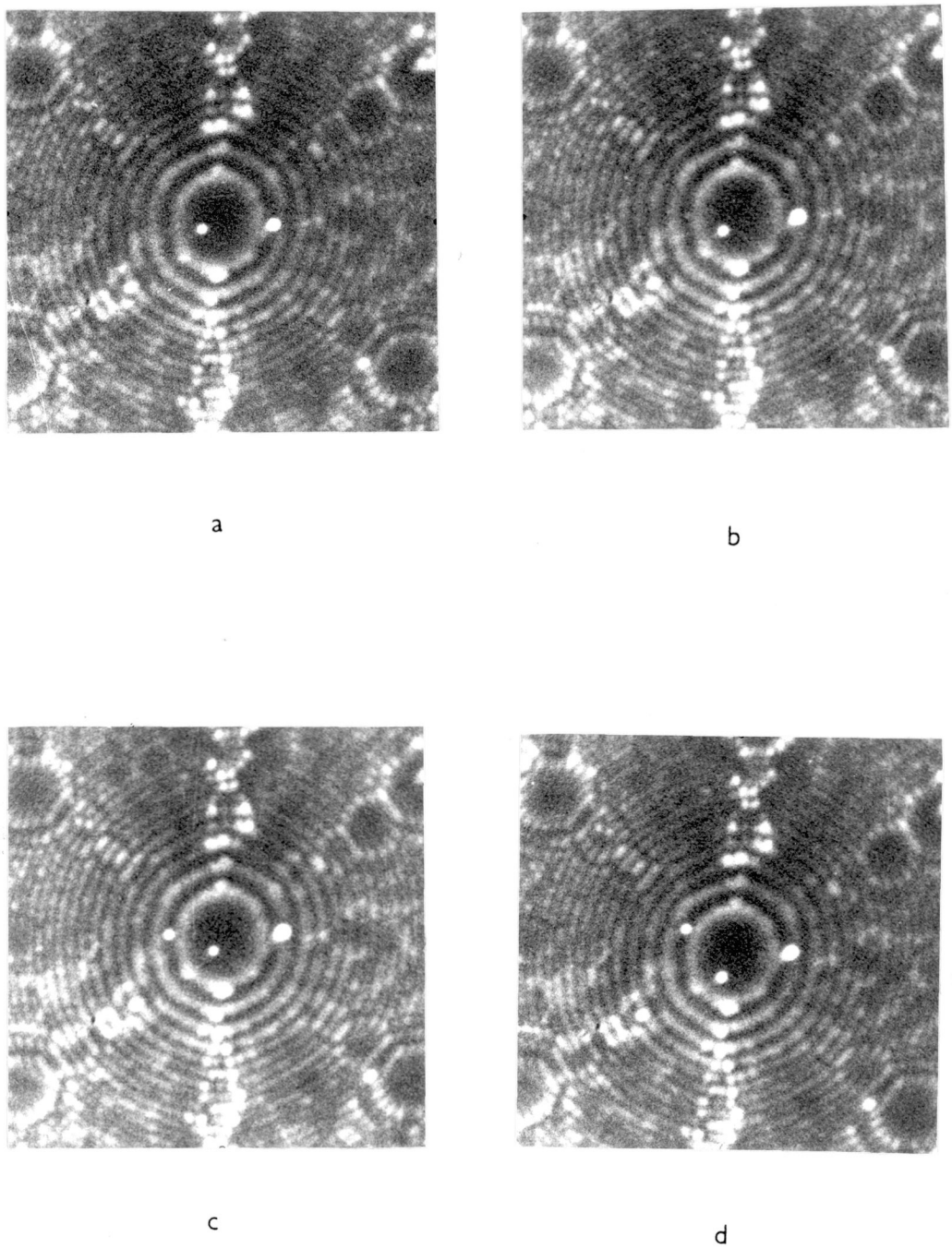


Figure 5.4 Migration of a single Rh adatom on W(110) in successive heating periods at 280 K.

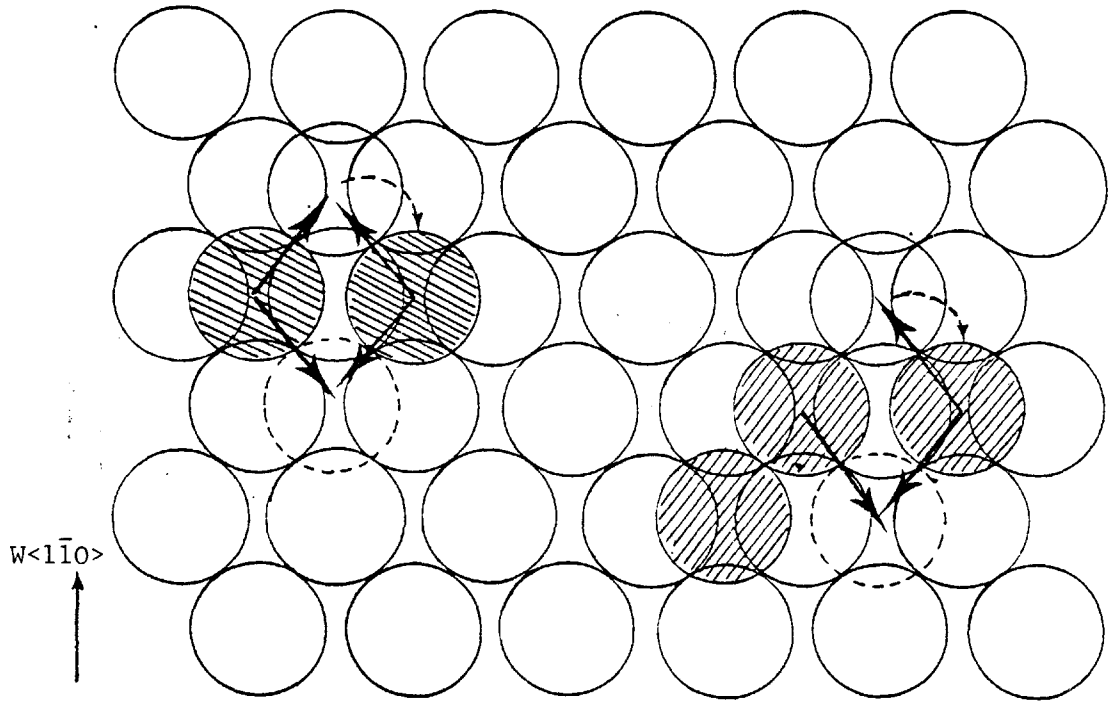


Figure 5.5 Schematic diagram showing the intermediate configurations of a dimer and trimer during migration by sequential jumping of one adatom at a time.

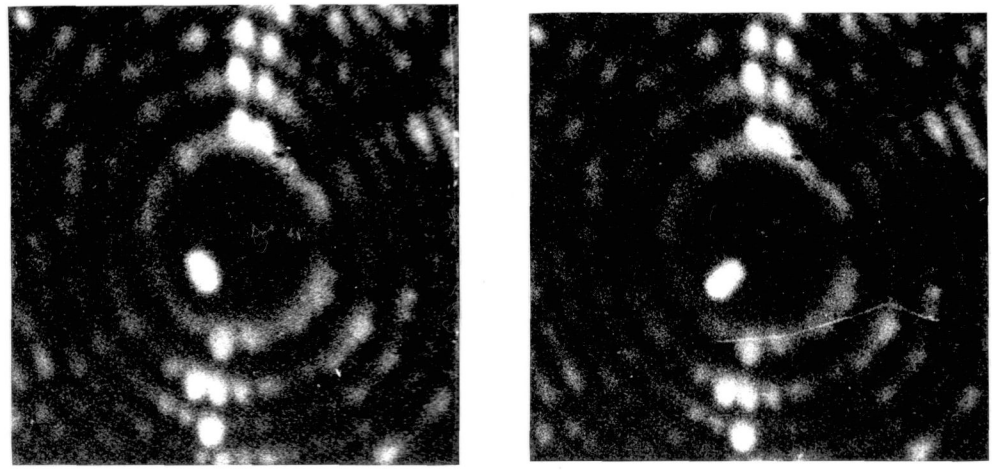


Figure 5.6 Diffusion of a Rh trimer on W(110) showing displacement of the cluster centre of mass and reorientation in successive heating periods at 300 K.

that in the temperature range for observable migration the proportion of observations involving cluster re-orientation was significantly less for tetramers than for trimers, which is similar to the behaviour of Pt clusters on W(110).

The mean square atomic displacement $\langle r^2 \rangle$ and the diffusion coefficient D were calculated following the method outlined in section 4.2.2, chapter 4. The temperature dependence of D according to equation 4.7, $D = D_0 \exp\{-\Delta E_{diff}/kT\}$, for the single adatom and linear clusters of three and four adatoms is shown in figure 5.7a and 5.7b, respectively, in Arrhenius plots of ln D versus 1/T. Table 5.1 summarizes the corresponding activation energies ΔE_{diff} and pre-exponential factors D_0, deduced by least squares analysis of the data using point weightings based on the number of displacements measured. The possible sources of error involved in the measurement of the temperature have been discussed in section 4.1.6. It has been estimated that this error amounts to ±2 K. Consequently the standard errors of ln D have considerably greater weight than errors in 1/T, justifying this assumption in the least squares analysis. The error in ΔE_{diff} is thus calculated from the standard error of each point. The D_0 values are very sensitive to changes in ΔE_{diff} due to the rather long extrapolation required for the intercept value. Consequently, small errors in ΔE_{diff} results in orders of magnitude error in D_0. The values quoted for D_0 are thus not accurate to more than an order of magnitude.

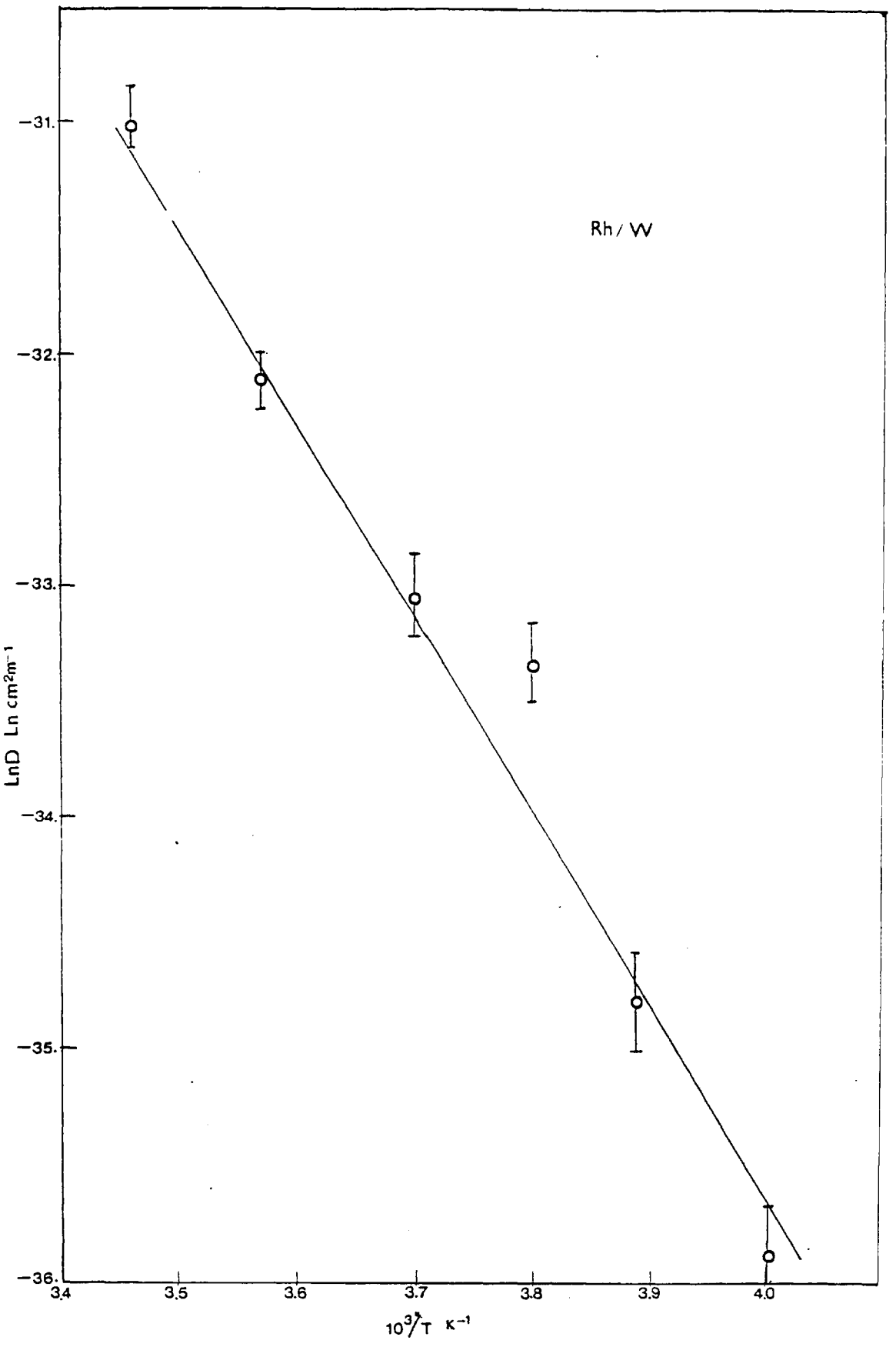


Figure 5.7a The temperature dependence of single adatom diffusion.

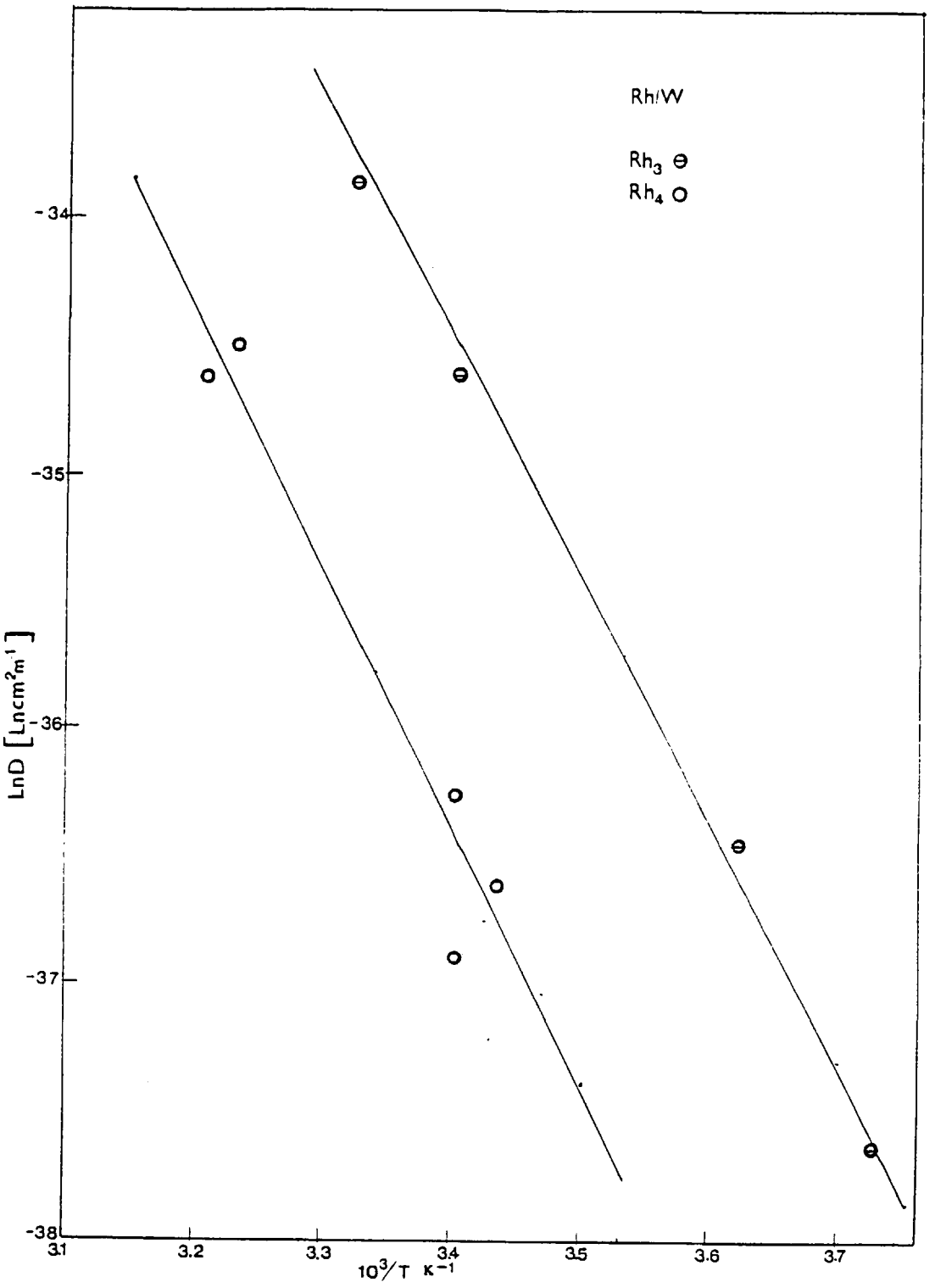


Figure 5.7b The temperature dependence of cluster diffusion.

Table 5.1 Activation energies ΔE_{diff} (kJ mol^{-1}) and pre-exponential factors D_0 (cm^2 s^{-1}) for Rh cluster diffusion on W(110) and Mo(110).

Substrate	Adsorbate	ΔE_{diff}	D_0
W(110)	Rh	70 ± 5	2.5×10^{-3}
	Rh_3	76 ± 8	6.1×10^{-4}
	Rh_4	85 ± 8	3.1×10^{-3}
Mo(110)	Rh	60 ± 6	1×10^{-3}

Table 5.2 Temperatures (K) for observable migration, T_m, rearrangement, T_r, and dissociation, T_d, of adatom clusters A_x and islands of more than 10 adatoms on W and Mo(110) surfaces.

Substrate	Adsorbate	$T_m(A_2)$	$T_D(A_2)$	$T_D(A_3)$	$T_D(A_4)$	T_r (islands)	T_D (islands)
W(110)	Ni	225	250	-	295	340	370
	Pd	190	220	-	>220	290	340
ref. 29	Pt	245	260	-	340	>410	410
	Rh	250	260	310	350	400	430
Mo(110)	Rh	230	250	<310	-	330	<400

Table 5.3 Activation energies for formation ΔE_f (kJ mol^{-1}) and dissociation ΔE_d (kJ mol^{-1}) of Rh dimer on W(110).

ΔE_f	ΔE_d
67 ± 5	83 ± 5

5.1.3 Cluster stability

Due to attractive interactions, collisions between migrating adatoms result in the formation of adatom clusters as depicted in figure 5.8. At sufficiently high temperatures, the clusters become unstable and dissociate as shown in figure 5.8 for a Rh_3 trimer which dissociated upon heating for 60 s at 320 K. The temperature required for an observable dissociation rate increased with the number of adatoms in the chain, suggesting that there is a non-additive contribution to the cluster binding energy. The temperatures at which migration and dissociation of Rh clusters, of various sizes, occurred at observable rates are listed in table 5.2. The thermal stability of clusters of Ni, Pd, Pt[29] and Ir[44] on W(110) has been examined previously in similar studies. The temperatures for migration and dissociation of clusters of these adsorbates are also listed in table 5.2 for comparison with the present studies. Like Pt and Ir on W(110), dissociation was the only change produced by heating that was observed for Rh chain clusters. The clusters probably dissociate by loss of adatoms from the ends of the chains[29].

The Rh dimers were stable only over a small temperature range above the onset of adatom mobility. At higher temperatures the rate of dimer dissociation increased with increasing temperature until the rate of dimer formation and dissociation reaction as depicted by the equation

$$Rh_2 \underset{k_2}{\overset{k_1}{\rightleftharpoons}} Rh + Rh \qquad (5.1)$$

approached equilibrium. This is shown in figure 5.9 where the fractions of heating cycles resulting in formation or dissociation is plotted against the temperature. The Arrhenius plots of $\ln(-\ln f_s)$ versus $1/T$

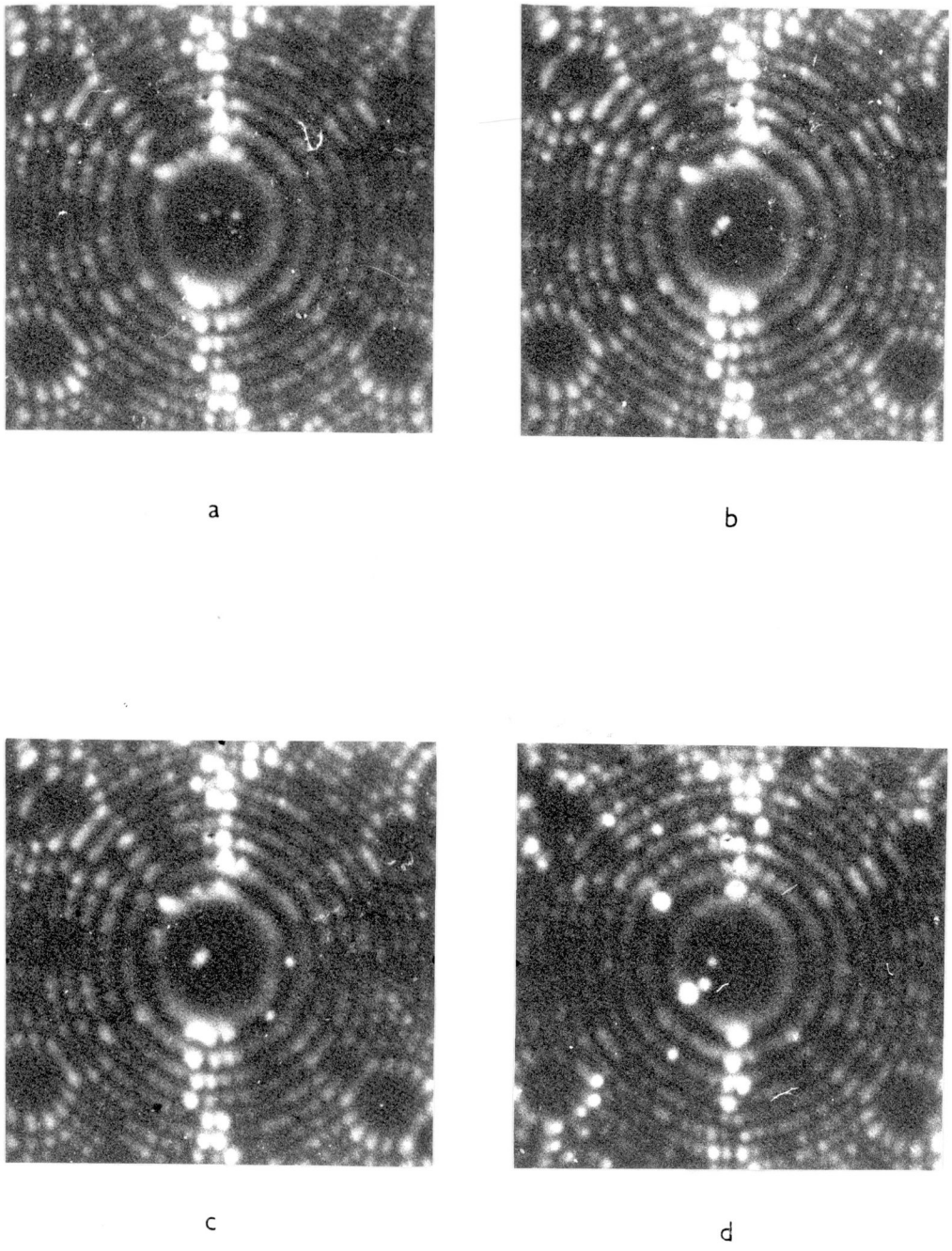


Figure 5.8 Micrographs showing the formation and dissociation of a Rh trimer. Three single adatoms (a) that first form a dimer and a single adatom (b) and then a trimer on heating at 280 K (c). The trimer in (c) dissociated (d) on heating at 315 K.

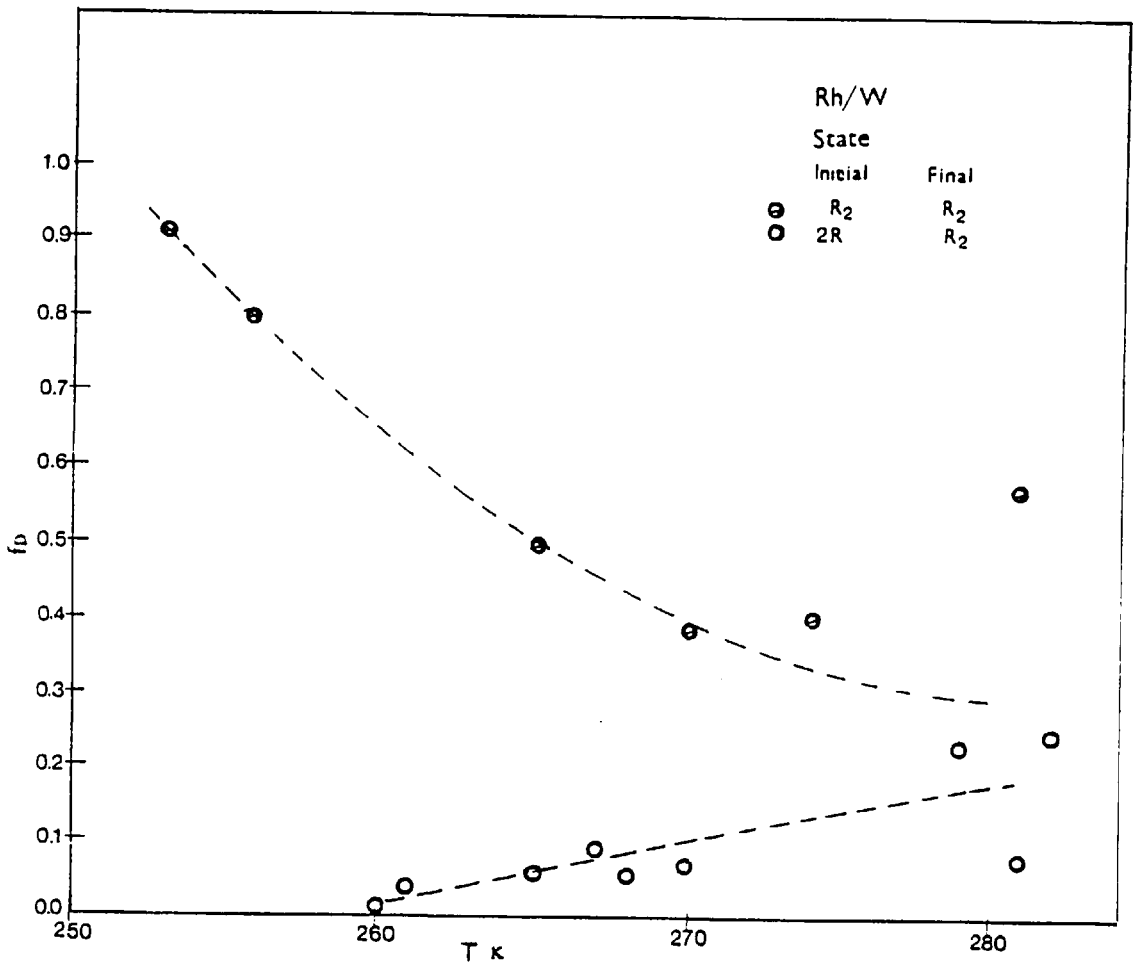


Figure 5.9 Plot of f_D versus T for dimer formation (O) and dissociation (θ).

for dimer formation kinetics and $\ln -\ln\left(\frac{f_d - f_d^e}{1 - f_d f_d^e}\right)$ versus 1/T for dimer dissociation kinetics, according to equations 4.13 and 4.16 (chapter 4) are shown in figures 5.10a and 5.10b, respectively. Table 5.3 lists the corresponding activation energies for formation, ΔE_f, and dissociation, ΔE_d, deduced by the same least squares analyses method used for the single adatom diffusion measurement.

The binding energy of the dimer can be deduced from the dissociation energy which includes the activation energy for diffusion. This is because an adatom must gain sufficient energy both to break the dimer bond and to move away over the energy barrier to migration between adsorption sites. Thus, the binding energy ΔE_b can be expressed as

$$\Delta E_b = E_d - E_{diff} \qquad (5.2)$$

Substituting into 5.2 the values for ΔE_{diff} and ΔE_d from tables 5.1 and 5.3, respectively, the Rh dimer binding energy is calculated to be 13 kJ mol^{-1}. It should be noted that ΔE_b is not simply the energy of the Rh-Rh bond but is a measure of the difference between the initial and final states of the whole system. The dissociation energy is thus governed by the balance between adatom-adatom interaction, E_{aa}, and the change in adatom-substrate interaction energy, E_{as}, upon dimerization. Thus, ΔE_b can be written as

$$\Delta E_b = E_{aa} + 2(E'_{as} - E_{as}) \qquad (5.3)$$

where E'_{as} is the adatom-substrate interaction for the adatoms in the dimer.

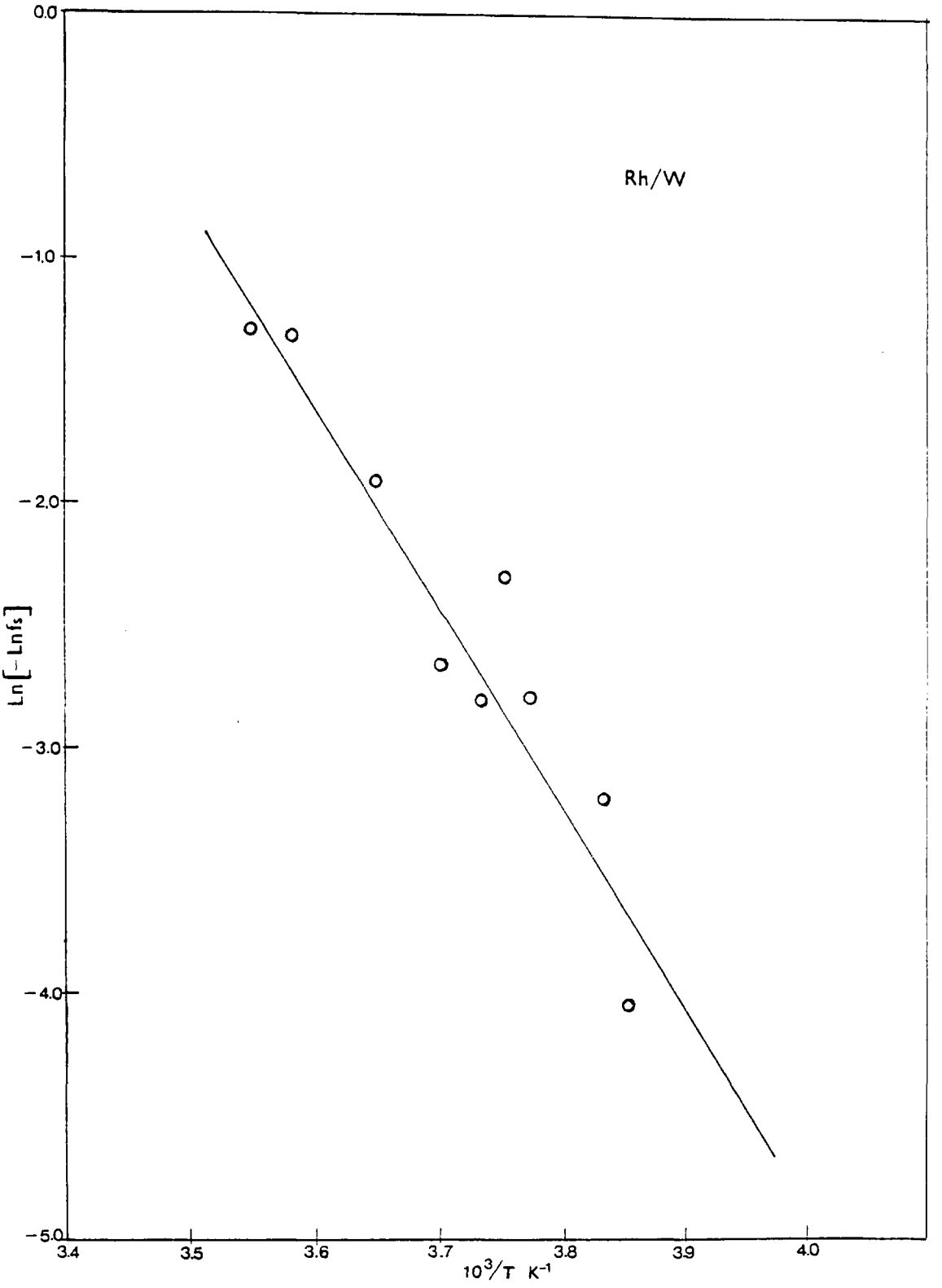


Figure 5.10a The temperature dependence of rate constant for dimer formation.

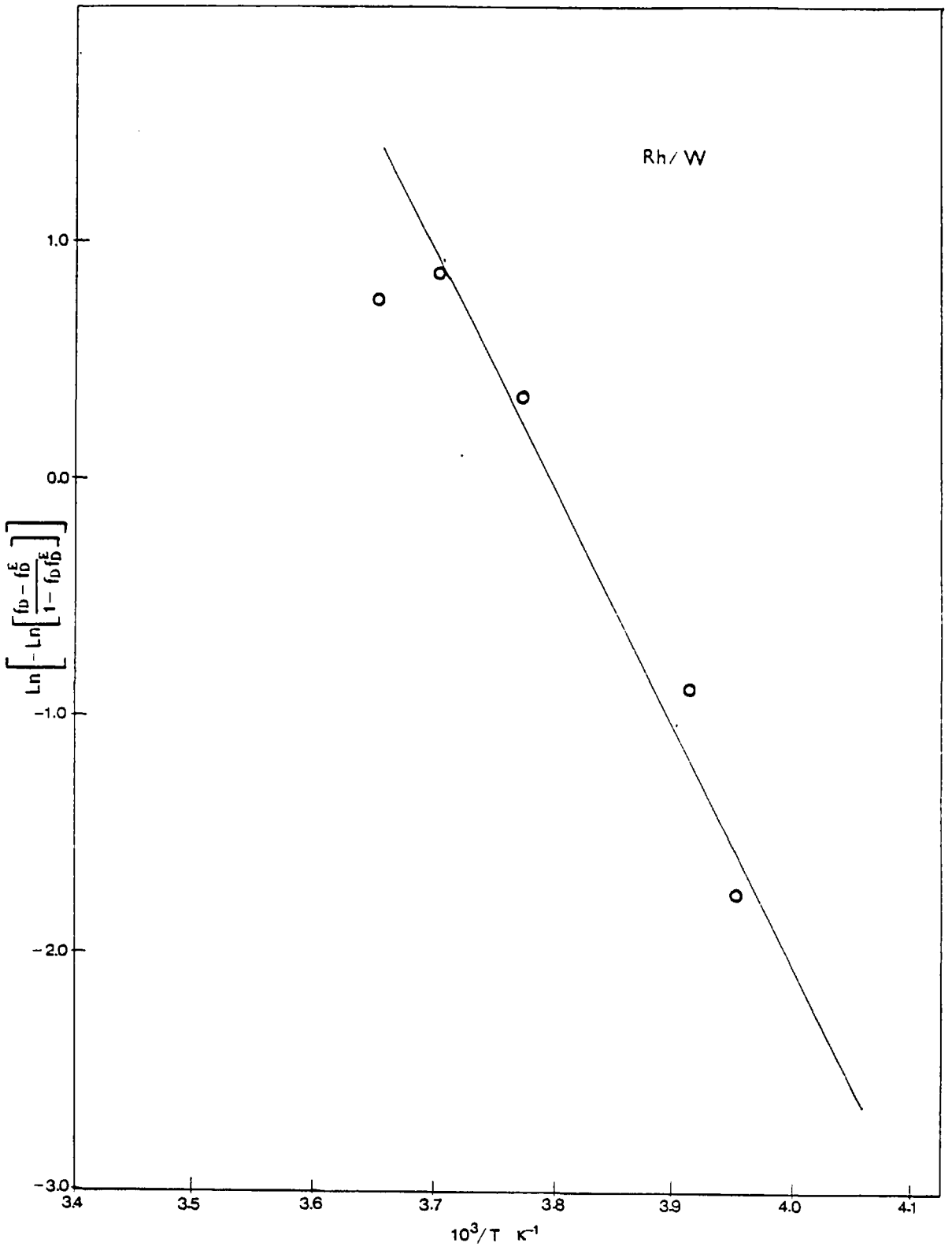


Figure 5.10b The temperature dependence of rate constant for dimer dissociation.

5.1.4 Film growth

Heating a deposit of Rh adatoms resulted in the formation of chain clusters aligned along the substrate close-packed directions, as described in section 5.1.1. The rate of nucleation of these clusters or cluster densities could not be studied quantitatively due to the small size of the (110) plane of the FIM tip. Qualitatively, it was found that at low temperatures a large number of short chain clusters could be grown, while increasing the substrate temperature during deposition resulted in the growth of a smaller number of longer chains. The effect of varying the deposition rate was not examined since increasing the deposition time would have increased the risk of contamination from the walls of the evaporator shields, which could degas due to radiative heating for prolonged periods.

Nucleation of two dimensional crystallites was seen to occur by addition of atoms at the point where two adatom chains lying along different <111> directions intersected, as illustrated schematically in figure 5.11. This appeared to be the most usual point at which two-dimensional Rh islands appeared, although nucleation has also been observed at points where chains intersected the (110) plane edge which is decorated with Rh adatoms. Figure 5.12 shows the nucleation of two two-dimensional islands, one at the edge of the W(110) plane and the other at the intersection of two chain clusters. The atomic arrangement in the two-dimensional nuclei could not be resolved in the micrographs. The observation of nucleation at chain-chain or chain-edge intersection is exactly as found by Tice and Bassett[44,45] for Pt and Ir on W(110) surfaces.

Once the two-dimensional nuclei had formed, further deposition and annealing resulted in the growth of two-dimensional islands at the

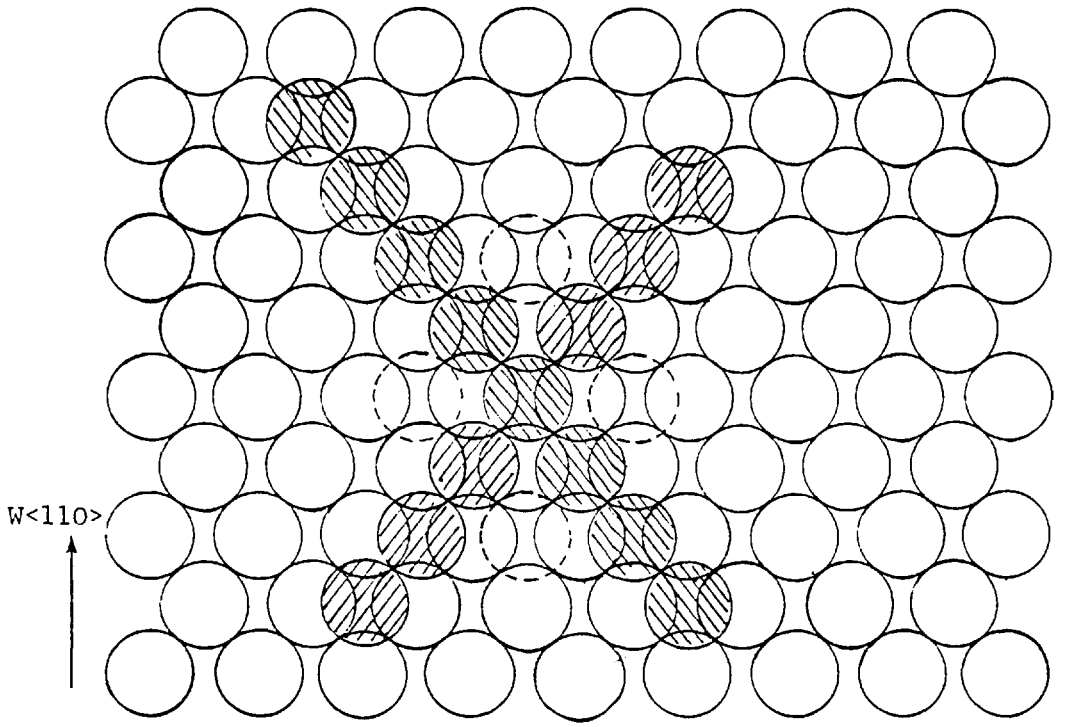


Figure 5.11 Schematic diagram showing possible nucleation sites (dashed circles) for two-dimensional growth at chain-chain intersection.

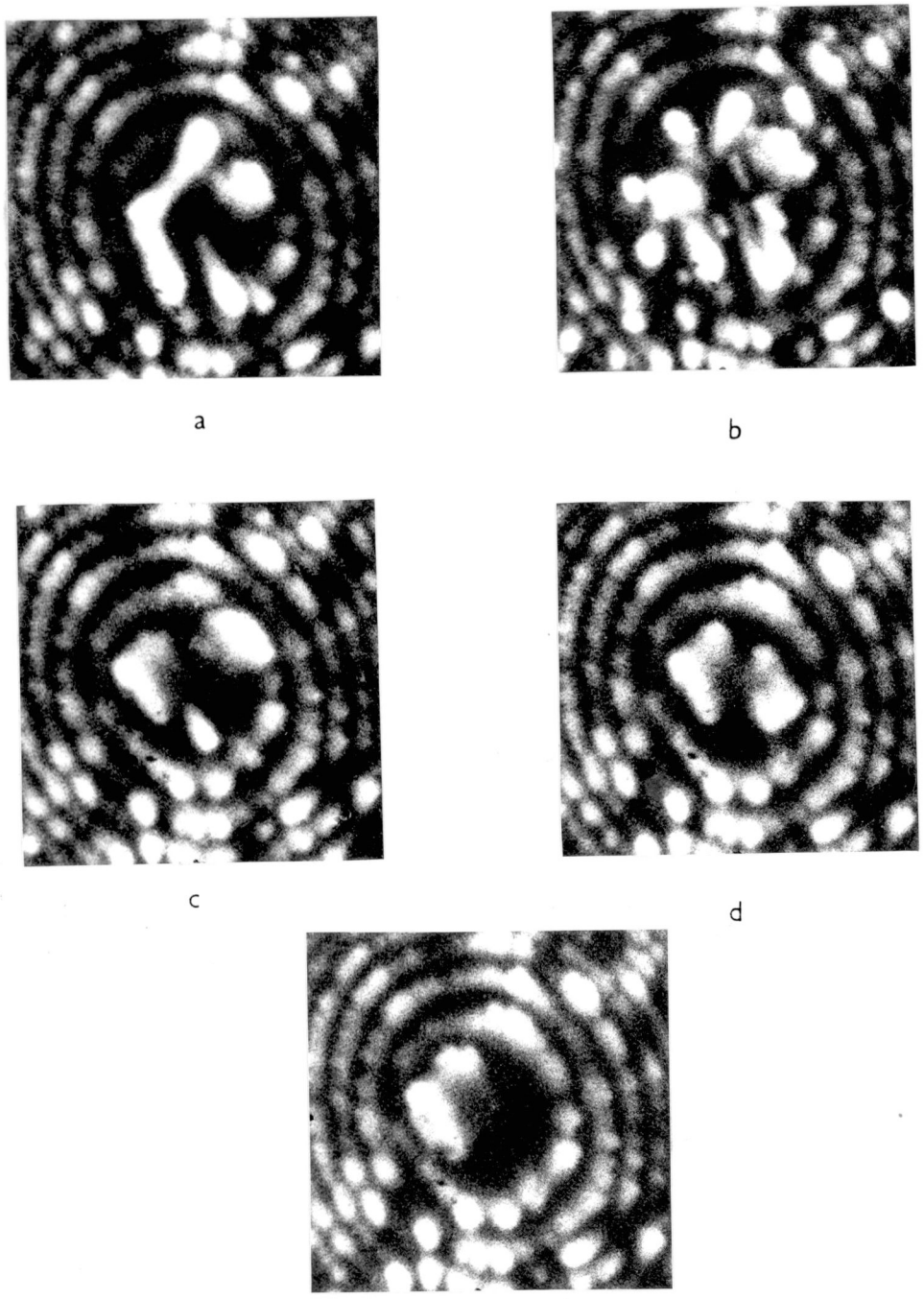


Figure 5.12 Micrographs showing the growth of rhodium islands on W(110). (a) Island nuclei formed at chain-chain intersection and at the (110) plane edge during deposition at 350 K. (b) Growth of the island nuclei and chains after further deposition at 78 K followed by annealing at 395 K. (c) Two islands and a small chain after heating the deposit in (b) at 400 K. (d) Migration and rearrangement of the islands on heating at 410 K; the top right island has migrated considerably and appears to be in "contact" with the other; the chain cluster in (c) has been agglomerated into the islands. (e) The islands coalesced after 100 s at 420 K.

expense of chain clusters. Adatoms deposited both on the substrate and on top of growing islands diffused to the island edges and were incorporated there. Continuing deposition to the monolayer stage resulted in a continuous film that appeared to replicate the features of the tungsten substrate, figure 5.13, as found previously for Ni, Pd, Pt[29] and Ir[44] on W(110).

Usually a continuous film grew around a single nucleus but if several nuclei had formed, growth around them resulted in multiple islands on the W(110) surface (figure 5.12). The islands appeared to migrate as a unit at around 430 K and gradually coalesced to a single large island (figure 5.13). The temperatures for migration, rearrangement and dissociation of islands are listed in table 5.2.

As noted previously, Fink and Ehrlich have recently reported the observation of atomically resolved two-dimensional islands of Pd, Pt and Ir on W(110), from which they assign a p(n×n), $n > 1$, type of structure for the islands. The islands were observed to undergo phase transitions until after thorough equilibrium, the structure of the islands appeared to be that of the underlying substrate. In contrast, the atomic structure of island clusters and its relation to the substrate lattice could not be obtained in the present study but angles between island edges and the substrate $\langle 1\bar{1}0 \rangle$ direction could be measured. Figure 5.14 shows a histogram of island edge angle with respect to the substrate $\langle 1\bar{1}0 \rangle$ direction. The angles were measured directly from micrographs. The islands were frequently found to have edges parallel to the substrate close-packed direction and the mean angle was determined to be 39 ± 5^{o} to the substrate $\langle 1\bar{1}0 \rangle$ direction. This is comparable to Pd islands on W(110)[29] which had edges at 38 ± 7^{o}

to W<1$\bar{1}$0> direction. The observed edge angle is consistent with an atomic arrangement similar to that of the substrate rather than a truly close-packed structure. However, the scatter in measured edge orientation is too large to justify any assignment of cluster structure on this basis. The possibility of multiple positioning of islands with a close-packed atomic arrangement cannot be ruled out since discontinuities were sometimes observed between islands which had come into contact before coalescing (figure 5.12). Such discontinuities have also been observed in the case of Ni and Pd islands on W(110) surfaces[29]. Pt islands on W(110) also appear close-packed since second layer Pt adatoms have been observed to diffuse below 150 K which is comparable to the temperature at which significant diffusion of Pt on Pt(111) surface occurs[29]. Similarly Rh adatoms deposited on Rh(111) surface are known to have considerable mobility at liquid N_2 temperature[128]. Second layer Rh adatoms were never observed in the present study, which may be indicative of an island structure which is close-packed or very nearly so.

The rate of loss of adatoms from the islands was studied by the method established by Bassett[29]. This involved generating a single large island and removal of Rh from all other regions of the tip surface by field evaporation, which is possible since Rh, like Pt, Ni, Pd and Ir, is selectively retained on the W(110) surface. Then, after heating for a given period at a preset temperature, the number of bright spots that appeared at the (110) steps when the tip was reimaged is counted (figure 5.15). The bright spots are Rh adatoms that have escaped over the step and appear to be pulled up by the imaging field to image very brightly. The rate of loss of

atoms from an island is given by

$$\frac{dn}{dt} = n_k \nu_k - R_R \qquad (5.4)$$

where n_k is the number of kink sites at the island edges, ν_k is the frequency of escape of atoms from kink sites and R_R represents a term involving the rate at which escaping adatoms return to the island after diffusion over the terrace and reflection at the step. The measured loss rate does not equal dn/dt since the return rate, R_R, is not known. If it is assumed that R_R is a constant independent of temperature, then we can obtain an estimate of the activation energy, ΔE_L, for loss of adatoms. The number of adatoms, n_m, lost in time t at temperature T can be expressed as

$$n_m = t\, n_k \nu_k = t n_k \nu_0 \exp\{-\frac{\Delta E_L}{kT}\} \qquad (5.5)$$

In the present work, heating cycles of 60 sec. duration were performed for six different islands, each containing about 100 Rh adatoms initially, and a mean value of n_m obtained at two different temperatures. From this, a value for ΔE_L of 123 ± 18 kJ mol^{-1} was obtained. ΔE_L contains two contributions, the energy of formation, E_f, of an adatom from a kink site and the energy of migration and loss from the plane. If the latter term is equated with the single adatom diffusion activation energy for Rh (70 kJ mol^{-1}), then E_f = 53 kJ mol^{-1}. It is noted that this value is considerably lower than the nearest neighbour bond energy, E_f', estimated from the energy of sublimation, E_{sa}, of rhodium using the relation[177] $E_{sa} = 6E_f'$, which yields E_f' = 97 kJ mol^{-1} for E_{sa} = 580 kJ mol^{-1} [178].

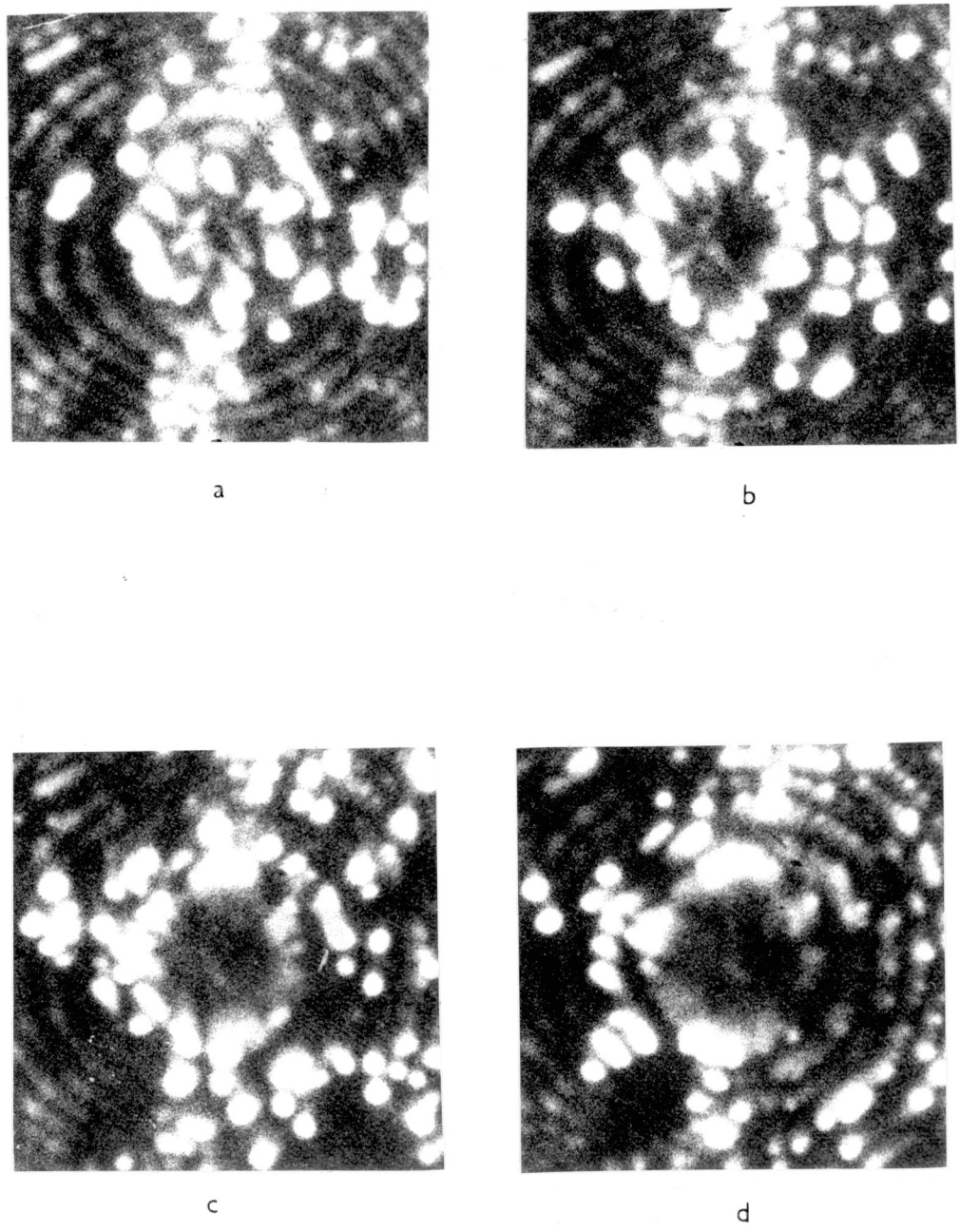


Figure 5.13 Micrographs showing the growth of a rhodium film on W(110). (a) Array of chain clusters grown by successive deposition of Rh at 78 K followed by annealing at 300 K. (b),(c) After further deposition onto the deposit in (a) and heating at 320 K. (d) A complete monolayer replicating the (110) region after further deposition and heating at 320 K, and field desorption of Rh from other surface regions. (The Rh vapour flux direction is at right angles to the tip axis, fig. 4.2, hence the asymmetry in the deposit coverage around the (110) steps.

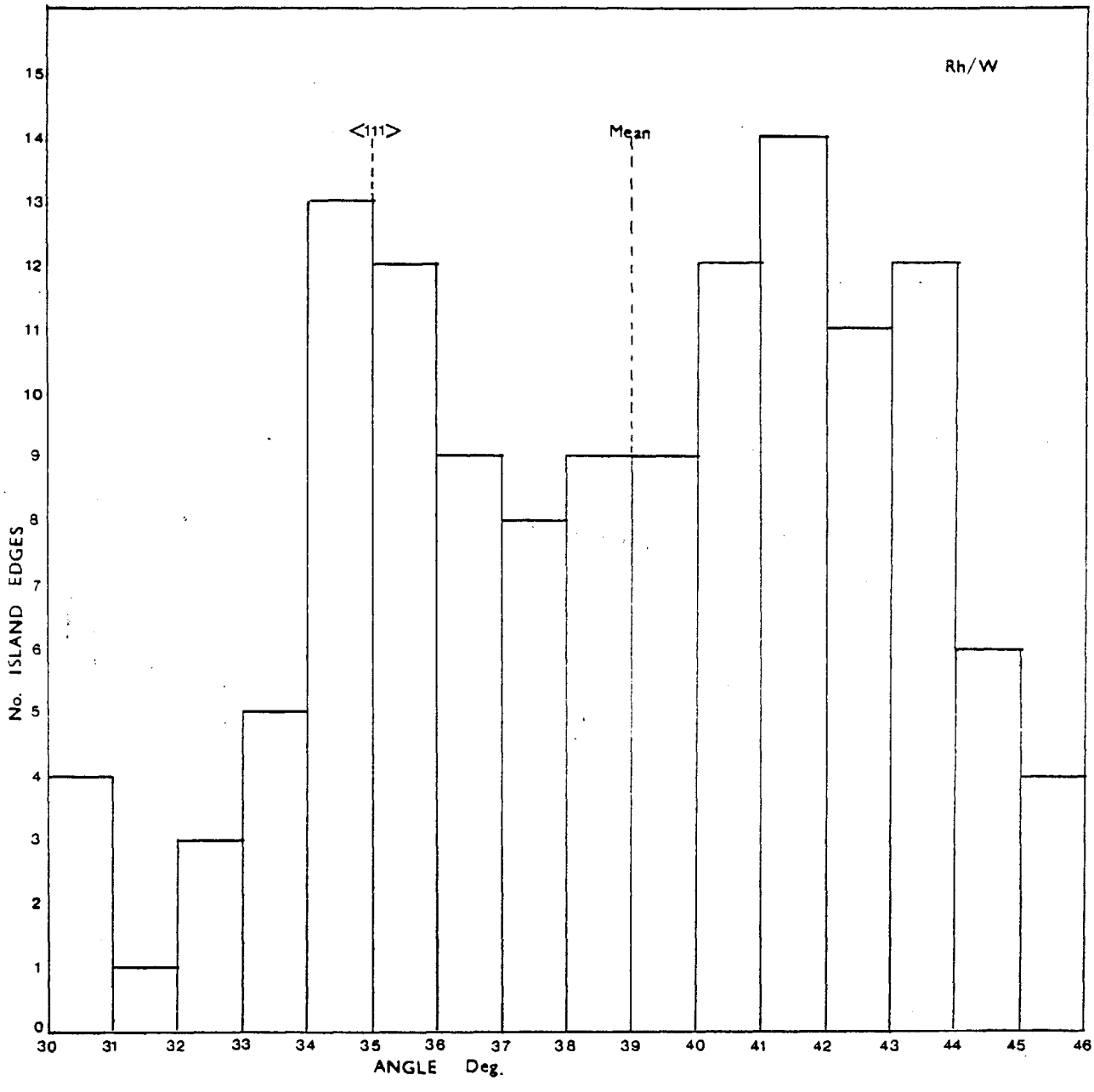
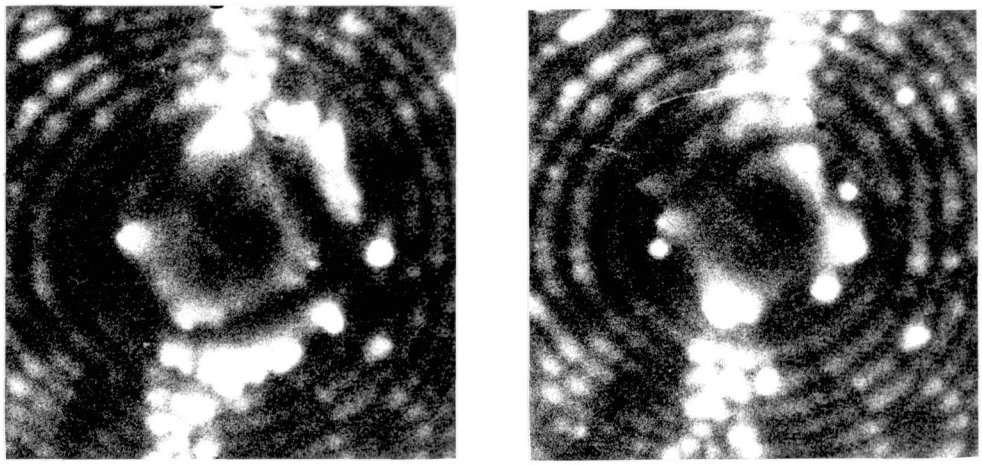
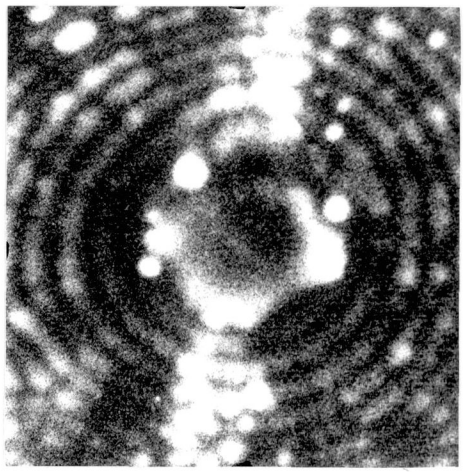


Figure 5.14 Island edge angle with respect to W<1$\bar{1}$0> direction.



a

b



c

Figure 5.15 Dissociation of a rhodium island on W(110) by heating for 60 s at (a) 420 K and (b),(c) 445 K. The bright spots are adatoms that have escaped from the island to sites at the (110) steps from where they are "pulled-up" by the imaging field.

5.2 Rhodium on Molybdenum

5.2.1 Adatom mobility

Figure 5.17 shows the two-dimensional migration of a Rh adatom expected on bcc Mo(110) surface. The mean square atomic displacement $\langle r^2 \rangle$ and the diffusion coefficient D for single adatom diffusion were calculated by the method outlined in section 4.2.2, chapter 4. The temperature dependence of D according to equation 4.7 is shown in figure 5.18 in an Arrhenius plot of ln D versus 1/T. The corresponding activation energy ΔE_{diff} and the pre-exponential factor D_o, deduced by the least square analysis used for Rh on W(110), are given in table 5.1.

5.2.2 Adatom cluster behaviour

Rh adatoms on a Mo(110) surface were observed to form linear chains as shown in figure 5.19. Qualitative studies of Pt and Ir on Mo(110) have also shown that these adsorbates form linear chains. Figure 5.20 shows Pt adatom chains on Mo(110) surface. The linear-chains in all cases were observed to be accurately aligned with the substrate <111> directions which are the close-packed directions on the surface. The tendency of these adatoms to form linear chain clusters rather than two-dimensional clusters is thus similar to that found on the W(110) surface.

Rh dimers on Mo(110) surface have been observed and their images showed the bond axis to be aligned parallel to the substrate <111> directions. Although the adatoms in the dimer were frequently resolved (figure 5.21) the adatom-adatom spacing in the dimer could not be determined due to the unknown magnification of the dimer images, as discussed in section 5.1.1. As suggested for Rh on W(110), the dimer adatoms are assumed to occupy nearest neighbour sites.

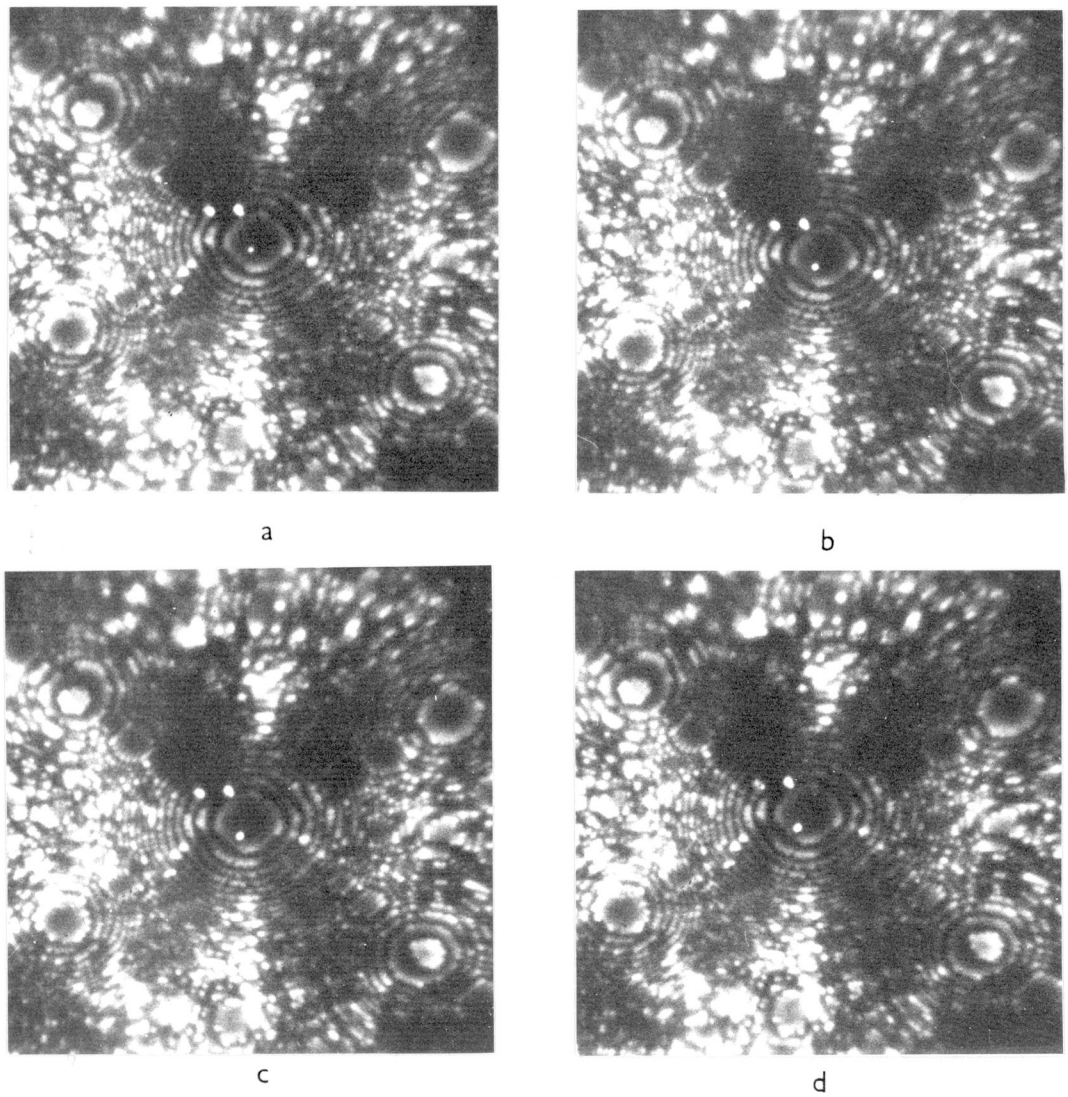


Figure 5.17 Migration of a single Rh adatom on Mo(110) in successive heating periods at 230 K.

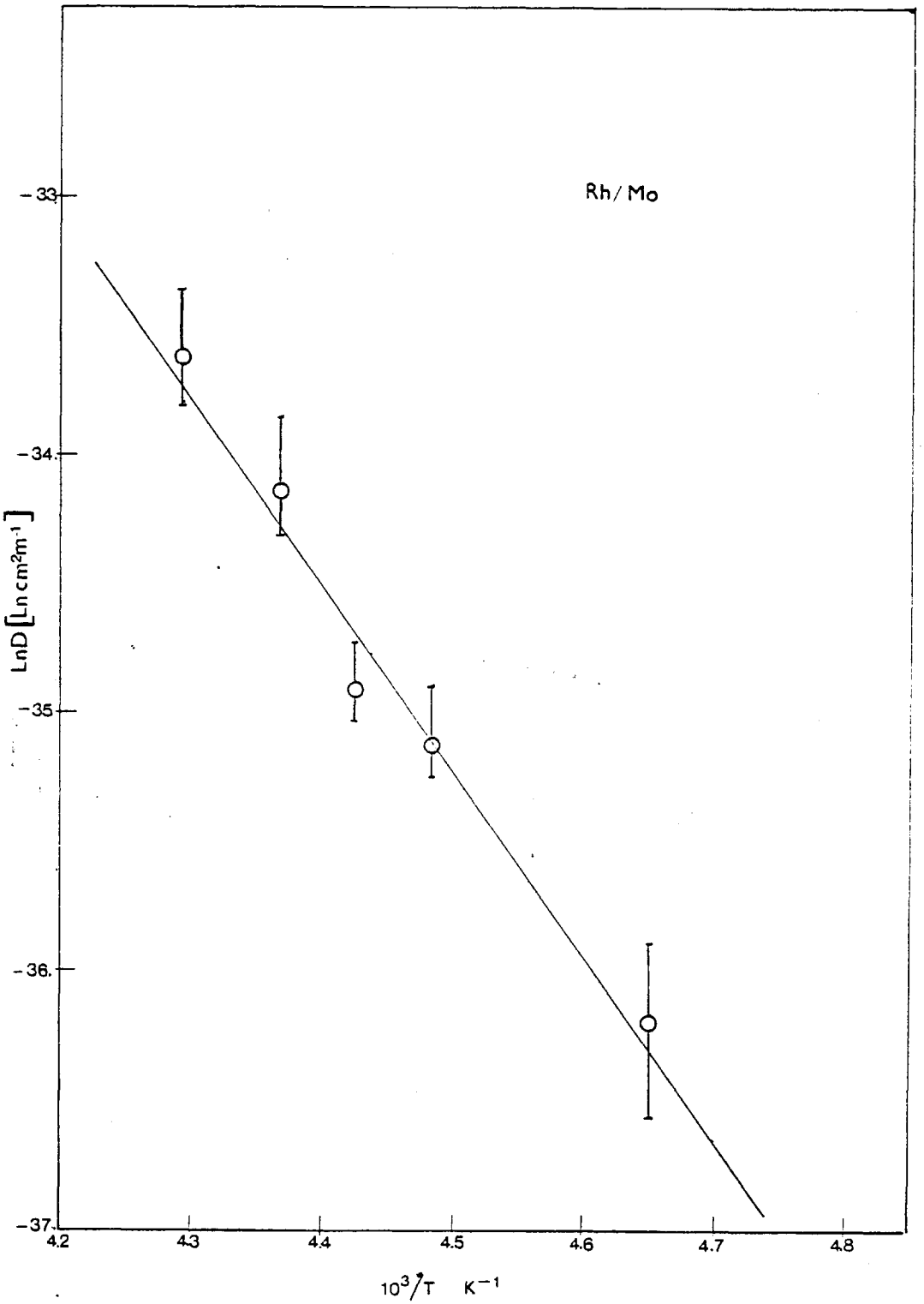


Figure 5.18 The temperature dependence of single adatom diffusion.

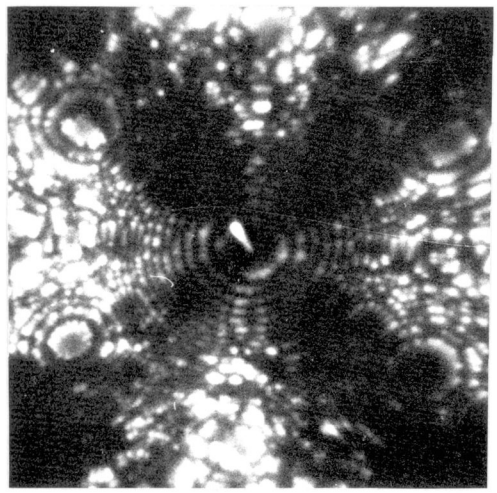


Figure 5.19 Micrograph showing a rhodium chain cluster grown by deposition of Rh on Mo(110) at 78 K followed by annealing at 290 K.

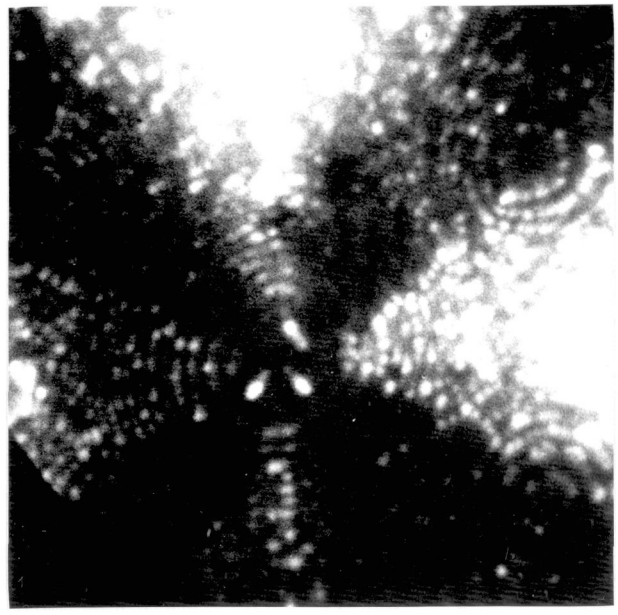


Figure 5.20 Micrograph showing platinum chain clusters grown by deposition of Pt on Mo(110) at 78 K followed by annealing at ≈280 K.

The migration of small Rh linear-chain clusters on Mo(110) has been observed qualitatively and found to be similar to that on the W(110) surface. Cluster migration involving reorientation and translation of the linear chain have been observed. Figure 5.21 and 5.22 show the migration on Mo(110) of a Rh dimer and trimer, respectively. The temperatures for observable migration of the clusters are listed in table 5.2.

The thermal stability of the clusters was examined and the temperatures at which cluster dissociation occurred at observable rates are listed in table 5.2. Figure 5.21 and 5.22 show the dissociation of a Rh dimer and trimer respectively. Just as for Rh_2 on W(110), Rh_2 on Mo(110) was stable only over a small temperature range above the onset of adatom mobility. Larger clusters were significantly more stable than dimers. The heating of Rh chain clusters produced movement or dissociation for chains of up to ten atoms, but chains containing ten or more atoms converted to two-dimensional island forms (figure 5.23). This behaviour is contrasted with that of Rh on W(110) in which case two-dimensional islands appeared only after the formation of nuclei at chain-chain or chain-step intersections. In fact, the behaviour of Rh on Mo(110) is more like that of Ni and Pd on W(110)[29] where chain clusters beyond a critical length converted to two-dimensional islands upon heating. Two-dimensional Rh islands on Mo(110) thus appear to be more stable than chains beyond a critical length of about ten atoms. The atomic structure of these small two-dimensional clusters could not be established. The atomic structure was unresolved and the island edges were generally unresolved.

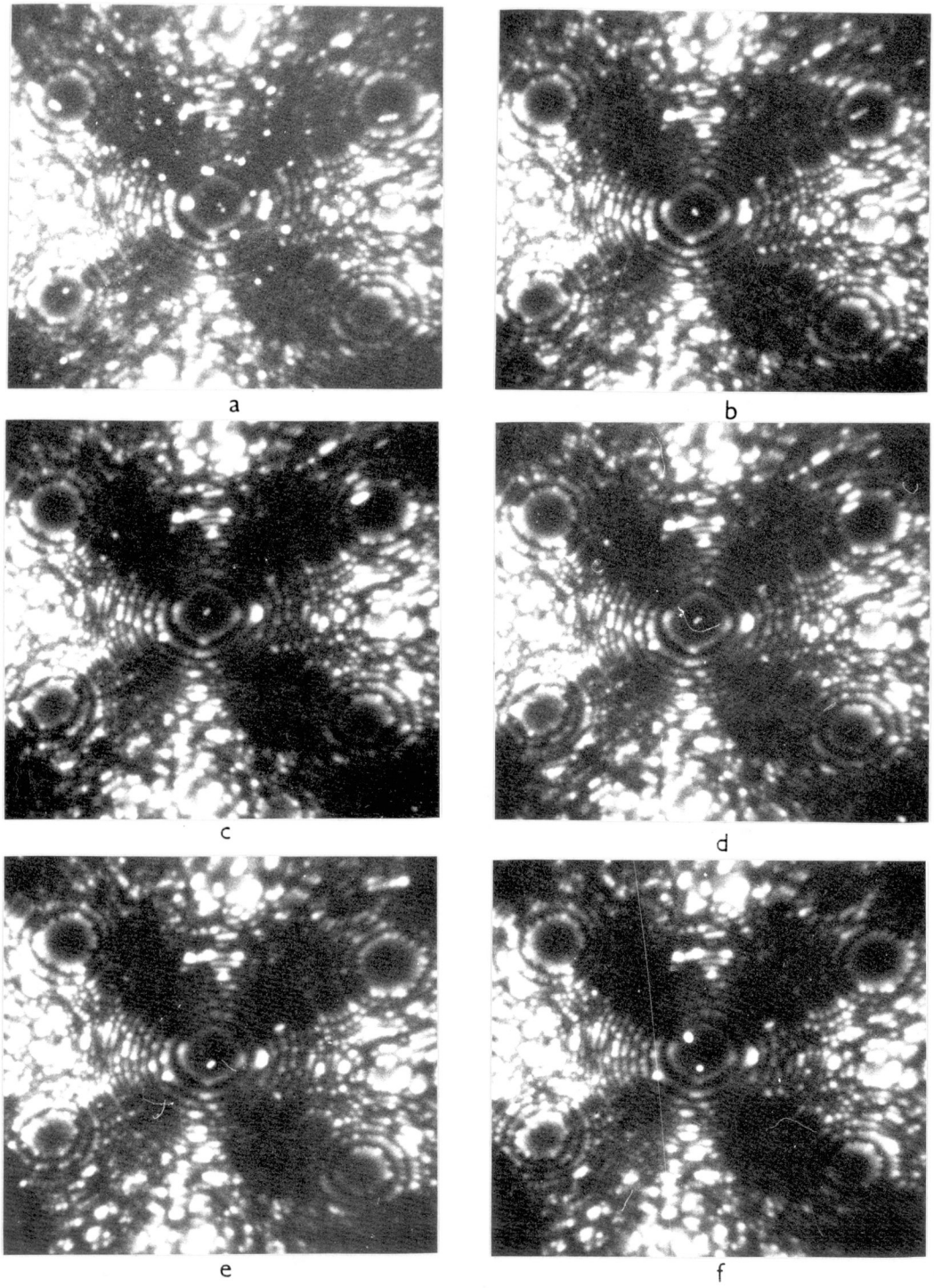


Figure 5.21 Sequence of micrographs showing the formation, migration and dissociation of a Rh dimer on Mo(110). Formation of the dimer (b) after heating the deposit of (a) for 60 s at 260 K. (c-e) Reorientation and migration of the dimer in successive heating periods at 245 K. (f) Dissociation of the dimer after 60 s at 270 K.

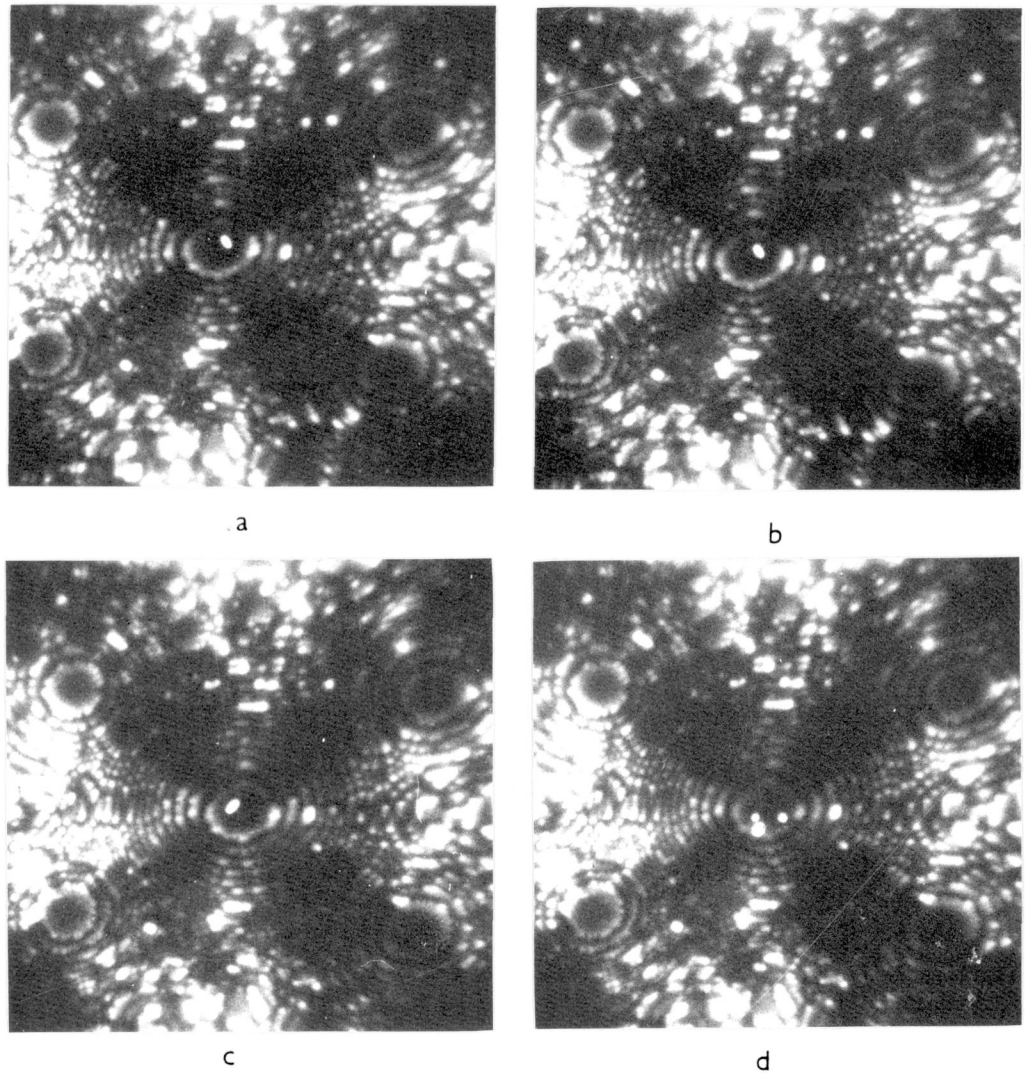


Figure 5.22 Micrographs showing the migration and dissociation of a Rh trimer on Mo(110). (a)-(c) Diffusion of the trimer showing displacement of the cluster centre of mass and reorientation in successive heating periods at 300 K. (d) Dissociation of the trimer after 60 s at 320 K.

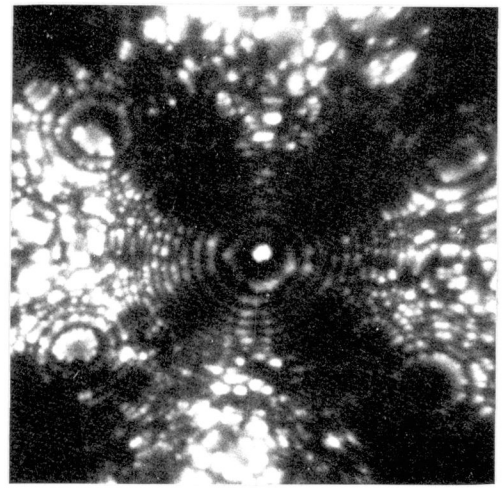
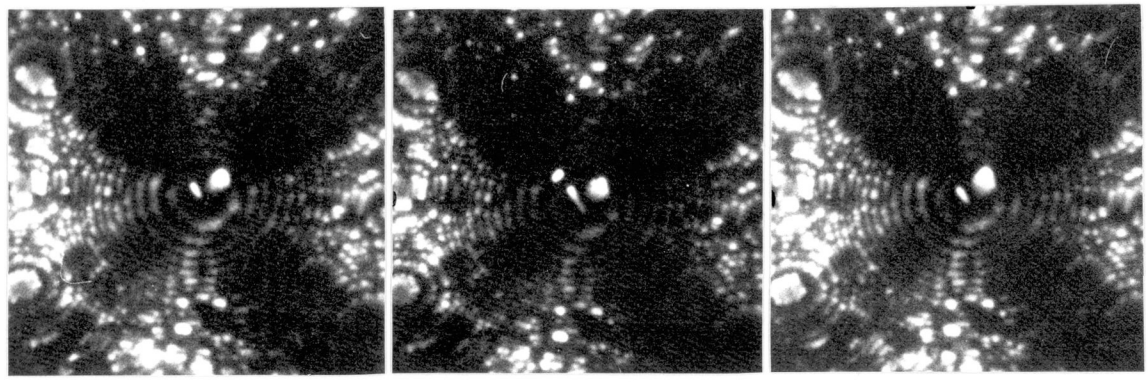


Figure 5.23 A two-dimensional rhodium island on Mo(110) formed after facile transformation of the linear chain cluster of figure 5.19 at 330 K.



a b c

Figure 5.24 (a) Formation of a small chain-cluster after further deposition at 78 K onto the deposit of fig. 5.23 followed by annealing at 290 K. (b) Growth of the chain-cluster and two-dimensional island in (a) by further deposition and heating at 290 K. (c) Partial dissociation of the chain-cluster after 60 s at 325 K; the detached adatoms appear to have been "engulfed" by the two-dimensional cluster.

5.2.3 Film growth

During deposition the formation of Rh chain clusters preceded the appearance of two-dimensional islands as found for Rh on W(110). However, conversion of linear to two-dimensional clusters of more than ten adatoms resulted in the appearance of islands at a very early stage compared to Rh on W(110). The comparable stability of small chain clusters and islands on Mo(110) often resulted in the appearance of new chain clusters even after island nucleation (figure 5.24). Such chains disappeared only as they became engulfed by the growing islands or after reaching the critical length, converted to two-dimensional forms upon annealing at about 330 K. Figure 5.25 shows the formation of multiple islands on Mo(110) after chain to island transformation upon annealing at >330 K. Single large islands could be generated by annealing at 420 K (figure 5.25). Continuing deposition resulted in the formation of continuous films that appeared to replicate the features of the Mo substrate, as found for Rh on W(110).

The temperatures at which islands rearranged or lost atoms were established and are given in table 5.2. Sharp images of Rh islands were seldom obtained and the atomic structure within islands could not be resolved. The measured angles between island edges and the substrate $<1\bar{1}0>$ direction showed a large scatter with no edge parallel to a major substrate direction. This makes it difficult to speculate upon the structure of Rh islands on Mo(110). However the close-packed nature of the islands is indicated by the fact that second layer Rh adatoms were never observed, presumably due to the high mobility of Rh adatoms deposited on top. As pointed out in section 5.1.4, Rh adatoms on Rh(111) surface are known to have considerable mobility at liquid N_2 temperature. Just as for Rh on W(110), Rh islands on Mo(110) often exhibited discontinuities in island images at points where

two islands had grown into contact (figure 5.26), indicating that multiple positioning of islands is possible.

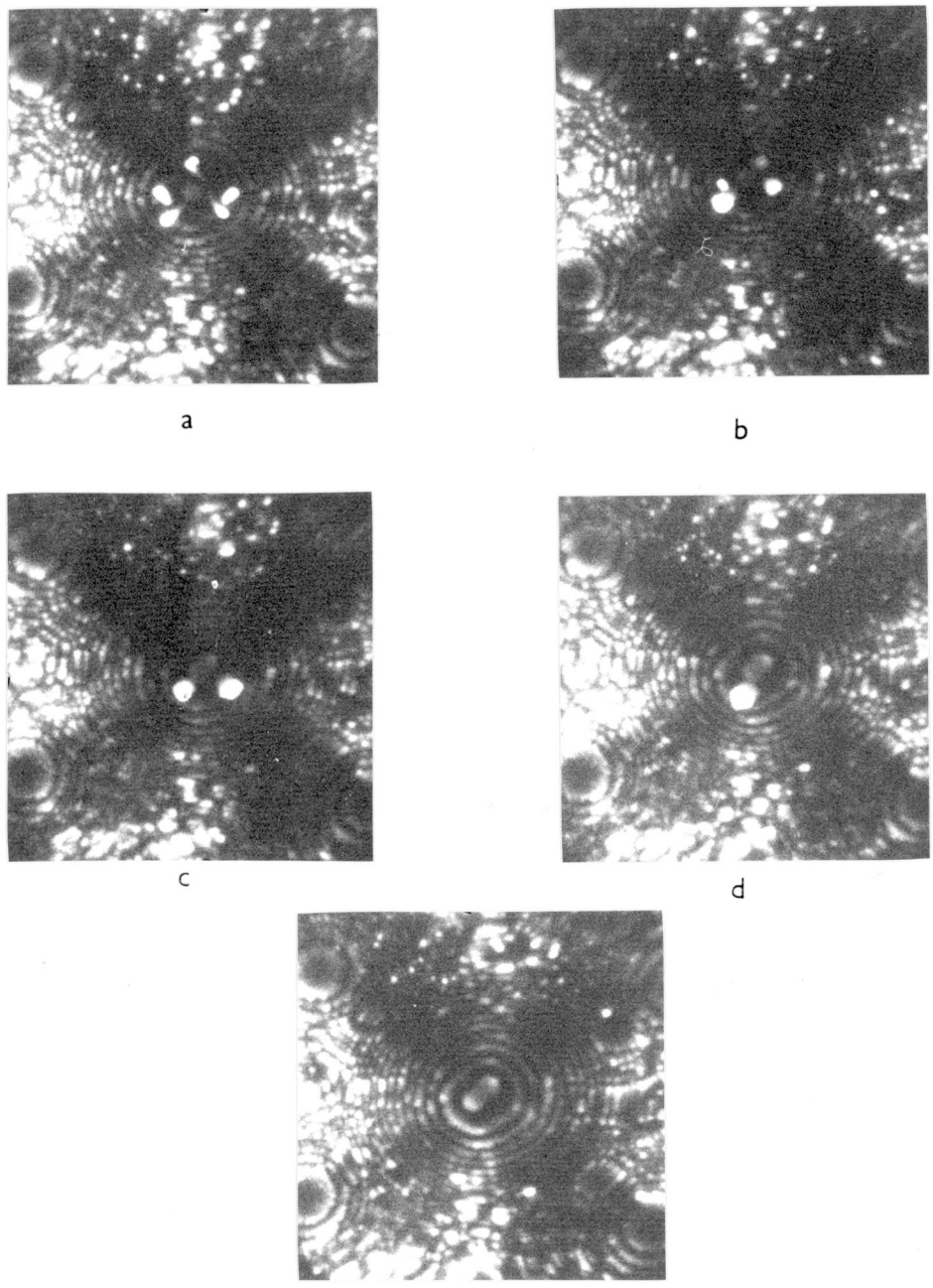


Figure 5.25 Micrographs showing the formation and growth of rhodium islands on Mo(110). (a) Chain-clusters formed after deposition of Rh at 78 K followed by annealing at ∿300 K. (b) Facile transformation of chain to island forms after 60 s at 330 K. (c),(d) Migration and growth of the islands after 60 s at 370 K. (e) Coalescence of the clusters to a single large island after 60 s at 430 K.

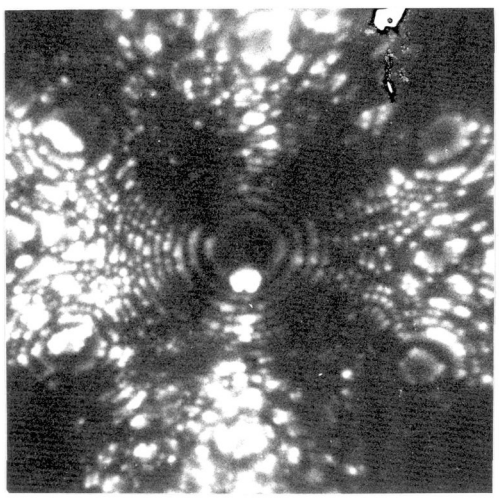


Figure 5.26 A Rh island with an internal interface formed after two islands came into contact.

6. EXPERIMENTAL STUDIES BY LOW ENERGY ELECTRON DIFFRACTION AND AUGER ELECTRON SPECTROSCOPY: RESULTS AND INTERPRETATION

To complement the atomic-scale studies made with the field ion microscope, the growth of vapour-deposited rhodium films on the (110) surfaces of both tungsten and molybdenum single crystals has been examined by AES and LEED, using the procedures outlined in chapter 4. Experiments were carried out to determine how the surface structure indicated by the LEED pattern varied with the rhodium coverage and with the heat treatment used during and after deposition of the rhodium film. In the majority of experiments rhodium was deposited on clean W or Mo surfaces, but a small number of experiments were carried out with the W or Mo surface covered with an adsorbed layer of either oxygen or carbon monoxide, in order to examine the extent to which these common contaminant gases could modify the film growth behaviour.

6.1 Rhodium on Tungsten

6.1.1 AES Characterization of Rh film growth

The Auger spectrum of the initial 'clean' surface is shown in figure 6.1a with the positions of Auger transitions for W, C and O marked from which it is evident that the last two were absent. An Auger spectrum of the W(110) with about a monolayer of Rh is shown in figure 6.1b. The coverage was estimated by using the procedure outlined in section 4.3.10, chapter 4. The observed energies of the major Auger transitions from the Rh overlayer are presented in Appendix A. The C(KLL) emission at 275 eV lies between the major Rh emissions at 260 eV and 306 eV. Because the C emission in the derivative

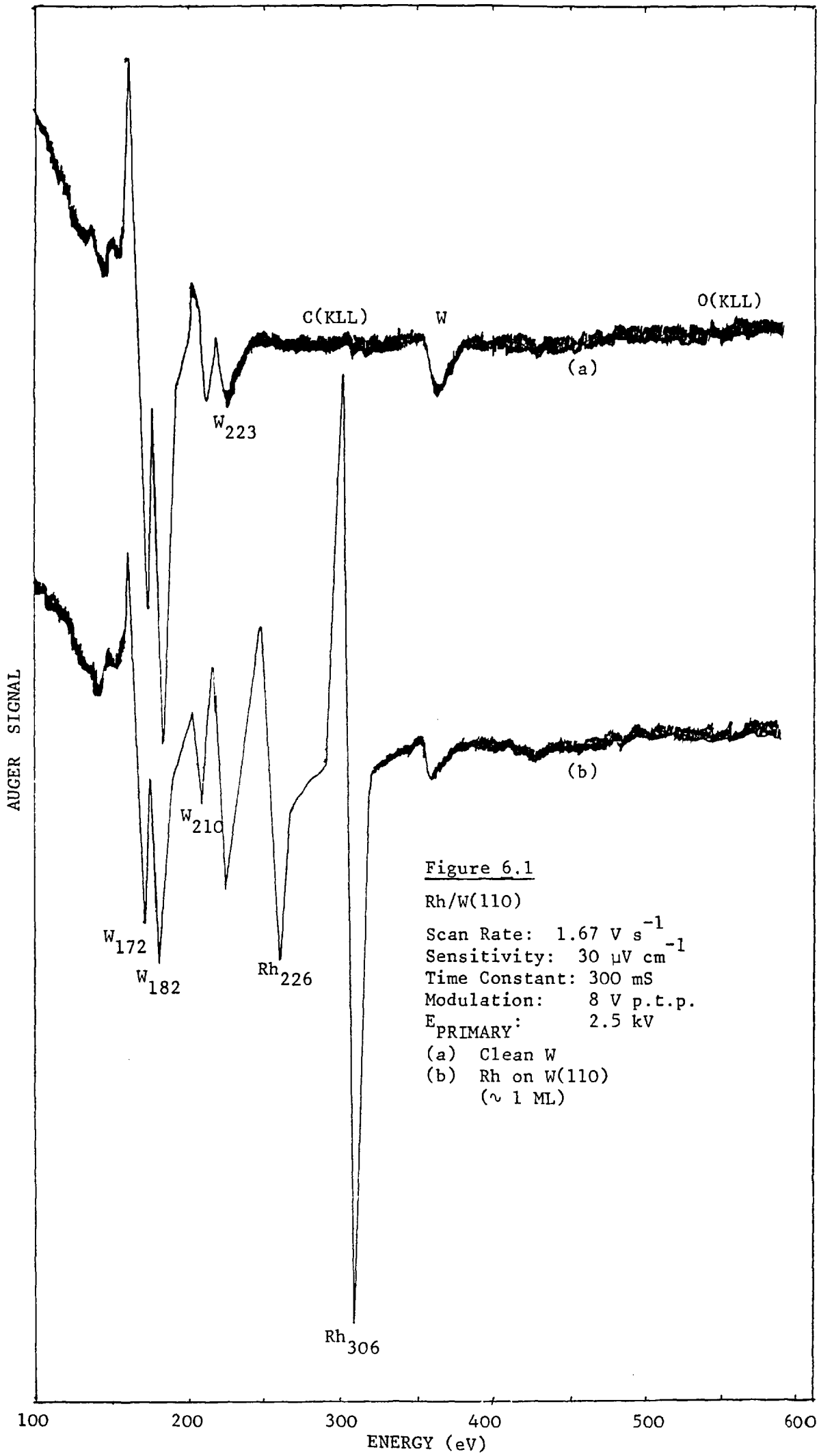


Figure 6.1

Rh/W(110)

Scan Rate: 1.67 V s^{-1}
Sensitivity: 30 μV cm^{-1}
Time Constant: 300 mS
Modulation: 8 V p.t.p.
$E_{PRIMARY}$: 2.5 kV
(a) Clean W
(b) Rh on W(110)
(∿ 1 ML)

Auger spectra is asymmetrical with a strong negative going slope, its presence in the Rh spectra is easily detected by the appearance of a noisy "dip" between the Rh emissions. This is clearly demonstrated in figure 6.2 which was taken after Rh was deposited from an inadequately degassed evaporator, resulting in CO contamination of the surface.

Comparisons of figures 6.1a and 6.1b shows that the Rh MNN emissions at 174 eV, 208 eV and 226 eV overlap the major W NNN emission at 172 eV and NNO emissions at 210 eV and 223 eV, respectively. To monitor Rh coverage by means of Auger signal versus time plots (AST), therefore, the peak-to-peak heights of the W NNN emission at 182 eV and the Rh MNN emission at 306 eV were measured. Both these emissions are well separated from the other emissions and therefore easily measured.

Figures 6.3a and 6.3b show the AST plots obtained at three different deposition temperatures. The deposition time for the completion of the monolayer, as calculated from the escape depth of the W Auger electrons in the Rh overlayer (Section 4.3.10, Chapter 4), is indicated. Due to noise in the AST plots sharp breaks expected at the completion of the monolayer for the usual Stranki-Krastanov or Frank-Van der Merwe growth mode are not observed. The noise is too random to be associated with any peculiar growth mode, such as the incomplete Frank-Van der Merwe growth observed for Au on Mo(110)[73], or to changes in the sticking probability associated with changes in the adsorbate structure with increasing coverage[72]. In the present case the noise can be attributed to two sources:

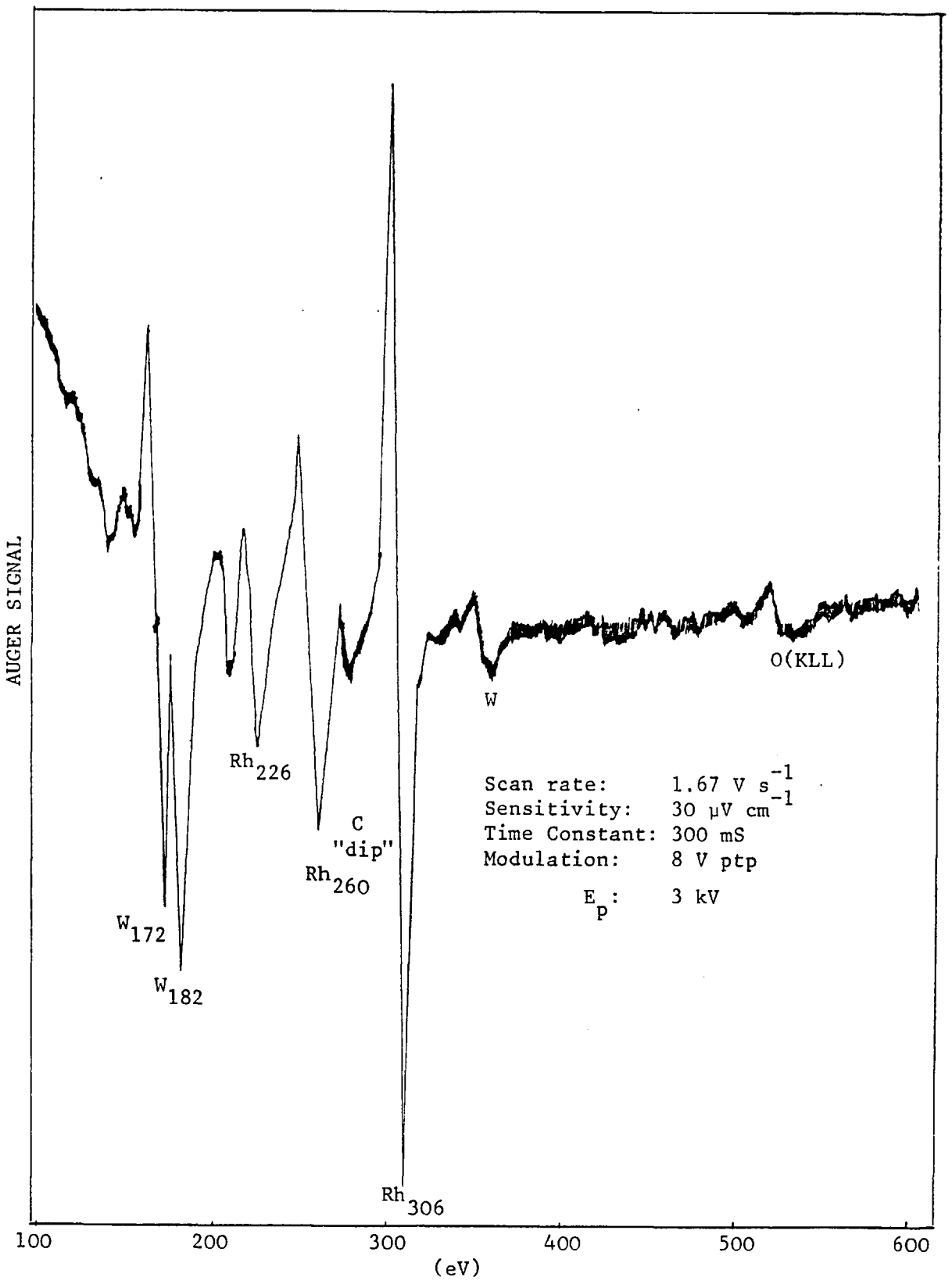


Figure 6.2 Auger spectra from W(110) after deposition of Rh and CO contamination from an inadequately degassed evaporator.

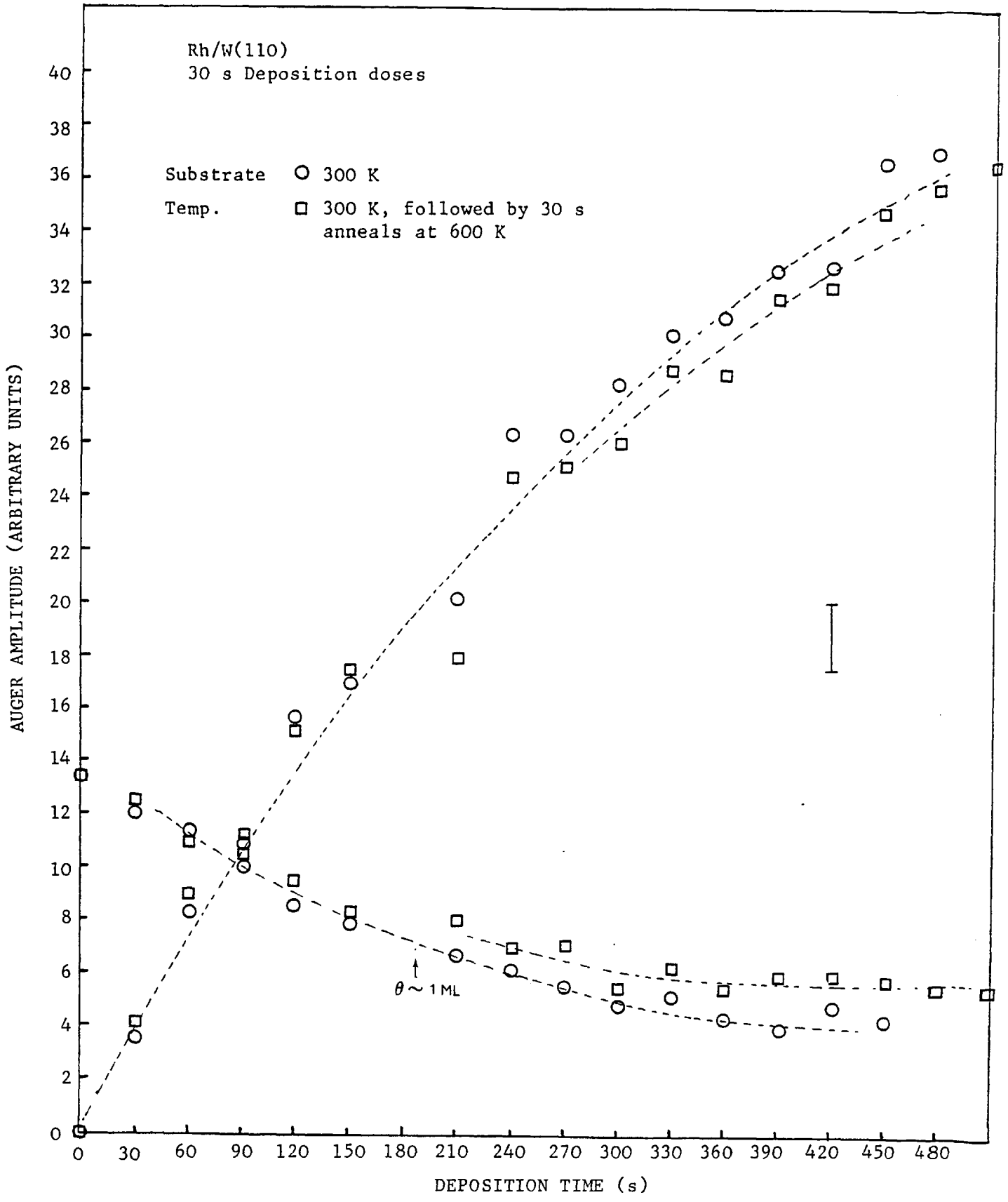


Figure 6.3a Plots of Auger amplitude versus deposition time.

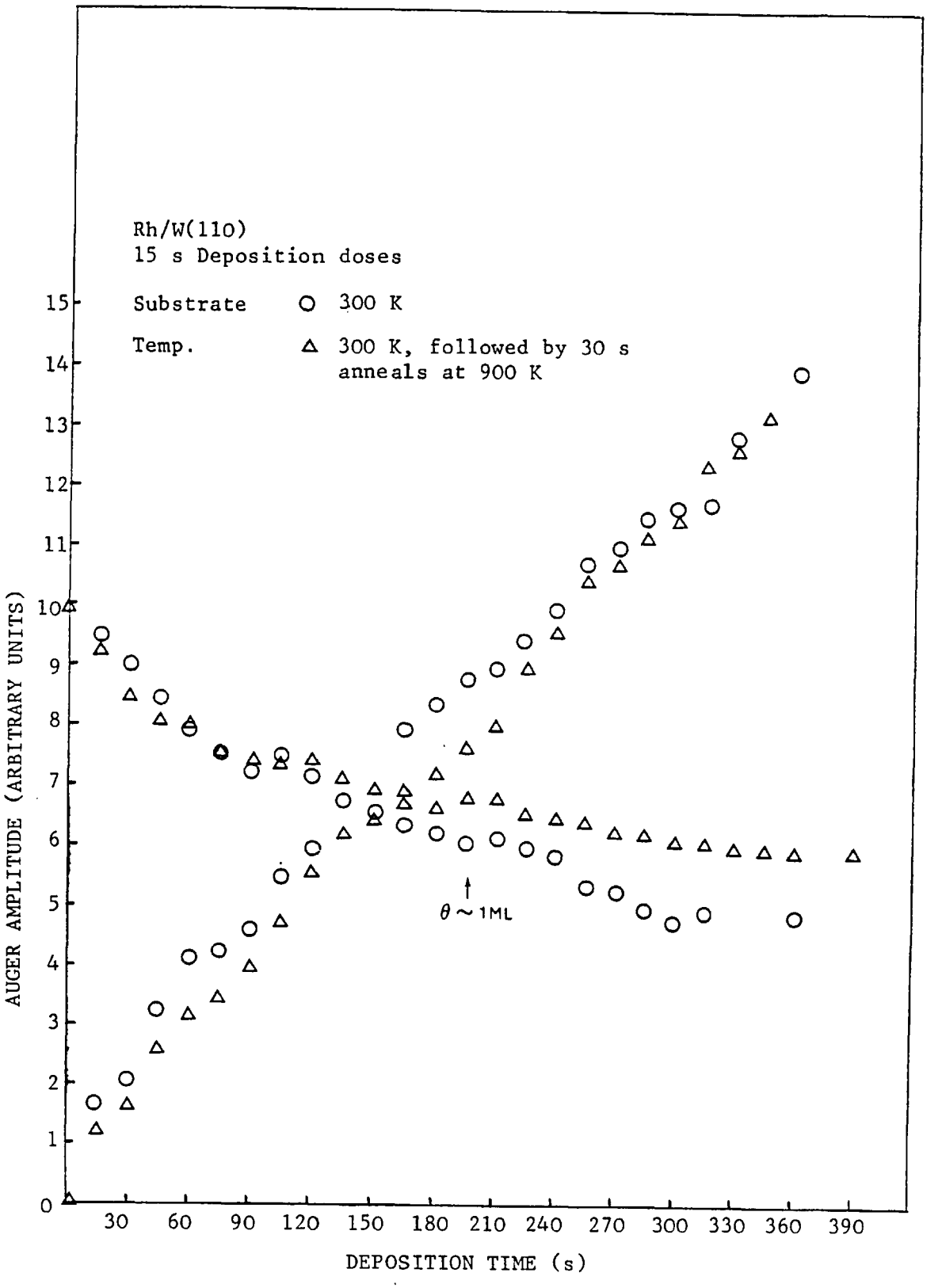


Figure 6.3b Plots of Auger Amplitude versus deposition time.

(i) A dependence of the Auger signal on the exact positioning of the specimen in front of the analyser after each deposition dose. Moving the specimen holder from the evaporator position to the analyser position often caused a slight change in the specimen tilt with respect to the primary electron beam.

(ii) Changes in the vapour flux with each deposition dose. This is confirmed in fact by FIM observations which showed that the number of atoms deposited on the tip surface varied considerably with each dose. This is especially true for an evaporator wire which has been used a lot and has consequently become thin in parts.

Qualitatively, the general form of the curves is in agreement with those obtained by Bauer and coworkers, for example, for Pd on W(110)[59]. Up to at least completion of the first layer, two-dimensional growth occurs as deduced from the initial decrease of the W Auger peak-to-peak height. For higher coverages and elevated temperatures the Rh Auger peak-to-peak height increases and the W Auger peak-to-peak height decreases less rapidly with increasing deposition time than for deposition at room temperature. It is tentatively suggested that this is indicative of the formation of three-dimensional crystallites for Rh in excess of the first monolayer. Diffusion of Rh toward the side or back of the crystal and diffusion into the crystal as the cause for the slow decrease of the W Auger peak-to-peak height could be ruled out since (i) diffusion measurements (appendix C) indicated that the Rh does not diffuse significantly over the crystal surface and (ii) no Rh could be detected in the Auger spectrum after thermal desorption of the overlayer. Some evidence for the formation of three-dimensional crystallites at elevated

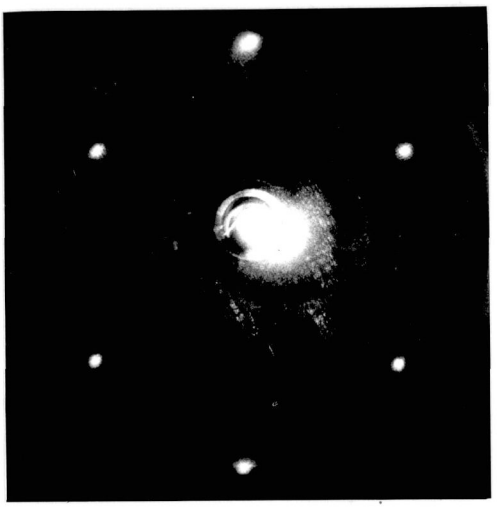
temperatures came from the LEED observations described in the following sections.

6.1.2 LEED Observations of Rh Overlayer structures

Figure 6.3 shows the LEED patterns, at different primary electron energies, of the initial clean surface. The reciprocal and real lattice unit cells of the W(110) surface are shown schematically in figures 6.4a and 6.4b, respectively.

(a) Room temperature deposition.

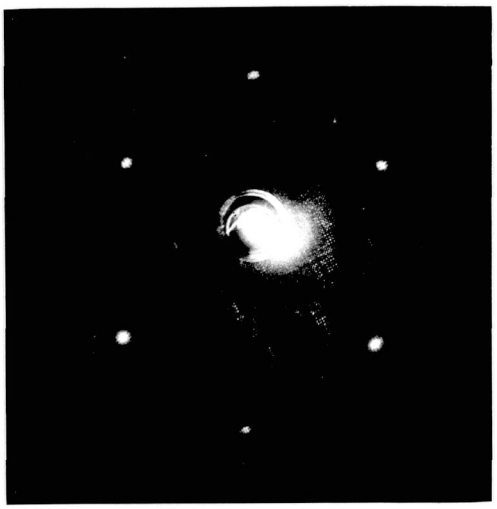
Rhodium deposited at room temperature produced a considerable increase in the LEED pattern background, which suggests considerable disorder on the surface. Similar behaviour has been reported for Au on W(110)[62] and Mo(110)[158] and Pd on W(110)[59]. With increasing coverage the W(110) spots appeared to lose intensity, and gradually faded away, while unsharp spots due to a Rh(111) layer appeared at an estimated coverage of over 5 monolayers. Sharp diffraction features were not observed at this stage since the overlayer lacked sufficient order. On heating the specimen at 1000 K, intensity in the background decreased and the Rh spots became sharp, indicating that the size of the ordered domains had increased. The LEED pattern corresponding to this structure is shown in figure 6.5. The reciprocal and real lattice unit cells of the Rh(111) surface are shown schematically in figures 6.6a and 6.6b, respectively. On heating the specimen at or above 1500 K the original W(110) spots reappeared due to partial desorption of the Rh, figure 6.7. The relative position of the spots shows that the Rh(111) lies parallel to W(110) with $Rh\langle 1\bar{2}1\rangle \| W\langle 1\bar{1}0\rangle$. The observed orientation relationship is shown schematically in figure 6.8. In the



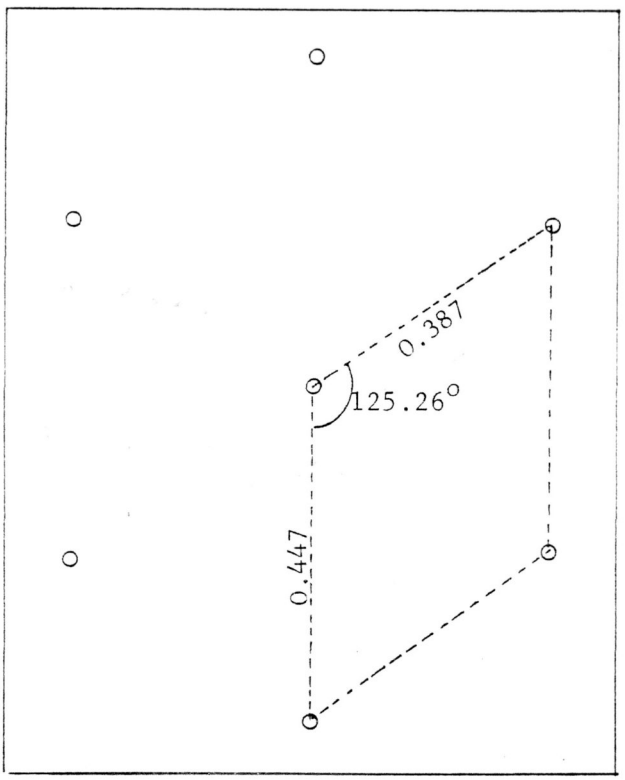
(a)



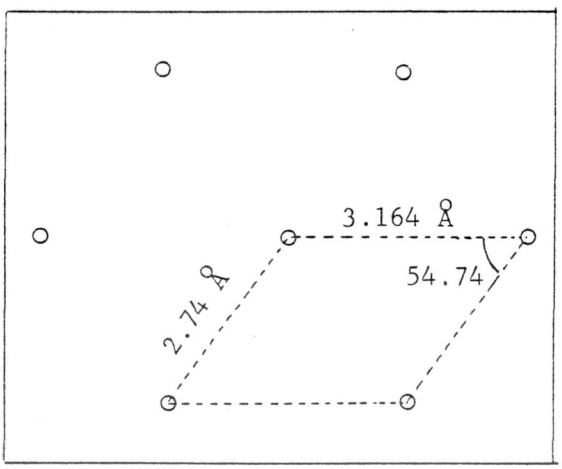
(b)



(c)



(d)



(e)

W<1$\bar{1}$0>

Figure 6.4 LEED patterns from clean W(110): (a) 64 V, (b) 70 V (e) 96 V; (d),(e) Reciprocal and real lattice unit meshes, respectively, for W(110).

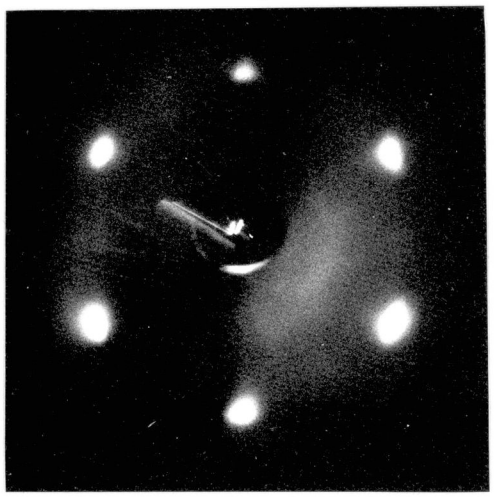


Figure 6.5 LEED pattern from W(110) after deposition of >5 ml of Rh at 300 K followed by annealing at 1000 K. The spots are due to Rh(111). (70 V).

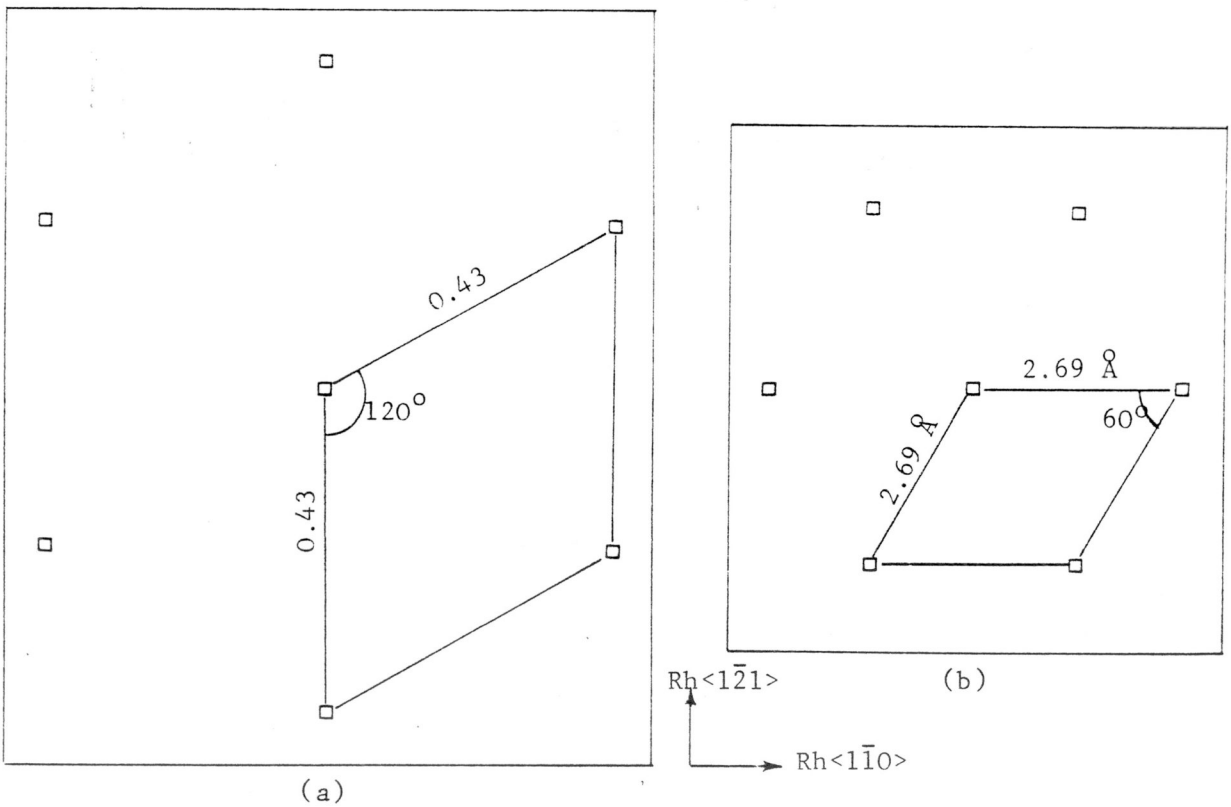


Figure 6.6 Reciprocal (a) and real (b) lattice unit meshes of the Rh(111) surface.

W<1$\bar{1}$0> direction, the bulk Rh lattice mismatch is approximately 4% while in the W<100> direction it is approximately 15%. This means that in the W<1$\bar{1}$0> direction, the W and Rh diffraction spots almost coincide and are difficult to distinguish clearly, as can be seen in figure 6.7.

(b) Effect of heating after deposition

Rh adsorption layers with coverage of approximately 0.3 monolayers, deposited at room temperature with subsequent annealing at 450-600 K after each deposition step, showed streaking in the W<111> directions between the spots of the W(110) pattern, figure 6.9. The streaks were sharper, the higher the annealing temperature. The extent of streaking between the W spots varied; in some experiments almost full streaking between the spots was observed, while in others, intensity at the half-order positions along the streaks was higher than nearer the W spots. The occurrence of streaks in the LEED patterns at low coverages is consistent with the formation of Rh adatom chains oriented along the W<111> directions with an adatom spacing equal to that in the substrate close-packed directions. Similar behaviour was observed in LEED studies of Ir on W(110)[159] which, like Rh, also forms linear chains oriented along the close-packed directions[44,157]. Figure 6.10 shows two possible mechanisms, involving anti-phase domains in the chain structures, for the formation of streaks in the LEED patterns. In model one (figure 6.10a) close-packed chains are formed in the W<111> directions with adatoms in each chain placed on lattice sites and adjacent <111> rows unoccupied. The adatoms within a domain are then in a (2×1) arrangement, as indicated in figure 6.10a. Anti-phase domains are then formed with boundaries indicated by the dashed line

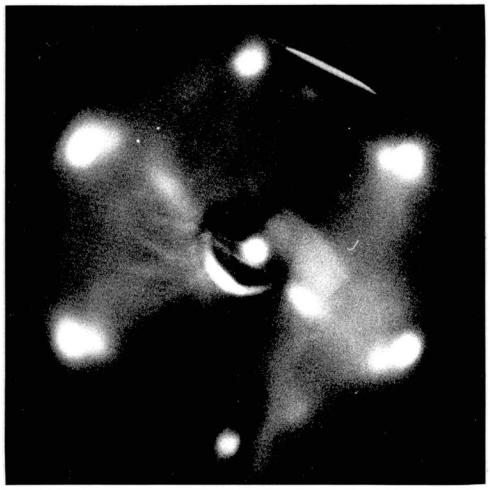


Figure 6.7 LEED pattern of Rh on W(110) after partial desorption of the Rh(111) overlayer of figure 6.5.

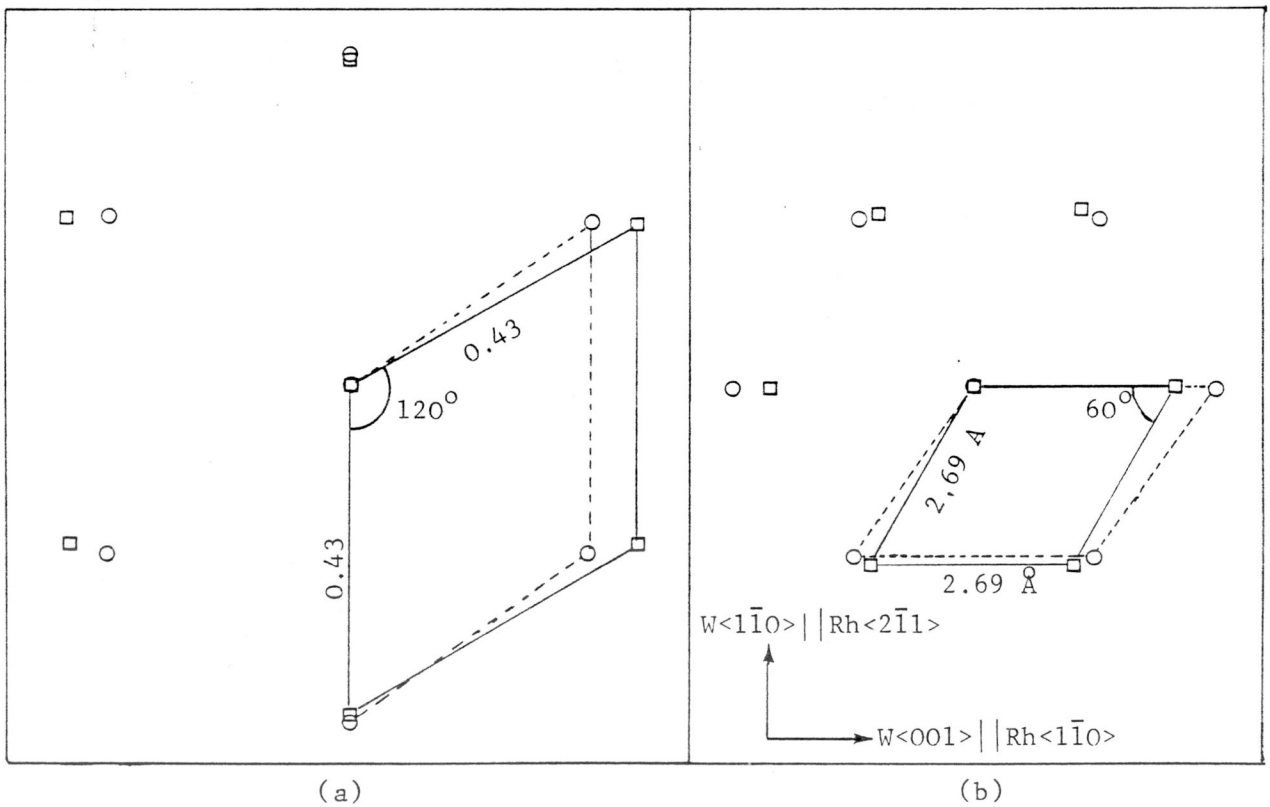


Figure 6.8 Reciprocal (a) and real (b) unit meshes corresponding to Rh(111)||W(110) in the Nishiyama-Wassermann orientation. Solid lines: Rh unit mesh; dashed lines: W unit mesh. This is the proposed structure producing the LEED pattern of fig. 6.7.

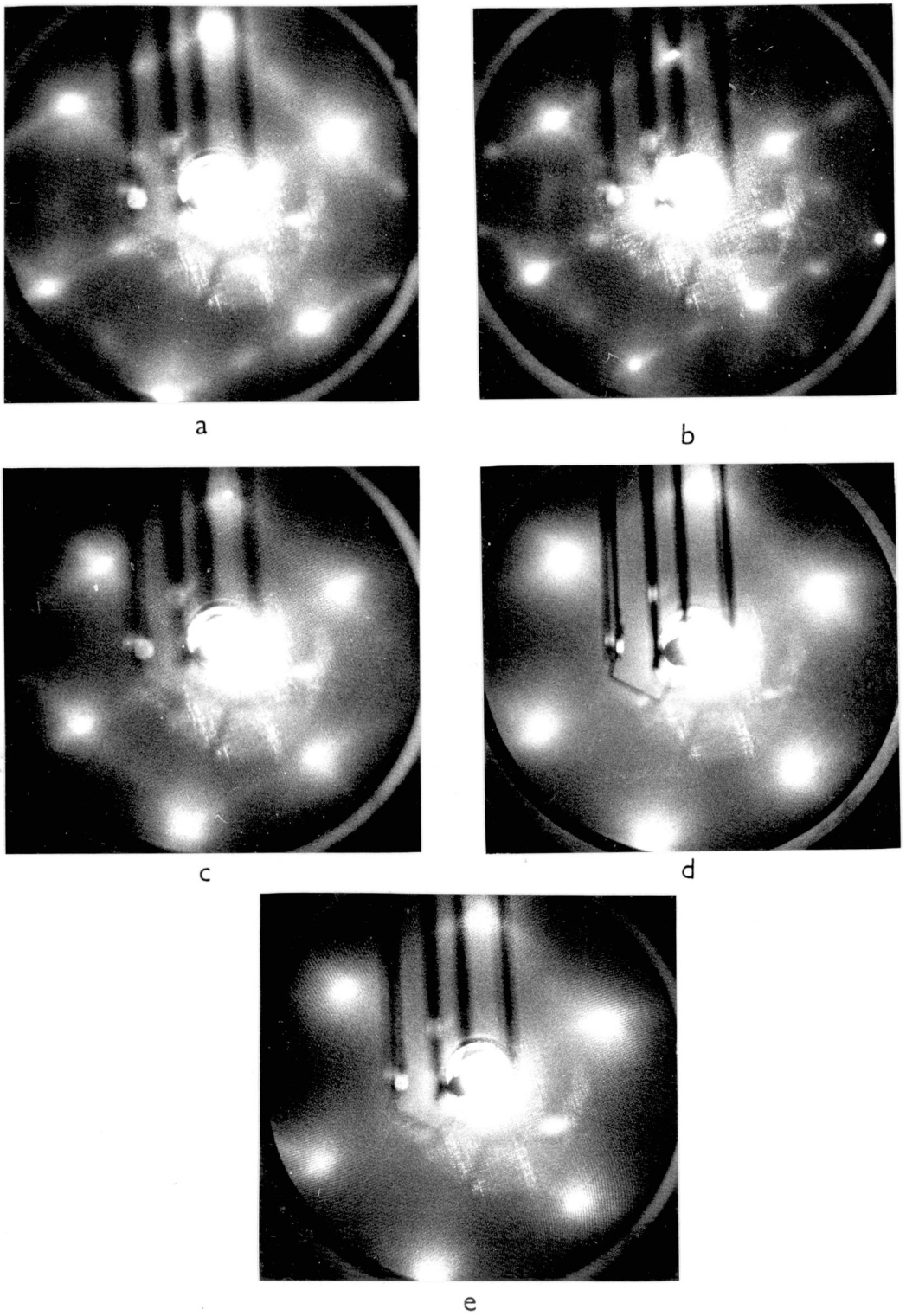


Figure 6.9 LEED patterns from Rh on W(110) after deposition in small doses at 300 K followed by annealing at 500 K. (a),(b) at ∿0.3 ml, showing streaks associated with Rh linear chains (66 V, 90 V); (c-e) diffuse (|x|) patterns with high background intensity with further deposition up to ≳1 ml.

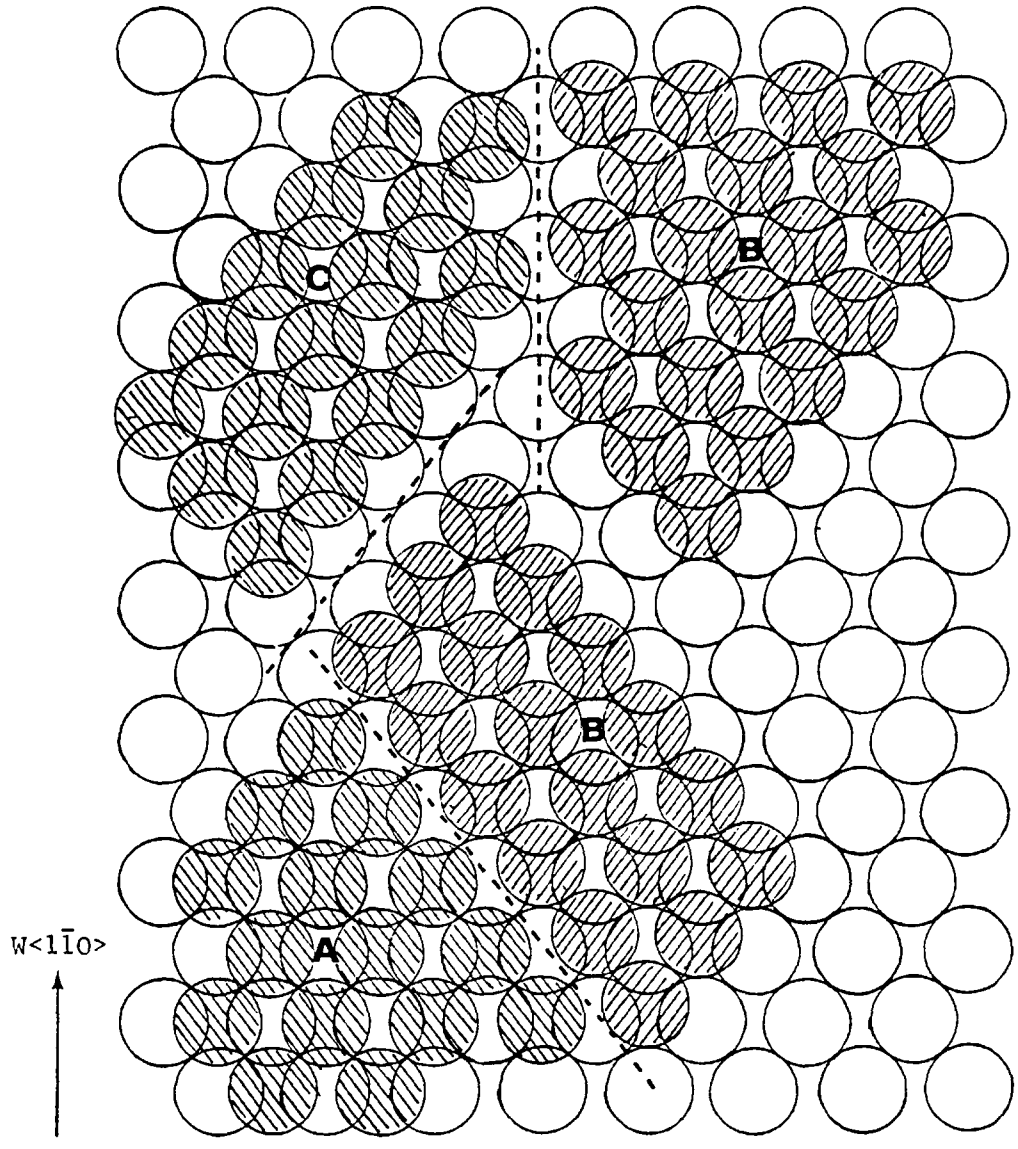


Figure 6.9g Schematic diagram showing domains of a pseudomorphic overlayer (shaded circles represent adatoms) on the W(110) surface (open circles). The domains are separated by anti-phase boundaries represented by the broken lines. This is possible on bcc (110) because adatoms can occupy lattice sites (domain A) or one of the two equivalent surface sites (domains B,C).

in figure 6.10a. Since both close-packed directions on W(110) are equivalent, chains can form along both the close-packed directions, resulting in half-order streaking in the LEED patterns. In model two, close-packed chains are formed in the W<111> directions with adatoms within each chain placed on one of three different sites in W(110) unit mesh, (two equivalent surface sites and one lattice site, figure 5.3, chapter 5), as indicated in figure 6.10b. Topographical adsorption energy plots for Cu[56] and Au[62] on W(110), calculated using pairwise interaction models, shows that the adatoms can sit on the W(110) surface with considerable degree of freedom to move in the troughs along the $<1\bar{1}0>$ direction. Thus, alternate chains can be randomly shifted relative to each other in the W$<1\bar{1}0>$ direction, resulting in adjacent chains having a variable distance between them. Anti-phase domain boundaries run parallel to the chain axis between adjacent chains. A similar model was proposed by Gerlach and Rhodin to interpret the streaking observed in the LEED patterns from Na on Ni(110), as discussed in section 3.1.3, chapter 3. The hard sphere model of figure 6.10b has a non-planar adlayer since chains with adatoms at lattice sites are raised above the surface plane relative to chains with adatoms at surface sites. However, it is possible that adatom relaxations cause the adlayer to become planar.

The two models proposed here to explain the streaking in the LEED patterns for low coverage Rh have been tested by laser-simulation experiments[160]. For convenience of drawing the simulation structures, domains with linear chains in only one close-packed direction were considered. Dot arrays, each containing over a thousand points in an area $\sim$10 cm × 10 cm, were drawn on transparent sheets of paper and photographed from a distance of 3-5 m. This gave negative images

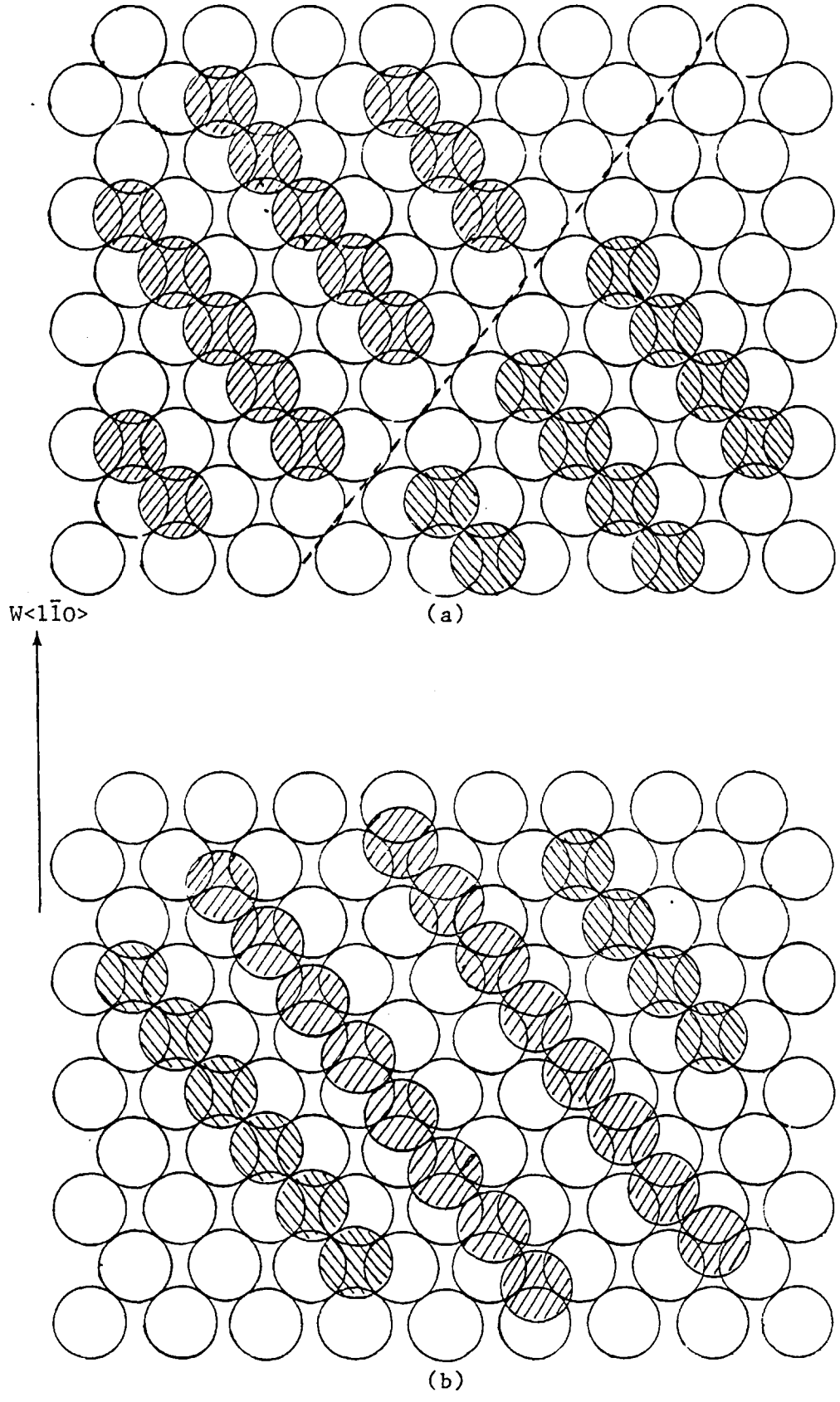


Figure 6.10 Proposed models of antiphase linear-chain structures. The inter-atomic spacing within chains is equal to the nearest neighbour tungsten spacing.
(a) Adatoms at lattice sites, forming (2×1) domains with anti-phase boundary indicated by the dashed line;
(b) Adatom-chains shifted randomly in the W<1$\bar{1}$0> direction.

(masks) ∿3 mm × 3 mm with clear spots representing atoms of the surface structure model. A light beam from a small He-Ne laser was shone through the negatives and the diffraction patterns displayed on a screen. The results are shown in figure 6.11. The laser-simulation diffraction patterns show streaking in the <111> directions for both the models. Half-order streaking was observed for model one (figure 6.11b), while model two gave integral order streaking (figure 6.11c). Observation of half-order as well as full streaking in the LEED patterns for low coverage Rh (and for Ir on W(110)) suggests that both types of chain structures are possible.

On further deposition, the streaks faded in intensity (figure 6.9c) and finally disappeared while the W(110) spots became broad (figures 6.9c-f). Quantitative studies of spot broadening during the initial stages of epitaxy of tungsten on W(110) have recently been made by Hahn and coworkers[54]. By measuring the angular profiles of the spots as a function of electron energy they were able to interpret spot broadening as due to the formation of a high density of small islands with anti-phase boundaries within the coherence area of their instrument. This is possible on the (110) surface even for a pseudomorphic overlayer since there can be more than one position within the (110) unit mesh. Figure 6.9g shows possible arrangement of anti-phase domains on W(110). It seems likely that the spot broadening observed in the present work is due to the formation of a high density of differently-positioned islands with anti-phase boundaries between them. With the coverage approaching one monolayer the diffraction spots were no longer uniformly broad but slightly elongated in the W<100> direction. W(110) spot broadening, with possible unresolved features near the tungsten spots, indicates that the monolayer islands of Rh on W(110) are very nearly

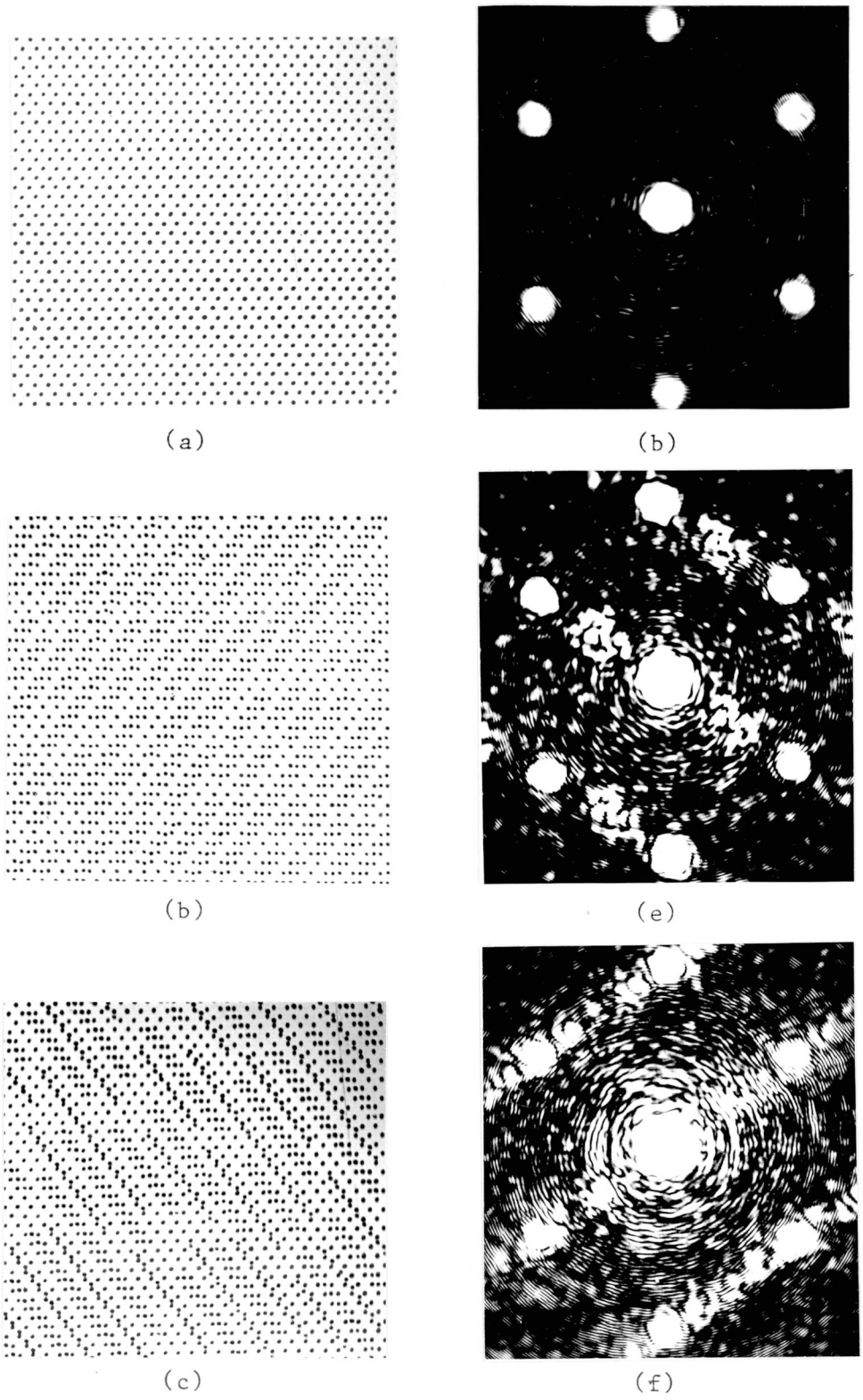
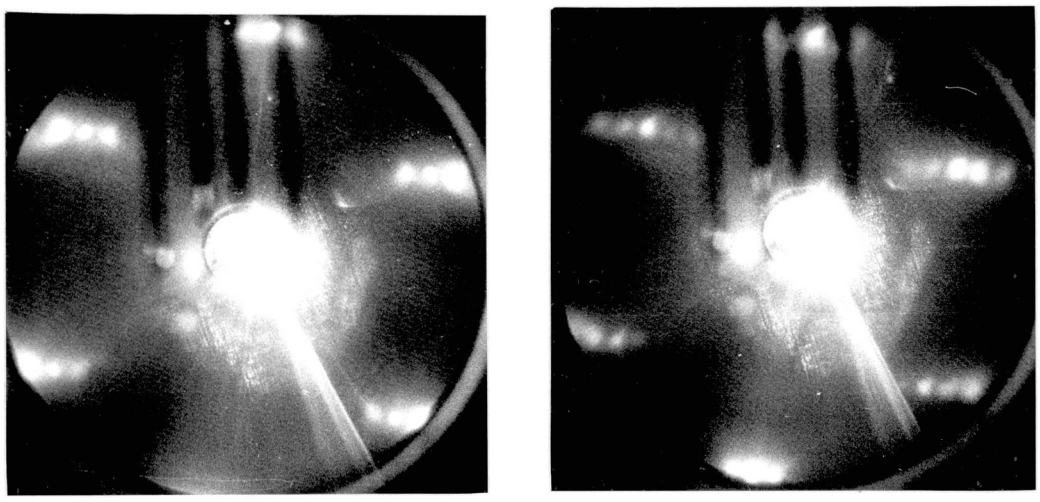


Figure 6.11 Laser simulations. (a)-(c) Simulation masks corresponding to the W(110) structure, linear chain structure model of fig. 6.10a, and the structure of fig. 6.10b, respectively. (d)-(e) Laser diffraction patterns corresponding to the structures (a)-(c), respectively.

pseudomorphic with the substrate. It is possible that the pseudomorphic type islands form at sites where chain structures (figure 6.10) along the two equivalent close-packed directions intersect. This mechanism of formation of two-dimensional islands of Rh on W(110) has been observed in FIM studies (cf. figures 5.11 and 5.12, chapter 5).

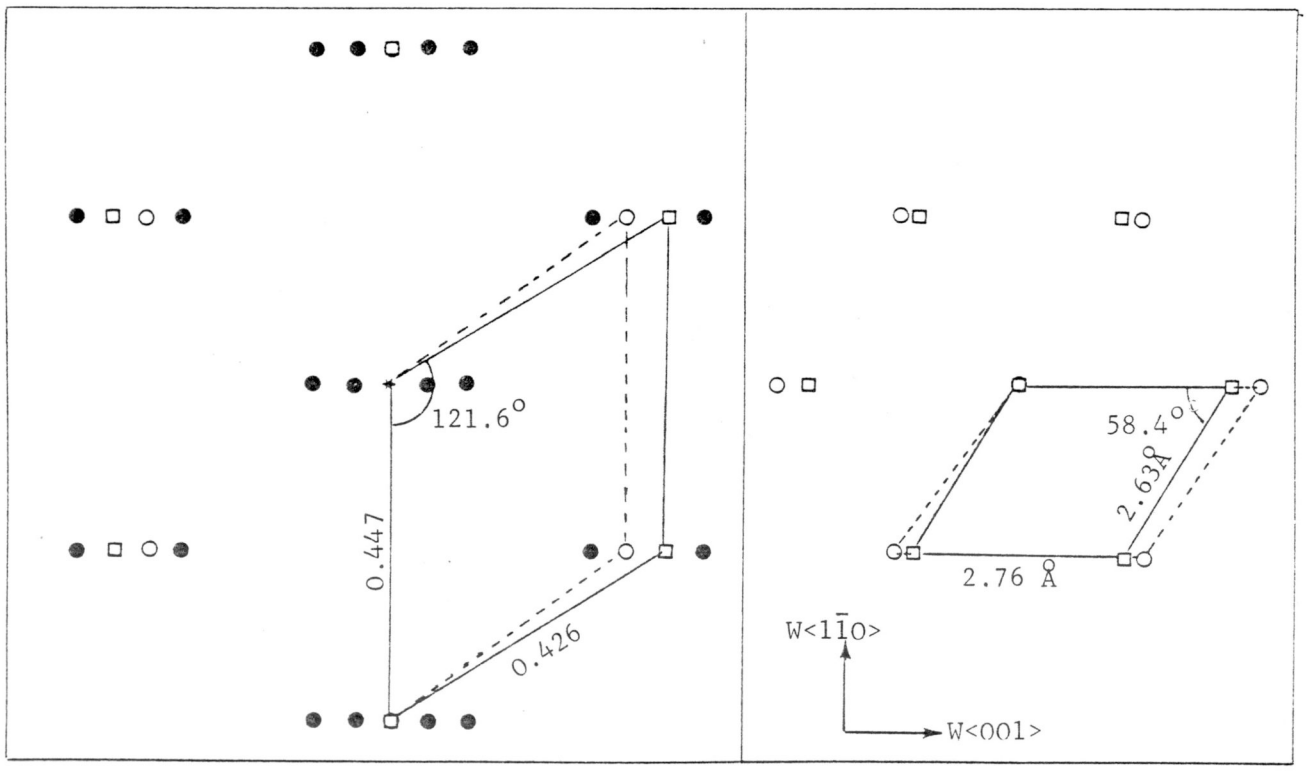
Deposition at 600 K beyond one monolayer coverage resulted in a sudden transformation of the LEED pattern with the appearance of well-resolved satellite spots which became sharper with continued deposition (figures 6.12a and 6.12b). A similar pattern is obtained for Cu on W(110)[55-57], and was first observed by Taylor[55], who interpreted it as due to Cu(111) with extra spots arising from multiple scattering between the copper and the underlying lattices (see section 3.1.4, chapter 3). Following Taylor's interpretation, it is proposed that the LEED pattern of figure 6.12 arises from both a strained Rh(111) layer and multiple diffraction between the strained Rh(111) and underlying lattices. Measurements of the satellite spot spacing show that the rhodium structure has a repeat distance of tungsten along the W<1$\bar{1}$0> direction and a repeat distance of 2.76 Å along the W(100) direction. The Rh nearest neighbour distance is thus reduced to 2.63 Å compared to 2.69 Å in bulk Rh(111). Figure 6.13a shows a schematic diagram corresponding to the observed LEED pattern, with the reciprocal lattice unit cell outlined. The corresponding real lattice unit cell is shown in figure 6.13b.

Upon heating the specimen at 900 K the multiple beam pattern of figure 6.12 was destroyed and the pattern shown in figure 6.14 was obtained. A corresponding slight drop in the Rh peak-to-peak height in the Auger spectrum was observed. The multiple beam pattern could be restored with further deposition of Rh at 600 K, as shown in the sequence



(a) 54 V (b) 65 V

Figure 6.12 LEED patterns from W(110) after deposition of >1 ml of Rh at 600 K showing satellite spots associated with multiple diffraction between a strained Rh(111) layer and the underlying lattice.



(a) (b)

Figure 6.13 Reciprocal (a) and real lattice (b) unit meshes corresponding to the patterns of fig. 6.12. Solid lines: Rh unit mesh; dashed lines: W unit meshes; filled circles: "extra" multiple diffraction spots.

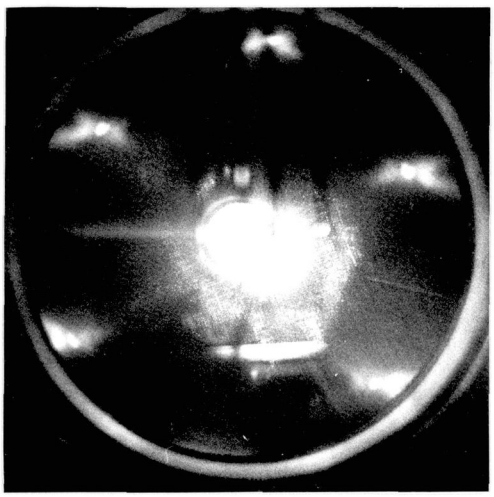
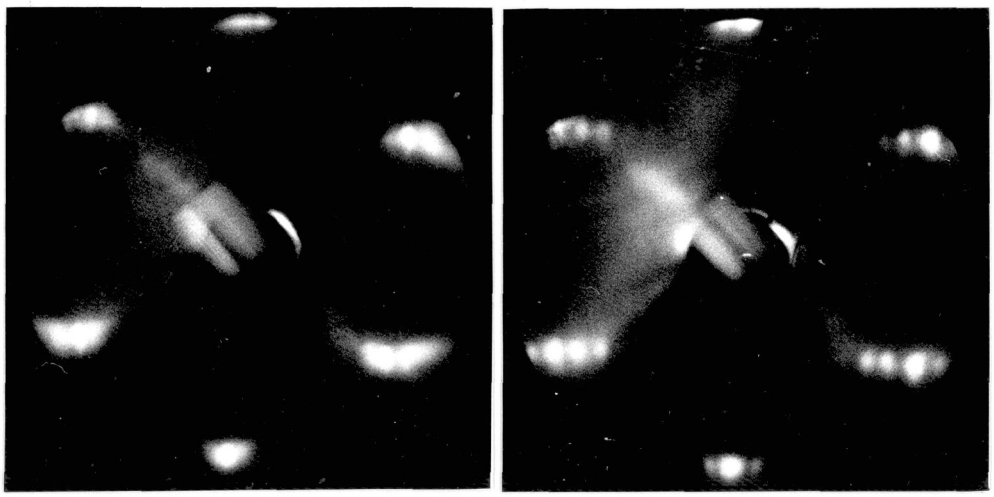


Figure 6.14 LEED pattern from Rh on W(110) obtained after heating at 900 K the surface producing the pattern of fig. 6.12. (54 V).



(a) (b)

Figure 6.15 The multiple diffraction pattern (fig. 6.12) was destroyed by heating the crystal at 900 K (a) and subsequently restored by further deposition at 600 K (b). (65 V).

of photographs of figure 6.15. This behaviour suggests that the strained Rh(111) structure proposed to explain the multiple beam pattern is in the form of two-dimensional islands which coalesce into three-dimensional crystallites after heating at 900 K. Further deposition then results in the growth of two-dimensional islands of the strained Rh(111) structure on top of the exposed parts between the three-dimensional crystallites.

With continued deposition at 600 K the Rh spots and the multiple diffraction spots of figure 6.12 gradually faded away and diffuse streaks appeared between the W(110) spots at a coverage of about two monolayers (figure 6.16a). After heating the specimen at 1100 K, the streaks and the tungsten spots became sharper while any remaining signs of Rh satellite spots disappeared. A corresponding decrease in the Rh Auger peak-to-peak height and an increase in the W Auger peak-to-peak height, by about 5%, was observed. (Significant change in the Auger peak-to-peak heights occurs only after 1500 K when significant desorption of Rh starts occurring.) Similar high coverage streaking at high annealing temperature has been observed for Ir on W(110)[159]. Figure 6.16b-f shows the effect of heating the specimen further at increasing temperature in the range 1100-1400 K. The streaks became sharper with increasing temperature until at 1400 K a transformation occurred in the LEED pattern. The streaks disappeared and the pattern of figure 6.16f was observed. This pattern is interpreted as due to Rh(111) crystallites double positioned on the W(110) surface. The epitaxial relationship is Rh(111)||W(110) with two equivalent orientations, Rh$\langle 1\bar{1}0\rangle$||W$\langle 1\bar{1}1\rangle$ and Rh$\langle \bar{1}10\rangle$||W$\langle \bar{1}11\rangle$. This orientation relationship is referred to as Kurdjumov-Sachs relationship (c.f. figure 1.7, chapter 1). The reciprocal and real lattice unit cells corresponding

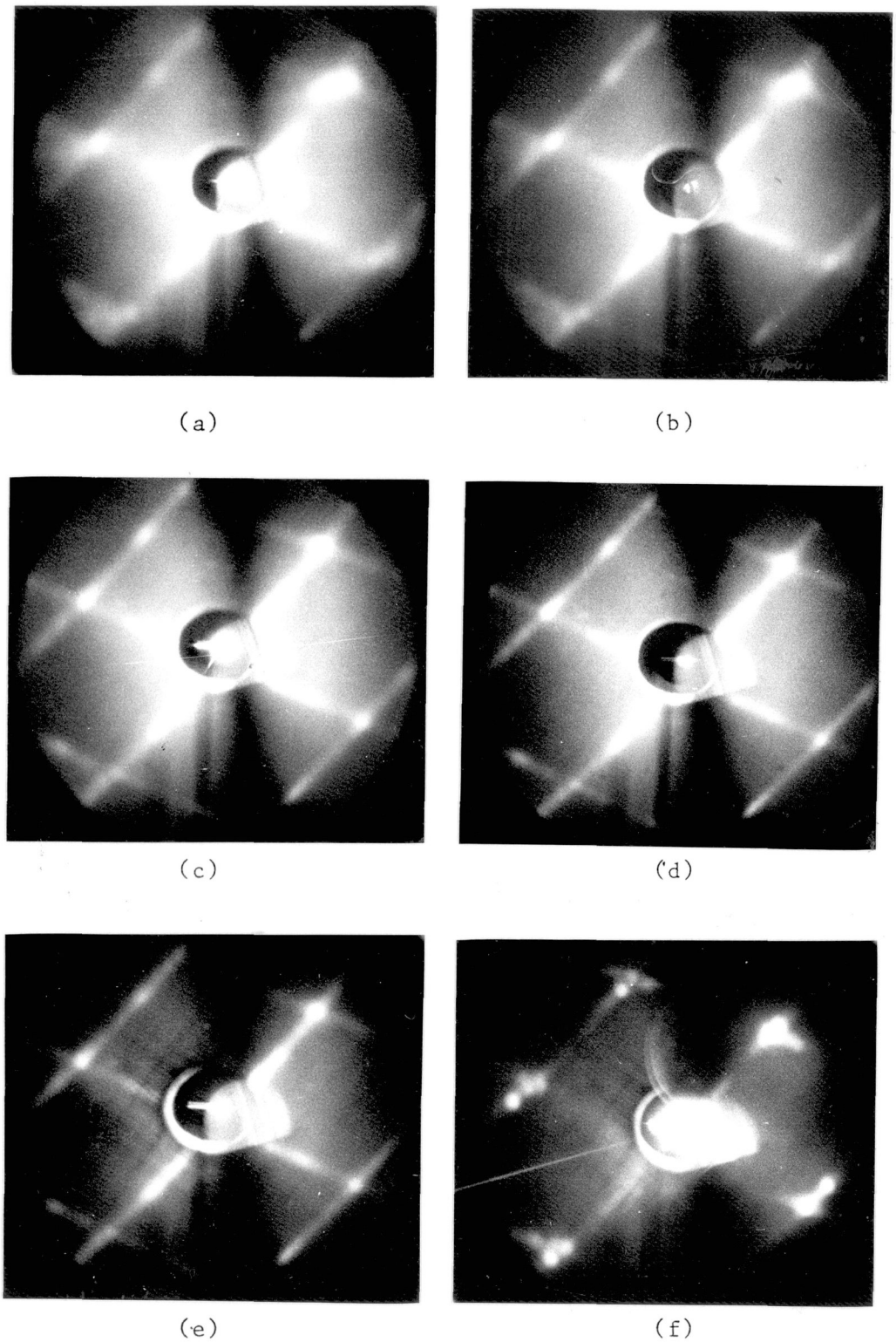


Figure 6.16 LEED patterns from Rh on W(110): (a) After deposition of ≥2 ml at 600 K; (b) after 20 sec. at 1100 K; (c) after 20 sec. at 1200 K; (d)(e) after successive heating periods at 1300 K; (f) after 60 sec. at 1400 K. (All at 74 V).

to the observed pattern of figure 6.16f are shown in figure 6.17a and 6.17b, respectively.

The gradual disappearance of the Rh and the multiple diffraction spots with the emergence of the streaks, while spots corresponding to the W(110) pattern remained visible, could suggest that the second layer strained Rh(111) structure of figure 6.13 transforms into three-dimensional crystallites with increasing coverage and temperature. The streaks (figure 6.16) could then be thought of as arising from a high density of three-dimensional crystallites of Rh(111) with anti-phase boundaries between them. A possible arrangement of Rh(111) crystallites on W(110) with an anti-phase boundary is shown in figure 6.18. At the highest temperatures before the onset of desorption, then, the anti-phase boundaries are removed as the crystallites rearrange and coalesce to give larger crystals of Rh(111)||W(110), with the effect that streaking in the LEED pattern disappears and well resolved Rh(111) spots appear, as in figure 6.16f.

6.1.3 Effect of oxygen on the growth of Rh films

Oxygen was admitted into the system following the procedures outlined in chapter 4. Figure 6.19a shows the half-order spots of the p(2×1) pattern of oxygen chemisorbed on the W(110) surface. The oxygen coverage for this pattern corresponds to 0.5 monolayers[161]. The corresponding Auger spectrum, showing the O(KLL) peak at 516 eV is shown in figure 6.20a. Rhodium was deposited on this surface at room temperature followed by anneals at 600 K after each dose. At a Rh coverage of about 0.3 monolayers, the half-order spots disappeared and, a broadening of the W(110) spots and an increase in the background was observed. The Auger spectrum indicated that the oxygen was still

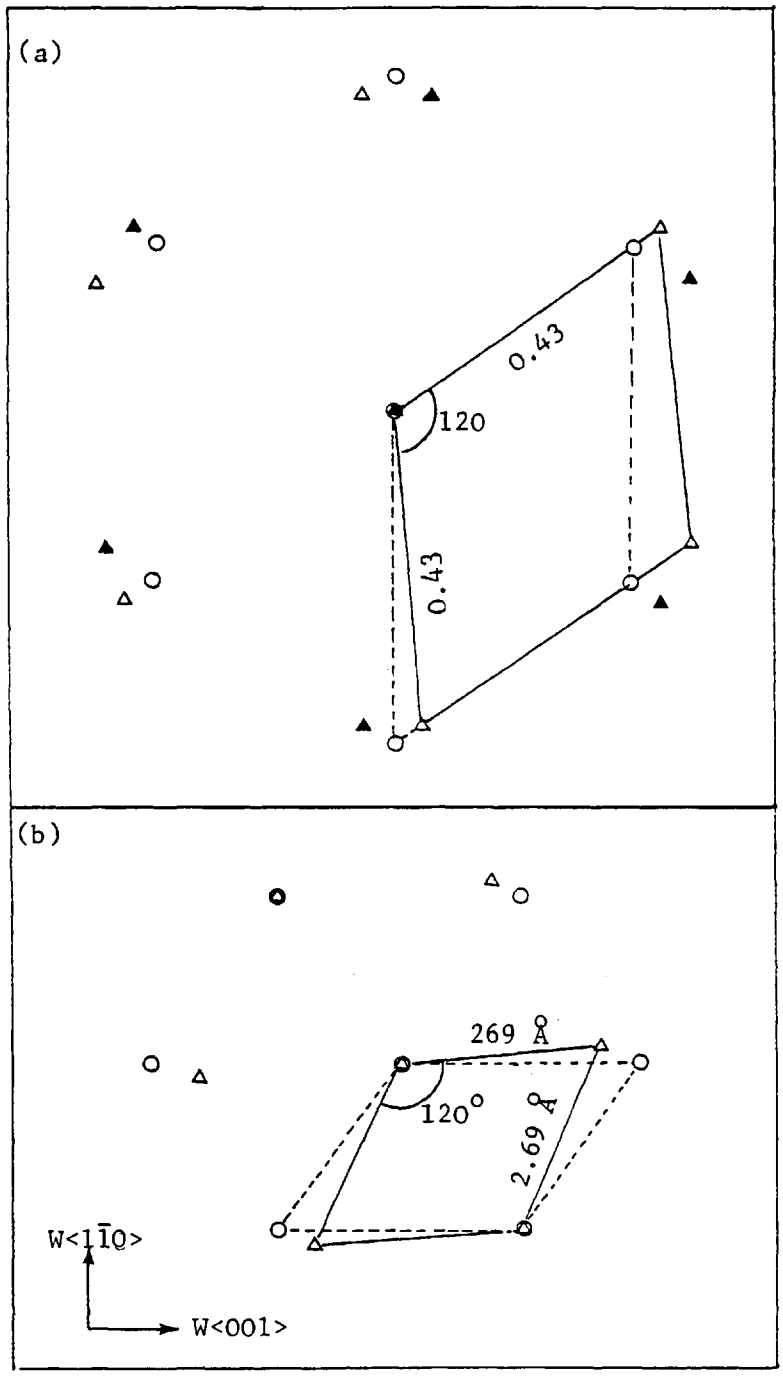


Figure 6.17 Proposed reciprocal unit mesh corresponding to the pattern of fig. 6.16f, showing Rh(111)||W(110) in the Kurdjumov-Sach orientation. (b) Real unit mesh of one of the two equivalent Rh domains of (a). Solid lines: Rh unit mesh; dashed lines: W unit mesh.

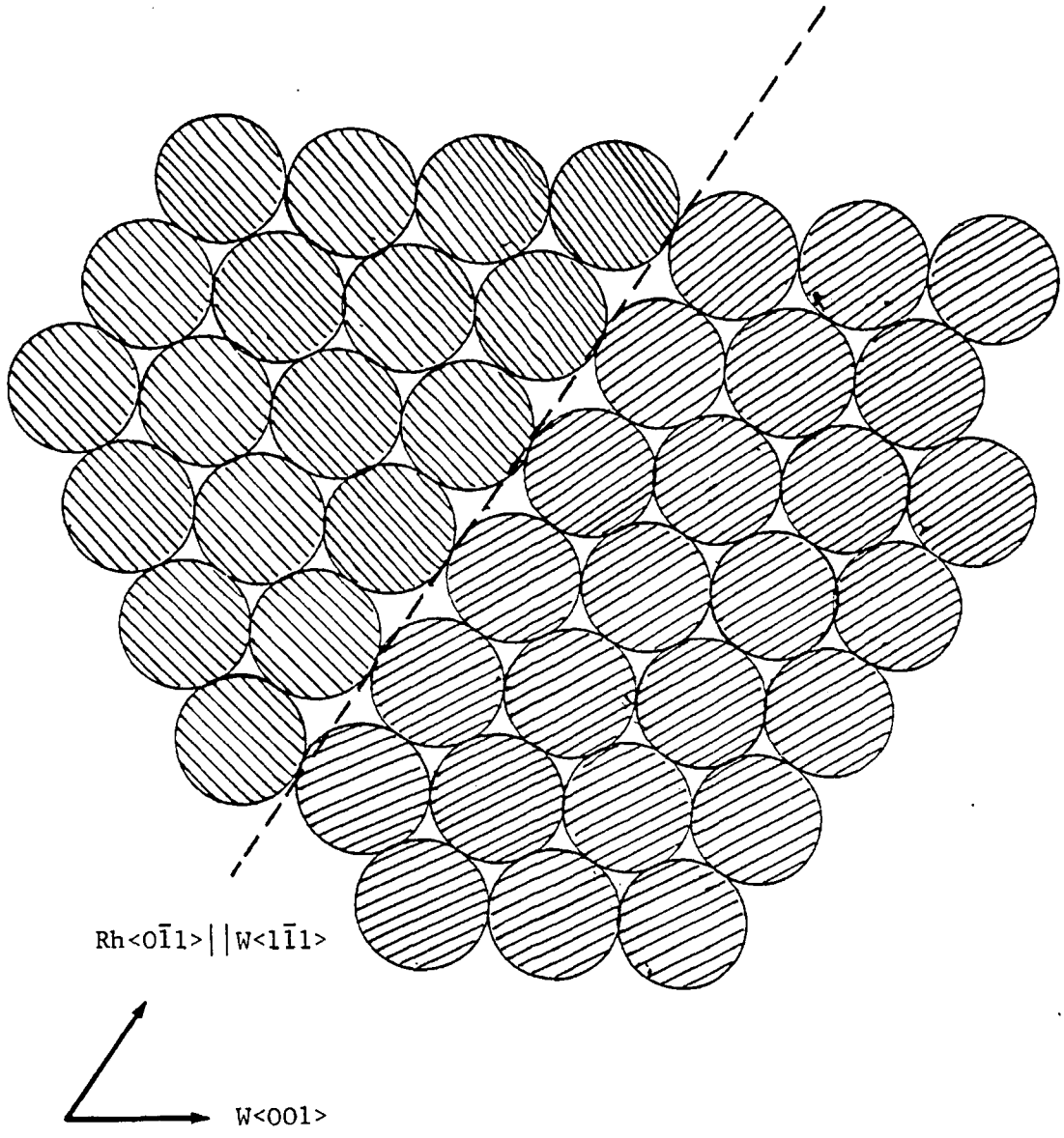


Figure 6.18 Two anti-phase domains of Rh(111) on W(110) in one of the two equivalent KS alignment. The substrate atoms are not shown for clarity. The anti-phase boundary along the W<1$\bar{1}$1> direction is represented by the broken line. Anti-phase domains of Rh(111) in the other KS alignment (see fig. 1.7) would be separated by a boundary in the other equivalent W<111> direction. A high density of such domains would be expected to produce streaking in LEED patterns along the W<111> directions, as in figure 6.16.

on the surface, figure 6.20b. Figure 6.19b shows the LEED pattern at a coverage of about 1 monolayer. The corresponding Auger spectrum is shown in figure 6.20c. The low-coverage streaking due to the Rh chain structures was not observed. Increasing the Rh coverage beyond 1 monolayer did not produce the multiple beam pattern due to the strained Rh(111) structure, which was observed on the clean surface. Instead, the pattern shown in figure 6.19c developed at a coverage of about 2 monolayers. Annealing the specimen at 1100 K at this stage resulted in the pattern of figure 6.19d. It was not possible to resolve the structure near the W(110) spots but the appearance of sharp streaks in the W<111> directions suggests that the structure producing the LEED pattern of figure 6.19d may be due to a high density of small Rh(111) crystallites double positioned on the W(110) surface, as discussed in the preceding section. The (2×2) pattern expected for oxygen on Rh(111)[163] was not observed. This further indicates that the Rh(111) crystallites are probably too small to allow an ordered oxygen structure to form on top by displacing the atoms from the tungsten surface. Annealing the specimen at 1400 K resulted in a further transformation of the LEED pattern, figure 6.19e. The Auger spectrum indicated no significant decrease in the Rhodium or Oxygen signals at this temperature. The oxygen is likely to be in a randomly adsorbed state on the Rh crystallites and on the surface regions between the crystallites. The pattern of figure 6.19e was also observed if oxygen was chemisorbed on top of a high coverage of Rh deposited at room temperature or at 600 K, with subsequent annealing of the specimen at about 1400 K.

The ability of oxygen to inhibit the formation of ordered structures on W(110) has been noted previously for both Au[62] and Cu[55]. In the

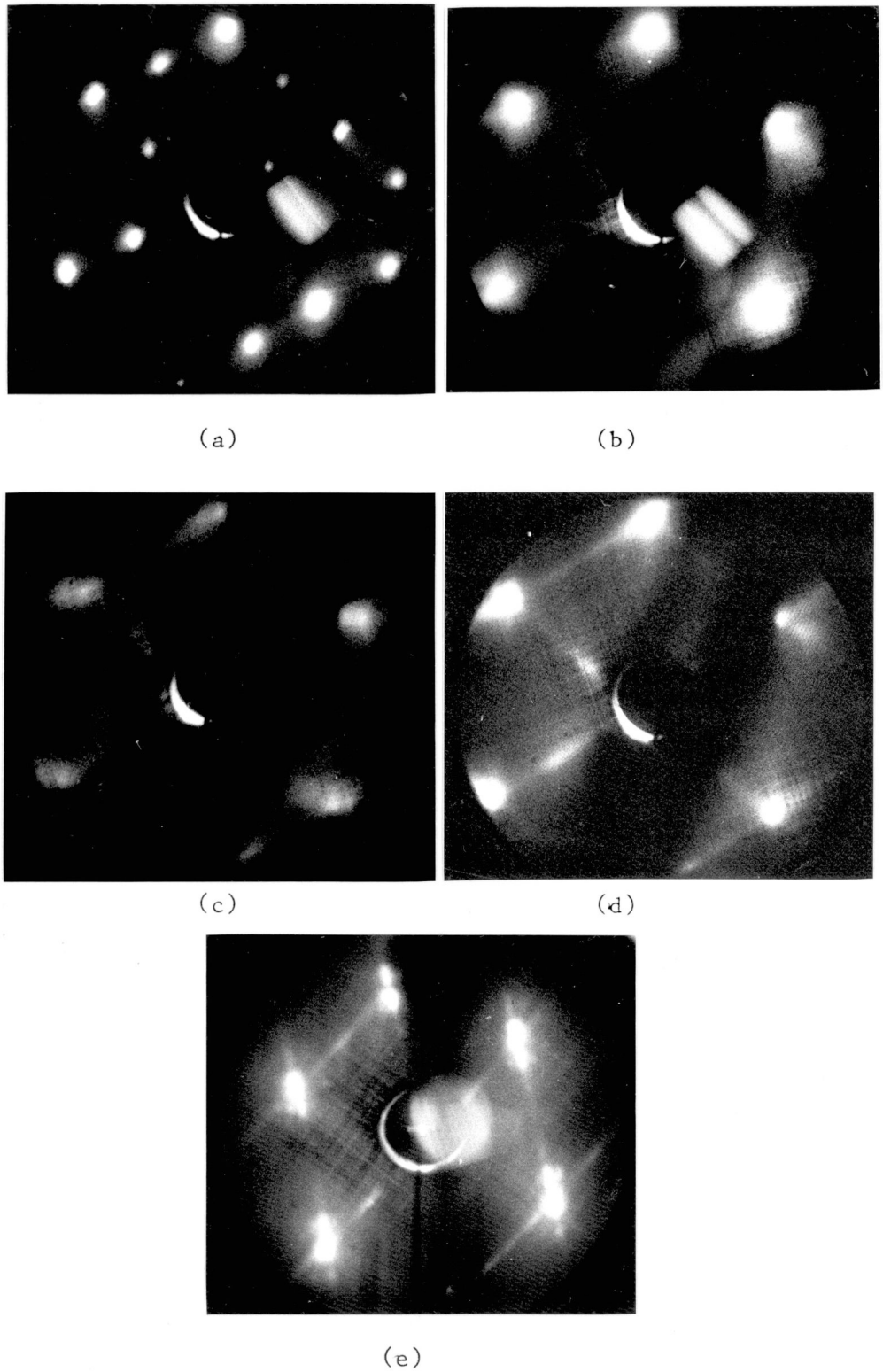


Figure 6.19 LEED patterns from Rh on W(110) in the presence of oxygen. (a) (2×1) pattern of oxygen on W(110); (b) after deposition of 1 ml of Rh at 600 K in incremental doses onto the surface producing the pattern in (a); (c) after further deposition of 1 ml at 600 K followed by annealing at (d) 1100 K, (e) 1400 K (All at 64 V).

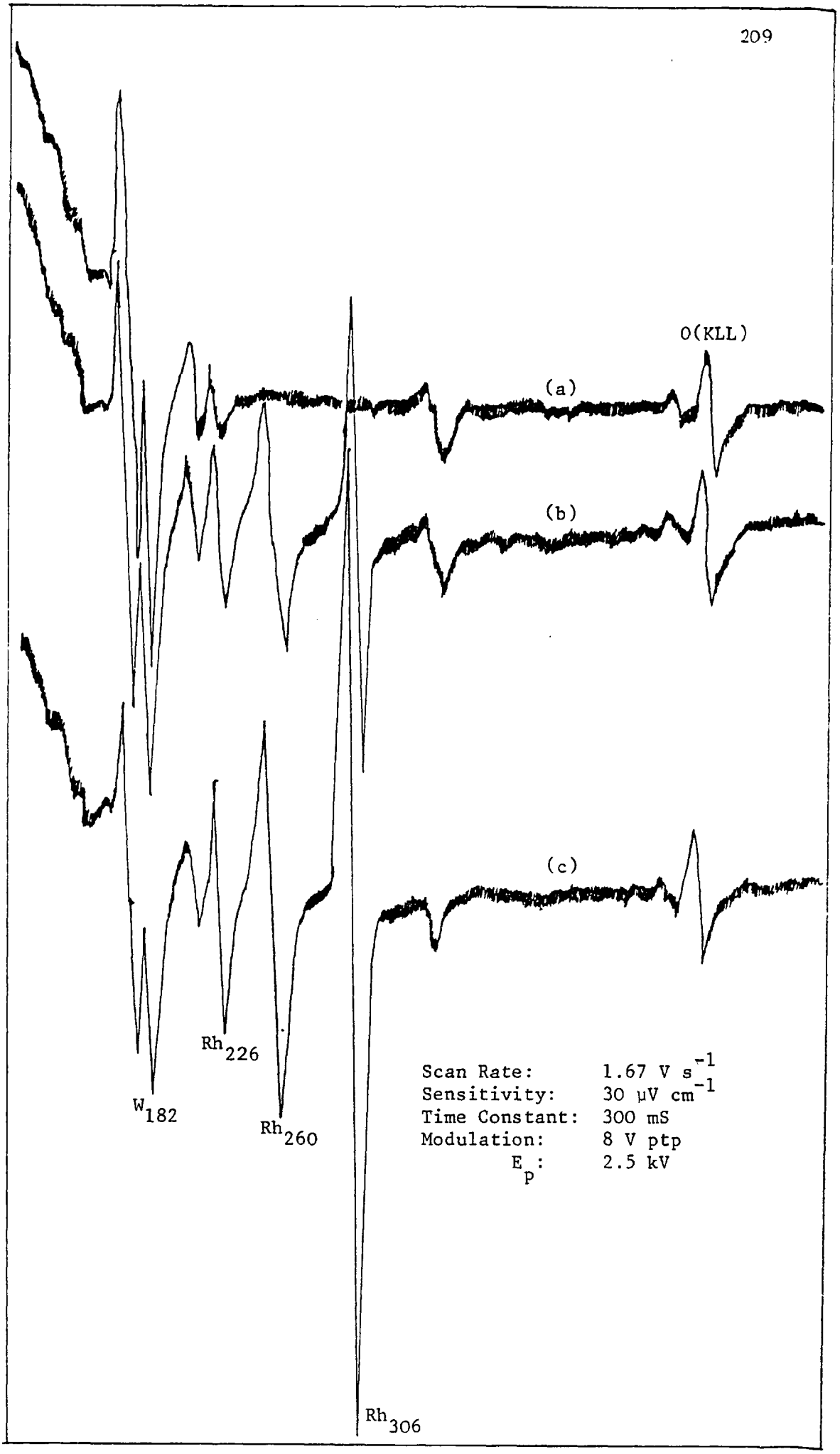


Figure 6.20 Auger Spectra from Rh on W(110) in the presence of oxygen.

present case, oxygen clearly inhibits the development of the chain structures at low coverage and the second layer strained Rh(111) structure.

6.2 Rhodium on Molybdenum

6.2.1 AES characterization of Rh film growth

Rhodium deposition on Mo(110) was examined following cleaning of the Mo(110) crystal as described in chapter 4. The Auger spectrum of the cleaned crystal showed only peaks due to Mo and no peaks that could be associated with C or O, figure 6.21a. Following deposition of Rh, the Auger spectrum, figure 6.21b, showed Rh peaks at energies identical to those for Rh on tungsten. Comparison between figures 6.21a and 6.21b shows that the major MNN emission of Mo at 226 eV overlaps the major MNN emission of Rh at 226 eV. For the AST plots the major MNN emissions of Rh at 306 eV and of Mo at 188 eV, both of which are well separated from other emissions, were selected.

Figure 6.22 shows the AST curves obtained at two different temperatures. The curves are similar to those obtained for Rh on tungsten. Sharp breaks at the monolayer deposition time were not observed for the reasons discussed in section 6.1.1. The monolayer deposition time, calculated from the attenuation of the Mo Auger electron peak-to-peak height using the procedure outlined in section 4.3.10, chapter 4, is indicated in figure 6.22.

As found for Rh on W(110), the Rh Auger electron peak-to-peak height for the annealed deposit increases and the Mo Auger peak-to-peak height decreases less rapidly within increasing deposition time beyond the monolayer coverage than for room temperature deposition. Assuming

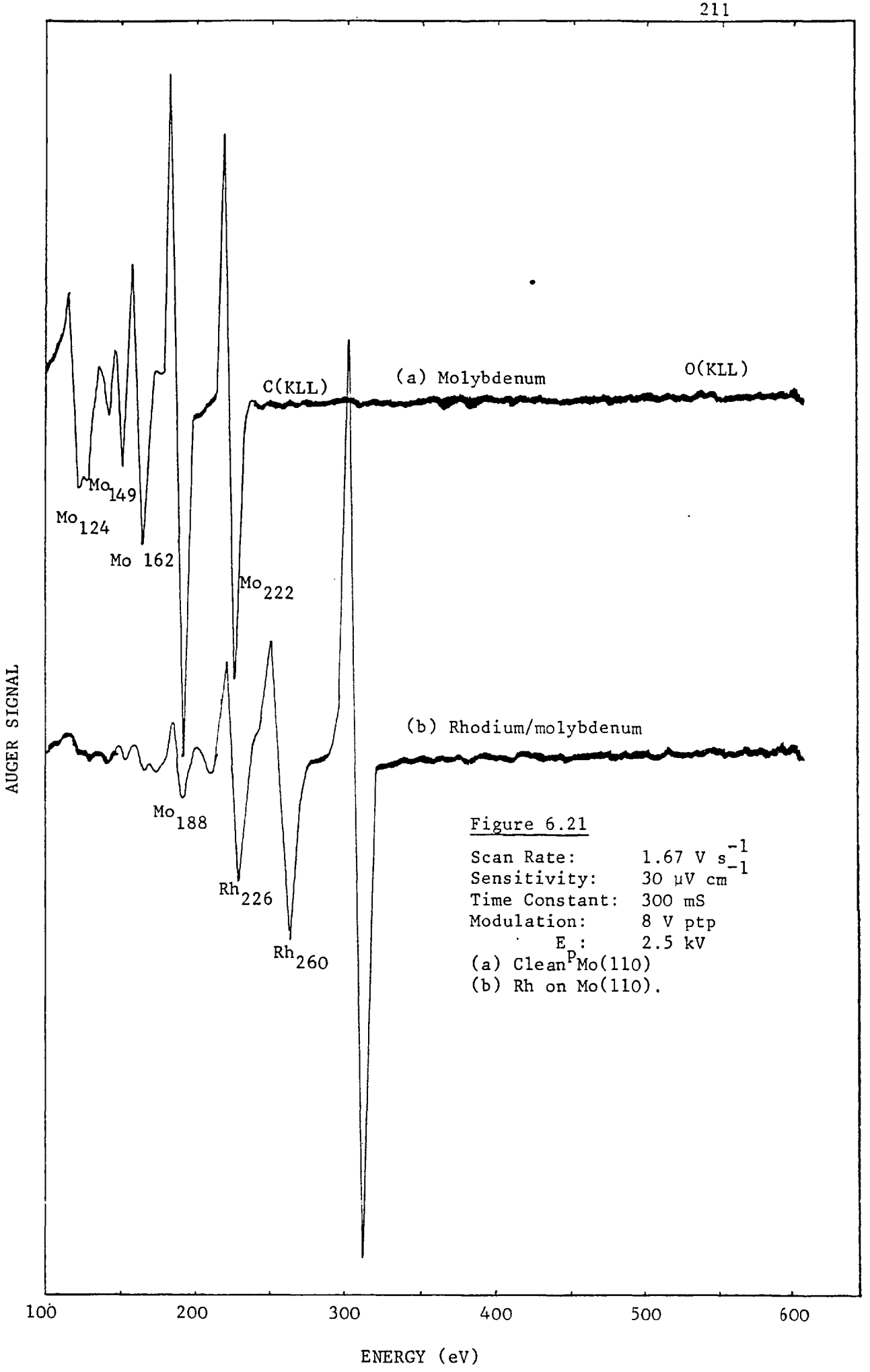


Figure 6.21

Scan Rate:	1.67 V s^{-1}
Sensitivity:	30 μV cm^{-1}
Time Constant:	300 mS
Modulation:	8 V ptp
E_p:	2.5 kV

(a) Clean Mo(110)
(b) Rh on Mo(110).

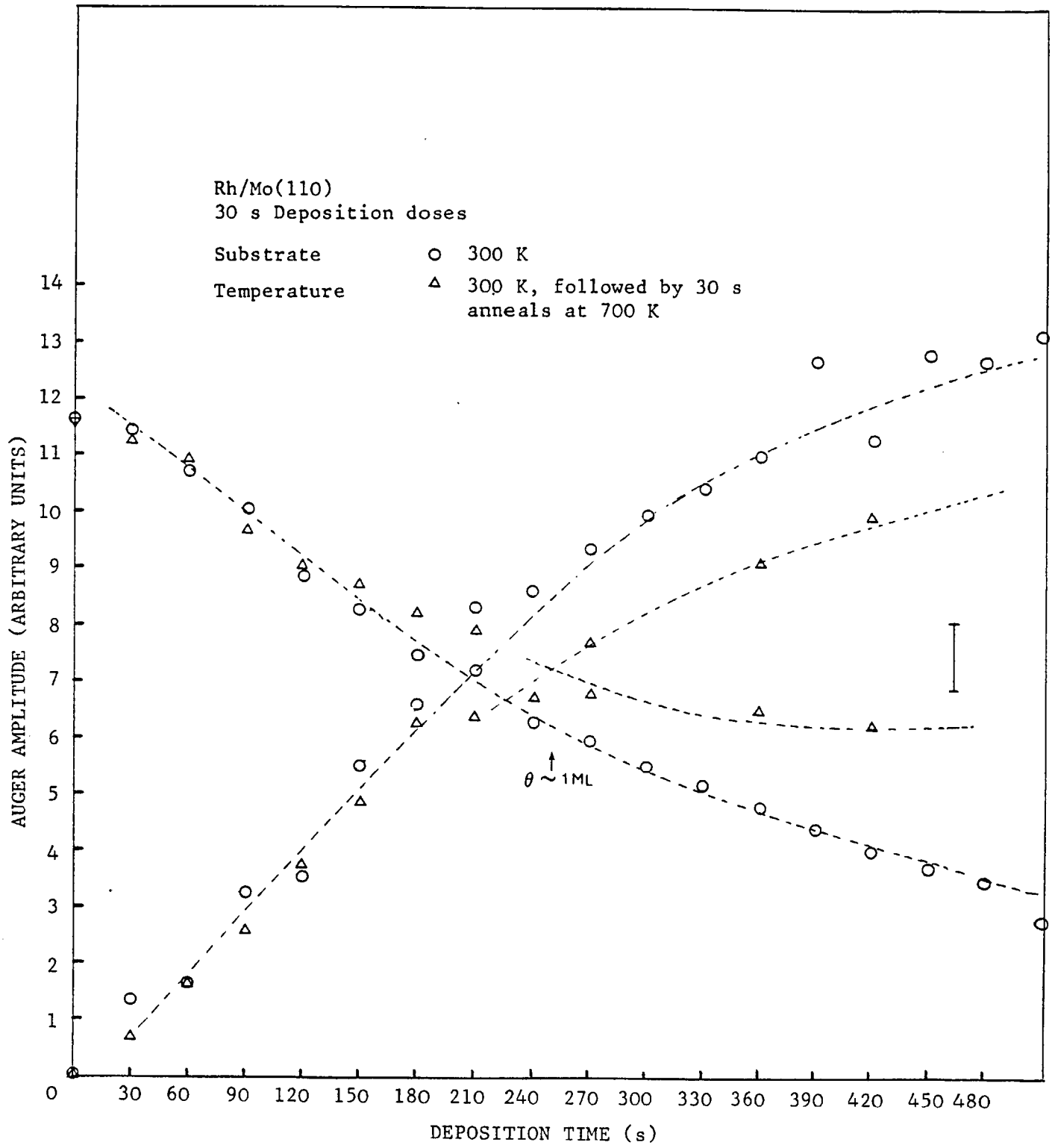


Figure 6.22 Plots of Auger Amplitude versus deposition time.

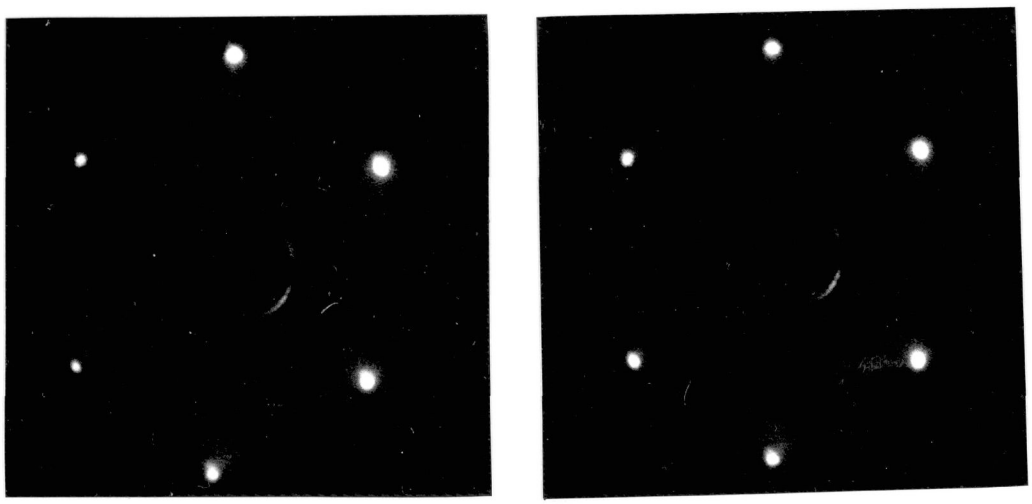
surface alloying does not occur, this is indicative of three-dimensional growth for the annealed deposits at coverages beyond the first monolayer. Surface diffusion and diffusion into the crystal as the cause for the slow decrease of the Mo Auger peak-to-peak height are thought to be unimportant for the same reasons as those given for Rh on W(110) in section 6.1.1.

6.2.2 LEED observations of Rh overlayer structures

Prior to Rh deposition, the cleaned Mo crystal gave the (1×1) LEED pattern expected for the (110) surface, figure 6.23. The reciprocal and real lattice unit cells are shown schematically in figure 6.24.

(a) Room temperature deposition

Room temperature deposition of rhodium caused broadening of the Mo(110) spots and a considerable increase in the background. The broadening of the spots indicates some ordering of the adsorbate at room temperature. This behaviour is in contrast to that of room temperature deposits on tungsten, which showed only a considerable increase in the background. The diffuse streaks observed at low Rh coverages on W(110), due to the chain structures (figure 6.10), were never observed on Mo(110). Increasing the coverage beyond 1 monolayer resulted in the pattern of figure 6.25a, which is similar to figure 6.12 for Rh on W(110). The satellite spots of figure 6.25a were not always well-defined but the pattern improved in sharpness when the specimen was heated at 500 K, figure 6.25b. A sharp pattern was also obtained if the specimen with about 1 monolayer of Rh was first annealed at about 500 K and subsequent deposition was done at room temperature.



(a) 60 V (b) 70 V

Figure 6.23 LEED patterns from clean Mo(110) surface.

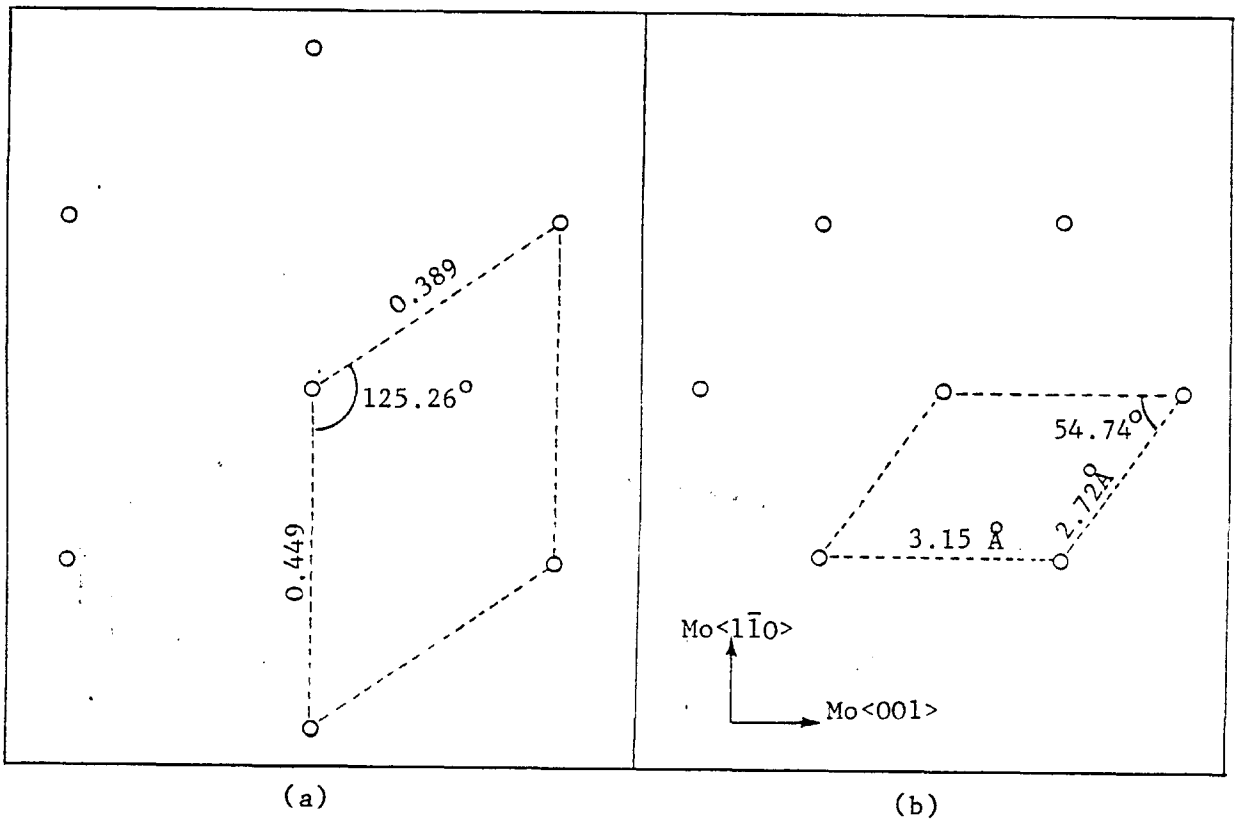
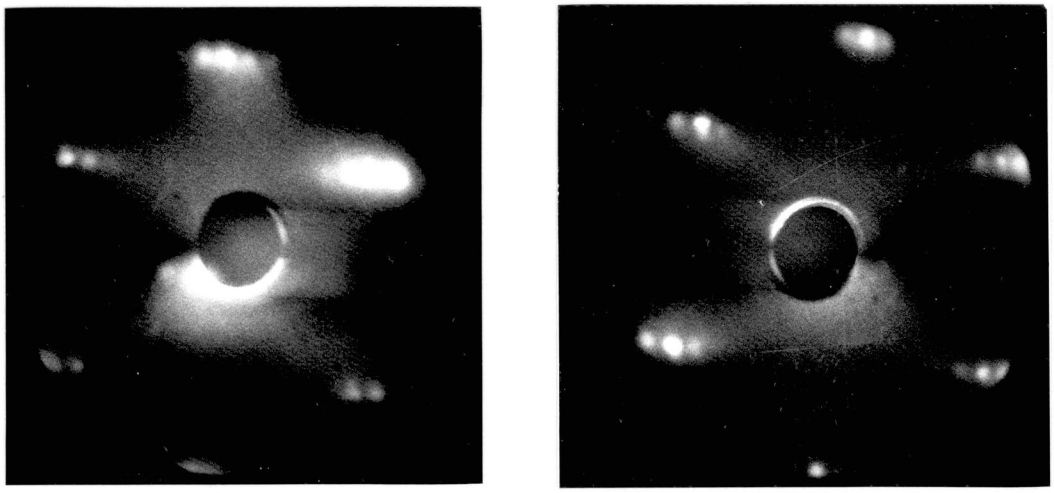


Figure 24 Reciprocal (a) and real (b) unit meshes of Mo(110) surface.



(a) (b)

Figure 6.25 (a) LEED patterns from Rh on Mo(110) after deposition of >1 ml of Rh at 300 K (a) followed by annealing at 500 K (b), showing satellite spots associated with multiple diffraction between a strained Rh(111) layer and the underlying lattice (64 V).

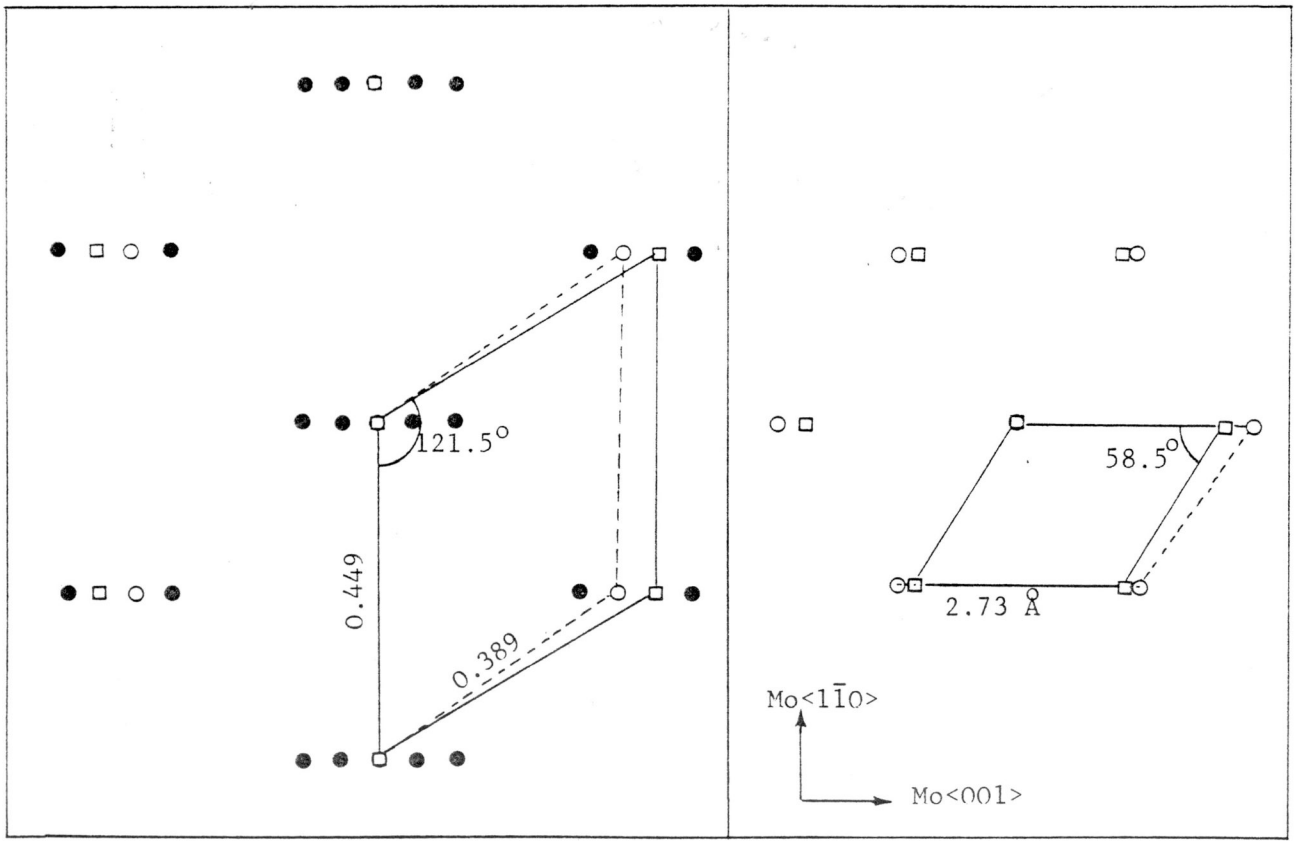
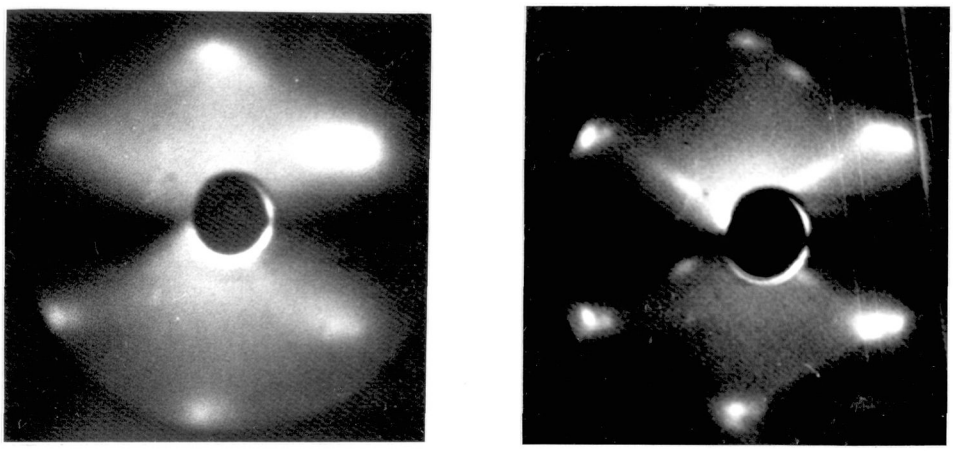


Figure 6.26 Schematic diagrams of the reciprocal (a) and real (b) lattice unit meshes corresponding to the patterns of fig. 6.25. Solid lines: Rh unit mesh; dashed lines: Mo unit mesh; filled circles: "extra" multiple diffraction spots.

Following the interpretation applied to the tungsten case, it is proposed that the pattern of figure 6.25 arises from a second layer strained Rh(111) structure and multiple diffraction between the strained Rh(111) structure and the underlying lattice. The strained Rh(111) structure has a repeat distance of Mo in the Mo<1$\bar{1}$0> direction and a repeat distance of 2.73 Å in the Mo<100> direction. The Rh nearest-neighbour distance in the strained structure is 2.61 Å. The strained Rh(111) structure on Mo(110) is thus identical to that on W(110) surface within the accuracy of the measurements. The reciprocal and real lattice unit cells corresponding to the strained Rh(111) structure on Mo(110) are shown schematically in figure 6.26.

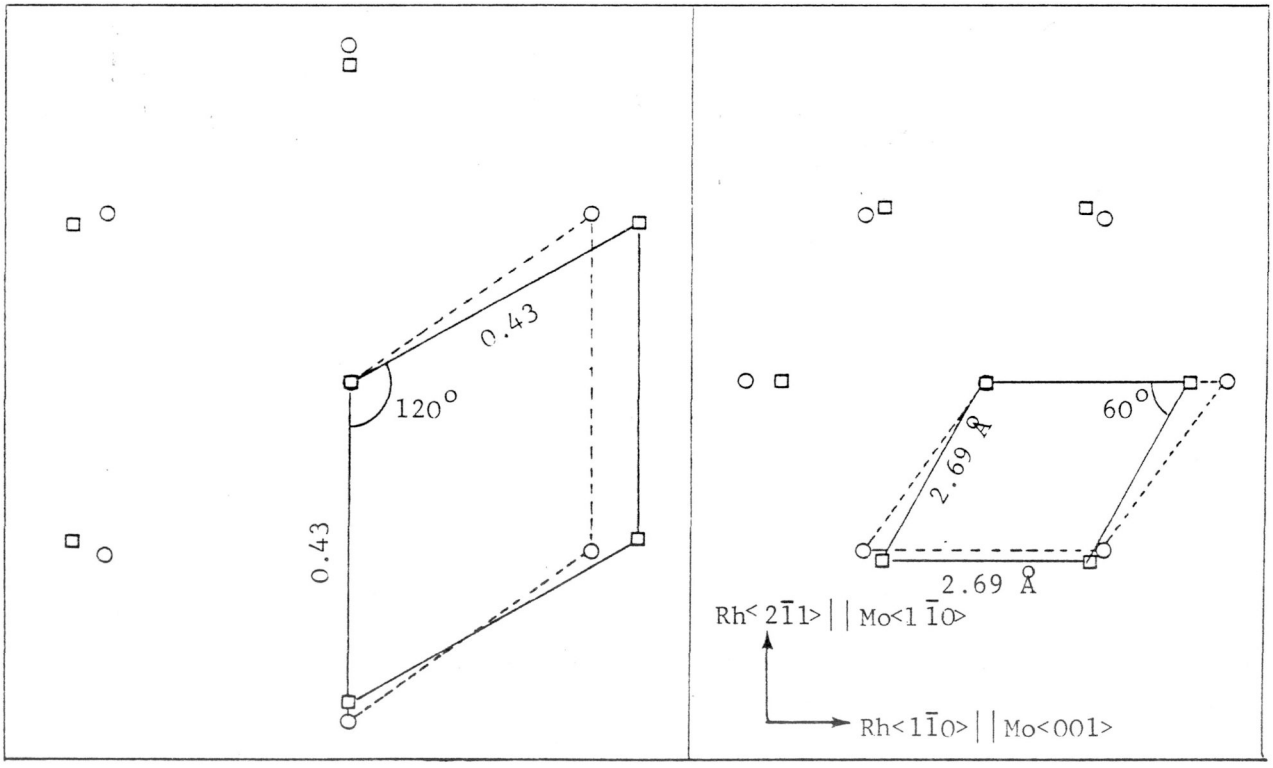
Upon annealing the specimen at 700 K the multiple beam pattern of figure 6.25 was destroyed. If deposition was then continued at room temperature the multiple beam pattern was restored. This behaviour is similar to that observed for the multiple-beam pattern of Rh on W(110). Following the interpretation given for Rh on W(110), it is suggested that the second layer Rh on Mo(110) is metastable and agglomerates into three-dimensional crystallites and the pseudomorphic first layer is exposed between the crystallites. When further deposition takes place at room temperature, the second layer strained Rh(111) is reformed in the region between the crystallites.

With continued deposition at room temperature the multiple diffraction spots gradually faded away, background intensity increased and a new pattern emerged at a coverage exceeding 2 monolayers, with diffuse streaks in the Mo<111> directions, figure 6.27a. The streaks and the spots became sharper after annealing the specimen at >700 K, figure 6.27b. The extra spots are interpreted as due to Rh(111) with the orientation relationship Rh(111)||Mo(110) and Rh<1$\bar{2}$1>||Mo<1$\bar{1}$0>.



(a) (b)

Figure 6.27 LEED patterns from Rh on Mo (110). (a) After deposition of about 2 ml of Rh at 300 K followed by (b) annealing at 700 K. (64 V).



(a) (b)

Figure 6.28 Reciprocal (a) and real (b) unit meshes corresponding to Rh(111)||Mo(110) in the Nishiyama-Wassermann orientation. Solid lines: Rh unit mesh; dashed lines: Mo unit mesh. This is the proposed structure producing the extra spots in the pattern of fig. 6.27b.

The reciprocal and real lattice unit cells corresponding to the pattern of figure 6.27 are shown in figure 6.28a and 6.28b, respectively.

It should be noted that the diffuse streaks appearing for the room temperature deposit in figure 6.27 were not always distinguished. Frequently, continued deposition at room temperature resulted in a gradual fading away of the Mo(110) spots with the emergence of diffuse Rh(111) spots, figure 6.29a. Figures 6.29a and 6.29b show the effect of annealing the specimen. Annealing at 1200 K resulted in considerable sharpening of the Rh(111) spots while above 1300 K partial desorption of the Rh occurred, resulting in the emergence of the original Mo(110) spots. The orientation relationship of the Rh(111) is the same as that depicted in figure 6.28. The mismatch of bulk Rh lattice in the Mo<1$\bar{1}$0> direction is about 5% while in the Mo<100> direction it is 14.5%. These values are similar to the mismatch values of bulk Rh(111) on W(110) (figure 6.8).

The rather surprising feature of these observations when compared to Rh on W(110) is the appearance of Rh(111) crystallites on the unannealed Mo surface with the epitaxial relation Rh<1$\bar{2}$1>||Mo(1$\bar{1}$0). This orientation was never clearly seen for Rh on W(110) in low temperature deposits.

(b) Effect of annealing room temperature deposits

On annealing a room temperature deposit of about 2 monolayers at 1100 K, the pattern shown in figure 6.30a was obtained. The intense streaking between the Mo(110) spots is similar to the streaking observed for Rh on W(110) at a similar coverage and annealing temperature (cf. figure 6.16). Figures 6.30b-e shows a sequence of patterns obtained by successive 60 sec. anneals at 1200 K. The streaks

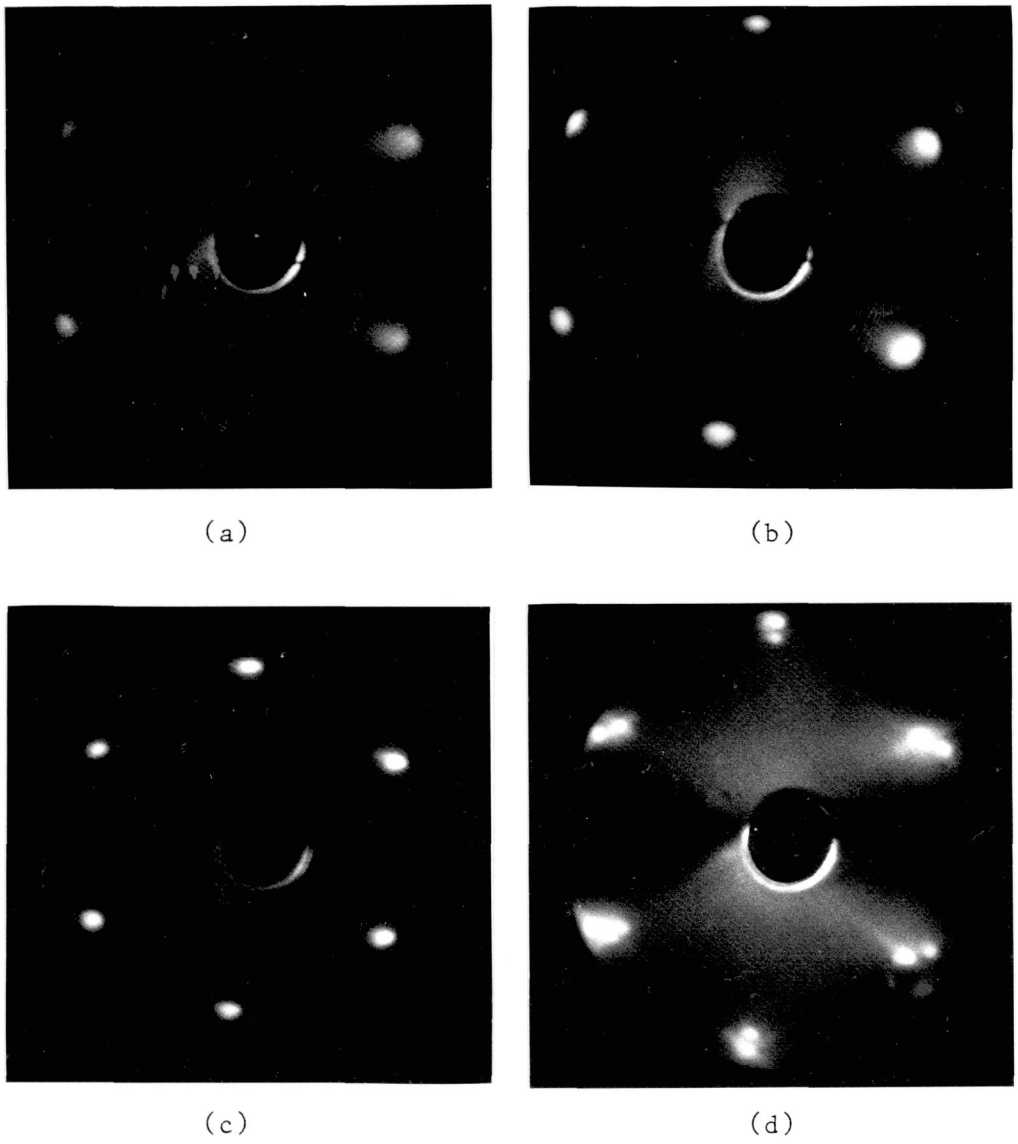
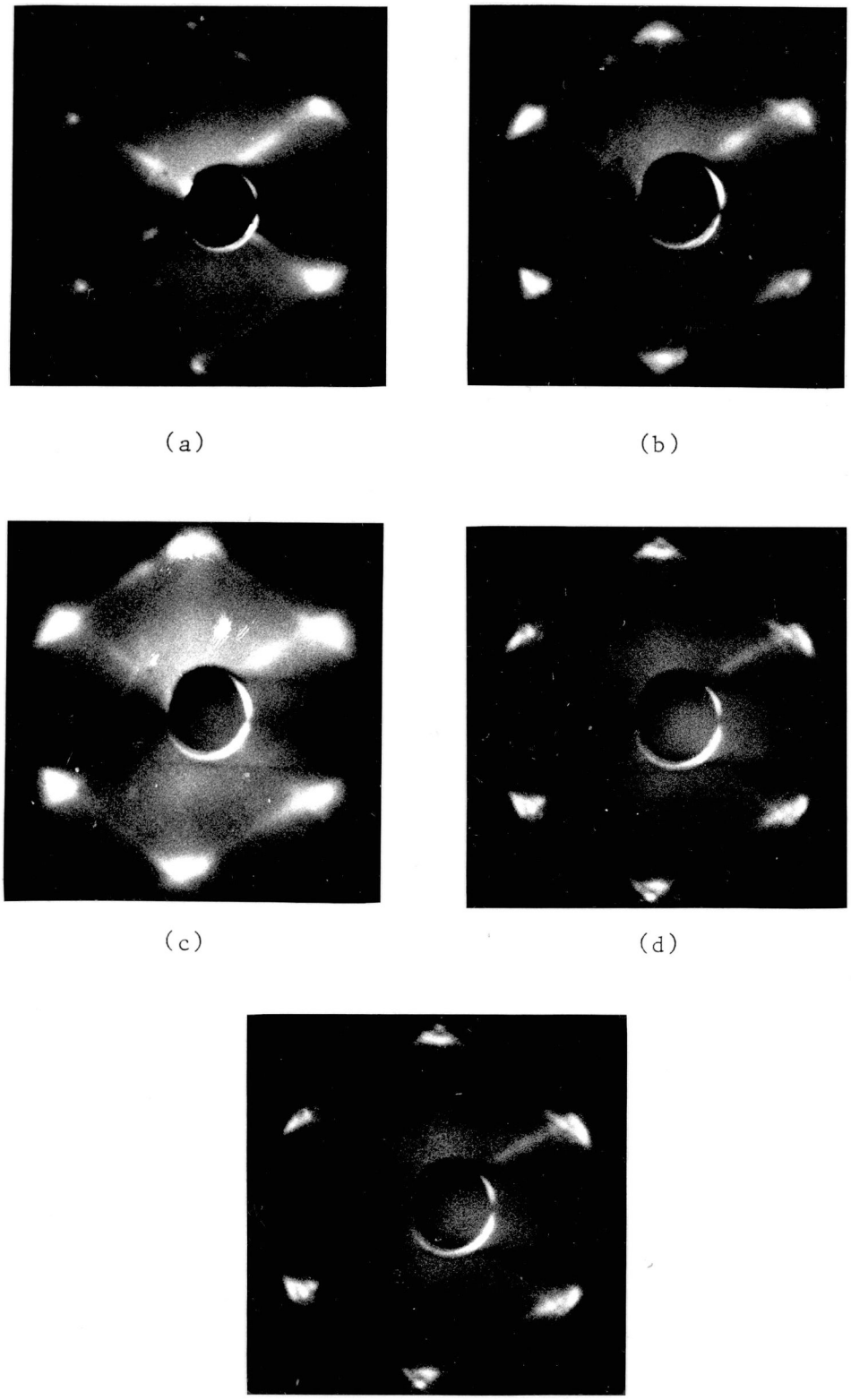


Figure 6.29 LEED patterns from high coverage Rh on Mo(110). (a) After deposition at 300 K showing diffuse spots due to Rh(111). (b),(c) After successive heating periods at 1200 K showing sharp Rh(111) spots and (d) following partial desorption of the Rh at 1300 K. The Mo spots have re-emerged in (d). The orientation of the Rh(111) overlayer corresponds to that of fig. 6.28.



(a) (b)

(c) (d)

(e)

Figure 6.30 LEED patterns from Rh on Mo(110). (a) After deposition of ≥2 ml of Rh followed by annealing at 1100 K. (64 V). (b)-(e) After successive heating periods at 1200 K. (80 V).

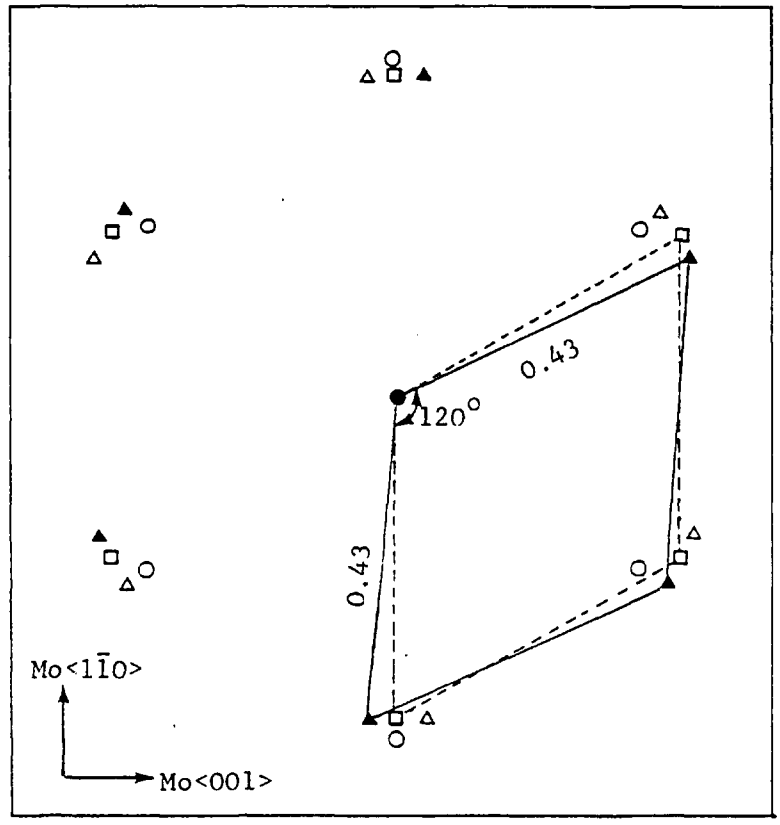
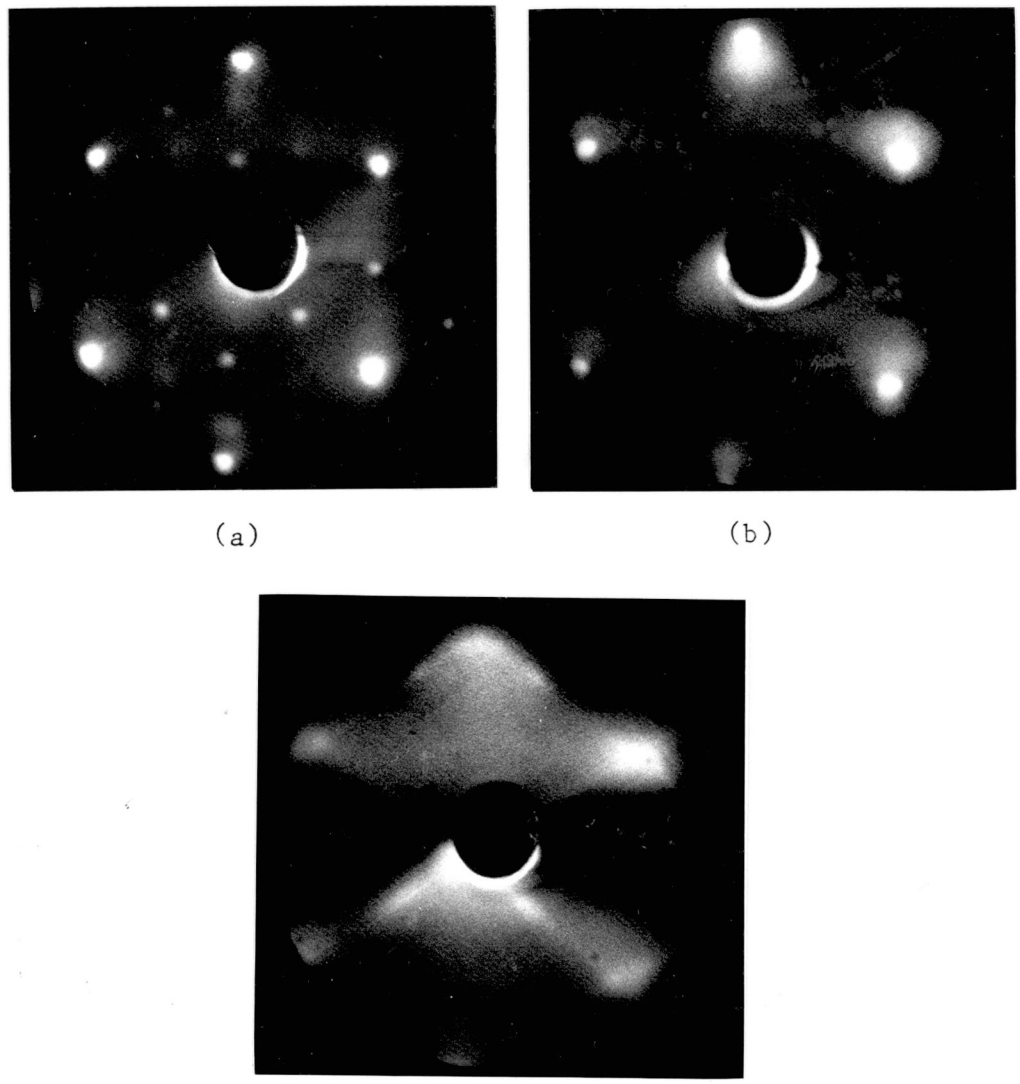


Figure 6.31 Reciprocal unit meshes of Rh(111) Mo(110) in both the Nishiyama-Wassermann (NW) and Kurdjumov-Sachs (KS) alignments. Mo; Rh (NW); , Rh (KS). All three domains of Rh are thought to be present on the Mo(110) surface producing the patterns of figure 6.30(d),(e).

lost intensity and extra features appeared in the vicinity of the Mo(110) spots. This suggests that the streaks may be due to a high density of three-dimensional crystallites with anti-phase relations between them, as was suggested for the similar streaks observed for Rh on W(110) (figure 6.18). The extra features in the LEED pattern of figure 6.30e are considered to be due to three different domain arrangements on the surface. The reciprocal lattice unit cells due to these domains are illustrated schematically in figure 6.31a. One domain is double positioned on the Mo(110) surface in the Kurdjumov-Sachs orientation relationship, i.e., Rh(111)||Mo(110) with Rh<1$\bar{1}$0>||Mo<1$\bar{1}$1> and Rh<$\bar{1}$10>||Mo<$\bar{1}$11>. The other domain, indicated by the dashed line in figure 6.31, is due to Rh(111)||Mo(110) with Rh<1$\bar{2}$1>||Mo<1$\bar{1}$0>, which is the Nishiyama-Wassermann orientation relationship observed for the high coverage room temperature deposits (figure 6.28).

6.2.3 Effect of oxygen on the growth of Rh films

Oxygen was adsorbed on Mo(110) surface following the procedures outlined in Chapter 4. Figure 6.32a shows a (2×2) pattern due to chemisorbed oxygen on Mo(110), corresponding to a coverage of 0.25 monolayers[134]. The corresponding Auger spectrum showing the O(KLL) peak at 516 eV is shown in figure 6.33a. Rhodium was deposited on this surface at room temperature. The half-order spots due to oxygen disappeared at sub-monolayer Rh coverages although the Auger spectrum showed that the oxygen was still present on the surface. This indicates that the Rh destroys the oxygen array on Mo(110), exactly as



(a) (b)

(c)

Figure 6.32 LEED patterns from Rh on Mo(110) in the presence of oxygen. (a) (2×2) pattern of oxygen on Mo(110), (75 V). After deposition of (a) <1 ml, (b) 2 ml of Rh at 300 K onto the surface producing the pattern in (a), (65 V).

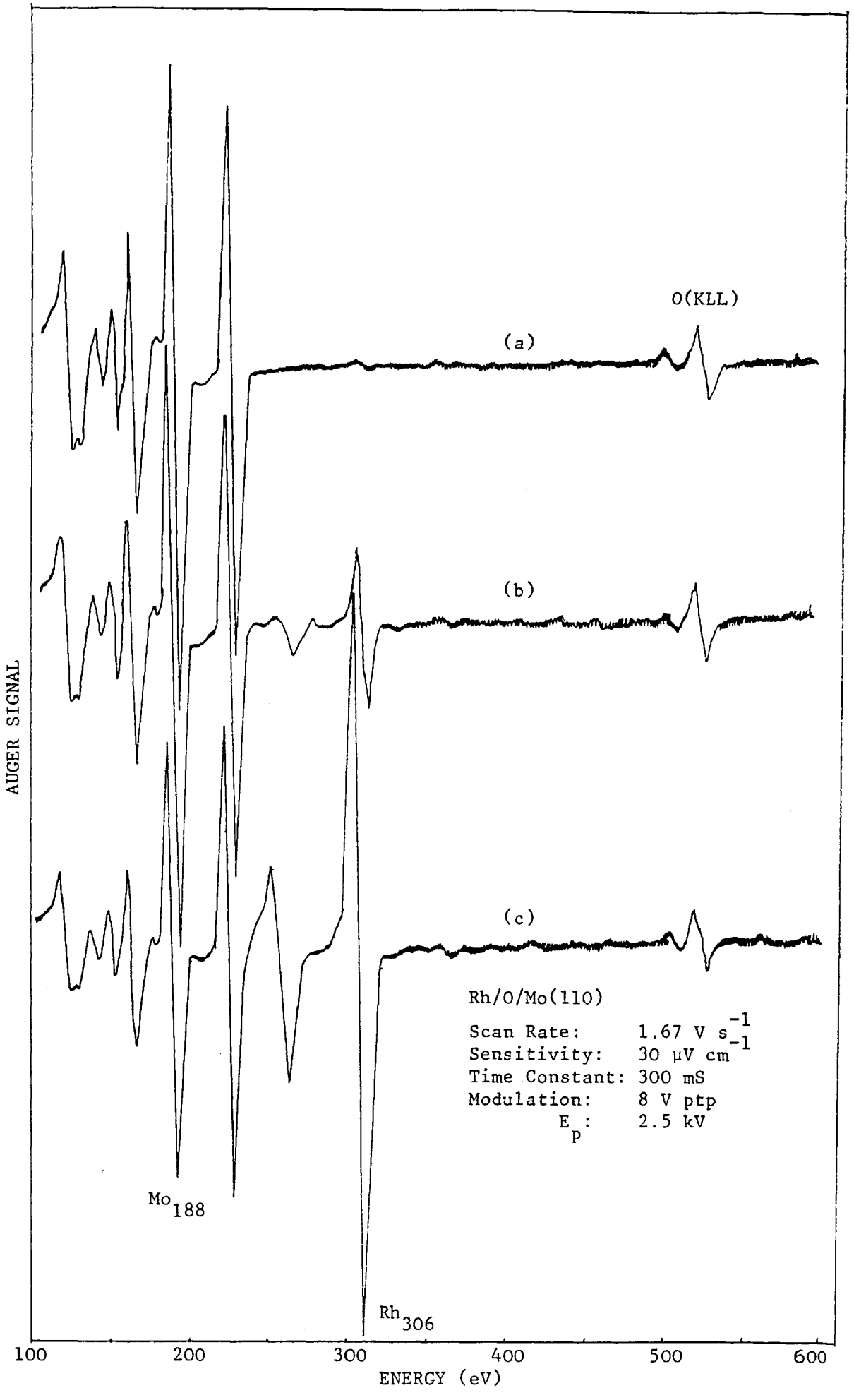


Figure 6.33 Auger Spectra from Rh on Mo(110) in presence of oxygen.

found on the W(110) surface. With increasing coverage the Mo(110) spots became broad, figure 6.32b. Increasing the coverage beyond 1 monolayer failed to produce the multiple beam pattern of figure 6.25. At a coverage exceeding 2 monolayers, diffuse streaks and a considerable increase in the background were observed, figure 6.32c, suggesting considerable disorder on the surface. The sequence of behaviour is similar to that observed for Rh on the oxidised W(110) surface. Annealing the specimen at about 1000 K resulted in a pattern similar to that observed for W(110) (figure 6.19e), with "extra" spots in the Mo<1$\bar{1}$0> direction.

6.2.4 Carbon-monoxide adsorption on Rh(111) overlayer

The adsorption of CO on Rh(111) crystal surfaces has been studied by Grant and Haas[162] and more recently by Castner, Sexton and Somorjai[163]. It is found that CO adsorption at room temperature produces an increase in background intensity at first, and later a diffuse split (2×2) pattern which is just discernible. The CO desorbs below 600 K[163].

In the present case, a thick layer of Rh (>10 monolayers) was deposited on the Mo(110) surface and the crystal annealed at about 1000 K. This produced a sharp Rh(111) pattern of the form shown in figure 6.29c. CO was then leaked into the system at a pressure of 1×10^{-8} torr. Exposures of up to 15 Langmuirs (1 Langmuir = 1×10^{-6} torr s) produced only an increase in the background intensity, suggesting that CO adsorption on the overlayer does occur but remains disordered. The presence of the CO was also observed in the Auger spectrum, figure 6.34a. Heating the specimen below 400 K resulted in CO desorption, as evidenced by the disappearance of the C and O peaks

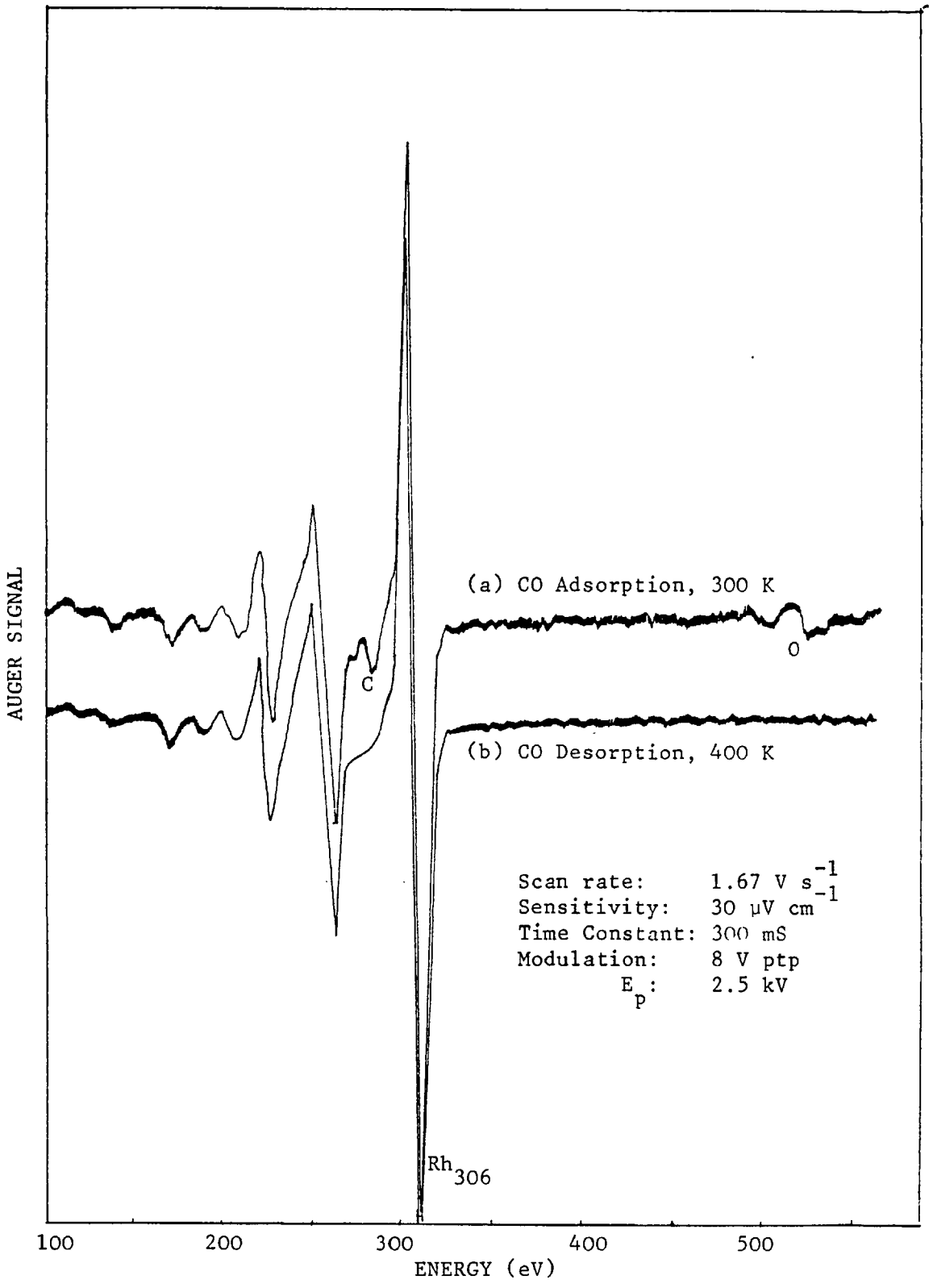


Figure 6.34 Auger spectra from Rh(111) on Mo(110) after (a) exposure to CO at 300 K and (b) desorption of CO on heating at 400 K. (Spectra taken at 300 K).

in the Auger spectrum, figure 6.34b, and the disappearance of the background intensity in LEED. Electron-beam-induced effects as the cause for the absence of any ordered structure of CO on the Rh overlayer can be ruled out since examination of the overlayer in LEED with a continuous flow of CO also failed to show any ordered structures of CO on the Rh(111) overlayer.

Since CO on Mo(110) does not desorb up to 1500 K[164], the low temperature desorption from the Rh overlayer suggests that the Rh(111) crystals in the overlayer are separated by regions which are not free of Rh but probably consist of the stable pseudomorphic Rh layer.

6.3 Summary of LEED and AES

To summarize, LEED and AES studies have been made of rhodium vapour-deposited on the (110) surfaces of tungsten and molybdenum.

Although sharp breaks were not observed in the Auger peak-to-peak height versus deposition time plots, the general shape of the plots qualitatively indicates a Stranski-Krastanov type of growth for Rh on both the surfaces.

Room temperature deposition on W(110) resulted only in an increase in the background LEED intensity. Well-defined patterns were obtained only at elevated temperatures. Heating a room temperature deposit of several monolayers in thickness resulted in unsharp diffraction spots of Rh(111) in the Nishiyama-Wassermann orientation relationship, $Rh\langle 1\bar{1}2\rangle \,||\, W\langle 1\bar{1}0\rangle$. Annealing below 600 K after each deposition dose resulted in the appearance of diffuse streaks in the LEED pattern at sub-monolayer coverages. These streaks are interpreted as due to linear chains of Rh along the W<111> directions. With increasing coverage

up to a monolayer, the streaks faded in intensity and the W(110) spots became broadened, which is interpreted as due to the formation of pseudomorphic type islands of Rh. Increasing the coverage beyond one monolayer resulted in the appearance of well-defined satellite spots in the W<100> direction. This pattern is interpreted as due to multiple diffraction between a strained Rh(111) structure and the underlying Rh monolayer and the W(110) surface. However, this second layer was found to be metastable, agglomerating into three-dimensional crystallites after annealing the specimen at 900 K. If deposition was continued beyond two monolayers, the multiple diffraction pattern faded and streaks appeared in the LEED pattern. Heating at about 1300 K resulted in the disappearance of these streaks and the appearance of new spots due to Rh(111) in the Kurdjumov-Sachs orientation relationship, Rh$\langle 1\bar{1}0\rangle$||W$\langle 1\bar{1}1\rangle$ and Rh$\langle \bar{1}10\rangle$||W$\langle \bar{1}11\rangle$. The high coverage streaks is interpreted as due to the formation of a high density of three-dimensional Rh(111) epitaxed crystallites with a random distribution of anti-phase domain boundaries along the close-packed W<111> directions.

In contrast to Rh on W(110), sub-monolayer coverages of Rh on Mo(110) only produced a broadening of the Mo(110) spots at room temperature. The streaking associated with Rh chains was never observed on Mo(110). Apart from these differences, the LEED patterns of Rh on Mo(110) were found to be similar to those on W(110). The LEED pattern changes on Mo(110) were observed to occur at relatively lower temperatures, indicating the greater mobility of Rh on Mo(110).

Small amounts of Rh were found to destroy the low coverage ordered

oxygen arrays on both W(110) and Mo(110). The oxygen prevented the development of the chain structures on the W(110) surface. The presence of oxygen also inhibited the formation of the second layer strained Rh(111) structure on both the surfaces.

7. A TIGHT BINDING MODEL CALCULATION

7.1 Introduction

Field ion microscope observations described in chapter 5 show that rhodium adatoms on tungsten and molybdenum (110) surfaces form linear chain clusters which have their axis accurately aligned parallel to the substrate <111> directions. Bonding in these clusters is thus directional and restricted. Other f.c.c. adsorbates[29] have also been observed to form linear chain clusters on W(110). It is clear by now that the formation of chain clusters is restricted to the later transition metals and thus appears to be linked to their electronic configuration. As stated earlier, one aim of the present work was to determine the electronic contribution to the stability of adsorbate clusters and establish whether the formation of linear-chain clusters for the later transition metals could be predicted theoretically. The procedure adopted to achieve this was to calculate self-consistently, within a d-electron tight-binding approximation, the local electronic structure and energy of a cluster of three adatoms adsorbed on the W(110) surface in two different geometrical configurations: (i) a linear-chain cluster aligned along the W<111> direction and, (ii) a two-dimensional triangular cluster. Two different adsorbates were examined in turn: (i) tungsten which has a half-filled d-band and is known experimentally[44] to form two-dimensional clusters, and (ii) rhodium which has a nearly filled d-band and, as noted above, forms linear-chain clusters. These two cases will be compared and the validity of the theoretical approach determined.

The basis of the model is that the system being considered is adequately described by a d-electron tight-binding approximation,

ignoring the sp conduction states. This is reasonable since a large number of properties of transition metals is adequately described within this approximation[81]. For example, the cohesive energy of bulk transition metals is largely due to the d electrons[165], and the same appears to be true for the binding energies of transition metal atoms adsorbed on transition metal surfaces[38].

In order to determine the relative stability of the two adsorbate configurations, it is necessary to find the energy difference between them. Within Hartree-Fock theory the total energy U_T of a system is given by[80]

$$U_T = U_d - U_{es} \tag{7.1}$$

where U_d is a summation of the energies of the occupied one-electron states (d-states in the present case) and U_{es} is the electrostatic term including both the core-core repulsion term and the double-counting electron-electron interaction term. In principle, the required energy difference between two systems, A and B, will be of the form

$$\Delta U_T = U_T^A - U_T^B = \Delta U_d - \Delta U_{es} \tag{7.2}$$

Evidence shows that the band energy term U_d largely accounts for the structure dependent part of the total energy[80]. Pettifor[166] has found that it accounts correctly for the occurrence of the fcc, bcc and hcp structures among the transition metals and Johannes and coworkers[167] have used it successfully to compare the three Laves phase alloys. Thus, when comparing similar structures ΔU_d should give the correct sign and general variation of the difference in total energy. An expression for ΔU_d has been written in closed form[168] but this was not

used here. Instead, the band energies and the local d-electron density of states of each orbital of the atoms concerned in a cluster were calculated. The summation of these quantities gave values for individual atoms. This procedure then enabled the determination of the contribution of individual orbitals and atoms to the difference in energy between the two cluster geometries. The d-electron energy of a single adatom at a saddle site on W(110) was also calculated and compared to its value at the lattice site. The difference in energy between the two sites should reflect the d-electron contribution to the activation energy barrier to adatom diffusion and can be compared to the experimental values. Calculations have been performed for both W and Rh on W(110).

The d-band energy $U_{d\alpha}$ of an orbital α is calculated as

$$U_{d\alpha} = \int_{-\infty}^{E_f} En_{\alpha}(E)\, dE \qquad (7.3)$$

where $n_{\alpha}(E)$ is the orbital density of states and E_f is the Fermi energy. The local density of states and related quantities were calculated using the recursion method[80]. The Fortran routines for this method were obtained from the Cambridge recursion library[169]. Computer programmes incorporating these routines were written in a general form, permitting calculations for any type of transition metal adsorbate on a bcc (110) surface. Subsequently, these programmes were adapted to a package given by Beer[170], who has used the recursion method to calculate the local density of states of bulk alloys. All the computational work was done on the CDC 6600/6400 system at Imperial College.

7.2 Details of the Calculation

7.2.1 The tight-binding Hamiltonian

The Hamiltonian of the system was represented in a basis set of localised orbitals, in this case the five d-orbitals centred on each atom. Non-orthogonality overlap integrals between orbitals on different sites were ignored and only two-centre integrals between orbitals on first and second neighbours of the bcc structure were retained. These are conventional approximations in tight-binding theory[171]. The two-centre integrals are expressed in the form of a linear combination of three hopping parameters, namely ddσ, ddπ, ddδ. These parameters were calculated as[172]

$$dd\chi = \left.\begin{matrix} -60 \\ +40 \\ -10 \end{matrix}\right\} (m_d S^2)^{-1} (S/R)^5 \text{ for } \chi = \left\{\begin{matrix} \sigma \\ \pi \\ \delta \end{matrix}\right. \qquad (7.4)$$

where m_d is the effective mass of the d-band, S is the Wigner-Seitz radius and R is the interaction distance. $M_d S^2$ is approximately related to the d-band width W_d by[172]

$$W_d \approx 25/m_d S^2 \qquad (7.5)$$

W_d and S for W and Rh are listed in table 7.1. The first and second neighbour distance, for both W and Rh were taken as 2.74 Å and 3.164 Å, respectively. These values were used in equations 7.4 and 7.5 to calculate the hopping parameters for W and Rh. The calculated values of the hopping parameters are listed in table 7.2. The tungsten adatom-adatom and adatom-substrate hopping parameters were set to the same value as the substrate atoms themselves. For the rhodium case, the

Table 7.1 Input parameters for the tight-binding calculation. The d-band width W_d (eV), Wigner-Seitz radius, S(Å), the number of d electrons per atom, Q^o, and the d-level, ε_d^o (eV), for tungsten and rhodium. (From ref.172,175)

	W_d	S	Q^o	ε_d^o
W	10.88	1.561	5	-6.2
Rh	7.89	1.49	8	-10.42

Table 7.2 The tight-binding hopping parameters ddσ, ddπ and ddδ for first (n) and second (nn) nearest neighbours for tungsten, rhodium and tungsten-rhodium. (Units: electron volts).

	Neighbour	ddσ	ddπ	ddδ
W-W	n	-1.5675	1.045	-0.2613
	nn	-0.7633	0.5088	-0.1272
Rh-Rh	n	-0.9007	0.6005	-0.1501
	nn	-0.4386	0.2924	-0.0731
W-Rh	n	-1.1882	0.7921	-0.1980
	nn	-0.5786	0.3857	-0.0964

adatom-substrate hopping parameters were set to the geometric mean of the Rh-Rh and W-W parameters.

7.2.2 Adsorption geometry

Figure 7.1 shows schematically the adsorbate cluster geometries used. (The significance of the numbers is explained below.) The adatoms were placed at the otherwise unoccupied lattice sites above the surface plane. The geometry of an adatom at a lattice site on the W(110) surface is such that each adatom has two first-neighbours in the yz plane and two second neighbours in the xz plane. The assumption that the adatoms occupy lattice sites on W(110) agrees with Cowan and Tsong[173] who concluded from mapping the sites visited by a diffusing W adatom that the adatoms were observed at lattice sites. In view of the lack of experimental evidence to suggest otherwise for Rh on W(110), it seems best to put the adatoms on lattice sites.

To calculate the d-electron contribution to the activation energy barrier to adatom diffusion, the energy was also calculated for the adatom at a saddle site (figure 7.1), where the adatom has just two first neighbours.

In all cases, relaxation of adatoms was not considered and the nearest-neighbour bond length was set to the bulk tungsten value (= 2.74 Å).

7.2.3 Evaluation of the recursion coefficients

The recursion method[80] can calculate the local density of states $n_{\alpha i}(E)$ which can be expressed as a diagonal element of the Green function

$$n_{\alpha i}(E) = -\pi^{-1} \operatorname{Im} G_{\alpha\alpha}(E,H) \qquad (7.6)$$

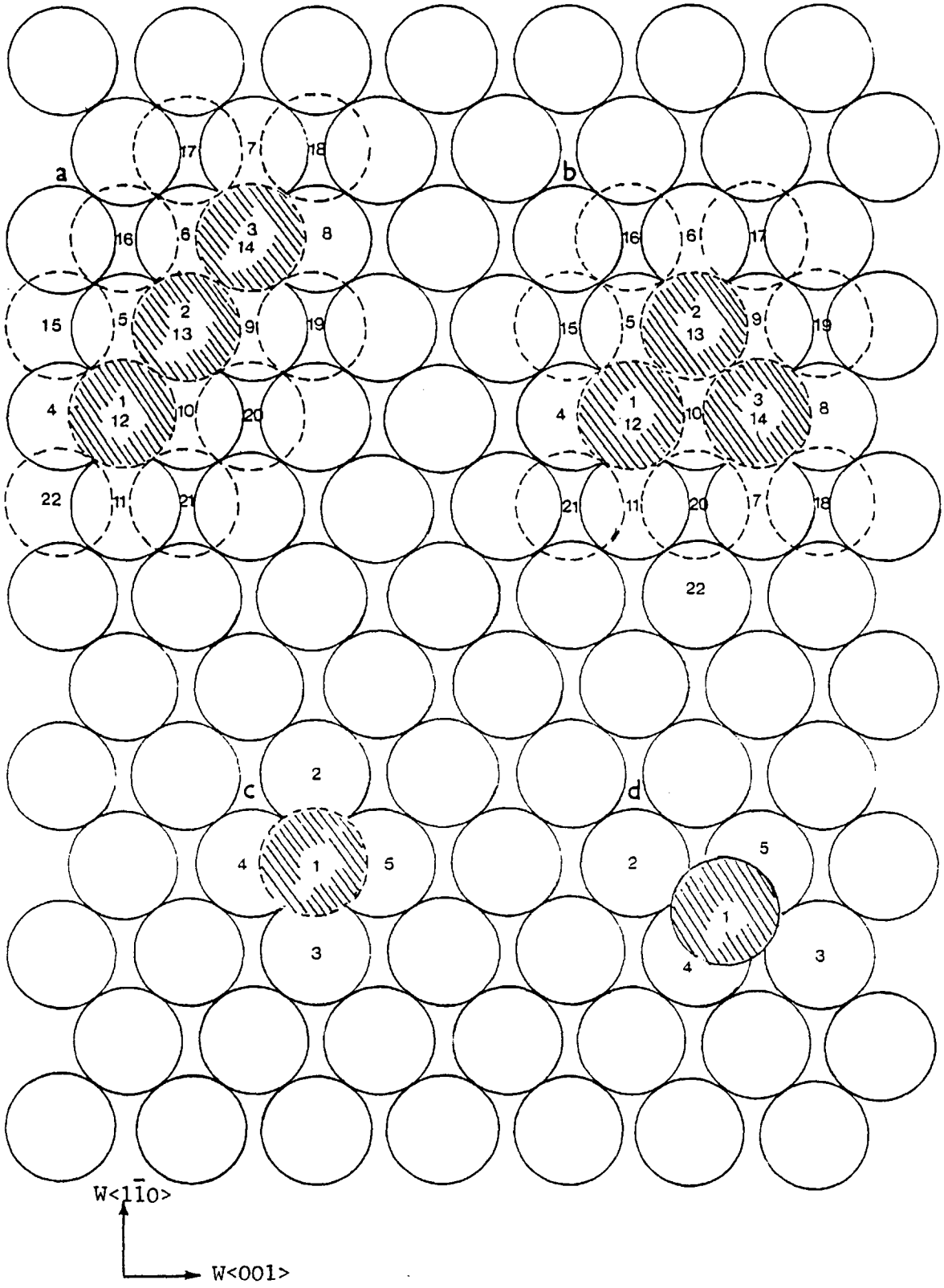


Figure 7.1 Adsorbate geometry on the W(110) surface. (a) Linear cluster, (b) triangular cluster, (c) single adatom at lattice site, (d) saddle site. Shaded circles: adatoms; solid open circles: surface W atoms; dashed open circles: 2nd layer W atoms. The nos. 1-22 in (a),(b) refer to the atoms of the "unit cell" (see text); Atoms 13, 14 and 15 are 2nd layer atoms directly underneath the adatoms. Similar unit cells were defined for (c),(d) but for clarity only the adatom and first (4,5) and second (2,3) neighbour surface atoms are shown here. Nearest neighbour interatomic spacing = 2.74 Å; adatoms in the clusters occupy lattice sites.

The α_i in the present case refers to the atomic-like d-orbitals at site i and H is the Hamiltonian of the system. The recursion method enables the Green function matrix elements to be written as a continued fraction

$$G_{\alpha 0} = \cfrac{1}{E - a_0 - \cfrac{b_1^2}{E - a_1 - \cfrac{b_2^2}{E - a_2 - \cdots\cdots}}} \qquad (7.7)$$

The coefficients a_i and b_i essentially represent the i^{th} neighbourhood environment of orbital α_0. The recursion method generates an orthonormal basis set such that the Hamiltonian transforms to one corresponding to a set of orbitals on a semi-infinite line with self energies a_i and near neighbour interactions b_i. The continued fraction continues indefinitely for an infinite system. In practice a finite block of atoms must be used to make the computation tractable. A block of 300 atoms was thus used to represent the tungsten substrate. The (110) surface plane of the block contained 50 atoms and adatoms were placed centrally on the plane. The continued fractions were evaluated to 14 levels. A flow diagram of the programs used to calculate the continued fraction coefficients is shown in figure 7.2.

7.2.4 Evaluation of integrals and self-consistency

Once a set of $\{a_i, b_i\}$ is calculated for a given orbital, the local density of states is obtained from them as a series of delta functions. The recursion library routines produce a smooth density of

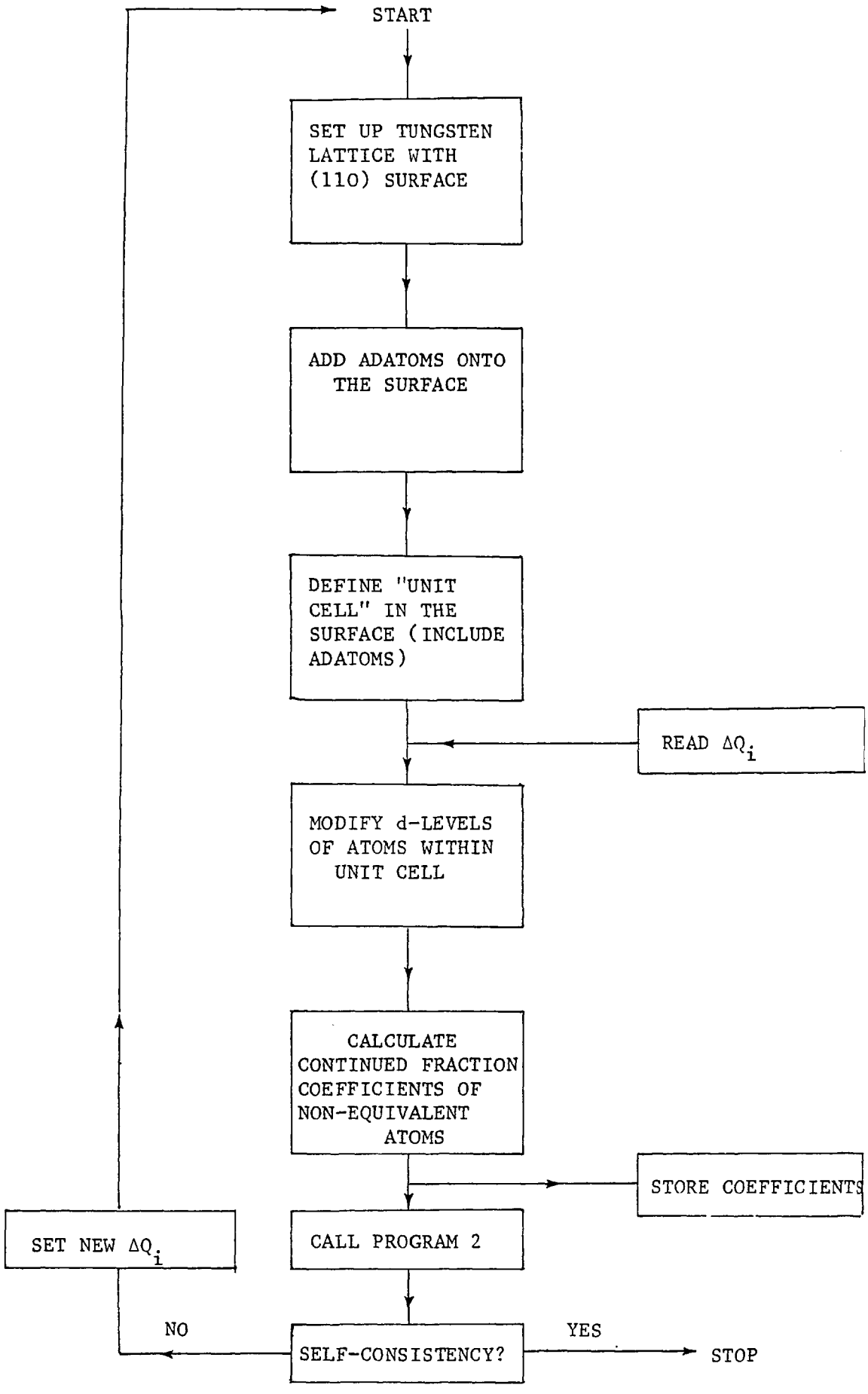


Figure 7.2 Flow diagram of program 1: Calculation of the continued fraction coefficients.

states by processing the delta functions as an integral and then differentiating the resulting function.

The calculation of the relative stability of the two adsorbate structures requires the evaluation of two integrals. The first determines the Fermi level E_f from

$$Z = \sum_{\alpha i} \int_{-\infty}^{E_f} n_{\alpha i}(E)\, dE \qquad (7.8)$$

where Z is the total number of electrons in the system and the summation is over all the five d-orbitals of each atom at site i. In principle equation 7.8 should be evaluated for the complete system, including all the substrate atoms and the adatoms. However, to make the calculation tractable the recursion coefficients $\{a_i, b_i\}$ and the corresponding local density of states were calculated for a finite number of atoms which included the adatoms and their near neighbours. Thus, for the two adsorbate clusters and the single adatom systems, a total of 22 atoms was considered (numbered 1-22 in figure 7.1). This group of atoms is referred to as the "unit cell". The computation time was further reduced by noting that some atoms are equivalent to others. The linear chain cluster has rotational symmetry about the z-axis through the centre adatom (numbered 2 in figure 7.1) while the triangular cluster has mirror symmetry in the plane perpendicular to the surface in the $\langle 1\bar{1}0 \rangle$ direction. This reduced the computation to the five d-orbitals of 11 atoms for the linear cluster and 14 atoms for the triangular cluster. Similarly, for the single adatom at the lattice site and the saddle site the calculations were made for only 9 and 10 atoms respectively. Since the atoms are structurally (and chemically in the case of Rh) not equivalent, charge transfers between atoms are expected.

However, z was maintained constant so that the total number of atoms in the group considered collectively kept the system neutral. Once E_f was calculated, the second integral could be carried out to calculate the d-band energy from equation 7.3.

The self-consistent change in the potential due to charge transfers between atoms was treated in a simple manner, assuming that only the diagonal elements of the Hamiltonian are important[80]. Having calculated E_f, the total occupancy Q_i of atom i is given by

$$Q_i = \int_{-\infty}^{E_f} N_i(E)\, dE \qquad (7.9)$$

where N_i is the total local density of states at site i, summed over the five d-orbitals. The net charge ΔQ_i at atom i is then given by

$$\Delta Q_i = Q_i - Q_i^o \qquad (7.10)$$

where Q_i^o is the atomic d charge of atom i. The five d orbitals were then assumed degenerate and their self-energies shifted to ε_d, given as[174]

$$\varepsilon_d = \varepsilon_d^o + U\Delta Q_i \qquad (7.11)$$

where U is an intra-atomic electrostatic interaction between orbital electrons and ε_d^o is the atomic d level of the atom. U was taken as 4 eV [175]. Values of ε_d^o and Q_i^o for W and Rh are listed in table 7.1. Self-consistency was achieved within this approximation by calculating the occupancy of each atom, shifting the self-energy according to equation 7.11 and recalculating the occupancy. This procedure was repeated until the change in the atom occupancy was $\lesssim 1 \times 10^{-3}$.

A double counting energy term $1/4U\Delta Q_i^2$, arising from the self-consistent charge transfer has to be subtracted from the d-band energy[174]. The total band energy at site i is thus given as

$$U_d^i = \int_{-\infty}^{E_f} E\, N_i(E)dE - \frac{1}{4} U\Delta Q_i^2 \qquad (7.12)$$

Using equations 7.10 and 7.11, equation 7.12 can be written as

$$\begin{aligned} U_d^i &= \int_{-\infty}^{E_f} (E - \varepsilon_d^i) N_i(E)dE + \varepsilon_d Q_i - \frac{1}{4} U\Delta Q_i^2 \\ &= \int_{-\infty}^{E_f} (E - \varepsilon_d^i) N_i(E)dE + (\varepsilon_d^o + U\Delta Q_i)(Q_i^o + \Delta Q_i) - \frac{1}{4} U\Delta Q_i^2 \end{aligned} \qquad (7.13)$$

The first term on the right hand side of 7.13 is the d-bond energy, U_b^i. The total d-band energy for the system is given by

$$\sum U_d^i = \sum U_b^i + \sum (\varepsilon_d^o Q_i^o + \varepsilon_d^o \Delta Q_i + U Q_i^o \Delta Q_i + \frac{3}{4} U\Delta Q_i^2)$$

Since $\Delta\Sigma Q_i = 0$ and ε_d^o and Q_i^o are the same for the two systems we are comparing, the difference in the band energy between the two systems is given by

$$\Delta \sum U_d^i = \Delta \sum U_b^i + \Delta \sum \frac{3}{4} U\Delta Q_i^2 \qquad (7.14)$$

Our results show (see later) that the charge-transfers are very similar in the two systems, hence the second term in 7.14 is negligible compared to the bond energy term. The results are thus discussed in terms of bond energies rather than band energies (see section 7.3.3).

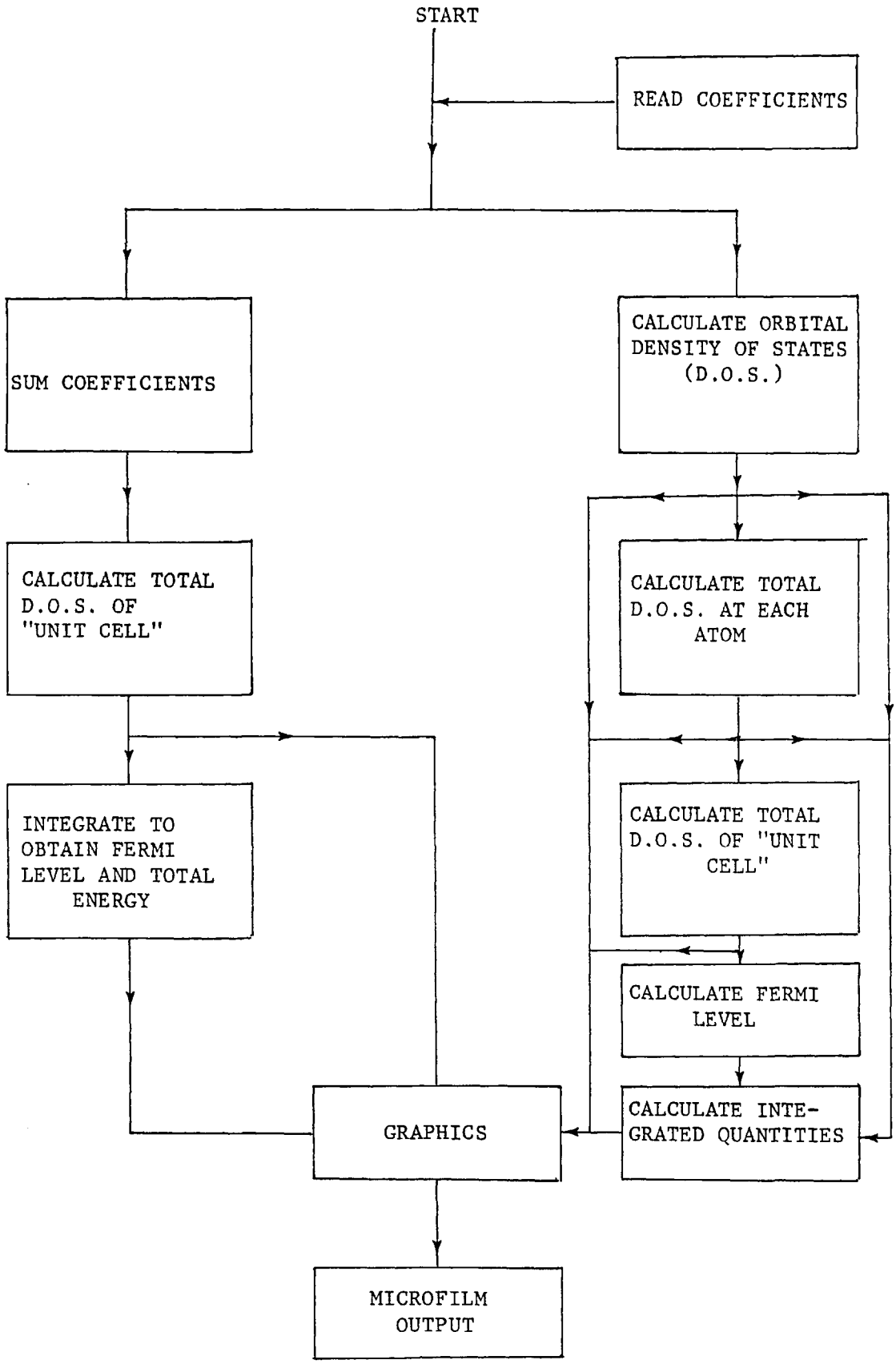


Figure 7.3 Flow diagram of program 2: Calculation of density of states and integrated quantities.

Figure 7.3 shows a flow diagram of the programs used to calculate the integrated quantities.

7.2.5 Accuracy in the calculation

As stated previously the continued fraction continues indefinitely for an infinite system. In practice a finite cluster is used and the continued fraction is terminated at some stage. The absolute accuracy of the calculation depends on the size and shape of the cluster and the number of fractions calculated. However, in comparing the integrated quantities between clusters with similar overall size and shape, it has been shown[80] that the errors cancel out and the difference is due to the different structure. In the present study, a rectangular block of 300 atoms was used and only the adsorbate geometry changed. The overall size and shape of the systems thus remained nearly the same in all cases. It is therefore assumed that the errors due to the finite cluster size cancel out when comparing two adsorbate geometries.

7.3 Results and Discussion

7.3.1 The pure surface

Figure 7.4 shows the local densities of states (d.o.s.) at an atom in the centre of the pure (adatom-free) W(110) surface. The two broad peaks are characteristic of the b.c.c. structure and correspond to bonding and anti-bonding states[81]. The sharp peaks at the band edges are remnants of the delta distribution of the d.o.s.[80]. Their appearance in the d.o.s. curves is due to lack of convergence in the smoothing procedure used in the recursion calculation. Aside from these artefacts at the band edges, the overall features in the d.o.s. are in

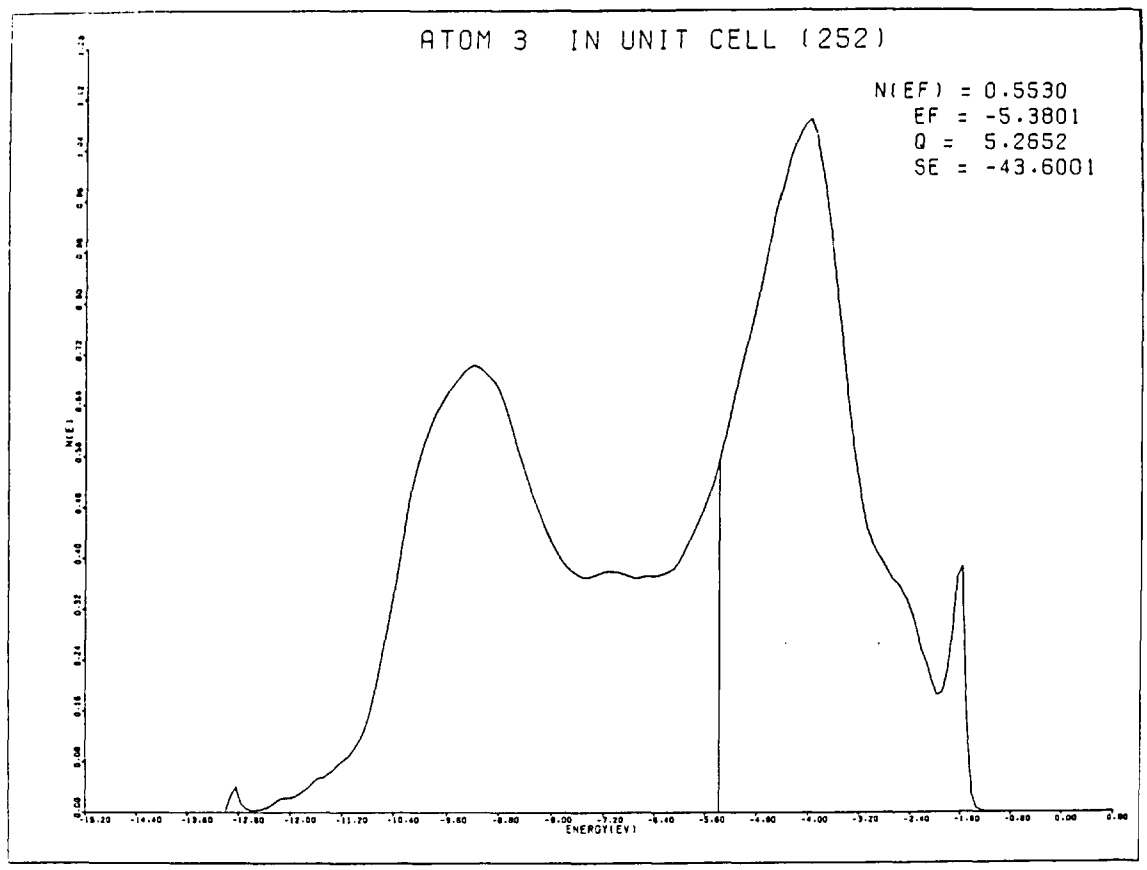


Figure 7.4 The local density of states on the W(110) surface. (N(EF) is the d.o.s. at the Fermi level, E_f; Q is the occupancy and SE is the d-band energy of the atom).

agreement with the calculation of Desjonqueres and Cyrot Lackmann[176], who used the moments method including spin-orbit coupling to obtain the d.o.s. at the W(110) surface.

7.3.2 Local densities of states for tungsten adatoms

The total d.o.s. at a single adatom at the lattice site is shown in figure 7.5a. The d.o.s. appears as a broadened resonance with little structure. The r.m.s. bandwidth, W_{rms}, is much smaller for the adatom d.o.s. than for the surface atom. This is understood in terms of the reduced co-ordination of the adatom. W_{rms} for a d-band is given as[80]

$$5W_{rms}^2 = \sum_i Z_i\{(dd\sigma)^2 + 2(dd\pi)^2 + 2(dd\delta)^2\} \qquad (7.15)$$

where the summation is over near neighbours. An adatom on W(110) has 4 ($Z_1 = 2$, $Z_2 = 2$) near neighbours while a surface atom has 10 ($Z_1 = 6$, $Z_2 = 4$) near neighbours. Thus, the narrowing of the d-band at the adatom is expected. The recursion method preserves the moments of the d.o.s.[80]. W_{rms} is related to the second moment, μ_2, by[80]

$$5W_{rms} = \mu_2 \qquad (7.16)$$

where

$$\mu_2 = \int_{-\infty}^{\infty} (E - \varepsilon_d)^2 n(E)dE \qquad (7.17)$$

μ_2 was calculated from 7.17 for a single adatom and underlying substrate atoms. The result was in agreement with values obtained using equations 7.15 and 7.16 (see appendix D1).

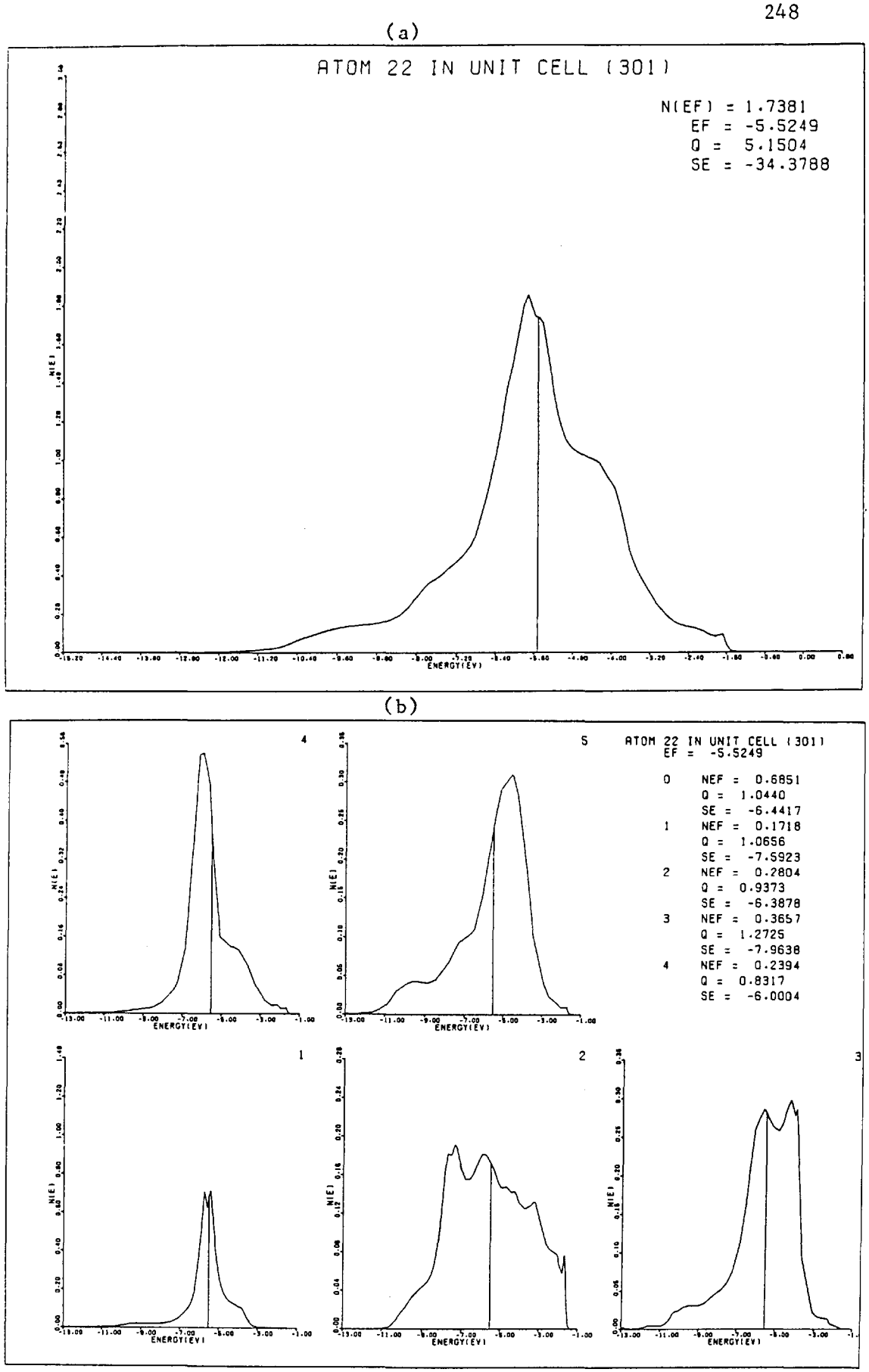
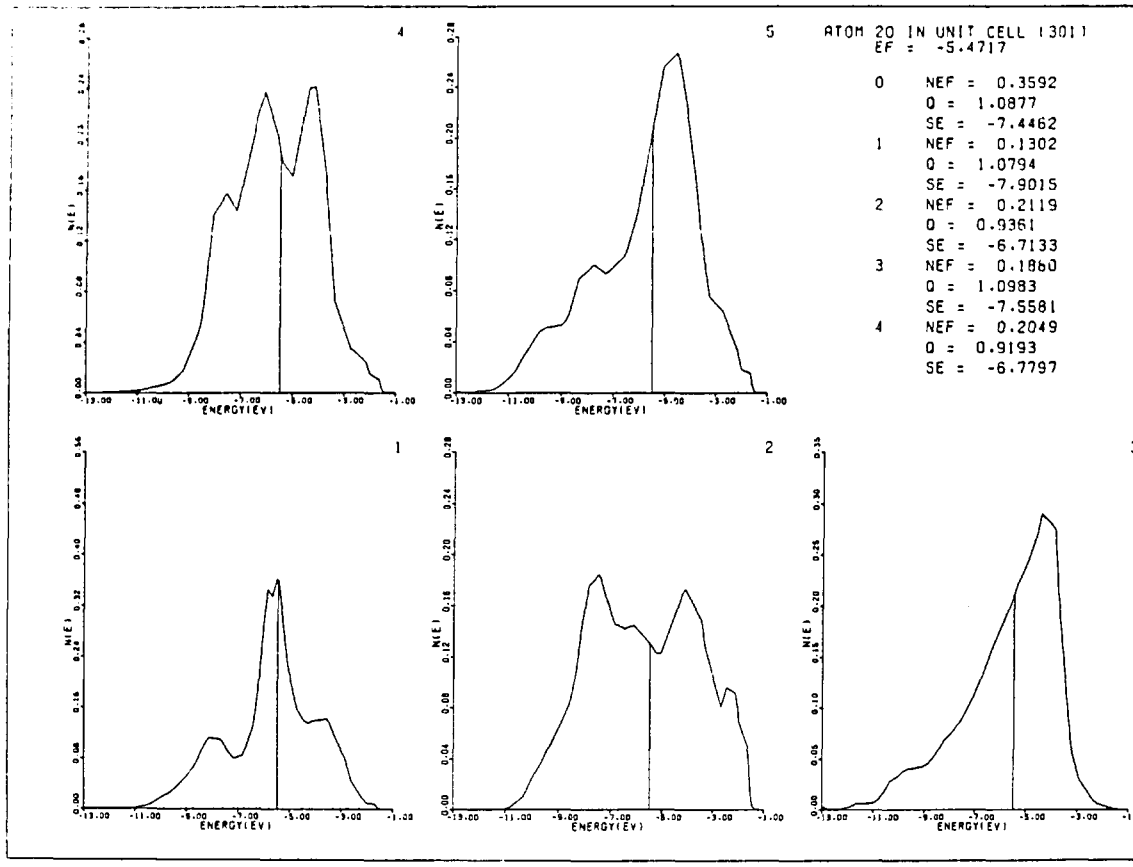


Figure 7.5 Density of states at a single tungsten adatom on the W(110) surface: (a) total d.o.s., (b) partial densities of states (the numbers 1-5 refer to the xy, yz, zx, x^2-y^2 and $3z^2-r^2$ orbitals, respectively).

Figure 7.5b shows the individual orbital d.o.s. at the adatom. The numbers 1-5 in the figure refer to the xy, yz, zx, x^2-y^2 and $3z^2-r^2$ orbitals, respectively. Comparing figures 7.5a and 7.5b, it is seen that the width of the total d.o.s. results mainly from the yz, zx and $3z^2-r^2$ orbitals. The discrete character of the in-plane xy and x^2-y^2 orbitals is expected since the bonding of an isolated adatom is directed towards the surface. These orbitals are essentially non-bonding and are more nearly filled compared to the other orbitals. The adatom has a total net charge of 0.15 electrons transferred from the substrate atoms of the "unit cell". The physical reason for this transfer of charge can be pictured in a simple manner. The narrow adatom d-band is centred below the Fermi level and could thus become more nearly filled than the band for surface atoms. However, the charge-transfer causes the d-level to rise, which prevents any extensive increase in the adatom charge. It should be noted that the charges actually lie on orbitals. Since the tail of one orbital overlaps the tail of another, the net charge-transfers probably largely cancel out[175].

As the adatom forms a bond with a second adatom at a neighbouring lattice site, the local d-band d.o.s. is expected to broaden due to the increased co-ordination. The net occupancy of the adatom orbitals consequently decreases and the d-level shifts downward. This can be seen by comparing figure 7.6a, which shows the orbital d.o.s. at adatom 1 in the trimer clusters, with figure 7.5 for the single adatom. In the clusters adatoms 1 and 2 are first neighbours and it is seen that this produces broadening and additional features in the orbital d.o.s., particularly for the in-plane xy and x^2-y^2 orbitals. The non-bonding character of these two orbitals for the single adatom is considerably reduced for adatom 1 of the cluster, bonding and anti-

(a)



(b)

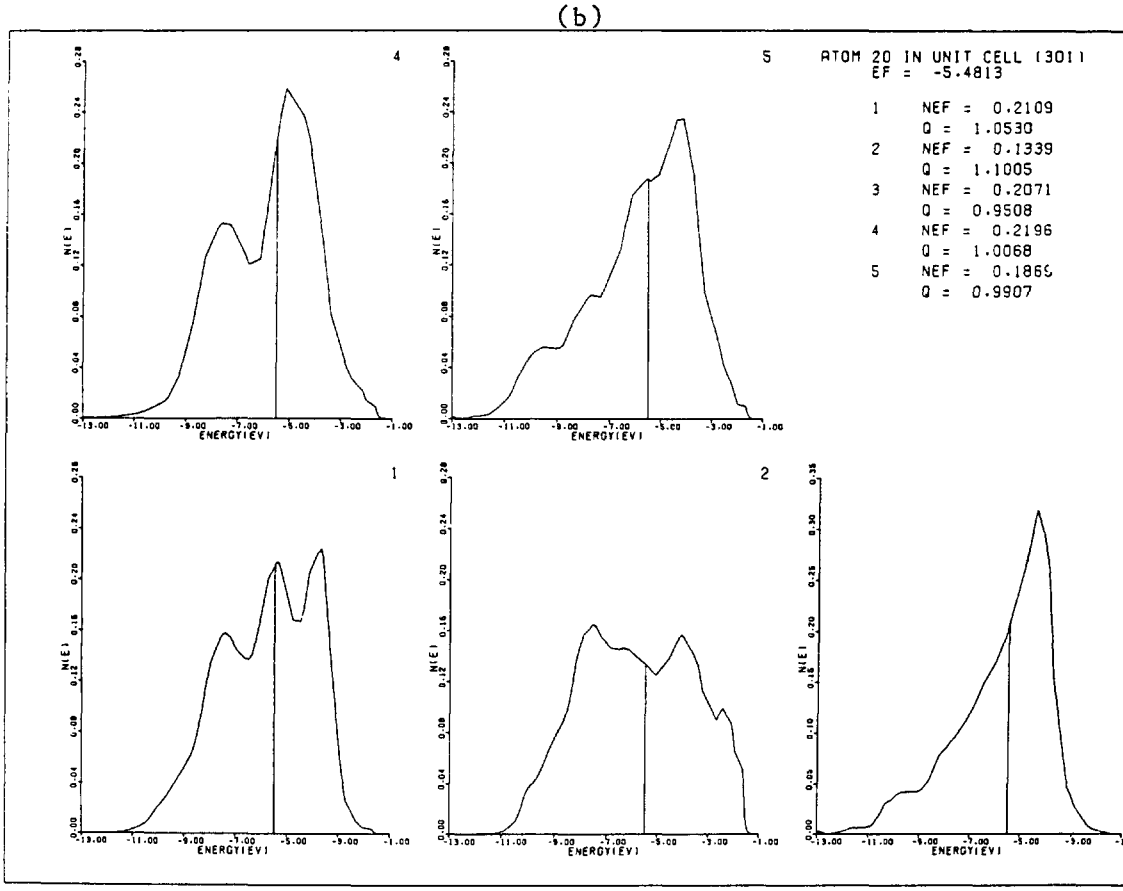


Figure 7.6 Orbital densities of states at adatom 1 of the (a) linear and (b) triangular cluster of tungsten.

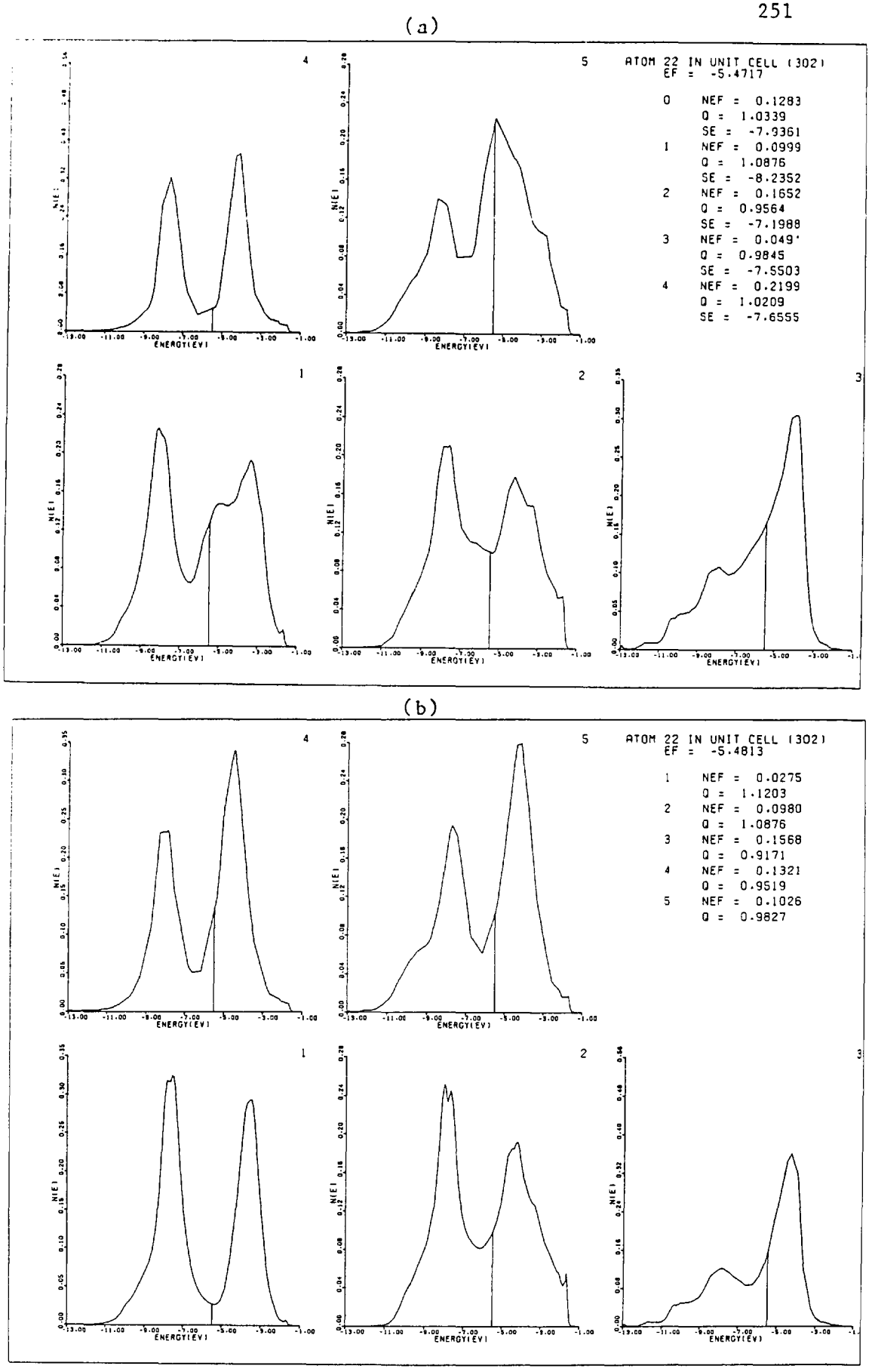


Figure 7.7 Orbital densities of states at adatom 2 of the (a) linear and (b) triangular cluster of tungsten.

bonding peaks appear and the occupancy decreases.

In both cluster configurations, adatom 2 forms two more first-neighbour bonds than a single adatom. This results in the virtual elimination of non-bonding peaks from the d.o.s. for the in-plane orbitals of adatom 2, which split almost completely into bonding and anti-bonding regions for both linear and triangular clusters, figure 7.7. The consequence of interaction with two in-plane adatoms are also seen in figure 7.6b which shows the orbital d.o.s. for adatom 1 of the triangular cluster. In this cluster, adatom 1 is a second-neighbour to adatom 3 so that the orbitals of the two adatoms interact directly. This splits the d.o.s. of the x^2-y^2 orbital into bonding and anti-bonding states and eliminates the non-bonding peak of the corresponding orbital in the linear-chain cluster, figure 7.6a.

7.3.3 Orbital and bond energies for tungsten adatoms

The modified self-energies, ε_d, the d-band structure energies, U_d, and the occupancy, Q, of individual orbitals of the non-equivalent adatoms and surface atoms are tabulated in appendix D2 for a tungsten adatom and for the linear and triangular clusters. The surface and adatom charges are also displayed in figures D1. As discussed in section 7.2.4 and for the purposes of demonstrating how adatom bonding is influenced by the number of neighbouring adatoms and cluster structure, it is more meaningful to work here in terms of bond energies U_b given for orbital α at site i as

$$U^i_{b\alpha} = \int_{-\infty}^{E_f} (E - \varepsilon^i_d) n^i_\alpha(E)\, dE \qquad (7.18)$$

To demonstrate the effect of interactions between adatoms, the bond energies of the orbitals for adatoms in clusters were calculated relative to the equivalent atoms and orbitals for the single adatom case using

$$U_{R\alpha}^{ic} = \int_{-\infty}^{E_f} (E - \varepsilon_d^{ic}) n_\alpha^{ic}(E) dE - \int_{-\infty}^{E_f'} (E - \varepsilon_d^{is}) n_\alpha^{is}(E) dE \qquad (7.19)$$

where the superscripts ic and is refer to the cluster and single atom sites, respectively. Thus, all bond energies for adatoms were calculated relative to the single adatom case, while for surface atoms 4, 5 and 10 in contact with the clusters, atom 4 in the single atom system provided the reference. Simiarly, atom 2 of the single atom system provided the reference for atom 6 in the linear cluster system and atom 11 of the triangular cluster system. The relative bond energies U_R^{ic} obtained this way are given in table 7.3 together with the total relative bond energies U_{RT}^{ic} which include the double counting contribution $\frac{1}{4} U\{\Delta Q_{ic}^2 - \Delta Q_{is}^2\}$. For a particular adsorbate species, in this case tungsten, the relative values reflect chiefly the effect of increasing the adatom co-ordination. This is readily seen by comparing the total bond energies of adatoms 1 and 2 in both linear and triangular clusters, since $U_R^{i=2}$ for adatom 2 with two neighbouring adatoms is approximately double $U_R^{i=1}$ for adatom 1 with only one near neighbour. The calculated relative bond energies are considered later with the data for rhodium.

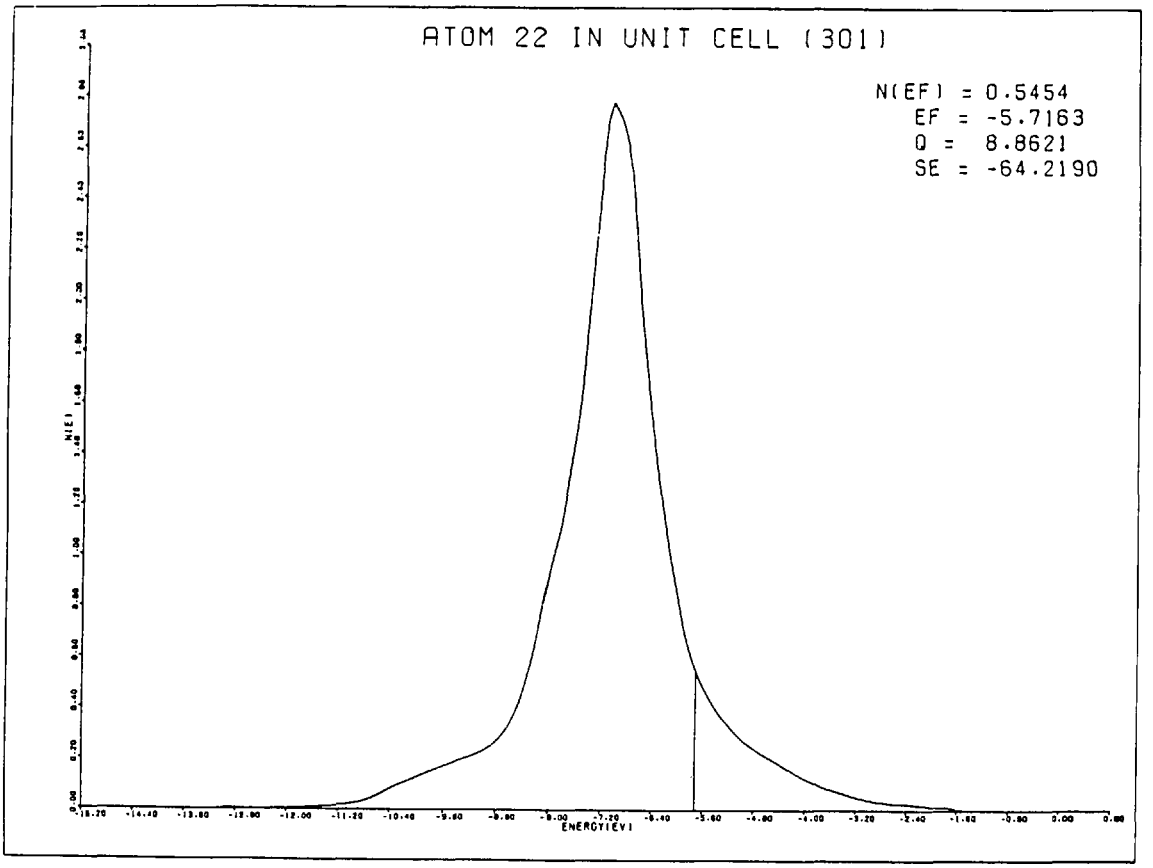
7.3.4 Densities of states and bond energies for rhodium on W(110)

Calculations were performed for Rh adatom clusters with identical geometry to that of W clusters, but using different input parameters to describe the adatoms and their coupling to each other and to the substrate (tables 7.1 and 7.2). The local d.o.s. and bond energies were calculated for the single adatom and for the linear and triangular clusters.

The orbital d.o.s. for a single rhodium adatom are shown in figure 7.8. As found for the single W adatom, the in-plane orbitals are essentially non-bonding in character but for Rh are almost completely filled. The major contribution to the width of the total local d.o.s. comes from the yz, zx and $3z^2-r^2$ orbitals. However, the total d.o.s. is narrower than for the single W adatom due to the weaker coupling of the Rh adatom to the substrate. This can be seen from the second moment of the d.o.s. at the single Rh adatom calculated from equations 7.15-7.17 (see appendix D.1). The ratio of the bandwidths W^{Rh}_{rms}/W^{W}_{rms} was calculated to be $\approx$0.6. The calculated net charge at the adatom is considerably larger compared to that at the W adatom, since in this case the d-band is narrower and lies further below the Fermi level.

The individual orbital d.o.s. at adatom 1 of the rhodium clusters are shown in figure 7.9. As found for the W case, comparison with the single adatom d.o.s. shows that the non-bonding character of the xy orbital of adatom 1 has decreased and the level has broadened, although without a clear splitting-off of bonding and anti-bonding peaks. Similar features are found in the d.o.s. of the x^2-y^2 orbital, although the orbital d.o.s. at adatom 1 of the triangular cluster shown in figure 7.9b shows that the direct overlap between adatoms 1

(a)



(b)

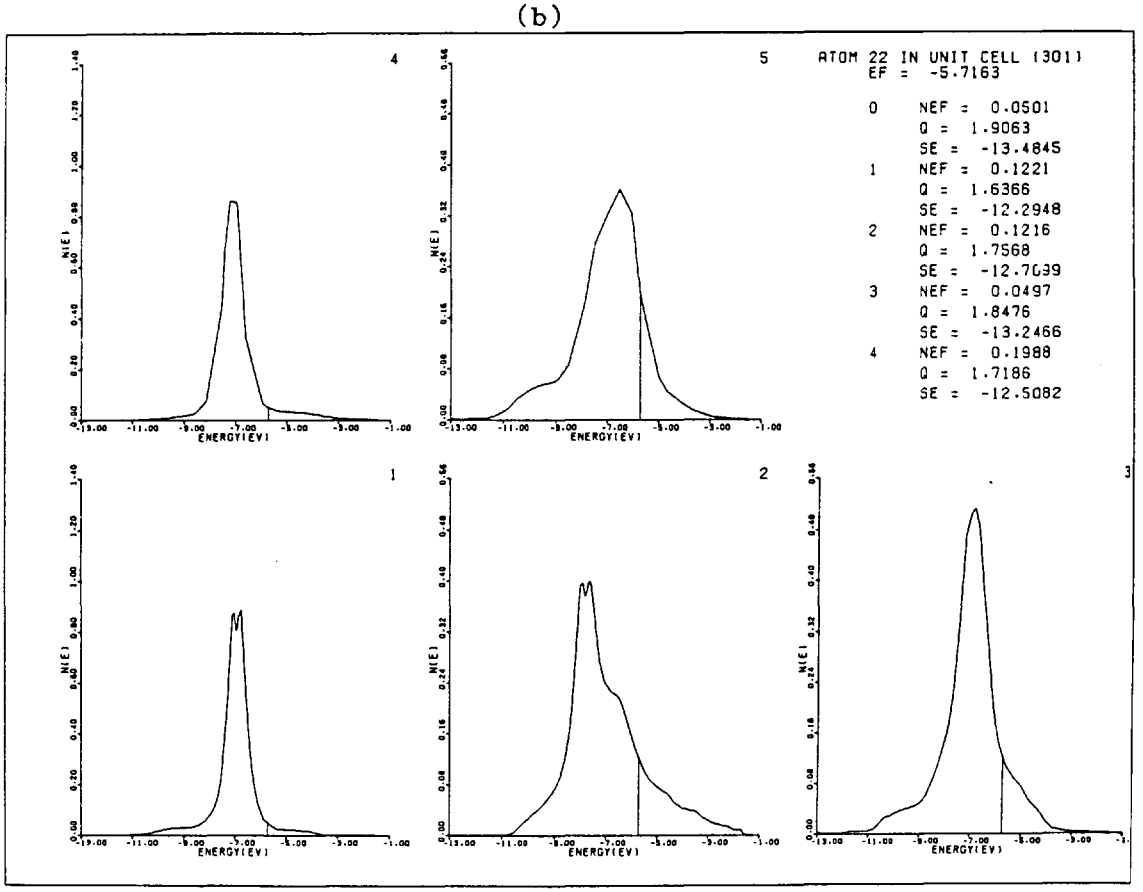


Figure 7.8 Density of states at a single rhodium adatom on the W(110) surface: (a) total d.o.s., (b) orbital densities of states.

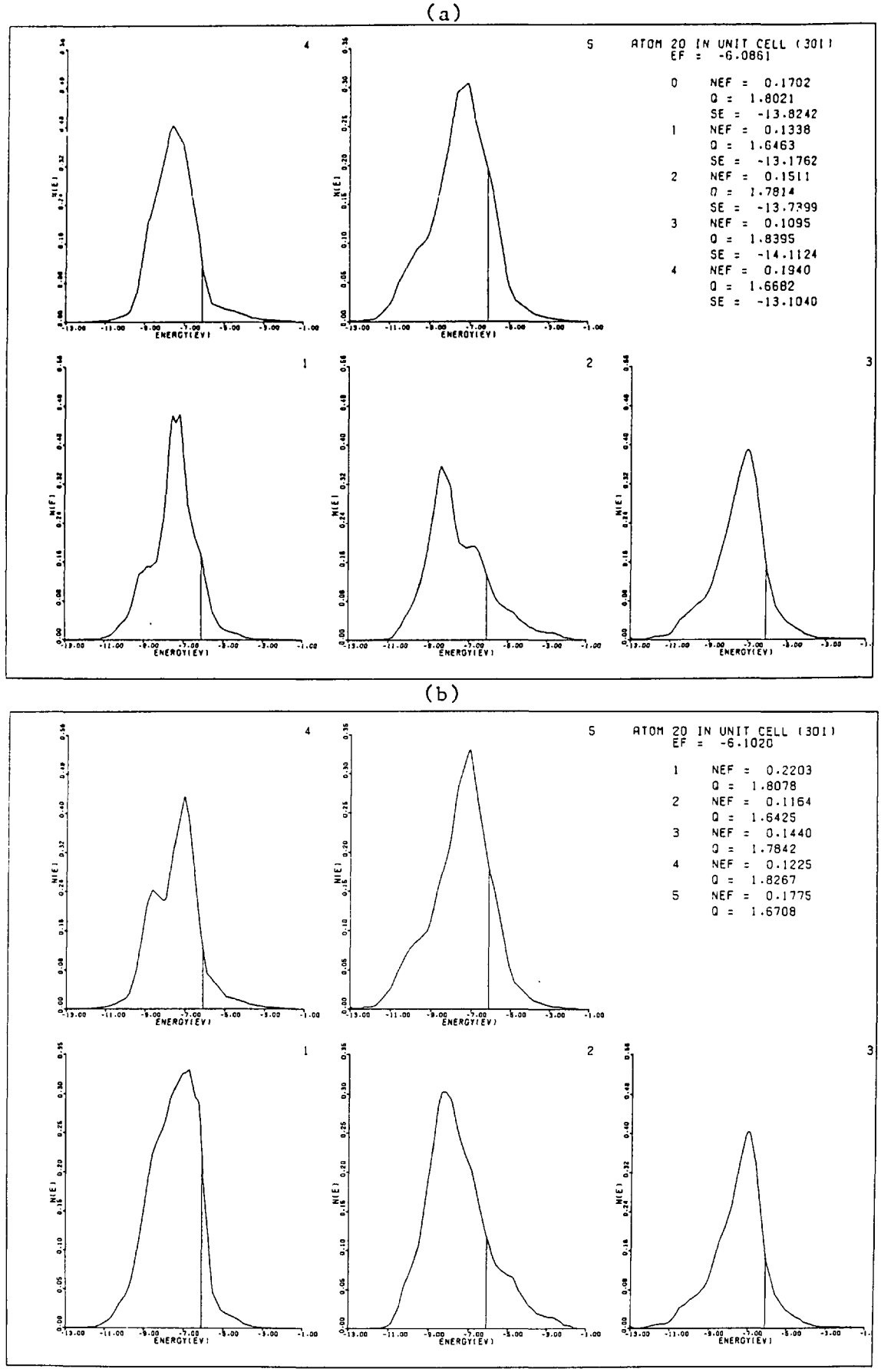


Figure 7.9 Orbital densities of states at adatom 1 of the (a) linear and (b) triangular cluster of rhodium.

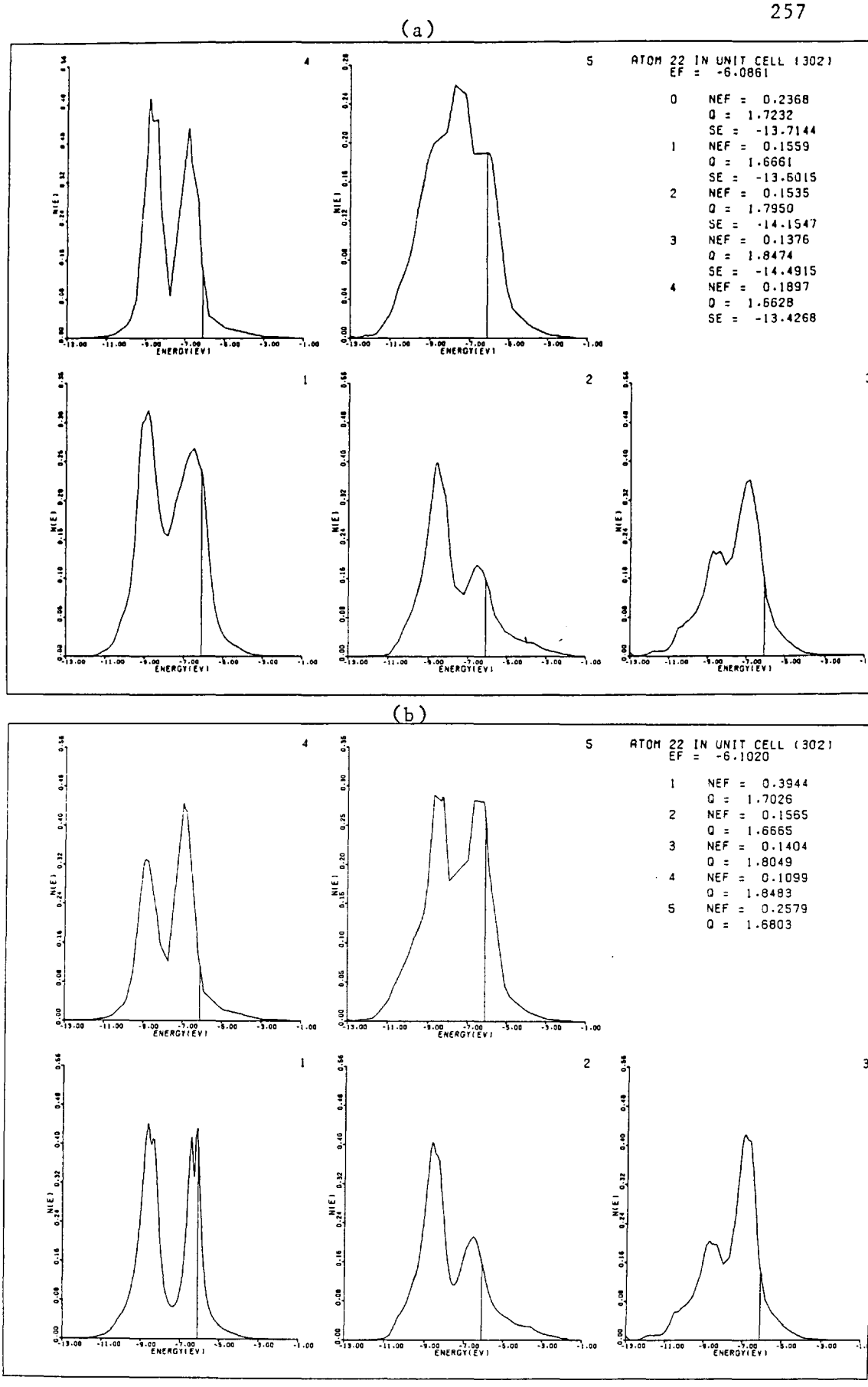


Figure 7.10 Orbital densities of states at adatom 2 of the (a) linear and (b) triangular cluster of rhodium.

and 3 results in the appearance of a bonding peak in the d.o.s. of the x^2-y^2 orbital.

The splitting into bonding and anti-bonding states are much more pronounced for the in-plane orbitals of adatom 2 of the clusters, figure 7.10, and these orbitals contribute significantly to the width of the total local d.o.s. The main changes in the d.o.s. at adatom 2 in going from the linear to the triangular configuration are a much clearer splitting of the xy orbital into bonding and anti-bonding regions and pronounced changes in the $3z^2-r^2$ orbital. The non-bonding peak in the d.o.s. of the $3z^2-r^2$ orbital is reduced considerably and distinct bonding and anti-bonding peaks appear.

The calculated net charges on the adatoms and adjacent surface atoms for a single Rh adatom, linear and triangular Rh clusters are shown in figures D4-6 (appendix D). The modified self energies, ε_d, the d-band structure energies, U_d, and the occupancy, Q, of individual orbitals of the non-equivalent atoms of the three structures are listed in appendix D2. The calculated relative bond energies, U_R, that will be used in the following discussion, are given in table 7.4.

7.3.5 The relative stability of linear and triangular clusters of tungsten and rhodium

The calculated total bond energies relative to the single adatom system for the atoms of the linear and triangular clusters of W and Rh are shown in figure 7.11. It is clear that the substrate atoms peripheral to the adatom clusters do not change significantly in energy. The extra stability of atom 10 beneath the triangular clusters reflects its interaction with two adatoms (1 and 3). These interactions are shown to be almost pairwise additive in appendix D3 where the energy of a bare surface atom is compared to its energy when it forms either

Table 7.3 Orbital and bond energies, U_R (eV), for atoms of the linear and triangular geometries of tungsten relative to the single adatom.

ATOM	ORBITAL					TOTAL *
	1 xy	2 yz	3 zx	4 x^2-y^2	5 $3z^2-r^2$	
			LINEAR CLUSTER			
1	-0.6557	-0.1366	-0.2436	-0.4761	-0.2053	-1.699
2	-1.3035	-0.2593	-0.4757	-0.9703	-0.3491	-3.3377
4	+0.0228	+0.0132	+0.0287	+0.0084	+0.0055	+0.0716
5	-0.0126	+0.0162	-0.051	-0.0053	-0.0365	-0.0942
10	-0.0124	+0.0058	-0.0601	+0.0049	-0.0419	-0.1025
11	+0.0149	+0.0085	+0.0184	+0.0016	-0.0107	+0.0291
			TRIANGULAR CLUSTER			
1	-0.8498	-0.1672	-0.2515	-0.5619	-0.2463	-2.0637
2	-1.4355	-0.2736	-0.5015	-0.8705	-0.5105	-3.573
4	+0.0199	+0.0292	+0.025	+0.0106	+0.0167	+0.0996
5	-0.06	+0.0201	-0.0502	+0.0086	-0.029	-0.0635
6	+0.016	+0.0128	+0.0417	+0.017	+0.0088	+0.0869
10	-0.0946	-0.3616	-0.2623	-0.1114	-0.3306	-1.162
11	+0.0255	-0.0018	+0.0291	+0.0077	-0.0042	+0.0454

*The total relative energy includes the double counting $\{\frac{1}{4}U\Delta Q^2\}$ term.

Table 7.4 Orbital and total bond energies, U_R (eV), for atoms, of the linear and triangular geometries of Rhodium relative to the single adatom case.

ATOM	ORBITAL 1 xy	2 yz	3 zx	4 x^2-y^2	5 $3z^2 - r^2$	TOTAL *
			LINEAR CLUSTER			
1	-0.17	+0.0055	+0.0281	-0.0069	-0.1173	-0.0599
2	-0.3418	+0.0261	+0.0359	+0.0033	-0.1832	-0.1972
4	+0.0096	-0.0183	+0.0234	-0.0356	-0.0177	-0.05
5	-0.0138	-0.0007	-0.025	+0.0096	-0.015	-0.0577
10	-0.0189	-0.0196	-0.051	-0.0068	-0.0204	-0.1316
11	-0.0061	-0.0181	+0.0003	-0.0151	-0.0259	-0.0699
			TRIANGULAR CLUSTER			
1	-0.1508	-0.0215	+0.0312	-0.0189	-0.1265	-0.0774
2	-0.351	+0.0268	+0.0562	+0.0039	-0.1228	-0.135
4	-0.0104	-0.0141	+0.0216	-0.0341	-0.0183	-0.0469
5	-0.0184	-0.0141	-0.0404	-0.0041	-0.014	-0.1067
6	-0.0125	-0.0277	-0.0096	-0.0272	-0.027	-0.1115
10	-0.0573	-0.2915	-0.1301	-0.0563	-0.1907	-0.7263
11	-0.0047	-0.0218	+0.0036	-0.0137	-0.0245	-0.0609

*The total relative energy includes the double counting $\{\frac{1}{2}U\Delta Q^2\}$ term.

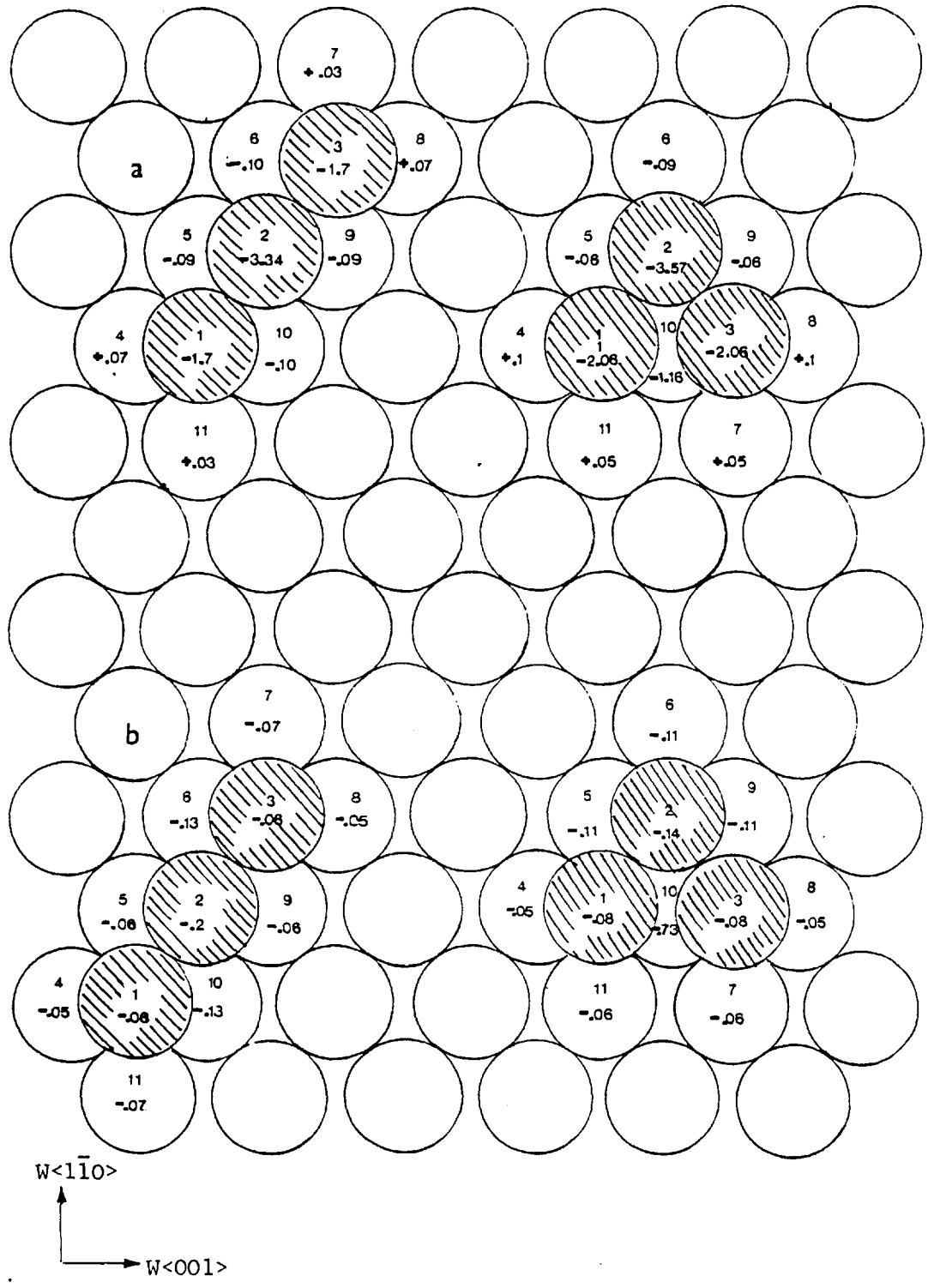


Figure 7.11 Total relative energies U_R (eV) for adatoms and near neighbour surface atoms of the linear and triangular structures of (a) tungsten and (b) rhodium on W(110).

one or two bonds to adatoms.

In tungsten clusters the adatoms are significantly stabilized and it is clear from the bond energies in table 7.3 that the largest contributions come from interactions of the in-plane orbitals, especially the xy orbitals that are directed along the bond directions. It is notable that the extra stability of atom 2 reflects an almost pairwise addition of its interactions with the other two adatoms. The in-plane orbitals are also mainly responsible for the greater stability of the triangular cluster relative to the linear cluster. The largest contribution to the increased stability of adatom 1 relative to adatom 1 of the linear cluster comes from the xy orbital, but the x^2-y^2 and $3z^2-r^2$ orbitals are important in stabilizing adatom 2 of the triangular cluster. Comparison of the orbital d.o.s. (figures 7.6a and 7.6b) shows that in the triangular cluster, the xy and x^2-y^2 orbitals of adatom 1 have broadened into bonding and anti-bonding states, while the non-bonding peaks have decreased. This is clearly seen in figure 7.12 which compares, on the same scale, the xy orbital d.o.s. of adatom 1 of the linear and triangular cluster. The significant contribution of the $3z^2-r^2$ orbital to the stability of adatom 2 in the triangular cluster comes from reduced occupation of non-bonding states and increased occupation of bonding states, as can be seen in figure 7.13 where the d.o.s. of the $3z^2-r^2$ orbital of adatom 2 in the two clusters are compared. Comparison of the orbital charges shown in figures 7.7a and 7.7b shows that the bonding is also enhanced by the greater splitting of the xy orbital, which leads to transfer of electron charge from the $3z^2-r^2$ orbital to states of lower energy in the xy orbital. These results indicate that for a half-filled band the depletion of the non-bonding states and broadening

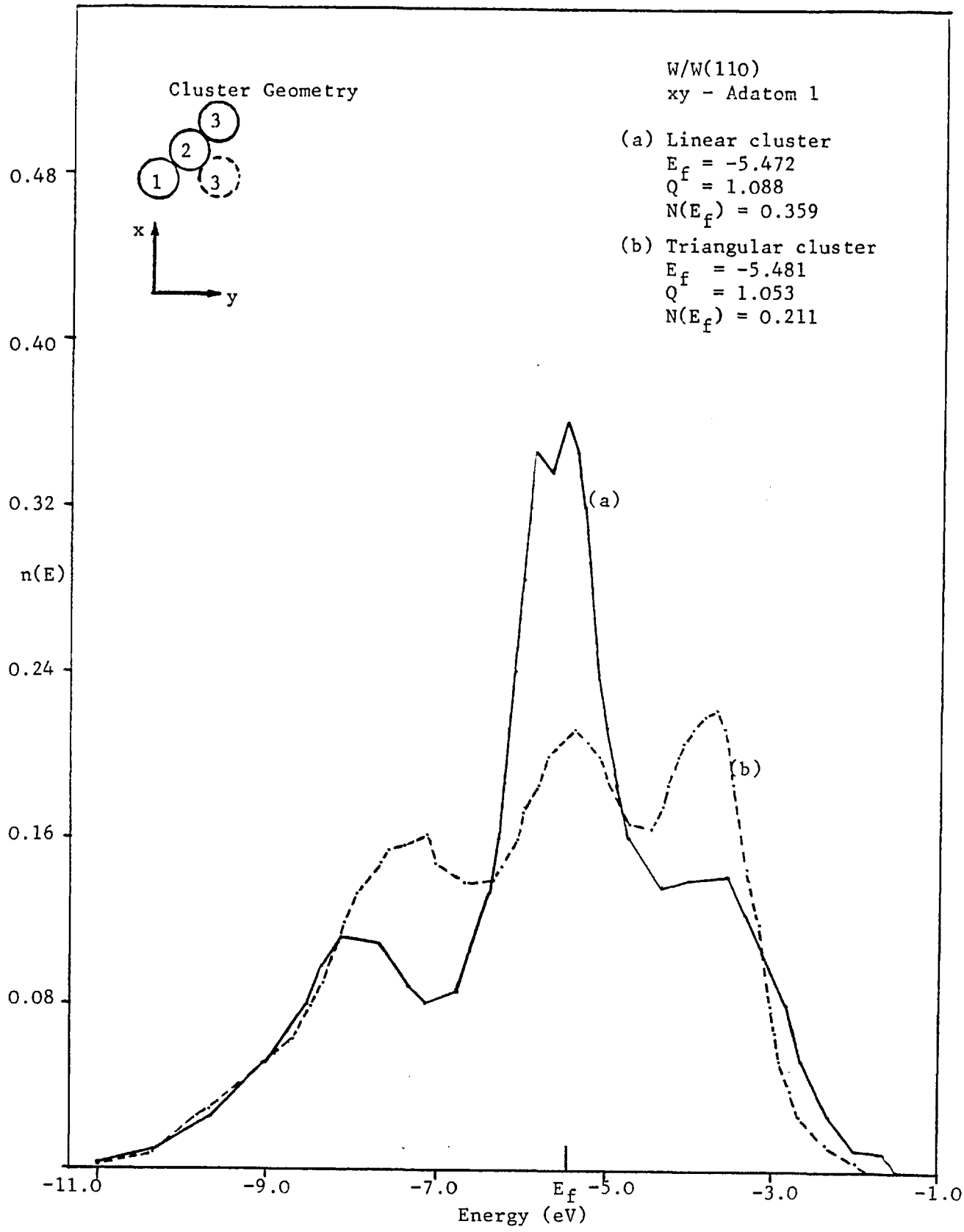


Figure 7.12 xy orbital density of states at adatom 1 of linear and triangular tungsten clusters.

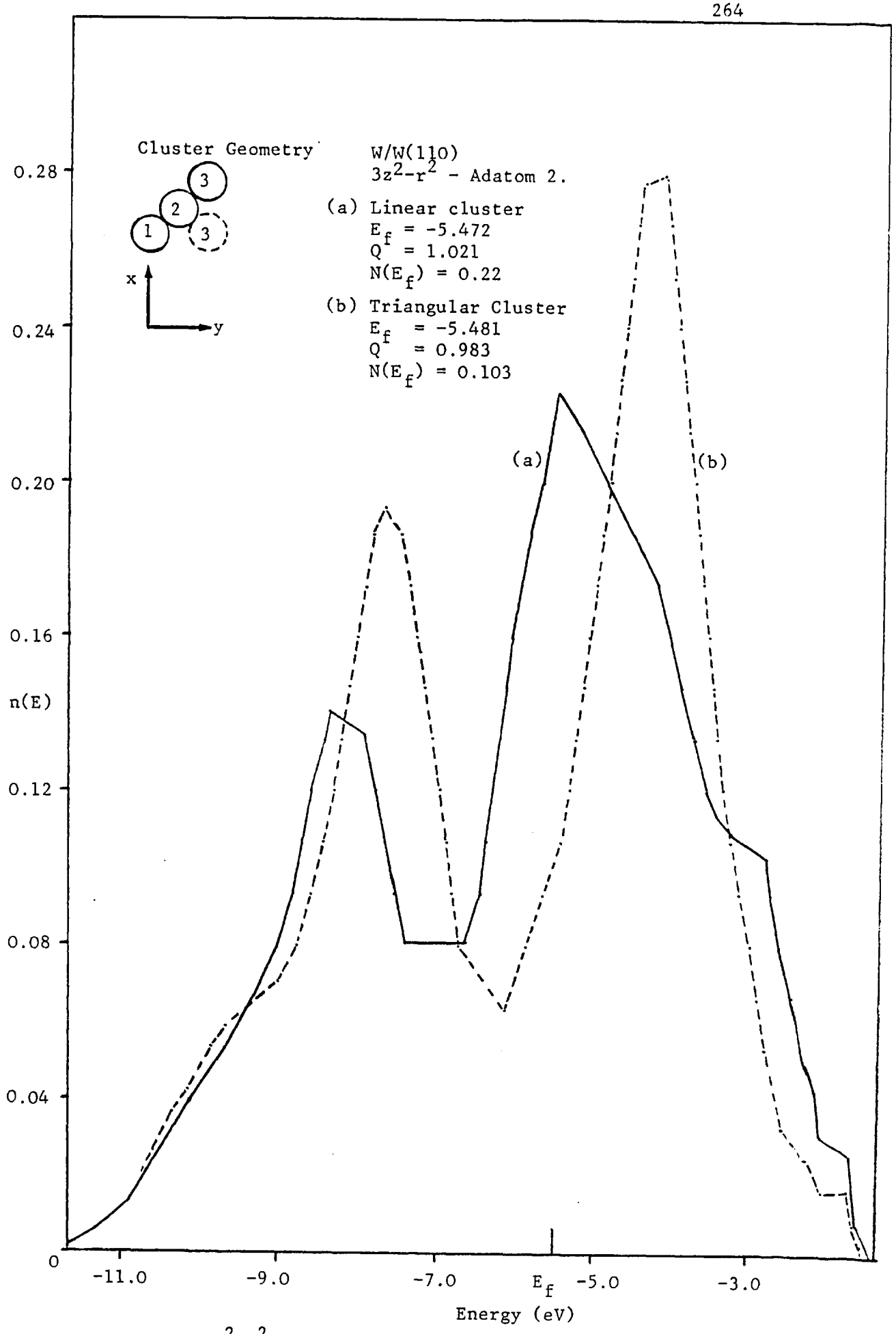


Figure 7.13 $3z^2-r^2$ orbital density of states at adatom 2 of the linear and triangular tungsten clusters.

into bonding and anti-bonding states would always tend to favour the triangular cluster. The total difference in the bond energies of the eleven atoms of the triangular and linear cluster was calculated to be -1.66 eV, clearly favouring the triangular cluster, in agreement with experimental observations.

For rhodium clusters the relative bond energies of the adatoms are small and indicative of weak bonding. Furthermore, the changes in going from the linear to the triangular cluster differ from the tungsten case (cf. figures 7.11a and 7.11b, and tables 7.3 and 7.4). The lower values for the bond energies can be understood in terms of a greatly reduced contribution from the nearly filled in-plane orbitals to the bonding. Comparison of the linear and triangular clusters shows that the energy of adatom 1 is very similar in both cases, while adatom 2 is significantly less stable in the triangular cluster. The total calculated energy of the adatoms is higher for the triangular cluster than for the linear cluster, and thus favours the linear geometry for the cluster. The origin of these differences can again be seen by comparing the orbital densities of states. The xy orbital d.o.s. at adatom 1 in the triangular cluster shows a broadening of the non-bonding peak into bonding and anti-bonding states, figure 7.14, similar to that found for W, though the division between the two states is not strong. Unlike the tungsten result, however, the xy orbital contributes less to bonding in the triangular cluster compared to the linear cluster. The reason for this is that the d.o.s. of the xy orbital in the triangular cluster is skewed toward the anti-bonding states which are also counted in calculating the energy, since the d-band is more than half-filled in this case. Table 7.4 shows that the main contribution to the higher energy of adatom 2 in the triangular cluster comes from

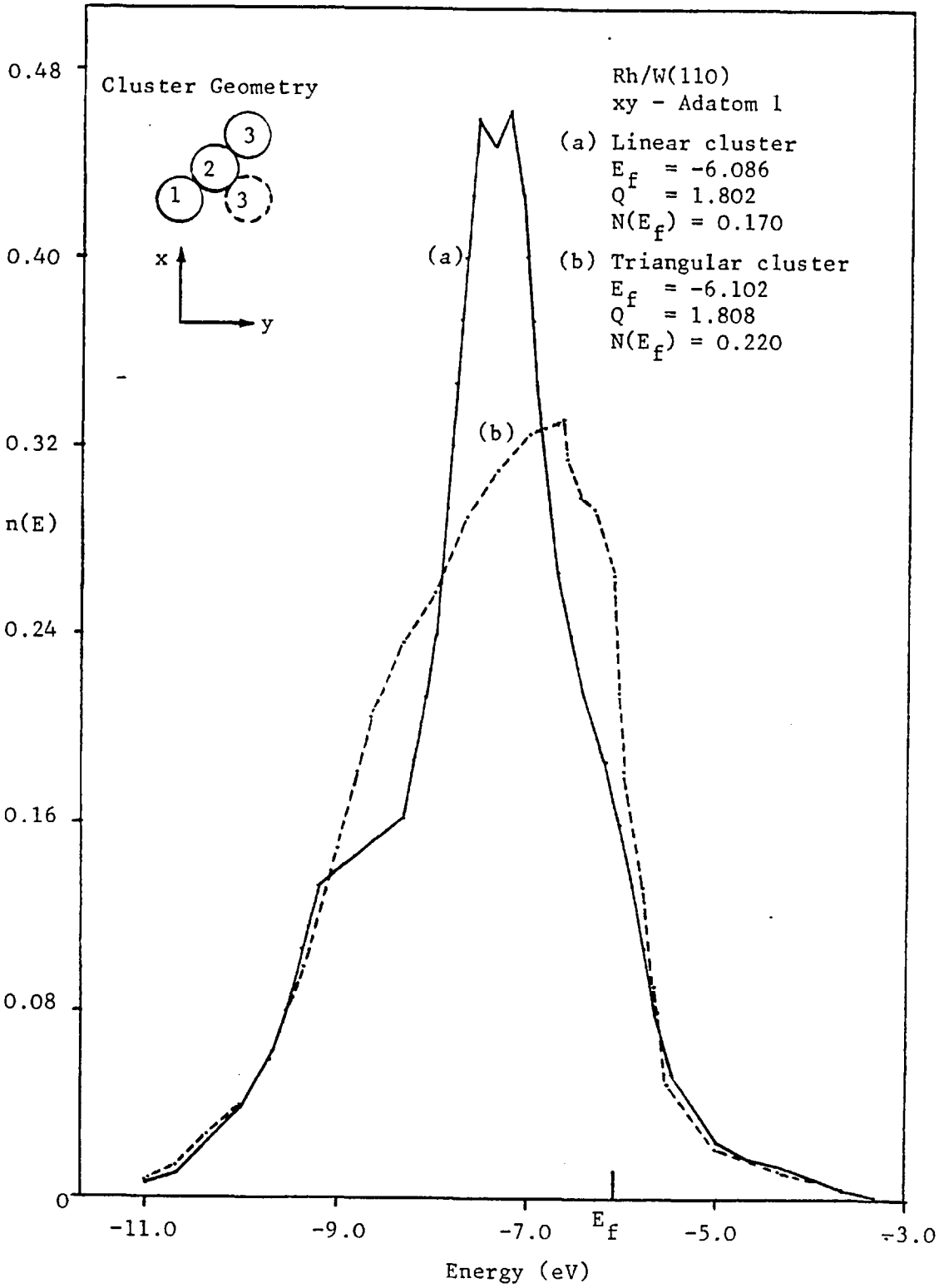


Figure 7.14 xy orbital density of states at adatom 1 of the linear and triangular rhodium clusters.

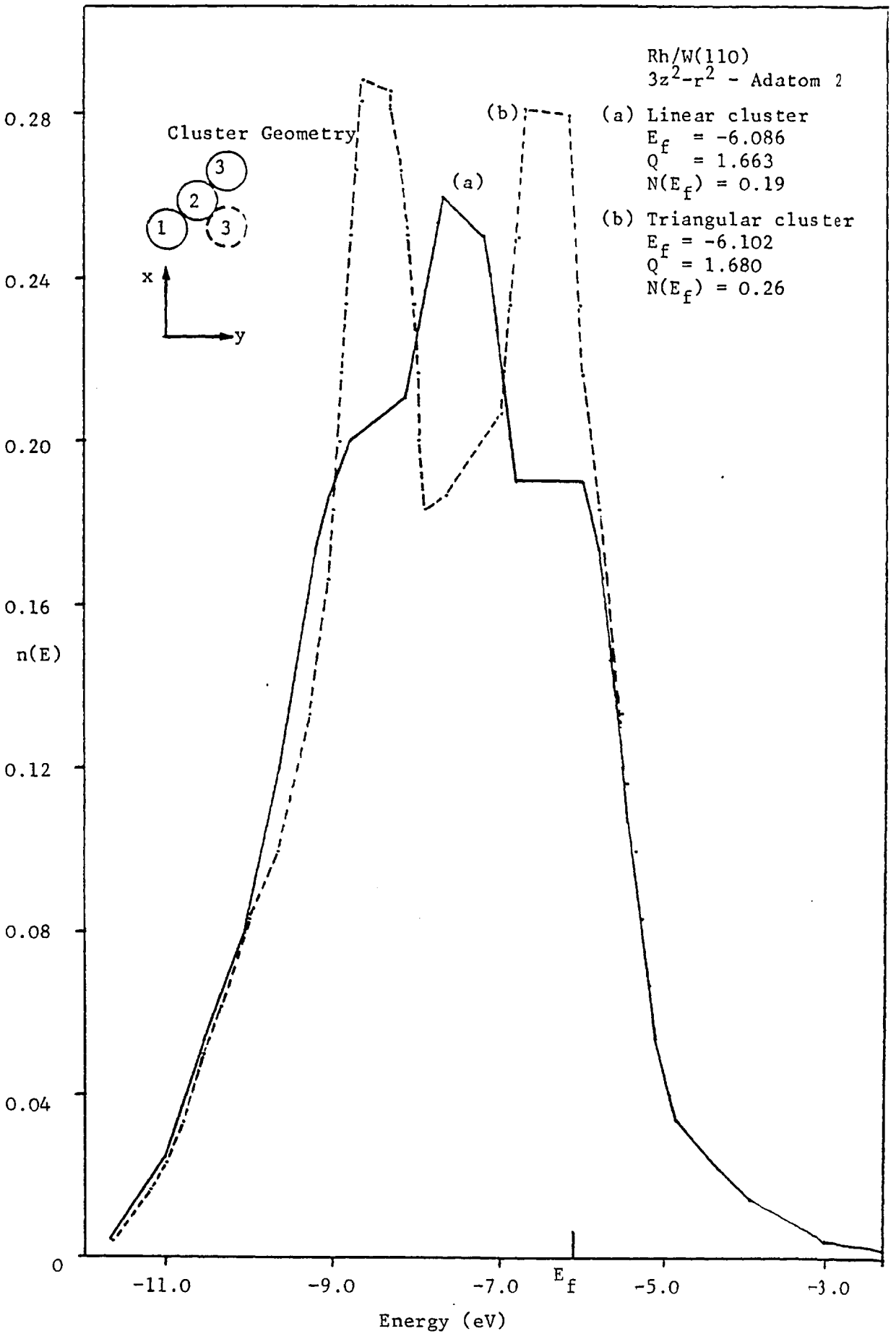


Figure 7.15 $3z^2-r^2$ orbital density of states at adatom 2 of the linear and triangular rhodium clusters.

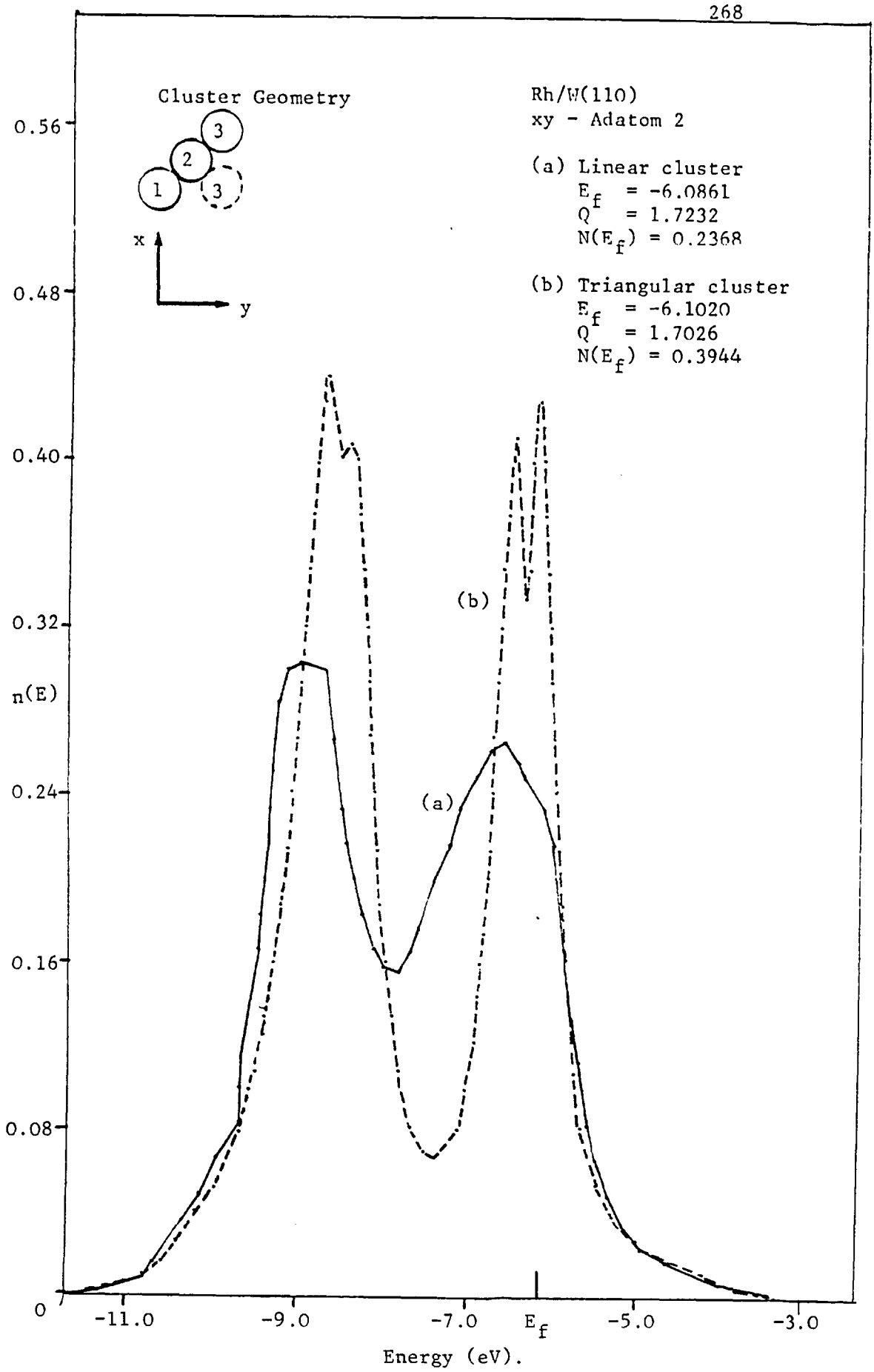


Figure 7.16 xy orbital density of states at adatom 2 of the linear and triangular rhodium clusters.

the $3z^2-r^2$ orbital. Comparison of the d.o.s. of the $3z^2-r^2$ orbital of adatom 2 in the two clusters shows that its non-bonding peak in the linear cluster is substantially reduced and broadened clearly into bonding and anti-bonding peaks, figure 7.15. Comparison of the orbital charges and d.o.s. shows that the greater splitting of the xy orbital d.o.s. of adatom 2, figure 7.16, leads to transfer of electrons from the non-bonding region of the xy orbital in the linear cluster to the anti-bonding region of the $3z^2-r^2$ orbital just below the Fermi level. This charge transfer is in the opposite sense to that in the tungsten cluster and favours the linear geometry for Rh. The instability of adatom 2 in the triangular cluster is not compensated by the small decrease in energy of adatoms 1 and 3, suggesting that the end adatoms with electrons in orbitals that are substantially non-bonding largely determine the stable structure for rhodium.

The total difference in bond energy between the eleven atoms of the Rh triangular and linear system was calculated to be -0.64 eV, in favour of the triangular system. This is contrary to the experimental observation but the trend in the stability of the triangular system in going from tungsten to rhodium is correct: the triangular cluster is more stable for tungsten than for rhodium.

7.3.6 Calculation of a core repulsion term

In the triangular clusters adatom 3 is a second neighbour to adatom 1, while in the linear clusters the two are further apart. It is therefore possible that core repulsion, which has been neglected in the above calculations and which would be expected to be more important in the triangular configuration, could be important in determining the correct structure. It is, for example, necessary to

consider hard core repulsion when comparing the b.c.c. with the close-packed structures at the end of the transition metal series[81].

An estimate of the magnitude of the repulsion term can be obtained in a simple manner, assuming a tenth power law for the interaction. The energy of an atom in the bulk is then given as[175]

$$U = \frac{1}{2} \Sigma \frac{A}{R^{10}} + U_b \qquad (7.20)$$

where A is a constant and the summation is over all the atoms in the solid. The factor 1/2 corrects for the double counting in the summation. In calculating the d-bond energy, U_b, only the first and second neighbour interactions, governed by a fifth power law (equation 7.4), were considered. Since an atom in the bulk has 8 first neighbours at a distance $\sqrt{3}/2\,R$ and 6 second neighbours at a distance R, U can be approximated by

$$U \quad \frac{1}{2} \{\frac{8}{\sqrt{3/2}} + 6\} \frac{A}{R^{10}} + \frac{B}{R^5} \qquad (7.21)$$

where U_b is written as B/R^5. Since at equilibrium $dU/dR = 0$, A can be estimated as

$$A \simeq -\frac{U_b}{15} R_{eq}^{10} \qquad (7.22)$$

The d-bond energy of an atom in the bulk of the 300 atom block was calculated to be -13.23 eV (see appendix D4). Using this value in equation 7.22 and substituting in the repulsion term in equation 7.20, the core repulsion between adatoms 1 and 3 was estimated to be +0.43 eV for the triangular cluster and +0.004 eV for the linear cluster. The repulsion term in the triangular cluster is thus important although its

inclusion in the energy of the tungsten clusters does not make much difference since the magnitude of the bond energy difference between the triangular and linear clusters is considerably greater. In the rhodium clusters, however, the difference in the bond energy between the two clusters is comparable to the repulsion term, which tends to make the linear cluster more favourable.

7.3.7 The d-electron contribution to diffusion energies

To calculate the d-electron contribution to the activation energy for adatom diffusion on the W(110) surface, a single adatom was placed at the saddle site (figure 7.1) and calculation performed using the procedures described for the single adatom at the lattice site. The d-bond energies were calculated for the adatom and four near neighbour surface atoms. These atoms are numbered 1-5 in figure 7.1 for the saddle site and the lattice site. The difference in the total bond energies between the two sites was then taken as the d-electron contribution to the diffusion activation energy.

The self-energy, ε_d, the d-band energy, U_d, and the occupancy, Q, for both the W and Rh adatom at the saddle site are listed in appendix D2. The calculated d-electron contribution to the diffusion energies are listed in table 7.5, together with the experimental values for the activation energy for adatom diffusion of W and Rh on W(110). The calculated values show the trend W > Rh, in agreement with the experimental results. However, the actual magnitudes differ from the experimental values by a factor of about two. This difference could be attributed to a number of factors. Firstly, the calculation neglects adatom relaxation, which is known to be important in the calculation

of diffusion activation energies using Morse potentials[35]. Secondly, the hopping integrals were calculated using bulk parameters. This approximation is better justified for an adatom at a lattice site than at a saddle site. It should also be noted that since the adatom at the saddle site is at a different distance above the surface than at the lattice point, changes in the sp electron distribution could make a significant contribution to the energy barrier.

Table 7.5 Activation energies for adatom diffusion of tungsten and rhodium on W(110) from the d-electron tight-binding calculation and experiment (units: electronvolts).

	Calculated	Experimental
W	1.5	0.83[(a)], 0.87[(b)]
Rh	0.35	0.73

(a) Ref. 19

(b) Ref. 20.

8. DISCUSSION

The results of the experimental and theoretical studies of the behaviour of rhodium on tungsten and molybdenum (110) surfaces have been described in the preceding chapters. In the following sections, these results are considered in relation to the behaviour outlined in chapter 1 of other transition metal adsorbates.

8.1 Single Adatom Diffusion

The activation energy of 70 kJ mol^{-1} found for rhodium adatom diffusion on W(110) is significantly lower than for tungsten adatom migration on this surface. This is in agreement with the tight-binding calculations and is thus consistent with the adsorbate binding energy to the surface being the main factor influencing the activation energies of adsorbate metals on W(110) increasing roughly linearly with the melting temperatures of the bulk adsorbates. The measured diffusion activation energy of Rh, which has a bulk melting temperature T_m = 2540 K, fits into this correlation, being higher than for Ni or Pd diffusion, in agreement with the order of the bulk melting temperatures. It should be noted that this contrasts with the situation for self-diffusion, for which the ordering of the activation energies inverts that of the melting temperatures for Pt and Rh. This may not be unreasonable, since in comparing the behaviour of a series of different adsorbate metal species on one particular surface, the features of the interatomic potential are expected to be different from those of the pure metal case. However, the anomaly in the behaviour of the pure metals probably indicates the limited usefulness of the melting point correlation.

On the basis of such correlations, the lower value of the activation energy for rhodium-adatom diffusion on Mo(110) as compared to W(110) reflects a weaker binding of Rh on Mo(110). Any size effects on the diffusion behaviour can be neglected since tungsten and molybdenum have very similar lattice parameters, the nearest neighbour distances in the two being 0.274 nm and 0.273 nm, respectively. The lower diffusion activation energy of Rh on Mo(110) is expected on the basis of the relative values of the sublimation energies. This can be seen qualitatively by estimating the adsorption energy of Rh on the two surfaces using Pauling's expression given in equation 1.2 of chapter 1. As noted previously, the electronegativities are very similar for the transition metals and the adsorption energy in equation 1.2 is thus given mainly by the sublimation energies, which are 580 kJ mol^{-1} for Rh and 651 kJ mol^{-1} and 848 kJ mol^{-1} for Mo and W, respectively[178]. The adsorption energy of Rh on Mo(110) is thus expected to be lower compared to that of Rh on W(110), and is consistent with the ordering of the diffusion activation energies on the two surfaces. The lower adsorption energy of Rh on Mo(110) is also expected on the basis of a weaker d-electron coupling of Rh to Mo on account of the narrower d-band width of Mo compared to that of W [176] (see figure E1, Appendix E, for the d-band widths of the transition metals).

As noted in chapter 1, the observed dependence for transition metal adatoms on W(110) of both the adatom binding energy and adatom diffusion activation energy on adsorbate electron configuration is qualitatively similar to the variation in the cohesive energy of the bulk metals and reflects the important contribution of the d-electrons to the bonding in these metals. According to Friedel[171], the parabolic trend in the cohesive energy reflects the sequential filling of bonding

and then anti-bonding states across the series. For the number of d-electrons per atom $N_d < 5$, electrons are added to bonding states and the cohesive energy therefore increases, whereas for $N_d > 5$ electrons are added to anti-bonding states, causing the cohesive energy to decrease. For the third transition series, the maximum in the cohesive energy occurs for tungsten since it has 5 d electrons. A similar explanation holds for the trend in the diffusion activation energy of the adsorbate metals on W(110) but in this case, it is notable that the maximum may occur for Re rather than for W. Bassett and Parsley[19] have suggested that this might be due to the existence of a narrow sub-band of non-bonding states which could accommodate an extra valence electron and postpone the fall in binding energy to adatoms with more than 5 d-electrons. Their qualitative argument receives some support from the tight-binding calculations of chapter 7. Examination of the local density of states at the in-plane $d_{x^2-y^2}$ and d_{xy} orbitals of the single adatom shows that they are narrower than at the orbitals in the plane perpendicular to the surface. For example, for the tungsten adatom, the ratio of the half-widths of the in-plane orbitals to the perpendicular $d_{3z^2-r^2}$ orbital is <0.5. The net result of this is that the individual d-orbital distributions do not all extend uniformly over the d-band range, as in the parabolic bulk band model of Friedel. Instead, the in-plane orbital band-widths are smaller and in the sequential filling of states the preferential filling of the almost non-bonding parts of these sub-bands leads to higher occupancies. For example, for the tungsten adatom, $Q_{x^2-y^2} = 1.27$ e whereas $Q_{3z^2-r^2} = 0.83$ e. This postpones the normal decrease due to anti-bonding occupancy, since electrons are transferred out of the perpendicular plane

orbitals. Qualitatively, this would at least give a flat curve near the middle of the series rather than a parabolic curve with a maximum at the middle. However, whether there exists a maximum at Re remains questionable, both theoretically and experimentally. The diffusion measurements of Bassett and Parsley[19] show a pronounced maximum at Re but their data were obtained with several adatoms on the W(110) plane. In contrast, Tsong and Kellogg's[20] measurements of the diffusion of the 5-d metals on W(110), obtained with only a single adatom at a time on a plane, shows a similar trend in the activation energy across the series but the values for W and Re are very similar (87 kJ mol^{-1} and 88 kJ mol^{-1}, respectively). Further experimental studies are desirable to establish the trend near the middle of the series. Theoretically, it should be possible to examine in detail the role of the non-bonding in-plane d-orbitals in determining the trend and this could be done using the tight-binding approach described in chapter 7.

8.2 Properties of Adatom Dimers

To interpret the properties of the rhodium adatom clusters, such as the Rh_2 dimer, it is necessary to consider a model for the cluster structure. Since the rhodium adatom dimers were observed on both tungsten and molybdenum (110) surfaces with the dimer bond axis oriented parallel to the substrate <111> directions, it is simplest to assume that the adatoms occupy nearest neighbour lattice sites. The adatoms then interact by direct orbital overlap. Such a model is speculative since as noted in chapter 5, the bond length and the location of the adatoms relative to the substrate cannot reliably be determined from

FIM micrographs. The assumption that the adatoms in the dimer are close-packed contrasts with that of Casanova and Tsong[34], who argue that because the individual adatoms of Ir_2 dimer on W(110) are resolved, the dimer is not close-packed but the bond length is twice the nearest neighbour distance. Like Ir_2 [44] and Pt_2 [29,44] on W(110) the adatoms of the Rh_2 dimer were frequently seen resolved in FIM micrographs. This contrasts with the situation for dimers of the early transition metals, such as W_2 or Ta_2, which are unresolved under similar conditions. However, resolution is not a definite indication of spacing, as assumed by Casanova and Tsong[34]. The adatoms may be resolved or not depending on distortions of the imaging gas ion beams originating above the protruding adatoms. This distortion may be dependent on adatom type, and electronic structure effects may thus influence the dimer imaging characteristics with pronounced differences between the early and late transition metals, just as in other dimer properties. For the present it is assumed that the adatoms in Rh_2 are close-packed, but the validity of this assumption will be examined further later.

The dissociation energy of 13 kJ mol^{-1} for Rh_2 dimer on W(110) is comparable to the dissociation energy of Pt_2 and Ir_2 dimer on W(110) and is consistent with the trend in the dissociation energy with the adatom d-electron configuration (figure 1.6). The relative instability of dimers with a more than half-filled d-band can be qualitatively understood from the results of the tight-binding calculations. As noted in the preceding section, the in-plane orbitals at a single Rh adatom are essentially non-bonding and more nearly filled than the perpendicular orbitals. The formation of a bond with another adatom by direct orbital overlap would mainly involve the in-plane orbitals,

the density of states of which will be split into broadened bonding and anti-bonding states. Associated with the level broadening would be shifts in the adatom self-energy due to self-consistency requirements. Qualitatively, for Rh_2 the anti-bonding states would be expected to be more nearly filled than for W_2 dimer. The lower stability of Rh_2 compared to W_2 is thus expected on this basis. However, such a simple scheme alone is not adequate since it predicts that Re_2 would be more stable than Pt_2 or Ir_2, which is inconsistent with the observed trend shown in figure 1.6. It is therefore necessary to consider other factors which might influence the stability of the dimers. Repulsion between dipoles associated with charges on the adatoms will reduce the adatom-adatom interaction but this does not appear to be the factor determining the trend in dissociation energies with electron configuration[41]. Tsong and Kellogg[39] have determined the dipole moment of the 5-d metal adatom on W(110) from the field dependence of adatom diffusion. Their results show that the dipole moments on the adatom are small and do not vary much across the series. Another possible factor is the hard-core repulsion between adatoms. A simplified calculation in chapter 7 showed that the core repulsion is proportional to the d-bond energy of an atom in the bulk of the metal. For a rectangular d-band density of states of width W_d containing N_d electrons, the core repulsion can be shown to be proportional to $W_d N_d(10-N_d)$. The d-band width of the transition series metals decrease with increasing N_d (figure E1, Appendix E). The core repulsion decreases with increasing N_d as one goes across a transition metal series. It would be expected to be greater for Re than for Ir or Pt, and combined with the effect of the sequential filling of the bonding and anti-bonding in-plane states could conceivably reduce the dissociation energy of Re_2 below that of Ir_2.

There are also effects associated with the shift in the adatom self-energy upon dimerization that need to be considered. A detailed calculation of the dimer bond energy, including a proper calculation of the core repulsion between adatoms, is desirable in order to fully understand the variation in the dimer binding energy with N_d. Qualitative considerations outlined above indicate that a satisfactory explanation could be obtained within a d-electron tight-binding calculation with the inclusion of a core repulsion term. The programmes developed in the present study could readily be used for this problem.

It should be noted that if the adatoms in the dimer, such as Rh_2, are at twice the nearest neighbour spacing, then there would be no direct interaction by orbital overlap but only a residual indirect interaction via the substrate conduction electrons[48]. It would then be essential to include sp conduction states in any calculation involving dimer binding energy. Indirect interaction has been assumed for Ir_2 by Casanova and Tsong[34] as noted above, and also by Fink, Faulian and Bauer[49] in interpreting their observations of interacting RePd and WPd adatoms on W(110). The same appears to be true of Fink and Ehrlich[50] who suggest an (n×n), n > 1 type of superstructures for their resolved islands of Ir, Pt and Pd on W(110). However, these assumptions contrast with LEED observations. For example, Schlenk and Bauer's[59] LEED results of Pd on W(110) does not show any patterns that could be attributed to superstructures of the form suggested by Fink and Ehrlich, although a distinct half-monolayer phase was detected by Butz and Wagner[63] in studying diffusion of Pd on W(110). Similarly, LEED studies of Pt[71,159] and Ir[159] on W(110) did not show any

superstructure LEED spots. Casanova and Tsong's assumption that the adatoms in dimers are at twice the nearest neighbour spacing implies that the adsorbate may form a (2×2) overlayer. However, LEED observations did not show any patterns due to a (2×2) overlayer. In fact, streaks were observed in the LEED pattern from submonolayer coverages of Rh on W(110) and as noted in chapter 6, similar streaks have been observed from Ir and Pt on W(110)[159]. The streaking is thought to be associated with chain structures and is consistent with FIM observations. If this is true, then the adatom spacing in the chain-clusters is equal to the nearest neighbour tungsten spacing and the interaction between adatoms in the chains is due to direct orbital overlap. This is clearly inconsistent with a dimer bond length other than that of nearest neighbour spacing. However, this is not conclusive evidence for dimer spacing since, as discussed in detail in section 8.3, the structures producing the LEED patterns may be quite different from those of the clusters observed in FIM studies.

8.3 Adsorbate Clustering

The uncertainty about the interatomic spacing in dimers and whether the interaction between the adatoms is direct or not carries over into consideration of the nature of larger clusters. If the adatoms in Rh_2 are not close-packed and the interaction is indirect, then the stability of the linear chains as compared to more close-packed two-dimensional structures could be due to the form of the long-range indirect interaction potential. However, the calculations of chapter 7 show that the relatively greater stability of the linear geometry for Rh clusters can arise as the result of direct adatom-adatom

orbital overlap. The crucial factor appears to be the behaviour of the non-bonding in-plane orbitals on formation of the cluster, although core repulsion probably also plays some part. When the adatom d-states are more than half-filled, the greater non-bonding character of the density of states for the linear cluster as compared to the two-dimensional form postpones the filling of strongly anti-bonding states and stabilizes the linear cluster.

If this direct interaction interpretation of the stability of the linear cluster suggested by the tight-binding calculation for W_3 and Rh_3 is correct, then stabilization of the linear chains would be expected for all transition metal adsorbates with more than half-filled d-bands. The observation of linear chain clusters for Rh extends the list of metals behaving in this way and confirms the view that linear cluster formation is general for metals from the second half of the transition series when adsorbed on W(110).

The tendency of the later transition metals to form linear chain clusters on W(110) clearly extends to the Mo(110) surface. This is expected since the electronic structure of tungsten and molybdenum are very similar, except for a narrower d-band width for Mo [176]. The main features of the tungsten calculation should thus carry over to the case of Rh_3 on Mo(110), although in this case the binding energy of the adatoms is expected to be smaller than on W(110) on account of the weaker coupling of Rh to Mo due to the narrower d-band width of Mo. Although the direct Rh-Rh coupling is the same as on W(110), the states formed by this coupling also couple to substrate orbitals and are probably influenced by the weaker Rh-Mo coupling. Since to a first approximation, the Rh-Rh core repulsion is unchanged

the relative stability of the linear-chain and island forms as compared to Rh on W(110) should be apparent from the weaker bond energy of the clusters on Mo(110). It is particularly interesting to note that chain clusters with more than about 10 Rh adatoms appeared to be unstable compared to two-dimensional forms. This behaviour is similar to that of Pd on W(110) and contrasts with the behaviour of Rh on W(110), in which case dissociation was the only change observable after heating. These results suggest that reducing the d-band width of either substrate or adsorbate appears to favour the close-packed island configuration.

It is clearly interesting to see how far the important features of the calculations can be generalised to predict the relative stability of the linear configuration as compared to the two-dimensional form. The calculations appear to suggest two contributions stabilizing the chain configuration.

(1) Orbital energy stabilization due to a greater non-bonding character of the in-plane states in the chain structure. This postpones the filling of the anti-bonding states as compared to island forms. The stabilization should increase with increasing splitting of the non-bonding states in going to the island form. The factors that influence the splitting are

(a) adatom-adatom overlap which (i) decrease with increasing N_d and (ii) increases in the order 3d < 4d < 5d as one goes down a transition metal group for a fixed N_d, since the d-band widths increase in this order (figure E1).

(b) Adatom-substrate overlap which increases in the order 3d < 4d < 5d for a fixed adatom.

(2) Core repulsion between adatoms, which is larger for island forms and hence increases the chain stabilization, the greater its magnitude. From the simple treatment considered in the preceding section, the core repulsion (i) decreases with N_d (for $N_d > 5$) and (ii) increases in the order 3d < 4d < 5d.

Another possible factor is the effects of varying the atomic size across the transition metal period since the interatomic d-orbital interactions have an R^{-5} dependence on the separation R. These effects probably vary with adsorbate in the same manner as those discussed above since they have their origin in the electron configuration.

The experimental data available to date appears to fit qualitatively into this simple scheme. For example, on the W(110) surface, going down the platinum group metal adsorbates Ni, Pd and Pt (fixed N_d), the stability of the linear chains increases in the order Ni(3d) < Pd(4d) < Pt(5d) [29], as expected from the above considerations. Going across the 4d series (variable N_d) the stability of the chain clusters increases in the order Rh (N_d = 8) > Pd(N_d = 9), and similarly for the 5d series adatoms, Ir (N_d = 8) $\gtrsim$ Pt (N_d = 9). For a fixed adsorbate on a variable substrate, only the results from the present study are available. These show that the stability of the linear Rh chain follows the trend Mo(110)(4d) < W(110)(5d).

Further experimental and theoretical studies are desirable to extend the range of adsorbate substrate systems examined. It is notable that though the Rh_2 dimer is relatively unstable on tungsten and molybdenum (110) surfaces, increasing the cluster size by addition of adatoms increases the cluster stability, just as seen previously for Pt and Ir on W(110) [29,44]. On symmetry grounds, the non-bonding levels would be expected to diminish non-monotonically and oscillate as a

function of the number of adatoms in the linear clusters, decreasing to a minimum for an even number of adatoms and increasing for an odd number of adatoms. These effects need to be examined in detail and may be helpful in understanding why for Rh, Ir and Pt on W(110), increasing the chain length increased the stability whereas for Rh on Mo(110) and Pd on W(110), facile transformation from the linear to two-dimensional forms occurred after a critical size of chain-cluster had formed.

The diffusion measurements for Rh_3 and Rh_4 clusters on W(110) appear to be similar to those for Pt adatom clusters on W(110) obtained by Bassett[28]. The lower mobility of the clusters is characterized by a larger activation energy and indicates increased bonding in clusters. A detailed analysis of the Rh adatom cluster diffusion has not been made in the present study due to lack of sufficient data. However, the similarity between the Rh and Pt adatom cluster diffusion on W(110) suggests that the mechanism of adatom cluster diffusion involves sequential adatom jumping, as suggested by Bassett[28]. This necessarily means that during migration, the adatoms must adopt non-linear configurations. It would be useful to model such configurations in the tight-binding calculations to understand more fully the mechanism of diffusion in clusters.

As noted in chapter 1, within the context of overall film growth, the effect of the substrate is important since the adatom-adatom compared to adatom-substrate interactions determine the growth mode. It would therefore be useful to extend the calculations and experiment to tantalum (110), which retains the b.c.c. structure but shifts the Fermi level down the band to a region where the density of states $N(E_f)$ is higher than for tungsten or molybdenum. From the simple scheme

considered above, the splitting of the non-bonding states would be expected to be greater for two-dimensional forms of adsorbates on Ta(110) than on W or Mo(110) surfaces. The latter transition series metals may thus be expected to form linear-chain clusters more stable than on W or Mo(110). To shift the Fermi level further up the d-band involves the added complication of a change in the substrate structure and its effect on the orbital energies. However, from the simple scheme considered above, it is conceivable that a chain/island situation exists for the later transition series metals on the close-packed surfaces of the h.c.p. and f.c.c. metals, but detailed theoretical and experimental studies need to be carried out to verify this. So far, experimental problems have arisen in FIM due to the high mobility of adsorbates on the close-packed surfaces of the f.c.c. metals such as Rh or Pt [121] at liquid nitrogen temperatures. However, it should be possible to do the experiments at much lower temperatures. At present, FIM appears to be the only technique capable of resolving whether the chain/island situation is general for transition metal adsorbate-substrate systems.

8.4 High Coverage Film Structure

Of the LEED patterns obtained from submonolayer coverages of Rh, and also Ir and Pt on W(110)[159], only the streaks appear to be consistent with FIM observations. As described in chapter 6, these streaks are thought to be associated with chain mosaic structures, with a close-packed inter-atomic spacing within chains. The absence of streaks in the LEED patterns from low coverages of Rh on Mo(110) is not unreasonable since FIM evidence shows that only small Rh chains were stable on this

surface. Under the conditions of the LEED experiments, facile transformation of chains to islands probably occurred and any remaining chains would be too small to be detected by LEED. If this is true, then the absence of streaks is to be expected from Pd on W(110) as FIM observations show that its behaviour is very similar to that of Rh on Mo(110). This appears to be the case in the LEED studies of Schlenk and Bauer[59] who do not report any evidence of streaks from Pd on W(110).

With increasing coverage up to about one monolayer, the LEED patterns obtained from Rh on both W and Mo(110) surfaces showed only strong background and diffuse spots. This has also been observed for other transition metals on the two surfaces. For example, Pd films deposited below 450 K W(110)[59], Au on W(110)[62] and Mo(110)[73] unless annealed at 700 K and 1000 K, respectively, and for Pt[71,159] and Ir[159] on W(110). The diffuse scattering in LEED makes detailed interpretation difficult. FIM studies show that it is unlikely that the overlayer is disordered. As discussed in chapter 6, the broadening of the (1×1) substrate spots is probably due to a high density of differently positioned or oriented patches, which is possible on the b.c.c. (110) surfaces even for a pseudomorphic overlayer. Pseudomorphism for the Rh monolayer is plausible on both W and Mo(110) surfaces considering the similar diameters of Rh (0.269 nm) and W (0.274 nm) and Mo (0.273 nm), and the greater Rh-substrate bond strength compared to Rh-Rh bond strength as indicated by their sublimation energies. When patches grow into contact, anti-phase boundaries or interfaces can arise as has been observed in the FIM studies. However, without a measurement of LEED spot intensity profiles to determine island sizes in the way recently shown by Hahn and co-workers[54], it is difficult to correlate these

observations with the islands seen in FIM studies. It would clearly be desirable to make these measurements in any future LEED studies. It should also be noted that any structure proposed for the patterns from the overlayers may be quite different from those observed in FIM studies[29,59]. This is because higher annealing temperatures are used in LEED studies to obtain good patterns. Also, the (110) surfaces of the FIM specimens are perfect step-free substrates whereas the crystal surfaces used in LEED experiments probably have a high density of steps. Even for a (110) surface oriented to within 1^{o} of the surface normal, a monoatomic step would be expected every 15 nm on average. At the temperatures used in LEED, adatoms are quite mobile and under these conditions the influence of the steps on the overlayer structure may be quite important. It is notable that FIM observations on a faulted tungsten tip apparently shows that clusters may preferentially form at dislocation-step termination sites (Appendix B).

LEED observations show that increasing the Rh coverage beyond one monolayer eventually results in the development of a Rh(111) overlayer on both W and Mo(110) surfaces, as expected for f.c.c. on b.c.c. (110) transition metal systems[79]. Room temperature deposits of Rh on W(110) were oriented in the Nishiyama-Wassermann (NW) alignment, i.e. $Rh\langle 1\bar{1}0\rangle||W\langle 001\rangle$, whereas annealed deposits showed streaks which have been attributed to domains of Rh(111) oriented in the Kurdjumov-Sachs (KS) alignment, i.e. $Rh\langle 0\bar{1}1\rangle||W\langle \bar{1}11\rangle$ and $Rh\langle 10\bar{1}\rangle||W\langle 1\bar{1}1\rangle$. High temperature annealing resulted in spots due to Rh(111) in the KS alignment. The absence of the NW alignment in the annealed deposits suggests that KS is the equilibrium alignment for Rh on W(110), which has also been observed for Ag[58,79] and Pd[59] on W(110). For Rh on Mo(110), the observed patterns are similar to those from Rh on W(110)

but in this case the LEED pattern from an annealed deposit shows spots which have been attributed to domains of Rh(111) in both NW and KS alignment. These results do not agree with the studies of Bruce and Jaeger[79], who have examined a variety of f.c.c.-b.c.c. metal pairs and shown that the epitaxial alignment is dependent on the ratio of the atomic diameters of adsorbate and substrate. They predict that Rh on W(110) should be oriented equally in the NW and KS alignment whereas on Mo(110) it should be in the KS alignment. Our results appear to be in the reverse order. The reasons for this discrepancy are not clear at present. Since the "final" alignment develops from the initial deposits, deviation from the expected alignment may occur if only a small thickness of deposits is examined[79], which may be the case in the present study. It is also possible that steps on the substrate may influence the epitaxial alignment, which may then deviate from that expected on a perfect substrate.

8.5 Concluding Remarks

In conclusion, the studies have demonstrated the importance of d-band filling in the initial stages of transition metal film growth. The calculations have shown how this comes about, with the role of the non-bonding d-states as sinks for electrons that would otherwise be anti-bonding when the bands are more than half-full. Much further work remains to be done to extend the calculations and experiments.

APPENDIX A

Table A1 Major Auger electron transitions observed from elements of interest in the present work. (Units: electronvolts)

ELEMENT	TRANSITION	ENERGY
Tungsten	$N_5N_5N_6$	$164^{(a)}$
	$N_5N_6N_7$	$171^{(a)}, 172^{(c)}$
	$N_5N_7N_7$	$181^{(a)}, 182^{(c)}$
	$N_4N_6O_{4,5}$	$208^{(d)}, 210^{(c)}$
Molybdenum	$M_5N_1N_{3,2}$	$124^{(b),(c)} 125^{(a)}$,
	$M_5N_3N_3$	$149^{(b,c)}, 153^{(a)}$
	$M_5N_1N_5$	$164^{(b)}, 162^{(c)}$, $166^{(a)}$
	$M_5N_3N_5$	$187^{(b)}, 188^{(c)}$
	$M_5N_5N_5$	$222^{(b,c)}$
Rhodium	$M_5N_1N_5$	$226^{(a,c)}$
	$M_5N_3N_5$	$260^{(a,c)}$
	$M_5N_5N_5$	$306^{(a,c)}$
Carbon	KLL	$271^{(b)}, 272^{(c)}$
Sulphur	$L_{2,3}V_2V_2$	$152^{(b)}, 150^{(c)}$
Oxygen	KLL	$518\text{-}520^{(c)}$

(a) From Ref. 179
(b) From Ref. 152
(c) Present study
(d) K. Rawlings, private communication

APPENDIX B

Deposition of Rhodium on a faulted tungsten tip

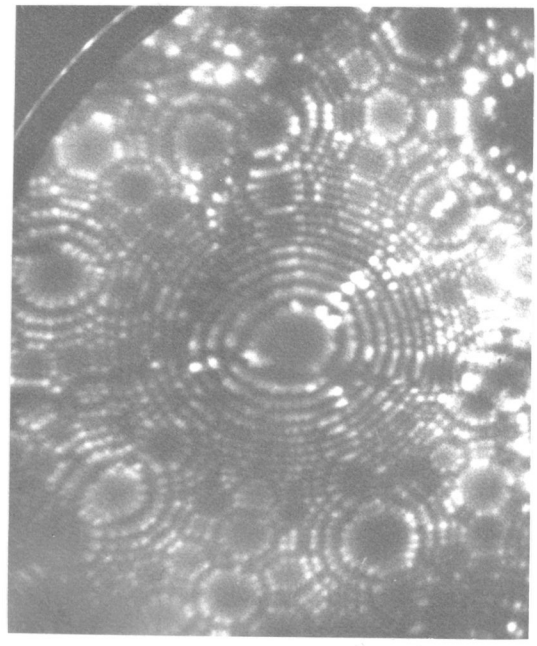
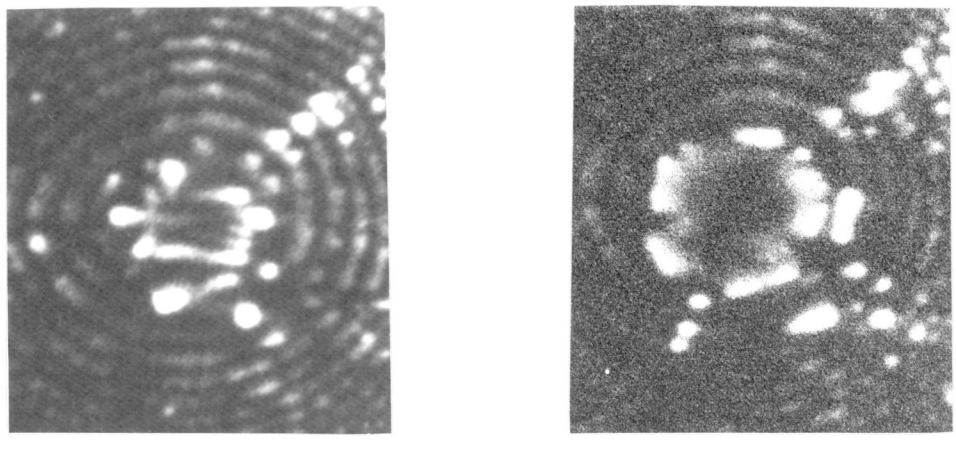
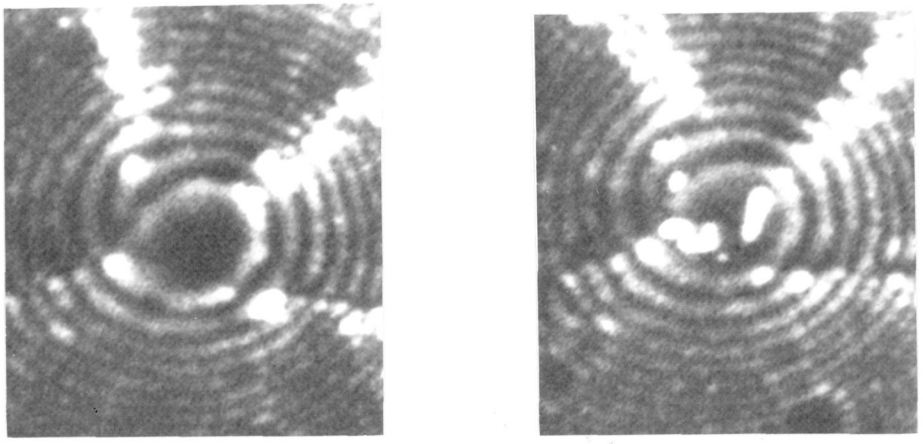


Figure B1 Low angle grain boundary in a tungsten specimen.



a b

Figure B2 (a) Linear-chain arrays grown by deposition of Rh on W(110) at 78 K followed by heating at 300 K; (b) A monolayer film after further deposition at 300 K onto the deposit of (a). The grain boundary has "propagated" into the monolayer film.



a b

Figure B3 (a) A spiral dislocation emerging in the W(110) pole after heating the specimen (of figure B1) at 1000 K followed by field-evaporation. (b) A linear chain cluster on the (110) plane and possibly a two-dimensional cluster nucleated at the origin of the spiral at the plane edge, after deposition of Rh at 78 K followed by heating at 300 K.

APPENDIX C

Surface diffusion of rhodium on W(110)

Rhodium was deposited on one part of the W(110) surface following the procedure given in section 4.4.3. The profile of the deposit is shown in the Auger peak-to-peak height versus distance plot, figure C1, curve A. The curve does not reflect a sharp boundary but exhibits a tail, indicating the poor resolution of the evaporator aperture used in depositing the Rh, and poor spatial resolution of the Auger electron beam. The coverage at the maximum Rh signal corresponds to about 5 monolayers. The evolution of the profile after four successive 60 sec. anneals at 1100 K is shown in figure C1. The diffusion profile reached a stable value after the second heating period (curve C). Significant diffusion of the overlayer does not appear to have occurred, as evidenced by the lack of extension of the tail. LEED patterns were observed at the end of the diffusion run and showed three distinct regions in the profile, as indicated on figure C1. Sharp diffraction spots due to Rh(111) were observed at the top of the profile while in the region exhibiting the tail, the LEED pattern resembled clean W(110). In between these two regions the LEED pattern showed sharp streaks between the W(110) spots, as in figure 6.16. The diffusion profiles themselves do not reveal any distinct coverage phases corresponding to these patterns, which is possibly due to the poor resolution of the Auger electron beam.

A detailed analysis of the diffusion profiles is not attempted here due to lack of sufficient data. Only two experimental runs were made due to the time consuming nature of these studies. The results from both runs were essentially the same except for an unexplained

anomaly in the first run, which showed that when the specimen was first annealed at 1100 K, the diffusion profile changed to that given by curve B in figure C1. With the second heating period, the profile moved to coincide almost with the original profile (A). With subsequent anneals, the behaviour was similar to that described in figure C1 for the second run.

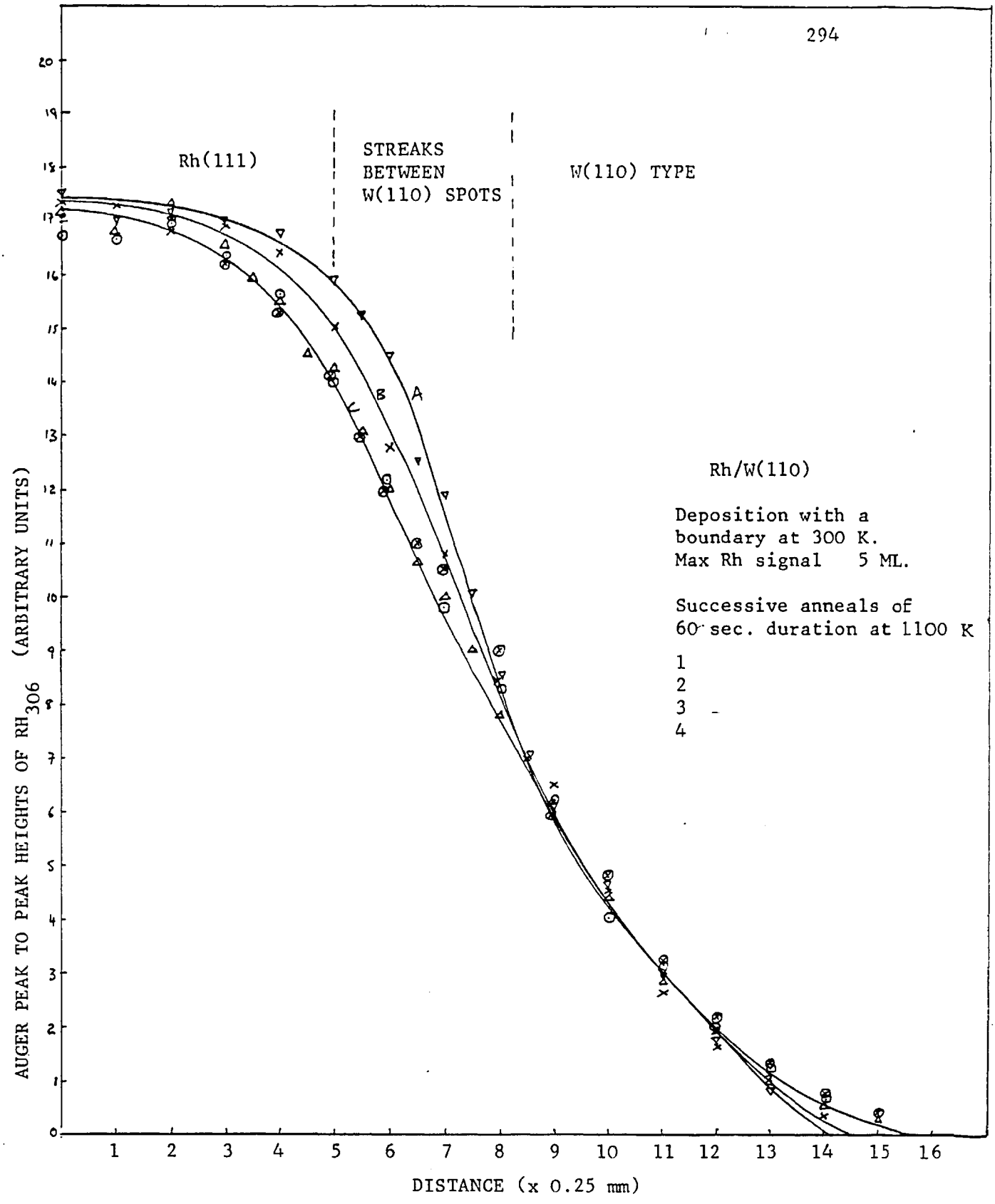


Figure C1. Evolution of a diffusion profile. Rh Auger amplitude versus distance plots after successive heating periods.

APPENDIX D

D1. The second moment of the density of states, for a single W(Rh) adatom at a lattice site on W(110), its near neighbours (atoms 2,4) and a bulk W atom. μ_2 was calculated from the d.o.s. at the atoms using equation 7.17, and μ_2' from equation 7.15.

Atom	No. of Neighbours		Second Moment	
	First	Second	μ_2	μ_2'
1	2	2	12.48	11.82
			(7.49)	(6.8)
2	6	5	34.94	34.34
			(34.43)	(33.87)
4	7	4	37.98	37.99
			(36.19)	(35.95)
Bulk	8	6	45.29	45.03

	ATOM NO.	$-\epsilon_d$	ORBITAL 1. xy		2. yz		3. zx		4. x^2-y^2		5. $3z^2-r^2$		TOTAL	
			$-U_d$	Q	$-U_d$	Q	$-U_d$	Q	$-U_d$	Q	$-U_d$	Q	$-U_d$	Q
SINGLE ADATOM GEOMETRY	1	5.624	6.442	1.044	7.592	1.066	6.388	0.937	7.964	1.273	6.00	0.832	34.379	5.15
	2	6.143	9.305	1.075	8.711	1.076	7.492	0.882	7.823	0.896	8.763	1.084	42.096	5.014
	4	6.183	9.326	1.063	9.053	1.051	7.78	0.908	8.24	0.926	8.956	1.055	43.25	5.003
LINEAR (TRIANGULAR) CLUSTER GEOMETRY	1	5.717 (5.792)	7.446 (7.519)	1.088 (1.053)	7.902 (8.141)	1.079 (1.101)	6.713 (6.878)	0.936 (0.951)	7.558 (7.199)	1.098 (1.007)	6.78 (7.307)	0.919 (0.991)	36.399 (37.042)	5.121 (5.102)
	2	5.863 (5.961)	7.936 (8.682)	1.034 (1.12)	8.235 (8.356)	1.088 (1.088)	7.199 (7.086)	0.956 (0.917)	7.55 (7.35)	0.985 (0.952)	7.656 (7.691)	1.021 (0.983)	38.576 (39.17)	5.084 (5.06)
	4	6.166 (6.166)	9.39 (9.362)	1.08 (1.075)	8.985 (9.006)	1.045 (1.051)	7.853 (7.832)	0.927 (0.923)	7.974 (7.978)	0.903 (0.904)	8.914 (8.909)	1.052 (1.053)	43.118 (43.09)	5.007 (5.007)
	5	6.232 (6.243)	9.453 (9.477)	1.073 (1.076)	9.132 (9.121)	1.058 (1.055)	7.782 (7.766)	0.893 (0.889)	8.147 (8.137)	0.919 (0.918)	9.013 (9.017)	1.05 (1.05)	43.527 (43.52)	4.993 (4.988)
	10	6.22 (6.327)	9.44 (9.637)	1.073 (1.073)	9.111 (9.838)	1.055 (1.094)	7.799 (7.806)	0.896 (0.85)	8.076 (8.372)	0.911 (0.924)	9.012 (9.255)	1.051 (1.026)	43.438 (44.91)	4.987 (4.968)
	11	6.104 (6.069)	9.235 (9.206)	1.073 (1.076)	8.746 (8.706)	1.09 (1.088)	7.427 (7.428)	0.88 (0.887)	7.817 (7.834)	0.901 (0.91)	8.707 (8.602)	1.08 (1.07)	41.932 (41.776)	5.024 (5.03)
	(6)	(6.104)	(9.241)	(1.074)	(8.705)	(1.084)	(7.477)	(0.892)	(7.765)	(0.895)	(8.657)	(1.075)	(41.85)	(5.02)

Appendix D2

Table D2I

The modified self-energies, ϵ_d (eV), the d-band structure energies U_d (eV) and the d electron occupancies for the non-equivalent tungsten adatoms and surface atoms in the single adatom, linear and triangular configurations. The results for the triangular case are bracketed.

	ATOM NO.	$-\varepsilon_d$	1. xy		2. yz		3. zx		4. x^2-y^2		5. $3z^2-r^2$		TOTAL	
			$-U_d$	Q	$-U_d$	Q	$-U_d$	Q	$-U_d$	Q	$-U_d$	Q	$-U_d$	Q
SINGLE ADATOM GEOMETRY	1	6.9768	13.485	1.906	12.295	1.637	12.71	1.757	13.247	1.848	12.508	1.719	64.219	8.862
	2	6.2992	9.421	1.068	8.897	1.080	7.539	0.875	8.005	0.907	8.689	1.043	42.551	4.974
	4	6.3884	9.559	1.072	8.966	1.036	7.765	0.890	8.327	0.936	8.803	1.020	43.424	4.956
LINEAR (TRIANGULAR) CLUSTER GEOMETRY	1	7.474 (7.496)	13.824 (13.887)	1.802 (1.808)	13.176 (13.210)	1.646 (1.643)	13.74 (13.796)	1.781 (1.784)	14.112 (14.068)	1.84 (1.827)	13.104 (13.169)	1.668 (1.671)	67.955 (68.128)	8.737 (8.732)
	2	7.653 (7.616)	13.714 (13.503)	1.723 (1.703	13.602 (13.542)	1.666 (1.667)	14.155 (14.143)	1.795 (1.805)	14.492 (14.429)	1.847 (1.848)	13.427 (13.438)	1.663 (1.680)	69.388 (69.043)	8.694 (8.701)
	4	6.629 (6.64)	9.823 (9.828)	1.075 (1.074)	9.042 (9.064)	1.007 (1.01)	8.126 (8.13)	0.916 (0.915)	8.313 (8.331)	0.895 (0.896)	8.896 (8.92)	0.995 (0.996)	44.200 (44.272)	4.887 (4.890)
	5	6.672 (6.70)	9.846 (9.889)	1.068 (1.069)	9.168 (9.169)	1.022 (1.016)	7.910 (7.959)	0.870 (0.872)	8.494 (8.474)	0.923 (0.91)	9.011 (9.055)	1.006 (1.008)	44 430 (44.519)	4.888 (4.874)
	10	6.683 (6.839)	9.875 (10.084)	1.069 (1.07)	9.165 (9.45)	1.017 (0.996)	7.931 (8.12)	0.868 (0.865)	8.431 (8.630)	0.909 (0.910)	9.048 (9.316)	1.009 (1.005)	44.450 (45.600)	4.873 (4.841)
	11	6.506 (6.534)	9.606 (9.608)	1.062 (1.058)	9.071 (9.10)	1.07 (1.069)	7.661 (7.682)	0.866 (0.866)	8.243 (8.232)	0.912 (0.907)	8.773 (8.803)	1.019 (1.02)	43.354 (43.425)	4.929 (4.919)
	(6)	(6.54)	(9.676)	(1.066)	(9.053)	(1.06)	(7.756)	(0.875)	(8.168)	(0.894)	(8.815)	(1.020)	(43.467)	(4.915)

Appendix D2

Table D2 II

The modified self-energies ε_d (eV), the d-band structure energies U_d (eV), and the d electron occupancies for the non-equivalent rhodium adatoms and surface atoms in the single adatom, linear and triangular configurations. The results for the triangular case are bracketed.

Table D2 III. The modified self-energies, ε_d (eV), d-band structure energies, U_d (eV), and the occupancies, Q, for the W(Rh) saddle site system.

ATOM	$-\varepsilon_d$	ORBITAL 1. xy		2. yz		3. zx		4. x^2-y^2		5. $3z^2-r^2$		TOTAL	
		$-U_d$	Q	$-U_d$	Q	$-U_d$	Q	$-U_d$	Q	$-U_d$	Q	$-U_d$	Q
	5.546	6.084	1.016	7.009	1.069	7.094	1.063	6.815	1.148	6.21	0.881	33.212	5.177
	(6.778)	(13.110)	(1.911)	(12.288)	(1.730)	(12.302)	(1.721)	(13.093)	(1.905)	(11.774)	(1.644)	(62.559)	(8.911)
	6.114	9.185	1.054	8.873	1.063	7.983	0.928	7.948	0.911	8.966	1.063	42.956	5.019
	(6.369)	(9.498)	(1.067)	(8.969)	(1.056)	(7.810)	(0.883)	(8.211)	(0.923)	(8.872)	(1.030)	(43.362)	(4.958)
	6.101	9.146	1.063	8.757	1.096	7.46	0.904	7.943	0.925	8.381	1.035	41.689	5.024
	(6.255)	(9.30)	(1.06)	(8.903)	(1.089)	(7.539)	(0.891)	(8.071)	(0.924)	(8.498)	(1.027)	(42.313)	(4.990)

(D3) The d-band structure energy of a bare atom in the W(110) surface was calculated to be -43.6 eV (figure 7.4). The d-bond energy, $U_b = \int_{-\infty}^{\varepsilon_f} (E-\varepsilon_d)N(E)dE$, of the atom is -12.6 eV (with ε_d = -6.2 eV). When the surface atom forms a first-neighbour bond with a W adatom, its d-bond energy is lowered by ∿0.3 eV (from table D2I, atom 4 in the single adatom system). In the triangular cluster, the d-bond energy of the surface atom, which forms two first-neighbour bonds with adatoms, is lowered by ∿0.7 eV (from table D2I, atom 10), thus reflecting the almost pairwise additivity of the interactions.

(D4) The non-selfconsistent d-band energy and occupancy of an atom in the bulk of the tungsten block, were found to be -43.76 eV and 4.924 electrons, respectively. With ε_d = -6.2 eV, the d-bond energy is ≃ -13.2 eV. It is interesting to note that this value is in good agreement with the d-band cohesive energy of ≃ -13.5 eV for tungsten, estimated by assuming a rectangular d-band density of states for which the d-electron contribution to the cohesive energy is given as,[81] $\Delta E(N_d) = \frac{W_d}{20} N_d(10-N_d)$, where W_d is the d-band width and N_d is the valence d electrons. (For tungsten, W_d = 10.8 eV and N_d = 5).

APPENDIX E

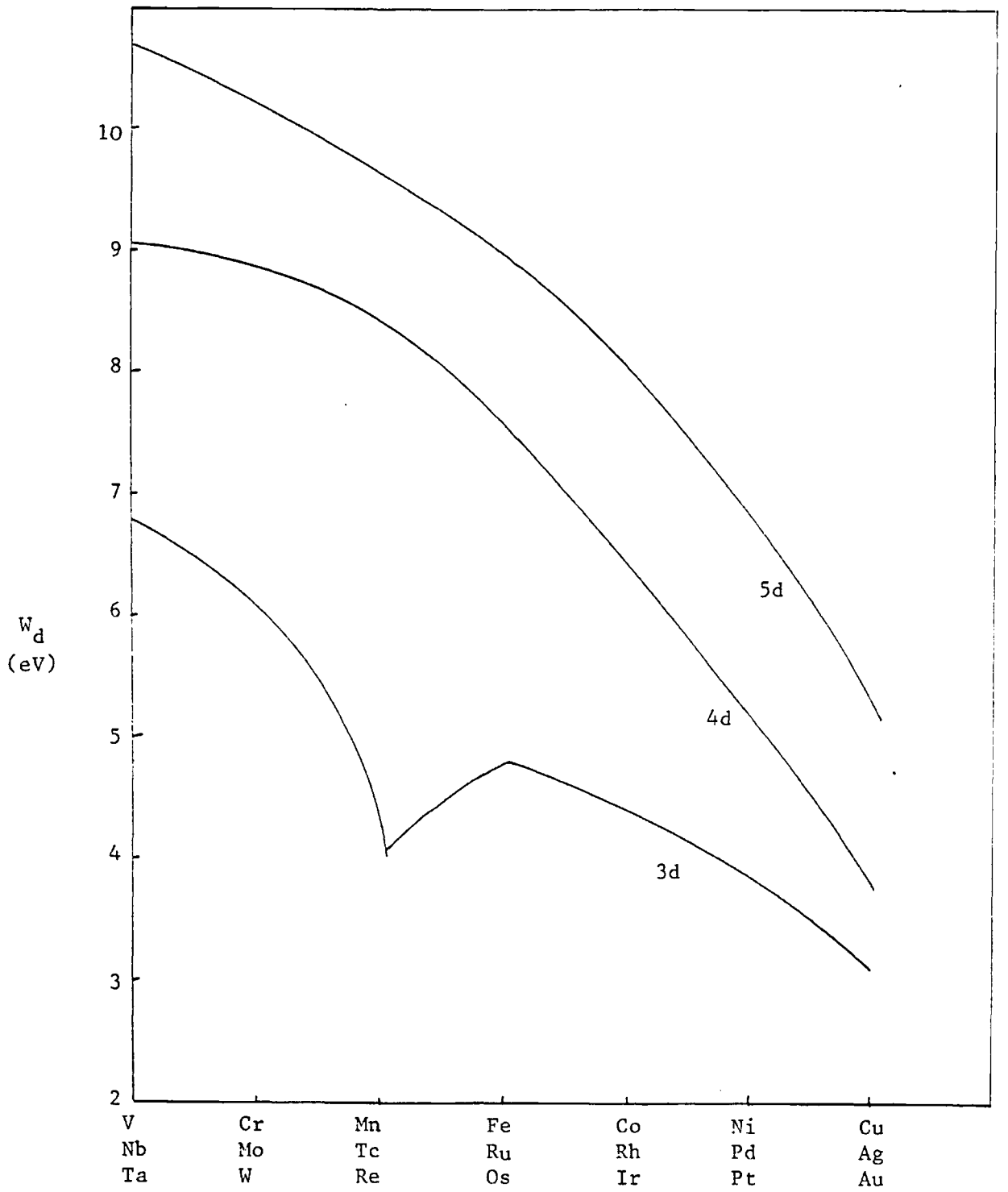


Figure E1 The d-band width of the transition series metals (ref. 44).

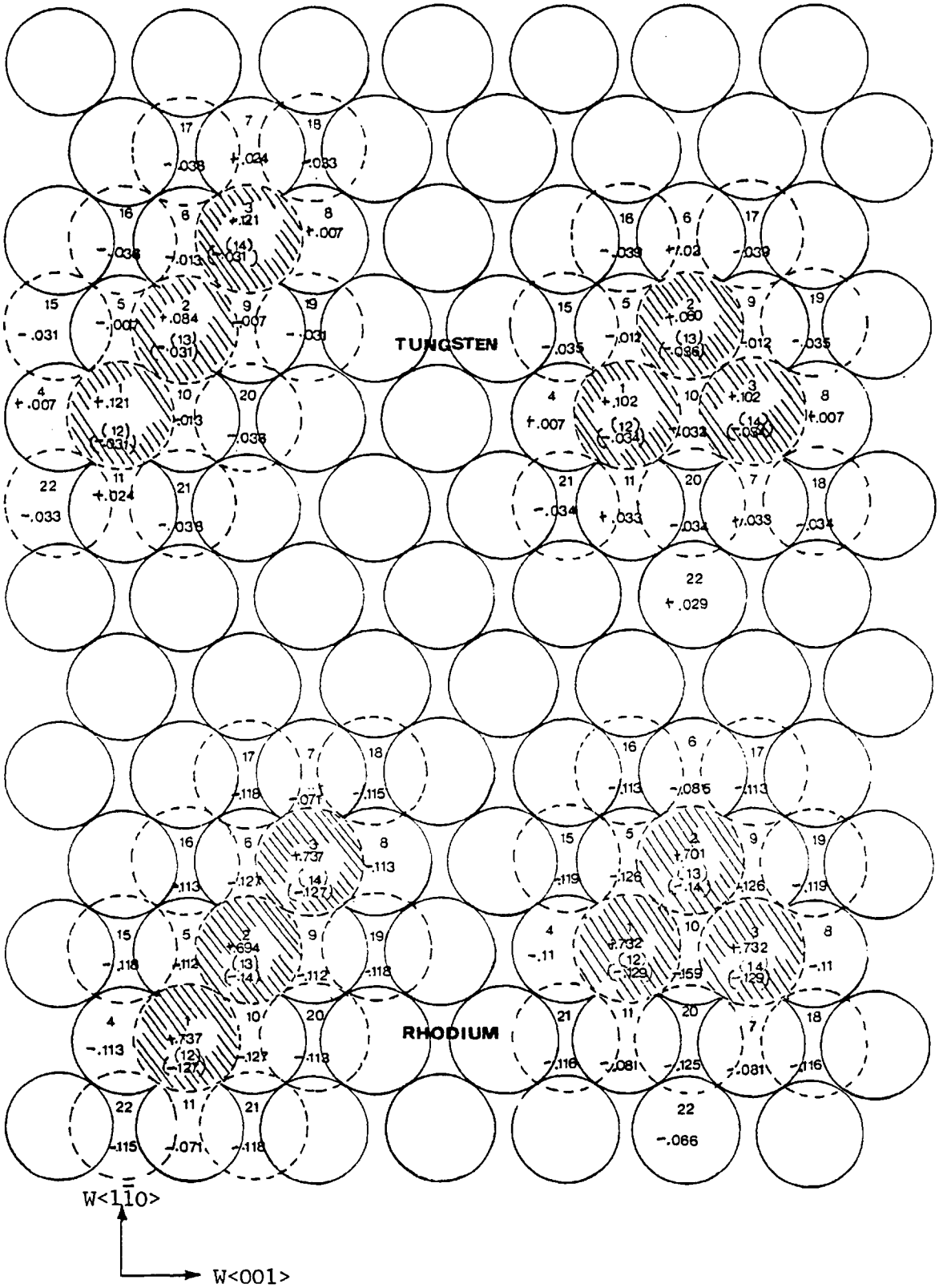


Figure D1 Charge transfers within the "unit cell".
Shaded circles: adatoms; dashed open circles: second layer substrate atoms; solid open circles: first layer substrate atoms.

REFERENCES

1. E. Bauer and H. Poppa, Thin Solid Films 12, (1972), 167
2. J.A. Venables and G.L. Price in Epitaxial Growth B, edited by J.W. Mathews (Academic Press 1975)
3. M. Prutton, Surface Physics, (Clarendon Press, Oxford, 1975).
4. R. Gomer, Field electron emission and ionization (Oxford University Press, 1961)
5. E.W. Muller and T.T. Tsong, Field Ion Microscopy (Elsevier, N.Y. 1969)
6. K.M. Bowkett and D.A. Smith, Field Ion Microscopy (N. Holland Amsterdam 1970)
7. J.P. Jones, Proc. Roy. Soc. A284, (1965), 469
8. J.P. Jones and A.D. Martin, Surface Sci. 41 (1974) 559
9. Z. Sidorski, T. Szelwicki and Z. Dworecki, Thin Solid Films, 75 (1981) 87
10. G.D.W. Smith and J.S. Anderson Surface Sci. 24 (1971) 459
11. A.J. Melmed, J. Appl. Phys. 36 (1965) 3585
12. A.J. Melmed, Surface Sci. 7 (1967) 478
13. W.R. Graham, D.A. Reed and F. Hutchinson, J. Appl. Phys., 43 (1972) 2951
14. E. Sugata, S. Ishii and K. Masui, Surface Sci., 24 (1971) 612
15. D.S. Whitmell, Surface Sci., 11 (1968) 37
16. D.W. Bassett, Surface Sci., 23 (1970) 240
17. D.W. Bassett in N.A.T.O.-ASI Conference proceeding, (Les Arcs 1981)
18. G. Ehrlich, Ann. Rev. Phys. Chem., 31 (1980) 603
    also G. Ehrlich, Physics Today, 34 (1981) 44
19. D.W. Bassett and M.J. Parsley, J. Phys. D 3 (1970) 707
20. T.T. Tsong and G. Kellogg, Phys. Rev. B 12 (1975) 1343

21. P.L. Cowan and T.T. Tsong, CRC Crit. Rev. Solid State Mater. Sci. 7 (1978) 289

22. W.R. Graham and G. Ehrlich, Thin Solid Films 25 (1975) 85

23. T. Sakata and S. Nakamura, Surface Sci., 51 (1975) 313

24. K. Stolt, W.R. Graham and G. Ehrlich, J. Chem. Phys. 65 (1975) 3206

25. W.R. Graham and G. Ehrlich, Surface Sci., 45 (1974) 530

26. P.G. Flahire and W.R. Graham, Thin Solid Films, 51 (1978) 175

27. D.A. Reed and G. Ehrlich, Phil. Mag., 32 (1975) 1095

28. D.W. Bassett, J. Phys. C. 9 (1976) 2491

29. D.W. Bassett, Thin Solid Films, 48 (1978) 237

30. P.G. Flahire and W.R. Graham, Surface Sci., 91 (1980) 463

31. G. Ayrault and G. Ehrlich, J. Chem. Phys. 60 (1974) 281

32. D.W. Bassett and P.R. Webber, Surface Sci., 70 (1978) 52o

33. R.T. Tung and W.R. Graham, Surface Sci., 97 (1980) 73

34. R. Casanova and T.T. Tsong, Phys. Rev. B 22 (1980) 5590

35. P.G. Flahire and W.R. Graham, Surface Sci., 91 (1980) 449

36. J. Wrigley and G. Ehrlich, Phys. Rev. Lett., 44 (1980) 449

37. E.W. Plummer and T.N. Rhodin, J. Chem. Phys., 49 (1968) 3479

38. F. Cyrot-Lackmann and F. Ducastelle, Phys. Rev. B 4 (1971) 2406

39. G.L. Kellogg, T.T. Tsong and P. Cowan, Surface Sci., 70 (1978) 485

40. T.T. Tsong and R. Casanova, Phys. Rev. B 22 (1980) 4632

41. D.W. Bassett and D.R. Tice, in "The Physical Basis for Heterogeneous Catalysis", edited by E. Crauglis and R.I. Jaffee (Plenum Press, N.Y. 1975)

42. D.W. Bassett and D.R. Tice, Surface Sci., 40 (1973) 499

43. D.W. Bassett and M.J. Parsley, Nature, 221 (1969) 1046

44. D.R. Tice, Ph.D. Thesis, University of London, (1975)

45. D.R. Tice and D.W. Bassett, Thin Solid Films, 20 (1974) 537

46. D.W. Bassett, in Surface and Defect Properties of Solids, 2 (The Chemical Society 1973)

47. M.R. Mruzik and G.M. Pound, J. Phys. F. 11 (1981) 1403

48. T.L. Einstein, C.R.C. Crit. Rev. Solid State Mater. Sci., 8 (1978) 181

49. H.W. Fink, K. Faulian and E. Bauer, Phys. Rev. Lett., 44 (1980) 1008

50. H.W. Fink and G. Ehrlich, Surface Sci. 110 (1981) L 611

51. J.P. Biberian and G.A. Somarjai, J. Vac. Sci. Technol. 16 (1979) 2073

52. G.E. Rhead, J. Vac. Sci. Technol. 13 (1976) 603

53. E. Bauer, J. Physique, 38 (1977) C4-146

54. P. Hahn, J. Claber, M. Henzler, J. Appl. Phys. 51 (1980) 2079

55. N.J. Taylor, Surface Sci., 4 (1966) 161

56. A.R. Moss and B.H. Blott, Surface Sci. 17 (1969) 240

57. E. Bauer, H. Poppa, G. Todd and F. Bonczek, J. Appl. Phys. 45 (1974) 5164

58. E. Bauer, H. Poppa, G. Todd and P.R. Davis, J. Appl. Phys. 48 (1977) 3773

59. W. Schlenk and E. Bauer, Surface Sci., 93 (1980) 9

60. S. Prigge, H. Roux and E. Buaer, Surface Sci., 107 (1981) 101

61. F. Soria and H. Poppa, J. Vac. Sci. Technol. 17 (1980) 449

62. P.D. Augustus and J.P. Jones, Surface Sci., 64 (1977) 713

63. R. Butz and H. Wagner, Surface Sci., 87 (1979) 69

64. M. Strongin, M. El-Batanouny and M.A. Pick, Phys. Rev. B, 22 (1980) 3126

65. R. Smoluchowski, Phys. Rev., 60 (1941) 661

66. K. Besocke and H. Wagner, Phys. Rev. B8 (1973) 4597

67. e.g. A.G. Fedorus and A.G. Naumovets, Surface Sci., 21 (1970) 426

68. T. Halicioglu, Thin Solid Films, 32 (1976) 169

69. L.C.A. Stoop, Thin Solid Films, 62 (1979) 115
Also see, Thin Solid Films, 42 (1977) 33

70. R.J. Gupta, Physical Rev. B23 (1981) 6265

71. A.G. Naumovets and A.G. Fedorus, Sov. Phys. Solid State 10 (1968) 627

72. A. Sepulveda and G.E. Rhead, Surface Sci. 66 (1977) 436

73. E. Gillet and B. Gruzza, Surface Science 97 (1980) 553

74. P. Akhter, J. Derrien, A.P. Janssen and J.A. Venables, Proc. Inst. Phys. Conf. Ser. 52 (EMAG 79) 383

75. K. Hartig, A.P. Janssen and J.A. Venables, Surface Sci. 74 (1978) 69.

76. L.A. Bruce and H. Jaeger, Phil. Mag. A36 (1977) 1331

77. L.A. Bruce and H. Jaeger, Phil. Mag. A37 (1978) 337

78. L.A. Bruce and H. Jaeger, Phil. Mag. A38 (1978) 223

79. L.A. Bruce and H. Jaeger, Phil. Mag. A40 (1979) 97

80. R. Haydock, V. Heine, M.J. Kelly in Solid State Phys. 35 (1980)

81. D.G. Pettifor, Calphad 1 (1977) 305

82. T.T. Tsong, Surface Sci., 70 (1978) 211

83. E.W. Muller, S.V. Krishnaswamy and S.B. Mclane, Surface Sci. 23 (1970) 112

84. T.T. Tsong and E.W. Muller, Phys. Rev. Letters, 25 (1970) 911

85. K.D. Rendulic, Surface Sci., 70 (1978) 234

86. K.D. Rendulic, Surface Sci., 47 (1975) 440

87. K.D. Rendulic, Surface Sci., 34 (1973) 581

88. D. McKinstry, Surface Sci., 29 (1972) 37

89. D.G. Brandon, in Field Ion Microscopy, edited by Hren and Ranganathan (Plenum N.Y. 1968)

90. R. Gomer and L.W. Swanson, J. Chem. Phys. 38 (1963) 1613

91. J.W. Gadzuk, Phys. Rev. B1 (1970) 2110

92. R.G. Forbes, Surface Sci., 70 (1978) 239

93. T.T. Tsong, J. Chem. Phys. 54 (1971) 4205

94. M. Vesely and G. Ehrlich, Surface Sci., 34 (1973) 547

95. A.R. Waugh, E.D. Boyles and M.J. Southon, Surface Sci., 61 (1976) 109

96. E. Bauer, in Techniques of Metals Research 2 (Interscience Publishers 1969)

97. M. Prutton, Metallurgical Reviews 16 (1971) 95

98. G. Ertl and J. Küppers, Low energy electrons and surface chemistry, (Verlag Chemie 1974)

99 M.W. Roberts and C.S. Mckee, Chemistry of the Metal-Gas Interface (Clarendon Press, Oxford 1978)

100. A Guinier, X-Ray Diffraction in Crystals (Freeman, San Francisco 1963)

101. J.B. Pendry, Low energy electron diffraction: the theory and its application to the determination of surface structure (Academic Press, N.Y. 1974)

102. R.L. Park, J.E. Houston and D.G. Schreiner, Rev. Sci. Instrum., 42 (1971) 60

103. G. Comsa, Surface Sci., 81 (1979) 57

104. G.C. Wang and M.G. Lagally, Surface Sci., 81 (1979) 69

105. M. Henzler, in Topics in Current Physics, Electron Spectroscopy for Surface Analysis, edited by H. Ibach, (Springer, Berlin 1977), 4 p.117

106. M. Henzler, in Advances in Solid State Physics, edited by J. Treusch (Festokörperprobleme XIX, Vieweg, 1979), p.193

107. P.J. Estrup and E.G. McRae, Surface Sci., 25 (1971) 1

108. C. Kittel, Introduction to Solid State Physics (J. Wiley and Sons, 1971)

109. R.L. Gerlach and T.N. Rhodin, Surface Sci., 17 (1969) 32

110. E. Bauer, Surface Sci., 7 (1967) 351

111. P.W. Palmberg and T.N. Rhodin, J. Chem. Phys., 49 (1968) 147

112. E.J. Scheibner and L.N. Tharp, Surface Sci., 8 (1967) 247

113. C.C. Chang, Surface Sci., 25 (1971) 53

114. R.W. Joyner and M.W. Roberts in Surface and Defect Properties of Solids, 4, The Chemical Society, London (1975) p.68

115. M.F. Chung and L.H. Jenkins, Surface Sci., 22 (1970) 479

116. N.J. Taylor, Rev. Sci. Instrum., 40 (1969) 792

117. T.W. Haas and J.T. Grant, Appl. Phys. Lett., 16 (1970) 172 (see also ref. 114).

118. M.P. Seah and W.A. Dench, Surface and Interface Analysis 1 (1979) 2

119. For example, P.A. Redhead, J.P. Hobson and E.V. Kornelson, The Physical Basis of Ultrahigh vacuum (Chapman and Hall, London 1968)

120. M.J. Parsley, Ph.D. thesis, University of London, 1969

121. P.R. Webber, Ph.D. thesis, University of London, 1977

122. A.P. Jansson and J.P. Jones, J. Appl. Phys. 4 (1971) 118

123. A.J.W. Moore, J. Phys. Chem. Solids, 23 (1962) 907

124. E.W. Muller, Surface Sci., 2 (1964) 484

125. W. Benecke, K. Faulian and E. Bauer, 25th International Field Emission Symposium, Oxford, 1977

126. G. Ehrlich and F.G. Hudda, J. Chem. Phys., 44 (1966) 1039

127. G. Ehrlich, J. Chem. Phys. 44 (1966) 1050

128. G. Ayrault, Ph.D. thesis, University of Illinois at Urbana-Champaign, 1974

129. T.T. Tsong, P. Cowan and G. Kellog, Thin Solid Films 25 (1975) 97

130. J. Topping, Errors of Observation and Their Treatment (Chapman and Hall, 1972)

131. K. Senkiw, Ph.D. thesis, University of London, 1980

132. T.E. Madey and J.T. Yates, Nuovo Cim. Suppl., 5 (1967) 483

133. W.H. Weinberg and R.P. Merril, J. Chem. Phys., 56 (1972) 2881

134. T.W. Haas and A.G. Jackson, J. Chem. Phys., 44 (1966) 2921

135. E.A. Wood, Crystal orientation manual, Columbia University Press, 1963

136. D. Tabor, J.M. Wilson and T.J. Bastow, Surface Sci., 26 (1971) 471

137. P. Wilmer, Ph.D. thesis, University of Southampton,

138. N.R. Avery, Surface Sci., 33 (1972) 107

139. R.M. Stern, App. Phys. Lett., 5 (1964) 218

140. R. Baudoing and R.M. Stern, Surface Sci., 10 (1968) 392

141. D.F. Ollis and M. Boudart, Surface Sci., 23 (1970) 320

142. W.H. Weinberg and R.P. Merril, J. Chem. Phys., 56 (1972) 2893

143. J.T. Grant and T.W. Haas, Surface Sci., 24 (1971) 332

144. T.W. Haas, J.T. Grant and G.J. Dooley III, J. Vac. Sci. and Tech., 7 (1970) 43

145. P.B. Sewell, D.F. Mitchell and M. Cohen, Dev. in Appl. Spect., 7A (1969) 61

146. L.H. Germer and J.W. May, Surface Sci., 4 (1966) 452

147. H.M. Kennett and A.E. Lee, Surface Sci., 48 (1975) 591

148. J. Chen and C.A. Papageorgopolous, Surface Sci., 20 (1970) 195

149. E.B. Bas and U. Baninger, Surface Sci., 41 (1974) 1

150. I. Szmerska and M. Lipska, J. Catal., 47 (1977) 144

151. S.L. Bernasek and G.E. Staudt, J. Catal., 45 (1976) 372

152. K. Kuminori, T. Kawai, T. Kondow, T. Onishi and K. Tamaru, Surface Sci., 46 (1974) 567

153. R.W. Joyner, J. Rickman and M.W. Roberts, Surface Sci., 39 (1975) 445

154. A.J. Melmed, J. Appl. Phys., 40 (1969) 2330

155. L.N. Tharp and E.J. Scheibner, J. Appl. Phys., 38 (1967) 3320

156. C.C. Chang, Surface Sci., 48 (1975) 9

157. D.W. Bassett, Surface Sci., 21 (1970) 181

158. B. Gruzza and E. Gillet, Thin Solid Films, 68 (1980) 345

159. B. Regan, D.W. Bassett and P.J. Dobson, private communication

160. M. Lipson, Optical Transforms (Academic Press, N.Y., 1972)

161. T. Engel, H. Niehus and E. Bauer, Surface Sci., 52 (1975) 237

162. J.T. Grant and T.W. Haas, Surface Sci., 21 (1970) 76

163. D.G. Castner, B.A. Sexton and G.A. Somorjai, Surface Sci., 71 (1978) 519

164. A.G. Jackson and M.P. Hooker, Surface Sci., 6 (1967) 297

165. C.D. Gelatt, H. Ehrenreich and R.E. Watson, Phys. Rev. B15 (1977) 1613

166. D.G. Pettifor, J. Phys. C 3 (1970) 367

167. R.L. Johannes and R. Haydock, J. Phy. F. 5 (1975) 2055

168. N.R. Burke, Surface Sci., 58 (1976) 349

169. C.M.M. Nex, Cambridge Recursion Method Library, Cavendish Laboratory, Cambridge

170. N. Beer, private communication

171. J. Friedel, in The Physics of Metals, edited by J.M. Ziman (University Press, Cambridge 1969)

172. D.G. Pettifor, J. Phys. F., 7 (1977) 613

173. P.L. Cowan and T.T. Tsong, Surface Sci., 67 (1977) 158

174. D.G. Pettifor, Solid State Comm., 28 (1978) 621

175. D.G. Pettifor, private communication

176. M.C. Desjonqueres and F. Cyrot-Lackmann, J. Phys. F. 6 (1976) 567

177. H.P. Bonzel and E.E. Latta, Surface Sci., 76 (1978) 275

178. G.C. Bond, Catalysis by Metals, (Academic Press, London and NY, 1962)

179. T.W. Haas, J.T. Grant, and G.J. Dooley, Phys. Rev. B, 1 (1970) 1449